UNIVERSITY OF SOUTHAMPTON

# THE CIRCUMSTELLAR ENVIRONMENTS OF BE STARS IN X-RAY BINARIES

By James Bernard Stevens

**Doctor of Philosophy**

Faculty of Science

Department of Physics and Astronomy

UNIVERSITY OF SOUTHAMPTON

# ABSTRACT

FACULTY OF SCIENCE
PHYSICS AND ASTRONOMY

**Doctor of Philosophy**

## THE CIRCUMSTELLAR ENVIRONMENTS OF BE STARS IN X-RAY BINARIES

By James Bernard Stevens

This thesis contains results from a long-term campaign to monitor the behaviour of Be/X-ray binary systems at multiple wavelengths. The work presented in this thesis concentrates on the application of Be/X-ray binary observations to contribute to the understanding of the Be star phenomenon itself. I present studies of the X-ray behaviour of these systems – effectively using the Neutron Star as a probe of the Be star's envelope – and seek correlation between this and the behaviour of the Be star inferred from optical and infrared observations. I attempt to model the X-ray light-curves as accretion from a circumstellar disc, and investigate the validity of these techniques by considering recent claims that the orbiting neutron stars in Be/X-ray binaries perturb the Be stars' circumstellar discs. Finally, I present a study of Be/X-ray binaries in the Magellanic Clouds, identifying optical counterparts to a number of recently discovered systems.

# CONTENTS

**CHAPTER 1 – BE STARS** ..... **18**

1.1 OBSERVATIONAL CHARACTERISTICS OF BE STARS ..... 18

*1.1.1 Emission Lines* ..... *20*

*1.1.2 Infrared excess* ..... *23*

*1.1.3 UV Observations* ..... *25*

*1.1.4 Direct imaging* ..... *25*

*1.1.5 The variability of Be stars* ..... *25*

1.1.1.1 Disc loss and regeneration ..... 26

1.1.1.2 V/R variability ..... 27

1.1.1.3 Short term variability ..... 27

*1.1.6 Population characteristics* ..... *27*

1.2 BE STAR CIRCUMSTELLAR ENVELOPES ..... 28

*1.2.1 Evidence for disc shaped envelopes* ..... *28*

1.2.1.1 Optical emission lines ..... 28

1.1.1.2 IR and radio continuum emission ..... 29

1.3 FORMATION OF BE STAR ENVELOPES ..... 30

1.3.1.1 Rotationally flattened discs ..... 31

1.3.1.2 The Wind Compressed Disc model ..... 31

1.1.1.3 Rotation-pulsation model ..... 36

1.1.1.4 The decelerated wind model ..... 37

1.1.1.5 Viscous Excretion Model ..... 37

1.4 V/R CYCLES AND ASSOCIATED VARIABILITY ..... 38

*1.1.1 One-armed global oscillations* ..... *39*

*1.1.2 Prograde or retrograde precession?* ..... *40*

1.5 SUMMARY ..... 42

**CHAPTER 2 – BE/X-RAY BINARIES** ..... **44**

2.1 HISTORICAL BACKGROUND TO X-RAY BINARIES ..... 45

2.2 BINARY STARS ..... 48

*2.2.1 Binary orbits* ..... *48*

*2.2.2 Roche potential and Roche lobes* ..... *48*

1.3 ENERGY SOURCE OF X-RAY BINARIES ..... 51

1.4 HIGH MASS X-RAY BINARIES ..... 51

*1.4.1 Supergiant X-ray binaries* ..... *53*

*1.4.2 Be/X-ray binaries* ..... *57*

1.5 ACCRETING NEUTRON STARS ..... 59

*1.1.1 X-ray pulsars* ..... *60*

*1.1.2 X-ray pulse arrival timing* ..... *60*
*1.1.3 X-ray pulse profiles* ..... *61*
*1.1.4 Centrifugal inhibition of accretion* ..... *63*
1.6 PERIODIC OUTBURSTS IN BE/X-RAY BINARIES ..... 64
1.7 BE/X-RAY BINARY EVOLUTION ..... 69
*1.7.1 Origin of High Mass X-ray binaries* ..... *69*
1.7.1.1 Surviving a supernova explosion ..... 69
1.7.1.2 Mass transfer in massive binaries ..... 70
*1.7.2 Neutron star kick velocities from supernova explosions* ..... *70*
*1.7.3 Do Be/X-ray binaries die in Gamma Ray Bursts?* ..... *71*
1.8 ISOLATED AND X-RAY BINARY BE STAR POPULATIONS ..... 72
*1.8.1 Spectral types* ..... *72*
*1.8.2 Interaction between neutron star and circumstellar disc* ..... *73*
1.9 NEUTRON STARS AS PROBES OF BE STAR DISCS ..... 76

**CHAPTER 3 – A LONG TERM STUDY OF THE BE/X-RAY BINARY 4U 1145-619 ..... 78**

1.1 SOURCE HISTORY ..... 79
1.2 OBSERVATIONS ..... 80
*1.2.1 UBV Photometry* ..... *80*
*1.2.2 Infrared Photometry* ..... *81*
*1.1.3 Optical Spectroscopy* ..... *83*
1.1.3.1 Hα and Hβ Spectroscopy ..... 83
1.1.1.2 Classification Region Spectroscopy ..... 86
1.3 ASTROPHYSICAL PARAMETERS ..... 88
*1.3.1 UBV Photometry* ..... *88*
*1.1.2 Strömgren Photometry* ..... *89*
1.1.1.1 Circumstellar and interstellar reddening and derived intrinsic photometric indices ..... 91
1.1.1.2 Luminosity ..... 92
1.1.1.3 Effective Temperature ..... 93
1.1.1.4 Radius ..... 93
1.1.1.5 Mass and Gravity ..... 94
*1.1.3 Optical Spectroscopy* ..... *94*
1.1.3.1 Spectral Classification ..... 94
1.1.1.2 Rotational Velocity ..... 95
1.1.1.3 Diffuse Interstellar Bands ..... 95
*1.1.4 4U 1145-619 – A model for the system* ..... *96*
*1.1.5 The nature of Be/X-ray binary systems* ..... *98*
1.4 DISCLOSS AND RELATED X-RAY ACTIVITY ..... 100
*1.4.1 Recent Be star activity* ..... *100*
*1.1.2 Collated source history* ..... *101*

1.1.1.1 Be star activity from optical and infrared data ..... 101
1.1.1.2 X-ray flux history ..... 104
*1.1.3 Correlations between Be star activity and X-ray emission* ..... *106*
*1.1.4 Accretion mechanisms* ..... *108*
1.5 SPECTRAL VARIABILITY ..... 109
1.6 SUMMARY ..... 118
*1.6.1 Astrophysical parameters* ..... *118*
*1.1.2 Discloss and related X-ray behaviour* ..... *119*
*1.1.3 Spectral variability* ..... *119*

**CHAPTER 4 – MODELLING THE X-RAY LIGHTCURVES OF BE/X-RAY BINARIES . 120**

1.1 INTRODUCTION ..... 121
1.2 BE/X-RAY BINARY X-RAY LIGHTCURVE MODEL ..... 122
*1.2.1 Accretion onto a compact object* ..... *122*
*1.1.2 The orbits of Be/X-ray binaries* ..... *124*
*1.1.3 Be star disc model* ..... *128*
*1.1.4 X-ray lightcurve model* ..... *128*
1.3 RESULTS ..... 130
*1.3.1 Dependence on Be star wind parameters* ..... *131*
1.3.1.1 Initial wind outflow velocity and power-law gradient ..... 131
1.3.1.2 Disc sound speed/temperature ..... 151
1.1.1.3 Disc rotation model ..... 153
*1.1.2 Dependence on orbital parameters* ..... *155*
1.1.1.1 Orbital eccentricity ..... 155
1.1.1.2 Orbital period ..... 158
1.4 MODELLING THE X-RAY LIGHTCURVE OF EXO 2030+375 ..... 159
*1.4.1 Source history* ..... *159*
*1.1.2 The X-ray lightcurve of EXO 2030+375* ..... *160*
1.5 POSSIBLE EVIDENCE FOR BE STAR DISC PERTURBATION BY AN ORBITING NEUTRON STAR ... 166
*1.1.1 Observations* ..... *167*
*1.1.2 Spectra variability* ..... *167*
1.1.2.1 Variability on timescales of minutes and hours ..... 167
1.1.1.2 Night to night variability ..... 168
*1.1.3 Cause of night to night variability* ..... *170*
1.6 SUMMARY ..... 172
*1.1.1 Model predictions* ..... *172*
*1.1.2 Model fit to the X-ray lightcurve of EXO 2030+375* ..... *174*
*1.1.3 Binary interaction* ..... *176*

**CHAPTER 5 – OPTICAL COUNTERPARTS TO BE/X-RAY BINARIES IN THE MAGELLANIC CLOUDS ..... 177**

1.1 INTRODUCTION ..... 178
*1.1.1 X-ray binaries in normal galaxies* ..... *179*
*1.1.2 High Mass X-ray Binaries in the Magellanic Clouds* ..... *179*
1.2 OBSERVATIONS ..... 182
*1.2.1 CCD Photometry* ..... *182*
*1.1.2 Systematic errors* ..... *186*
*1.1.3 Optical spectroscopy* ..... *187*
1.3 RESULTS AND DISCUSSION OF INDIVIDUAL SOURCES ..... 189
*1.3.1 RX J0032.9-7348* ..... *189*
*1.1.2 RX J0049.1-7250* ..... *193*
*1.1.3 AX J0051-722* ..... *196*
*1.1.4 RX J0051.8-7231* ..... *198*
*1.1.5 RX J0053.8-7226* ..... *200*
*1.1.6 RX J0054.9-7226* ..... *205*
*1.1.7 RX J0101.0-7321* ..... *209*
*1.1.8 RX J0117.6-7330* ..... *212*
1.1.1.1 Spectral classification ..... 214
*1.1.9 EXO 0531.1-6609* ..... *216*
*1.1.10 H0544-644* ..... *219*
1.4 DISCUSSION ..... 223

**CHAPTER 6 – CONCLUSIONS AND FURTHER WORK ..... 226**

6.1 SUMMARY OF SIGNIFICANT RESULTS ..... 226
*6.1.1 4U1145–619* ..... *226*
*6.1.2 Be/X-ray binary lightcurve models* ..... *227*
*6.1.3 Optical counterparts to Magellanic Cloud Be/X-ray binaries* ..... *227*
6.2 POSSIBILITIES FOR FURTHER INVESTIGATION ..... 228
*6.2.1 Disc perturbation by orbiting neutron star* ..... *228*
*6.2.2 Enhanced X-ray lightcurve models* ..... *228*
*6.2.3 Identification of optical counterparts to Be/X-ray binaries* ..... *229*
*6.2.4 Association of LMC/SMC HMXBs with SNRs* ..... *229*

**ACKNOWLEDGEMENTS ..... 230**

**BIBLIOGRAPHY ..... 233**

# FIGURES

FIGURE 1-1. HA, FE II λ5317 AND HE I λ5876 EMISSION LINE PROFILES FOR NINE BE STARS. FE II AND HE I FLUX SCALES ARE EXPANDED BY A FACTOR OF 10 RELATIVE TO THE HA SCALE. TAKEN FROM HUMMEL & VRANKEN (1995). EACH ARE NORMALISED TO THE LOCAL CONTINUUM, THEN OFFSET SO THAT THE CONTINUUM FLUX IS APPROXIMATELY 1.0 (HA), 0.0 (FE II) AND -1.0 (HE I) ..... 21

FIGURE 1-2. INFRARED SPECTRA OF EXO 2030+375 – TAKEN FROM REIG, STEVENS, COE *ET AL.* (1998) ..... 22

FIGURE 1-3. SPECTRAL ENERGY DISTRIBUTIONS OF BE STARS A ERI, Φ PER, Δ CEN AND X OPH. FLUXES ARE NORMALISED TO THE 518.3-Å FLUX FOR ALL EXCEPT Φ PER (NORMALISED TO 724.1-Å). THE SOLID LINES IN EACH CASE REPRESENT THE BEST FIT KURUCZ MODELS WITH PARAMETERS AS ANNOTATED ON EACH PLOT ..... 24

FIGURE 1-4. WIND COMPRESSED DISC MODEL PREDICTIONS. LEFT: THE RATIO OF TERMINAL WIND VELOCITY TO STELLAR ESCAPE VELOCITY AS A FUNCTION OF SPECTRAL TYPE. RIGHT: THE THRESHOLD ROTATION VELOCITY FOR DISC CREATION AS A FRACTION OF THE STELLAR ESCAPE VELOCITY AS A FUNCTION OF SPECTRAL TYPE. TAKEN FROM BJORKMAN (1994). ..... 32

FIGURE 1-5. TWO-DIMENSIONAL SCHEMATIC OF A WIND COMPRESSED DISC. THE WIND STREAMLINES ARE SHOWN BEING DEFLECTED TOWARD THE EQUATOR. THE INSET DIAGRAM SHOWS THE STANDING SHOCKS FORMING EITHER SIDE OF THE EQUATOR. TAKEN FROM BJORKMAN & CASSINELLI (1993). ..... 33

FIGURE 1-6. DISTRIBUTION OF V/R CYCLE PERIODS BY SPECTRAL TYPE. OPEN CIRCLES REPRESENT STARS KNOWN OR SUSPECTED TO BE BINARIES. TAKEN FROM OKAZAKI (1996). ..... 41

FIGURE 1-7. V/R VARIATIONS IN THE HA LINE OF HD245770, WITH A PERIODICITY OF ~ 18 MONTHS (TAKEN FROM NEGUERUELA ET AL. (1998). ..... 41

FIGURE 2-1. X-RAY IMAGE OF THE GALACTIC PLANE FROM THE EXOSAT GALACTIC SURVEY, SHOWING THE CONCENTRATION OF BRIGHT X-RAY POINT SOURCES AT LOW GALACTIC LATITUDES, AND TOWARDS THE CENTRE OF THE GALAXY. ..... 45

FIGURE 2-2. SKY DISTRIBUTIONS OF (TOP) HIGH-MASS X-RAY BINARIES AND (BOTTOM) LOW-MASS X-RAY BINARIES. THE OPEN CIRCLES IN THE LOWER MAP REPRESENT GLOBULAR CLUSTER SOURCES. THE MAPS ARE BASED ON THE CATALOGUE OF VAN PARADIJS (1995). ..... 47

FIGURE 2-3. EQUIPOTENTIAL SURFACES OF A CLOSE BINARY SYSTEM, SHOWING THE L1 AND L2 LAGRANGIAN POINTS AND THE ROCHE LOBE. ..... 49

FIGURE 2-4. HERTZSPRUNG-RUSSEL DIAGRAM WITH THE POSITIONS OF THE OPTICAL COUNTERPARTS TO SUPERGIANT AND BE STAR X-RAY BINARIES MARKED. ..... 53

FIGURE 2-5. ROCHE GEOMETRY CALCULATED FOR A SYSTEM WITH MASSES AND ORBITAL SEPARATION SIMILAR TO THE SUPERGIANT X-RAY BINARY CEN X-3. ..... 54

FIGURE 2-6. MASS-TRANSFER VIA A STRONG STELLAR WIND IN A SUPERGIANT X-RAY BINARY. THE SUPERGIANT IS TIDALLY AND ROTATIONALLY DISTORTED, ITS WIND IS ENHANCED THROUGH THE LINE OF CENTRES BY THE GRAVITATIONAL INFLUENCE OF THE COMPACT COMPANION, LEADING TO A TIDAL STREAM THROUGH THE INNER LAGRANGIAN POINT ($L_1$) ..... 55

FIGURE 2-7 . MASS TRANSFER VIA ROCHE LOBE OVERFLOW IN A SUPERGIANT X-RAY BINARY. THE SUPERGIANT FILLS ITS ROCHE LOBE, AT THE INNER LAGRANGIAN POINT ($L_1$) THE NET GRAVITY IS ZERO, AND MATERIAL FALLS INTO THE GRAVITATIONAL WELL OF THE COMPACT OBJECT, FORMING AN ACCRETION DISK. ..... 56

FIGURE 2-8. X-RAY LIGHTCURVE OF THE SUPERGIANT X-RAY BINARY SMC X-1. THE RED CURVE REPRESENTS ONE-DAY AVERAGE FLUXES PUBLICLY AVAILABLE FROM THE RXTE ASM, THE BLUE CURVE IS A 10-DAY MOVING AVERAGE OF THE COUNT-RATE. ..... 57

FIGURE 2-9. SCHEMATIC OF A BE/X-RAY BINARY SYSTEM. THE ECCENTRICITY OF THE NEUTRON STAR'S ORBIT CAUSES IT TO ENCOUNTER VARYING VELOCITY/DENSITY WIND MATERIAL THROUGHOUT THE ORBITAL CYCLE. ..... 58

FIGURE 2-10. SCHEMATIC OF AN X-RAY PUSLAR SHOWING HOW THE PULSATIONS RESULT FROM A MISALIGNMENT OF THE MAGNETIC AND ROTATION AXES OF THE NEUTRON STAR. X-RAYS ARE EMITTED IN BEAMS FROM THE MAGNETIC POLES WHICH SWEEP ACROSS THE LINE OF SIGHT LEADING TO PERIODIC PULSES OF X-RAY FLUX. ..... 61

FIGURE 2-11. CORBET DIAGRAM (AFTER CORBET 1986) SHOWING THE DIFFERENT RELATIONSHIPS BETWEEN ORBITAL PERIOD AND PULSE PERIOD FOR X-RAY PULSARS IN SUPERGIANT SYSTEMS (WIND-FED AND ROCHE-LOBE OVERFLOW-FED) AND IN BE STAR SYSTEMS. ..... 63

FIGURE 2-12. SUMMARY OF ALL DETECTED OUTBURSTS OF TRANSIENT PULSARS SEEN BY BATSE SINCE THE LAUNCH OF THE COMPTON GAMMA RAY OBSERVATORY. NOTE THE PERIODICITY EVIDENT IN THE RECURRENT OUTBURSTS OF SOURCES GRO J2058+42, A0535+262, 4U 1145-619, 2S1845-024 AND EXO 2030+375. ..... 67

FIGURE 2-13. X-RAY LIGHTCURVE FOR 4U1145–619, PLOTTED USING PUBLIC DATA TAKEN FROM THE *RXTE* ASM. THE PREDICTED DATES OF X-RAY OUTBURSTS ARE INDICATED WITH GREEN LINES. ..... 68

FIGURE 2-14. SPECTRA OF THE BE/X-RAY BINARY 4U0115+634 SHOWING THE EVOLUTION OF THE HA AND HE I LINES OVER ~1.5 YEARS FROM SHELL PROFILES TO V/R CYCLES. TAKEN FROM NEGUERUELA ET AL. (1998). ..... 75

FIGURE 3-1. TOP: INFRARED *J, H, K* AND *L* LIGHTCURVES FOR V801 CEN, THE BE STAR COMPONENT OF THE X-RAY BINARY 4U1145-619, OBTAINED FROM THE SAAO BETWEEN 1993 AND 1998.

BOTTOM: J – K INDEX FOR THE SAME PERIOD. REFER TO TABLE 3-2 FOR A COMPLETE LOG OF OBSERVATIONS AND RESULTS. ..... 82

FIGURE 3-2. HA LINE PROFILES OF V801 CEN BETWEEN 1993 AND 1998. SPECTRA WERE OBTAINED FROM THE SAAO AND THE AAT. ALL SPECTRA WERE NORMALISED TO A SPLINE FIT TO THE LOCAL CONTINUUM, AND OFFSET TO ONE ANOTHER IN INCREMENTS OF 1 FLUX UNITS. ..... 85

FIGURE 3-3. CLASSIFICATION REGION SPECTRUM OF V801 CEN, THE BE STAR COMPONENT OF THE X-RAY BINARY 4U1145–619. THE DISPLAYED SPECTRUM IS A COMPOSITE OF TWO OBSERVATIONS MADE ON 21$^{ST}$ AND 23$^{RD}$ JUNE 1997 ..... 87

FIGURE 3-4. LOCATION OF V801 CEN IN COLOUR-COLOUR DIAGRAM. THE ACTUAL PHOTOMETRIC INDICES ARE SHOWN IN TABLE 3-1. ALSO PLOTTED IS THE REDDENING VECTOR, WITH DATA POINTS PLOTTED AT INCREMENTS OF 0.05 IN *E(B-V)*. ..... 89

FIGURE 3-5. OBSERVED LATITUDE DISTRIBUTION OF BE/X-RAY BINARY SYSTEMS IN GALACTIC CO-ORDINATES. ALSO PLOTTED IS THE DISTRIBUTION OF MASSIVE STARS (+/- 1$z_0$), CORRECTED FOR THE SUN'S DISTANCE ABOVE THE GALACTIC PLANE. ..... 99

FIGURE 3-6. COLOUR-MAGNITUDE DIAGRAM FOR V801 CEN, USING Y AND (B – Y) DATA TAKEN FROM ESO'S LONG-TERM PHOTOMETRY OF VARIABLES PROJECT CATALOGUES (STERKEN ET AL. 1995). ..... 102

FIGURE 3-7. TOP AND SECOND PANEL: LIGHTCURVES OF 4U1145-619 FOR THE PERIOD 1978--1994, IN STRÖMGREN FILTER BANDS, DATA TAKEN FROM PAKULL ET AL. (1980), ESO'S LONG TERM PHOTOMETRIC VARIABLE PROJECT CATALOGUES (STERKEN ET AL. 1995), DENSHAM & CHARLES (1982), AND FROM HAMMERSCHLAG-HENSBERGE ET AL. (1980). ARROWS SHOW THE DATES OF DETECTED X-RAY OUTBURSTS, AND ARE SIZED TO GIVE A CRUDE INDICATION OF THE INTENSITY OF THE OUTBURST. THIRD PANEL: IR *K* BAND LIGHTCURVE FROM 1978-1996; THE OPEN CIRCLES REPRESENT OUR DATA, OTHER DATA TAKEN FROM GLASS (1979), AND WATERS ET AL. (1988). BOTTOM PANEL: EW(HA) PLOT, 1978-1996. OPEN CIRCLES AGAIN REPRESENT OUR OWN DATA, OTHER DATA TAKEN FROM COOK AND WARWICK (1987B). NOTE THE TWO PREVIOUS EPISODES OF DISC-LOSS INDICATED BY A DECLINE IN THE OPTICAL LUMINOSITY OF THE SOURCE. MOST RECENT DATA SHOW A THIRD SUCH DISC-LOSS EVENT. ..... 103

FIGURE 3-8. THE X-RAY LIGHTCURVE OF 4U1145-619 FOR THE PERIOD 1973 – 1996, IN THE 2 – 10 KEV RANGE. ALL VALUES EXCEPT THE *EXOSAT* ME POINTS ARE CALCULATED ASSUMING A POWER LAW SPECTRUM. THIS IS TO FACILITATE COMPARISON OF MEASUREMENTS MADE IN DIFFERENT ENERGY BANDS, AND VALUES MAY BE IN ERROR BY AS MUCH AS A FACTOR OF 2 FROM ONE SATELLITE TO ANOTHER. NOTE THAT THE *GRANAT* POINT IS AN UPPER LIMIT. REFERENCES FOR X-RAY DATA ARE: *VELA*, PRIEDHORSKY & TERREL 1983; *ARIEL V*, WATSON, WARWICK & RICKETTS 1981; *EINSTEIN*, MEREGHETTI ET AL. 1987; *EXOSAT*, MEREGHETTI ET

AL. 1987; COOK & WARWICK 1987A, 1987B; *GRANAT*, GREBENEV ET AL. 1992; *BATSE*, WILSON ET AL. 1994; *RXTE*, CORBET & REMILLARD 1996. ..... 105

FIGURE 3-9. LINE PROFILES AND FIRST DERIVATIVES FOR THE HA LINE OF V801 CEN. ..... 115

FIGURE 3-10. RELATIONSHIP BETWEEN PROJECTED ROTATIONAL VELOCITIES ($\Delta V_K$) AND STRENGTH OF LINE EMISSION (EW), FOR HA (LEFT) AND HE I (6678 Å) (RIGHT). ..... 115

FIGURE 3-11. RELATIONSHIP BETWEEN THE STRENGTH OF LINE EMISSION AND RADIUS OF EMITTING REGION FOR HA (LEFT) AND HE I (6678 Å) (RIGHT). ..... 117

FIGURE 4-1. GEOMETRY OF A BE/X-RAY BINARY ORBIT, ILLUSTRATING DEFINITIONS OF TERMS USED IN THE DERIVATION OF ORBITAL PROPERTIES. ..... 125

FIGURE 4-2. X-RAY LIGHTCURVE MODEL PREDICTIONS FOR A SYSTEM WITH ORBITAL PARAMETERS EQUAL TO THOSE OF THE BE/X-RAY BINARY 4U1145-619. THE MODEL IS AS DESCRIBED IN SECTION 4-2, THE POWER-LAW GRADIENT $N = 2.0$, THE OUTFLOW VELOCITY AT THE STELLAR SURFACE HAS BEEN VARIED FROM 0 TO 1000 KM $S^{-1}$ ..... 133

FIGURE 4-3. X-RAY LIGHTCURVE MODEL PREDICTIONS FOR A SYSTEM WITH ORBITAL PARAMETERS EQUAL TO THOSE OF THE BE/X-RAY BINARY 4U1145-619. THE MODEL IS AS DESCRIBED IN SECTION 4-2, THE POWER-LAW GRADIENT $N = 2.25$, THE OUTFLOW VELOCITY AT THE STELLAR SURFACE HAS BEEN VARIED FROM 0 TO 500 KM $S^{-1}$ ..... 135

FIGURE 4-4. X-RAY LIGHTCURVE MODEL PREDICTIONS FOR A SYSTEM WITH ORBITAL PARAMETERS EQUAL TO THOSE OF THE BE/X-RAY BINARY 4U1145-619. THE MODEL IS AS DESCRIBED IN SECTION 4-2, THE POWER-LAW GRADIENT $N = 2.5$, THE OUTFLOW VELOCITY AT THE STELLAR SURFACE HAS BEEN VARIED FROM 0 TO 100 KM $S^{-1}$ ..... 137

FIGURE 4-5. X-RAY LIGHTCURVE MODEL PREDICTIONS FOR A SYSTEM WITH ORBITAL PARAMETERS EQUAL TO THOSE OF THE BE/X-RAY BINARY 4U1145-619. THE MODEL IS AS DESCRIBED IN SECTION 4-2, THE POWER-LAW GRADIENT $N = 2.75$, THE OUTFLOW VELOCITY AT THE STELLAR SURFACE HAS BEEN VARIED FROM 0 TO 50 KM $S^{-1}$ ..... 139

FIGURE 4-6. X-RAY LIGHTCURVE MODEL PREDICTIONS FOR A SYSTEM WITH ORBITAL PARAMETERS EQUAL TO THOSE OF THE BE/X-RAY BINARY 4U1145-619. THE MODEL IS AS DESCRIBED IN SECTION 4-2, THE POWER-LAW GRADIENT $N = 3$, THE OUTFLOW VELOCITY AT THE STELLAR SURFACE HAS BEEN VARIED FROM 0 TO 20 KM $S^{-1}$ ..... 141

FIGURE 4-7. X-RAY LIGHTCURVE MODEL PREDICTIONS FOR A SYSTEM WITH ORBITAL PARAMETERS EQUAL TO THOSE OF THE BE/X-RAY BINARY 4U1145-619. THE MODEL IS AS DESCRIBED IN SECTION 4-2, THE POWER-LAW GRADIENT $N = 3.25$, THE OUTFLOW VELOCITY AT THE STELLAR SURFACE HAS BEEN VARIED FROM 0 TO 10 KM $S^{-1}$ ..... 143

FIGURE 4-8. X-RAY LIGHTCURVE MODEL PREDICTIONS FOR A SYSTEM WITH ORBITAL PARAMETERS EQUAL TO THOSE OF THE BE/X-RAY BINARY 4U1145-619. THE MODEL IS AS DESCRIBED IN

SECTION 4-2, THE POWER-LAW GRADIENT $N = 3.5$, THE OUTFLOW VELOCITY AT THE STELLAR SURFACE HAS BEEN VARIED FROM 0 TO 6 KM $S^{-1}$ ..... 145

FIGURE 4-9. X-RAY LIGHTCURVE MODEL PREDICTIONS FOR A SYSTEM WITH ORBITAL PARAMETERS EQUAL TO THOSE OF THE BE/X-RAY BINARY 4U1145-619. THE MODEL IS AS DESCRIBED IN SECTION 4-2, THE POWER-LAW GRADIENT $N = 3.75$, THE OUTFLOW VELOCITY AT THE STELLAR SURFACE HAS BEEN VARIED FROM 0 TO 3 KM $S^{-1}$ ..... 147

FIGURE 4-10. X-RAY LIGHTCURVE MODEL PREDICTIONS FOR A SYSTEM WITH ORBITAL PARAMETERS EQUAL TO THOSE OF THE BE/X-RAY BINARY 4U1145-619. THE MODEL IS AS DESCRIBED IN SECTION 4-2, THE POWER-LAW GRADIENT $N = 4$, THE OUTFLOW VELOCITY AT THE STELLAR SURFACE HAS BEEN VARIED FROM 0 TO 1.5 KM $S^{-1}$ ..... 149

FIGURE 4-11. X-RAY LIGHTCURVE MODEL PREDICTIONS FOR VARIOUS ADOPTED SOUND SPEEDS IN THE BE STAR DISC. ..... 152

FIGURE 4-12. X-RAY LIGHTCURVE MODEL PREDICTIONS FOR DIFFERENT MODELS OF ROTATIONAL VELOCITY IN THE BE STAR DISC. IN EACH CASE THE ORBITAL PARAMETERS OF THE SYSTEMS HAVE BEEN CHOSEN EQUAL TO THOSE OF THE BE/X-RAY BINARY 4U1145-619, THE POWER-LAW GRADIENT $N = 3.0$, AND THE INITIAL OUTFLOW VELOCITY OF THE BE STAR'S WIND $V_0 = 1.0$ KM $S^{-1}$. THE VALUE OF A HAS BEEN VARIED FROM -0.5 (KEPLERIAN DISC) TO –1.0 (CONSERVATION OF ANGULAR MOMENTUM IN THE OUT-FLOWING MATERIAL). ..... 154

FIGURE 4-13. X-RAY LIGHTCURVE MODEL PREDICTIONS FOR VARIOUS ORBITAL ECCENTRICITIES. IN EACH PLOT, THE ORBITAL PARAMETERS (EXCEPT ECCENTRICITY) HAVE BEEN CHOSEN EQUAL TO THOSE OF THE BE/X-RAY BINARY 4U1145-619, THE WIND PARAMETERS – ANNOTATED ON EACH PLOT – WERE KEPT CONSTANT, AND THE ORBITAL ECCENTRICITY VARIED FROM 0 TO 0.5..... 157

FIGURE 4-14. X-RAY LIGHTCURVE MODEL PREDICTIONS FOR VARIOUS ADOPTED ORBITAL PERIODS. IN EACH CASE THE INITIAL OUTFLOW VELOCITY WAS KEPT CONSTANT AT 1 KM $S^{-1}$ AND THE DISC POWER-LAW GRADIENT CONSTANT AT $N = 3.5$. ..... 159

FIGURE 4-15. X-RAY LIGHTCURVE OF THE BE/X-RAY BINARY EXO2030+375. DATA FROM THE *ALL SKY MONITOR* ON THE *ROSSI X-RAY TIMING SATELLITE* WERE FOLDED ON THE ORBITAL PERIOD OF 46.02-DAYS AND AVERAGED IN BINS OF 0.04-ORBITAL PHASE. ..... 162

FIGURE 4-16. X-RAY LIGHTCURVE AND MODEL FITS FOR EXO 2030+375 ..... 163

FIGURE 4-17. LEFT: HA LINE PROFILES OF V801 CEN ON THE NIGHT OF 1997 APRIL 12. SPECTRA WERE OBTAINED AT INTERVALS OF A FEW MINUTES, AND HAVE BEEN BINNED INTO APPROXIMATELY 30 MINUTE BINS. RIGHT: RESIDUALS AFTER SUBTRACTION OF A MEAN SPECTRUM. ..... 168

FIGURE 4-18. LEFT: HA LINE PROFILES OF V801 CEN ON 5 CONSECUTIVE NIGHTS IN 1997 APRIL. WHERE MULTIPLE SPECTRA WERE OBTAINED ON ONE NIGHT, A MEAN OF THESE SPECTRA IS SHOWN. RIGHT: RESIDUALS AFTER SUBTRACTION OF THE 14TH APRIL SPECTRUM. ..... 169

FIGURE 4-19. LEFT: HE I (Λ = 6678) LINE PROFILES OF V801 CEN ON 5 CONSECUTIVE NIGHTS IN 1997 APRIL. WHERE MULTIPLE SPECTRA WERE OBTAINED ON ONE NIGHT, A MEAN OF THESE SPECTRA IS SHOWN. RIGHT: RESIDUALS AFTER SUBTRACTION OF THE 14TH APRIL SPECTRUM..... 170

FIGURE 5-1. 3 X 3 ARC-MINUTE FINDING CHART FOR THE RX J0032.9-7348 WITH PROPOSED COUNTERPART MARKED AS OBJECT NUMBER 1. ..... 191

FIGURE 5-2. EMISSION-COLOUR DIAGRAM FOR OBJECTS IN THE FIELD OF RX J0032.9-7348. THE PROPOSED COUNTERPART IS MARKED AS OBJECT NUMBER 1. LEFT-HAND PLOT SHOWS ALL OBJECTS IN CCD FRAME, RIGHT HAND PLOT SHOWS THOSE OBJECTS WITHIN 124 ARC-MINUTES (TWICE THE UNCERTAINTY RADIUS) OF THE BEST X-RAY POSITION. OBJECTS LYING WITHIN THE UNCERTAINTY RADIUS ARE PLOTTED AS FILLED CIRCLES. (SEE ALSO NOTE CONCERNING AXIS LABELS IN SECTION 5.2.2). ..... 192

FIGURE 5-3. HA SPECTRUM OF THE PROPOSED COUNTERPART TO RX J0032.9-7348..... 192

FIGURE 5-4. 3 X 3 ARC-MINUTE FINDING CHART FOR RX J0049.1-7250 WITH PROPOSED COUNTERPART MARKED AS OBJECT NUMBER 1. ..... 194

FIGURE 5-5. EMISSION COLOUR DIAGRAM FOR OBJECTS IN THE FIELD OF RX J0049.1-7250. THE PROPOSED COUNTERPART IS MARKED AS OBJECT NUMBER 1. LEFT HAND PLOT SHOWS ALL OBJECTS IN CCD FRAME, RIGHT HAND PLOT SHOWS THOSE OBJECTS WITHIN 44 ARCMINUTES (TWICE THE UNCERTAINTY RADIUS) OF THE BEST X-RAY POSITION. OBJECTS LYING WITHIN THE UNCERTAINTY RADIUS ARE PLOTTED AS FILLED CIRCLES. (SEE ALSO NOTE CONCERNING AXIS LABELS IN SECTION 5.2.2). ..... 195

FIGURE 5-6. 3 X 3 ARC-MINUTE FINDING CHART FOR AX J0051-722 WITH PROPOSED COUNTERPART MARKED..... 197

FIGURE 5-7. HA SPECTRUM OF THE PROPOSED OPTICAL COUNTERPART TO AX J0051-722. ..... 197

FIGURE 5-8. 3 X 3 ARC-MINUTE FINDING CHART FOR RX J0051.8-7231. THE CANDIDATE COUNTERPART OBSERVED IN THIS WORK IS MARKED AS OBJECT NUMBER 2, THE OBJECT MARKED AS NUMBER 1 IS THE OBJECT REPORTED TO SHOW HA ACTIVITY BY ISRAEL ET AL..... 199

FIGURE 5-9. HA SPECTRUM OF STAR 2 – A CANDIDATE COUNTERPART TO RX J0051.8-7231. ..... 199

FIGURE 5-10. 3 X 3 ARC-MINUTE FINDING CHART FOR RX J0053.8-7226 WITH PROPOSED COUNTERPART MARKED AS OBJECT NUMBER 1. THIS OBJECT IS A DOUBLE – THE EASTERNMOST COMPONENT IS PROPOSED AS THE BE STAR COUNTERPART. ..... 201

FIGURE 5-11. EMISSION-COLOUR DIAGRAM FOR OBJECTS IN THE FIELD OF RX J0053.8-7226. THE LEFT HAND PLOT SHOWS ALL OBJECTS IN THE CCD FRAME, THE RIGHT HAND PLOT SHOWS ALL

OBJECTS WITHIN 30" (TWICE THE POSITIONAL UNCERTAINTY) OF THE X-RAY POSITION. OBJECTS LYING WITHIN THE UNCERTAINTY RADIUS ARE PLOTTED AS FILLED CIRCLES. (SEE ALSO NOTE CONCERNING AXIS LABELS IN SECTION 5.2.2). ..... 203

FIGURE 5-12. HA SPECTRUM OF THE *EASTERN* COMPONENT OF THE PAIR OF STARS MARKED AS OBJECT 1 IN FIGURE 5-10 ..... 204

FIGURE 5-13. HA SPECTRUM OF THE F2 STAR ~2 ARCSEC WEST OF THE PROPOSED BE STAR OPTICAL COUNTERPART. ..... 204

FIGURE 5-14. FINDING CHART FOR RX J0054.9-7226 ..... 206

FIGURE 5-15. EMISSION-COLOUR DIAGRAM FOR OBJECTS IN THE FIELD OF RX J0054.9-7226. THE LEFT HAND PLOT SHOWS ALL OBJECTS IN THE CCD FRAME, THE RIGHT HAND PLOT SHOWS ALL OBJECTS WITHIN 20" (TWICE THE POSITIONAL UNCERTAINTY) OF THE X-RAY POSITION. OBJECTS LYING WITHIN THE UNCERTAINTY RADIUS ARE PLOTTED AS FILLED CIRCLES. (SEE ALSO NOTE CONCERNING AXIS LABELS IN SECTION 5.2.2). ..... 207

FIGURE 5-16. HA SPECTRUM OF THE PROPOSED OPTICAL COUNTERPART TO RX J0054.9-7226 ..... 207

FIGURE 5-17. LOW RESOLUTION FLUX CALIBRATED SPECTRUM OF THE PROPOSED OPTICAL COUNTERPART TO RX J0054.9-7226 ..... 208

FIGURE 5-18. 3 X 3 ARC-MINUTE FINDER CHART FOR RX J0101.0-7321. ..... 210

FIGURE 5-19. *HA* VS. $R_C$ DIAGRAM FOR OBJECTS IN THE FIELD OF RX J0101.0-7321. (SEE ALSO NOTE CONCERNING AXIS LABELS IN SECTION 5.2.2) ..... 211

FIGURE 5-20. *HA* SPECTRUM OF THE PROPOSED OPTICAL COUNTERPART TO RX J0101.0-7321 ..... 211

FIGURE 5-21. EMISSION-COLOUR DIAGRAM FOR OBJECTS IN THE FIELD OF RX J0117.6-7330. THE LEFT HAND PLOT SHOWS ALL OBJECTS IN THE CCD FRAME, THE RIGHT HAND PLOT SHOWS ALL OBJECTS WITHIN 20" (TWICE THE POSITIONAL UNCERTAINTY) OF THE X-RAY POSITION. OBJECTS LYING WITHIN THE UNCERTAINTY RADIUS ARE PLOTTED AS FILLED CIRCLES. (SEE ALSO NOTE CONCERNING AXIS LABELS IN SECTION 5.2.2). ..... 213

FIGURE 5-22. CLASSIFICATION REGION SPECTRUM OF THE PROPOSED COUNTERPART TO RX J0117.6–7330. THE SPECTRUM IS A COMPOSITE OF SPECTRA OBTAINED ON 1996 JANUARY 18$^{TH}$ AND OCTOBER 6$^{TH}$. ..... 213

FIGURE 5-23. 3 X 3 ARC-MINUTE FINDER CHART FOR EXO 0531.1-6609. ..... 216

FIGURE 5-24. EMISSION-COLOUR DIAGRAM FOR OBJECTS IN THE FIELD OF EXO 0531.1-6609. THE LEFT HAND PLOT SHOWS ALL OBJECTS IN THE CCD FRAME, THE RIGHT HAND PLOT SHOWS ALL OBJECTS WITHIN 18" (TWICE THE POSITIONAL UNCERTAINTY) OF THE X-RAY POSITION. OBJECTS LYING WITHIN THE UNCERTAINTY RADIUS ARE PLOTTED AS FILLED CIRCLES. (SEE ALSO NOTE CONCERNING AXIS LABELS IN SECTION 5.2.2). ..... 217

FIGURE 5-25. HA SPECTRUM OF THE NORTHERN COMPONENT OF THE PAIR OF CANDIDATE OPTICAL COUNTERPARTS TO EXO 0531.1-6609. ..... 218

FIGURE 5-26. LOW-RESOLUTION FLUX CALIBRATED SPECTRUM OF THE NORTHERN COMPONENT OF THE PAIR OF CANDIDATE OPTICAL COUNTERPARTS TO EXO 0531.1-6609 ..... 218

FIGURE 5-27. FINDING CHART FOR H0544-665 WITH PROPOSED COUNTERPART MARKED AS OBJECT NUMBER 1. ..... 219

FIGURE 5-28. EMISSION-COLOUR DIAGRAM FOR OBJECTS IN THE FIELD OF H0544-665. THE LEFT HAND PLOT SHOWS ALL OBJECTS IN THE CCD FRAME, THE RIGHT HAND PLOT SHOWS ALL OBJECTS WITHIN 1' (TWICE THE POSITIONAL UNCERTAINTY) OF THE X-RAY POSITION. OBJECTS LYING WITHIN THE UNCERTAINTY RADIUS ARE PLOTTED AS FILLED CIRCLES. (SEE ALSO NOTE CONCERNING AXIS LABELS IN SECTION 5.2.2) ..... 220

FIGURE 5-29. HA SPECTRUM OF THE PROPOSED COUNTERPART TO H0544-665 ..... 221

FIGURE 5-30. LOW-RESOLUTION FLUX CALIBRATED SPECTRUM OF THE PROPOSED COUNTERPART TO H0544-665. ..... 221

FIGURE 5-31. RELATIONSHIP BETWEEN EW(HA) AND R-HA FOR OPTICAL COUNTERPART CANDIDATES IN THIS STUDY ..... 224

# TABLES

TABLE 3-1. PHOTOMETRY OF V801 CEN, THE BE STAR COMPONENT OF THE X-RAY BINARY 4U1145-619, OBTAINED FROM THE SAAO ON 11TH NOVEMBER 1997. THE INDICES ARE PLOTTED ON A *COLOUR-COLOUR* DIAGRAM, ALONG WITH REDDENING VECTOR IN FIGURE 3-4..... 80

TABLE 3-2. INFRARED PHOTOMETRY OF V801 CEN, OBTAINED FROM THE SAAO, 1993 TO 1998..... 81

TABLE 3-3. LOG OF SPECTROSCOPIC OBSERVATIONS OF V801 CEN BETWEEN 1993 AND 1998. THE UNCERTAINTY IN EQUIVALENT WIDTH MEASUREMENTS IS TYPICALLY OF THE ORDER OF 10%, AND ORIGINATES PRIMARILY FROM UNCERTAINTIES IN THE DETERMINATION OF THE LOCAL CONTINUUM LEVEL..... 84

TABLE 3-4. STRÖMGREN PHOTOMETRIC DATA USED IN THE DETERMINATION OF THE ASTROPHYSICAL PARAMETERS OF V801 CEN, TAKEN FROM HAMMERSCHLAG-HENSBERGE ET AL. (1980)..... 90

TABLE 3-5. GAUSSIAN FITS TO HEI LINES IN THE SPECTRUM OF V801 CEN..... 95

TABLE 3-6 DERIVED ASTROPHYSICAL PARAMETERS OF V801 CEN, THE OPTICAL COUNTERPART TO THE BE/X-RAY BINARY 4U 1145-619. COLUMN 2 LISTS THE PARAMETERS DERIVED IN STEVENS ET AL. (1997), COLUMN 3 LISTS THE RESULTS OF THIS WORK..... 97

TABLE 3-7. MEASURED PROPERTIES OF THE HA EMISSION LINE OF V801 CEN FROM 1993 TO 1997 116

TABLE 3-8. MEASURED PROPERTIES OF THE HE I (6678 Å) EMISSION LINE OF V801 CEN FROM 1993 TO 1997..... 116

TABLE 4-1. ORBITAL PARAMETERS INPUT TO THE LIGHTCURVE MODEL TO INVESTIGATE THE EFFECTS OF VARYING BE STAR DISC PARAMETERS (CHOSEN TO BE THOSE OF THE BE/X-RAY BINARY SYSTEM 4U1145–619)..... 130

TABLE 4-2. ORBITAL PARAMETERS OF THE BE/X-RAY BINARY EXO 2030+375 TAKEN FROM STOLLBERG ET AL. (1997)..... 163

TABLE 5-1. OPTICALLY UNIDENTIFIED X-RAY SOURCES IN THE MAGELLANIC CLOUDS OBSERVED IN THIS STUDY. COLUMN 4 GIVES THE UNCERTAINTY RADIUS (90%) FOR THE BEST X-RAY POSITION..... 181

TABLE 5-2. LOG OF CCD IMAGING OBSERVATIONS MADE WITH THE 1.0-M TELESCOPE AT THE SAAO. *CONTINUED OVERLEAF.*..... 184

TABLE 5-3. LOG OF SPECTROSCOPIC OBSERVATIONS MADE WITH FROM THE AAT AND WITH THE 1.9-M TELESCOPE AT THE SAAO..... 187

TABLE 5-4. PHOTOMETRY OF OBJECTS WITHIN THE 90% CONFIDENCE X-RAY ERROR CIRCLE OF RX J0032.9-7348..... 190

TABLE 5-5. PHOTOMETRY OF THE OBJECTS WITHIN THE X-RAY ERROR CIRCLE OF RX J0049.1-7250. ..... 195

TABLE 5-6. PHOTOMETRY OF THE TWO COMPONENTS OF THE DOUBLE STAR MARKED AS OBJECT NUMBER 1 IN THE FINDING CHART IN FIGURE 5-10. ..... 203

TABLE 5-7. RESULTS OF GAUSSIAN FITS TO HA AND HB IN SPECTRA OF THE CANDIDATE COUNTERPART TO RX J0053.8-7226 (EASTERN COMPONENT OF DOUBLE OBJECT NUMBER 1 IN FIGURE 5-10). ..... 203

TABLE 5-8. OPTICAL PHOTOMETRY OF THE COUNTERPART TO RX J0117.6–7330. ..... 212

*"During our professional careers, all of us have encountered terms and phrases which have left us bewildered as to their meaning. In some instances, I suspect that the bewilderment extends to the author."*

George W. Collins

# Chapter 1 – Be Stars

In this chapter I present a review of our current knowledge of the Be star phenomenon. I first describe the observational characteristics with which we identify stars of this type, and the physical properties that can be inferred from these observable properties. I then review past attempts to describe unified models of the Be star phenomenon – both *ad hoc* models which intend only to *describe* the observable properties, and physical models which attempt to provide a physical basis to *explain* the observable properties. I describe some of the problems yet to be overcome in order to reach a full understanding of the Be star phenomenon; discussing inconsistencies between the models and observations, and proposals for how theory and observation might be reconciled.

## 1.1 Observational characteristics of Be stars

The use of the suffix 'e' applied to the spectral type of a star to denote the presence of emission lines in the stellar spectrum was first proposed to the International Astronomical Union in 1922 by A. Fowler. He proposed however that the 'e' suffix should be omitted from those spectral types whose members normally displayed such emission lines in their spectra. This definition remains almost unchanged to this day – we now exclude supergiant stars (stars of luminosity class I or II). A working definition generally accepted by the astronomical community is that of Jaschek, Slettebak & Jaschek (1981):

> *"A non-supergiant B-type star whose spectrum has, or had at some time, one or more Balmer lines in emission."*

The term 'Be star' has however grown to become a generic term for a class of object, whose members show similar observational characteristics which are discussed later in this section. As there are some late O-type stars, and some early A-type stars which show similar observational characteristics, and there are no reasons to believe that these characteristics arise from different physical mechanisms in the earlier or later spectral types, it is convenient to allow these objects to belong within the definition. Throughout this work therefore, I have adopted the definition proposed by Jaschek et al. broadened slightly to include early A-type and late O-type non-supergiant stars with similar properties. The line emission of Be stars is reviewed in more detail in Section 1.1.1.

In addition to emission in the Balmer lines, Be stars show a luminosity excess at long wavelengths, causing a Be star of a given spectral type to appear brighter at infrared wavelengths than a B-type star of the same spectral type. The infrared excess is reviewed in detail in Section 1.1.2. As this excess flux is most apparent at infrared wavelengths it is generally referred to as an *infrared excess*, though the excess flux is still significant in the optical region of the spectrum – while acknowledging that the term can therefore be misleading, I shall conform to convention in this work and refer to the excess flux as an *infrared* excess.

Be stars commonly show variability in the earlier described observable properties on many timescales, from hours to years, though there are examples of Be stars which show no variations at all on observable timescales. Emission lines are seen to vary in strength, sometimes disappearing altogether, leaving the Be star indistinguishable from a normal B type star. Line shapes vary on long timescales – most evidently in the V/R cycles described in Section 1.1.5.2 – and also display transient features on timescales of hours.

### 1.1.1 Emission Lines

Our definition of a Be star relies upon the presence of emission in the Balmer series of Hydrogen. The strongest emission – and therefore the most common diagnostic of Be stars – is seen in the Hα line; optical spectra often reveal emission – albeit weaker – in Hα, Hβ and successively higher order transitions. Clark (1997, *et al.* 2000) showed from UKIRT spectra that Be stars also display emission in the Paschen and Brackett series of Hydrogen. In Figure 1-2 (taken from Reig, Stevens, Coe *et al.*) we show Paschen and Brackett emission lines in infrared spectra of the Be star counterpart to the Be/X-ray binary EXO 2030+375.

Emission lines show many profiles, single or double peaked, symmetric or asymmetric. Often (especially in Hβ and later lines of the Balmer series) an emission core is superposed on broader absorption wings (see for instance the Hα profile for 17 Tau in Figure 1-1).

Another commonly observed line profile is termed a 'shell profile', characterised by emission lines reversed by narrow absorption cores; stars that display such line profiles are often termed 'shell stars' and often show narrow absorption in many metallic lines. Many stars have been observed to change from classic Be star line profiles to 'shell' profiles and *vice versa* (Hα profile of ψ Per in Figure 1-1).

In addition to the presence of Hydrogen emission, Be stars also often show He I lines in emission, as well as many singly ionised metals. More 'extreme' Be stars (those with EW(Hα) ≥ 10 Å) frequently show Fe II lines in emission. Figure 1-1 – taken from Hummel & Vranken (1995) – shows Fe II λ5317 and He I λ5876 lines in addition to Hα lines for 9 Be stars.

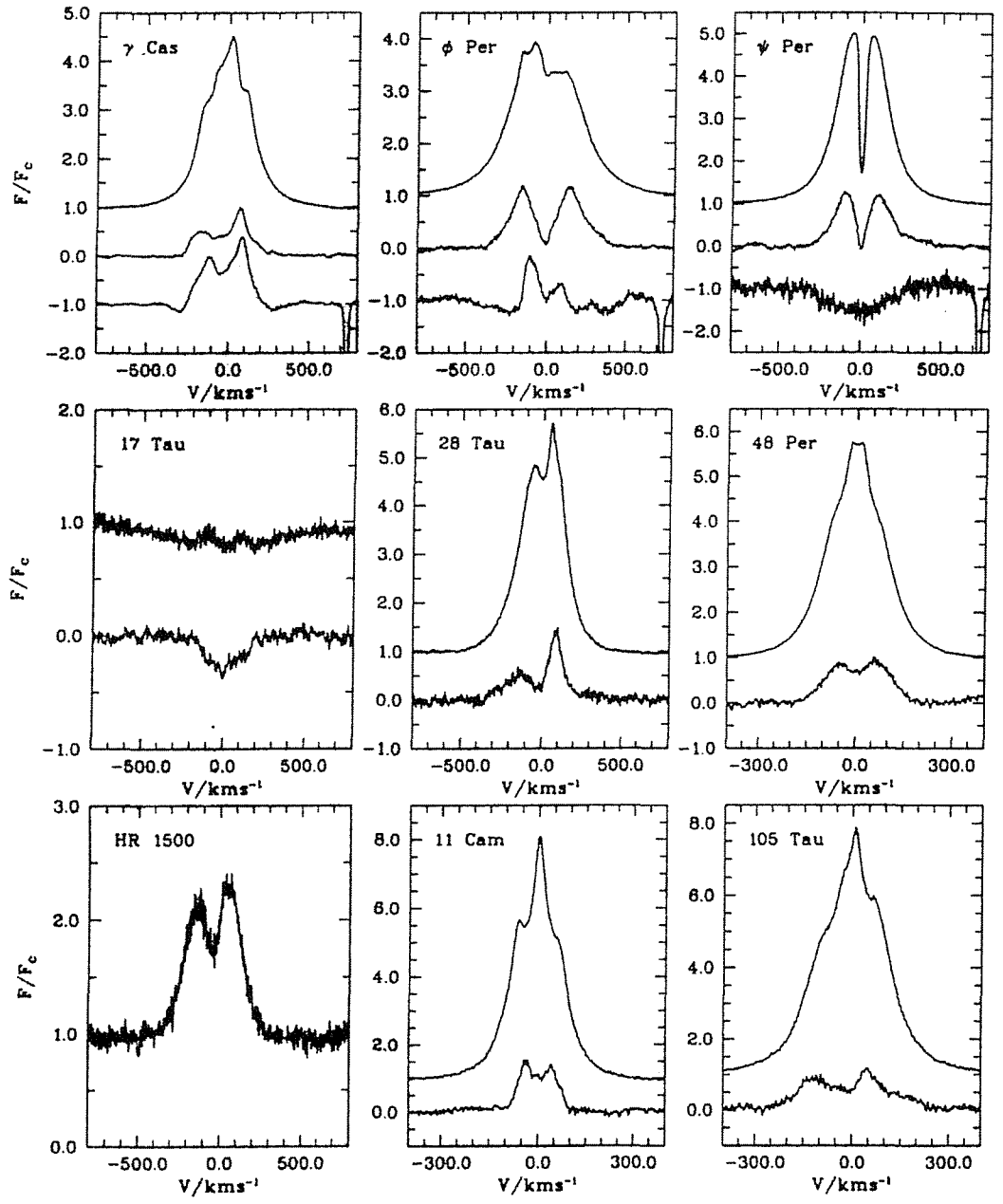


**Figure 1-1.** Hα, Fe II λ5317 and He I λ5876 emission line profiles for nine Be stars. Fe II and He I flux scales are expanded by a factor of 10 relative to the Hα scale. Taken from Hummel & Vranken (1995). Each are normalised to the local continuum, then offset so that the continuum flux is approximately 1.0 (Hα), 0.0 (Fe II) and -1.0 (He I)

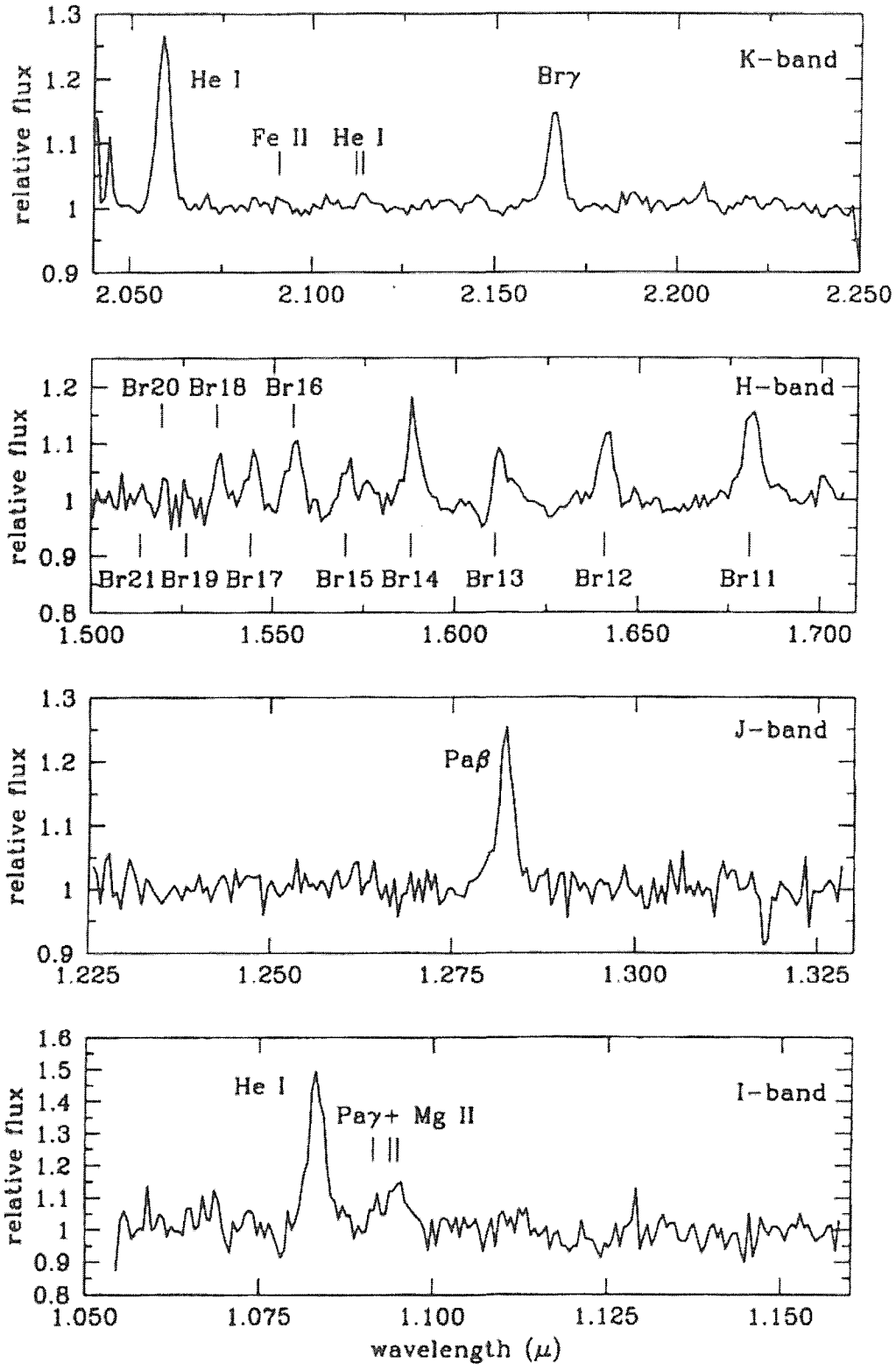


**Figure 1-2.** Infrared spectra of EXO 2030+375 – taken from Reig, Stevens, Coe *et al.* (1998).

### 1.1.2 Infrared excess

Apart from emission in the Balmer series, the infrared excess is a major characteristic of Be stars. At IR wavelengths the excess flux can be large enough to produce an extra few magnitudes of luminosity. Figure 1-3 shows the energy distribution of 4 Be stars (α Eri, φ Per, δ Cen and χ Oph) with best fit Kurucz models (Waters 1986) showing clear excess flux at long wavelengths in all cases except α Eri.

Even at optical wavelengths the contribution to the continuum flux can be significant – in Chapter 3 (and in Stevens et al. 1997) I show that the *V* band excess flux in the Be star V801 Cen can be as large as $\delta V \sim 0.6$ magnitudes. The excess flux, noticed first through infrared photometry, is also significant at wavelengths longer than the *JHKL* infrared photometric indices – Coté & Waters (1987) studied a sample of 101 Be stars with the *IRAS* satellite and found the excess flux present at wavelengths between 12 and 60μ. At optical and infrared wavelengths the excess can be approximated by a power law distribution, however, at longer wavelengths (mm and radio) few Be stars have been detected. Taylor et al. (1990) detected only 6 Be stars from a sample of 21, whereas their upper limits to those undetected are mostly below the flux expected by extrapolating from IR flux distributions. Observations such as these have led to a commonly held belief that some mechanism causes a change in disc structure at a certain radius leading to a change in the spectral gradient.

Waters (1986) developed an *ad hoc* model to fit to infrared excesses derived from IRAS observations of four Be stars. The model consisted of a disc with some opening angle θ and a density distribution of the form:

$$\rho \sim \rho_0 \left( \frac{r}{R_*} \right)^{-n} \qquad (1\text{-}1)$$

in which the IR excess flux is produced via free-free and bound-free emission powered by photospheric UV continuum photons.

The model was found to reproduce the IR excess well, but with densities much greater, and with higher mass loss, than is suggested by observations of UV resonance lines. Hence it would appear that different regions of the wind have very different physical conditions.

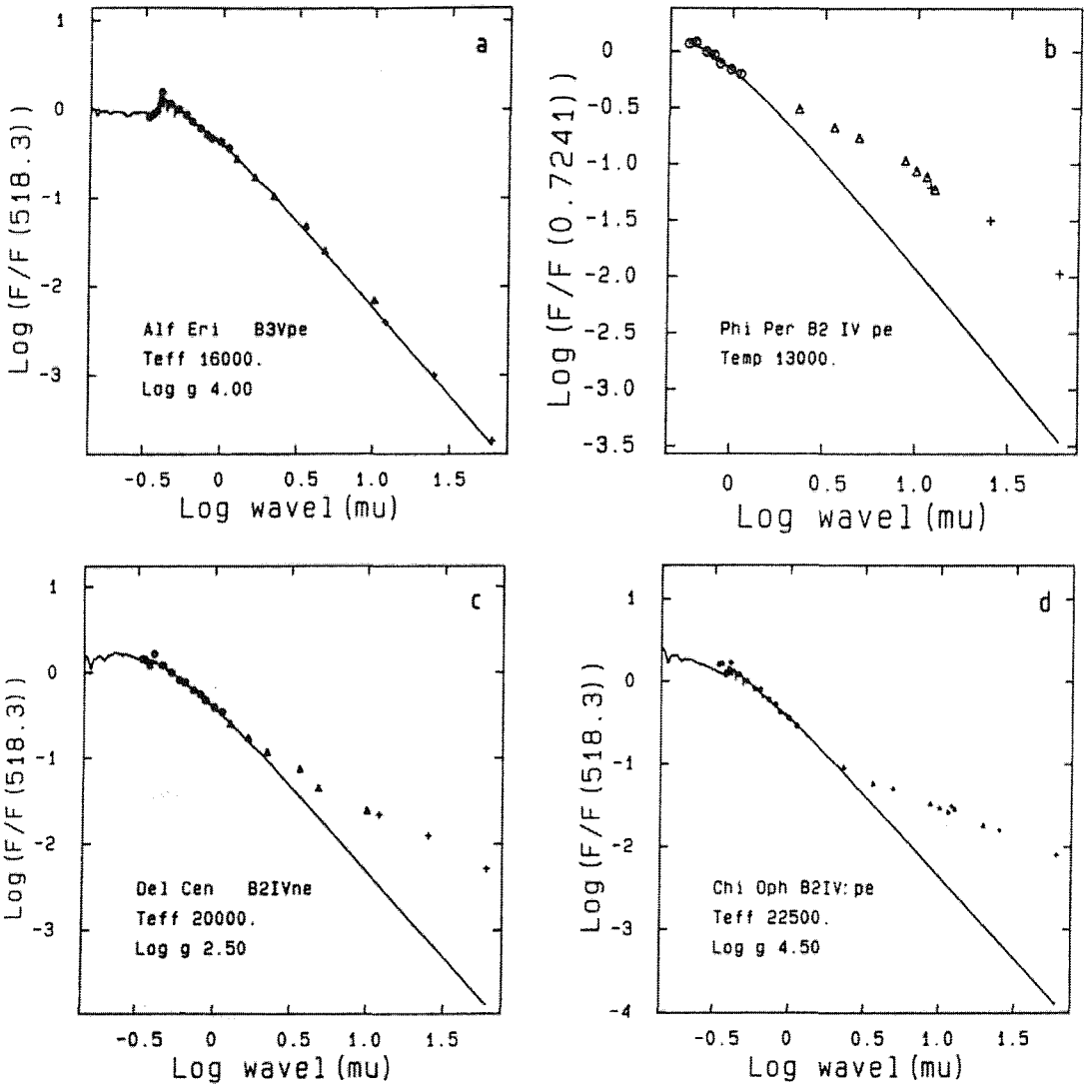


**Figure 1-3.** Spectral energy distributions of Be stars α Eri, φ Per, δ Cen and χ Oph. Fluxes are normalised to the 518.3-Å flux for all except φ Per (normalised to 724.1-Å). The solid lines in each case represent the best fit Kurucz models with parameters as annotated on each plot.

### 1.1.3 UV Observations

At first sight, observations of Be stars at UV wavelengths appear to be contradictory to those at optical and infrared wavelengths. Whilst optical and infrared emission lines show little deviation from rest wavelengths – indicating wind outflow velocities little more than ~100 km $s^{-1}$ – the wavelength shifts of UV line profiles often indicate wind velocities up to ~1000 km $s^{-1}$. From *I.U.E.* observations of V801 Cen – the optical counterpart to the Be/X-ray binary 4U1145-619 and subject of Chapter 3 – Bianchi & Bernacca (1980) found evidence for a wind with terminal velocity of 1800 km $s^{-1}$. In Chapter 3 I present optical spectra of the same object which show no evidence for outflow velocities greater than 100 km $s^{-1}$. Attempts to resolve this apparent paradox generally involve proposals of more than one component to the stellar envelope, often with a low-density/high-velocity polar wind and a high-density/low-velocity equatorial wind. Such models are discussed in greater depth in Section 1.2.

### 1.1.4 Direct imaging

Be stars have recently been imaged at optical (Hα) and radio wavelengths (Vakili, Mourard & Stee 1994, Dougherty & Taylor 1992). The Be star ψ Per was included in both studies and the alignment of the images is good. The linear polarisation of ψ Per is found to be perpendicular to the major axis. Thus the most direct observations point to a disc-like geometry for the circumstellar envelope. It is generally accepted that the envelopes of Be stars are disc-like. However, beyond this, the detailed geometry is unclear.

### 1.1.5 The variability of Be stars

As already mentioned, variability is a frequent characteristic of Be stars, and affects all of the observed properties. Individual Be stars show different degrees of variability, some may appear unchanged for long periods (of the order of years), while others change from Be star to normal B star in periods of the order of months –

with the Hα emission line reversing to show normal absorption. The underlying cause of this variability is not fully understood, not least because the cause of the Be phenomenon itself is not known, but through our *ad hoc* models we can at least infer some properties of the circumstellar envelopes of Be stars through the study of correlations between the observed properties as they vary.

#### 1.1.5.1 Disc loss and regeneration

One of the more easily understood variations that Be stars display is variability in the degree of Be characteristics that it displays, generally understood as a variation in the size or density of the circumstellar envelope that gives rise to these properties. As has been mentioned already, stars have been observed to change from Be to B-type stars and back again, indicating complete loss and/or generation of a circumstellar envelope. Other stars may show less extreme variability indicating only a gain or loss of part of their circumstellar envelope. These variations manifest themselves as reductions in the strength of Hα emission and the infrared excess.

Dougherty & Taylor (1994) studied archival *JHK* IR data of a sample of 125 Be stars; their sample was chosen to include stars with at least 2 separate observations, from a number of surveys covering a 19 year period. Of this sample, ~18 per cent showed variability according to the authors' criteria. The timescales of variability extended to 73 days, and in some cases were as short as 18.5 days – the latter a lower limit owing to the sampling timescale used. The amplitude of variability fell in the range 0.2 – 1.2 magnitudes in the *K* band. The degree of variability was shown to increase with wavelength – consistent with the variability being due to changes in the strength of a continuum component with a 'redder' spectral slope than that of the stellar photosphere. Clark (1997) points out that stars displaying variability on timescales shorter than 18.5 days would have been missed by Dougherty & Taylor's study (and many Be stars have been found in other studies to show variability on these timescales), and that the percentage of variable Be stars is probably a lot higher than 18 per cent.

#### 1.1.5.2 V/R variability

Be star emission line profiles can be divided into symmetric and asymmetric profiles, and into single or double peaked profiles. It is common to parameterise double peaked profiles by measuring the ratio of strength of the two peaks. Termed the *V/R* ratio – where *V* is the maximum flux in the shorter wavelength (*violet*) peak, and *R* is the maximum flux in the longer wavelength (*red*) peak – variability in this ratio is hence termed 'V/R variability'. Be stars often display cyclical variability in this parameter. The characteristics of these variations, and possible causes, are discussed in greater depth in Section 1.4.

#### 1.1.5.3 Short term variability

The shortest timescale variability displayed by Be stars is in the form of transient absorption features in the line profiles. These features – termed Discrete Absorption Components (DACs) – also show time variation in wavelength, tending to move across the line profile implying Doppler shifting of a rotating or pulsating entity giving rise to the absorption.

### 1.1.6 Population characteristics

Many studies of Be stars statistics have been made to determine the proportion of Be type stars per spectral type bin. It is important however to take into account the overluminosity of Be stars compared to B stars of similar mass and age, the spectral type changes during constant mass evolution, and the spectral type change due to rapid rotation.

Briot & Zorec (1994) calculated statistics taking into account the following:

- Be stars are intrinsically brighter than B type stars, and this excess flux is greater for the earlier type Be stars. If statistics are calculated up to some limiting magnitude, a larger volume of Be stars than B stars will be included, thus artificially increasing the Be/B ratio.

- Stars' apparent spectral types change as they evolve (with constant mass) from the main sequence up the giant branch. Hence in any comparison of populations, we must consider the ZAMS spectral type of a star, rather than its current spectral type.
- Because of the rapid rotation of Be stars, the spectral type of a particular star must be corrected to that which it would show if it were not rotating.

Their results show that the observed maximum occurrence of Be stars at a spectral type of B2 remains when evolutionary and intrinsic brightening effects are taken into account, but shifts to B1 when rotational effects are considered.

## 1.2 Be star circumstellar envelopes

The consensus amongst authors of works on Be stars is that the observable properties of these stars result from the existence of an extended envelope. This envelope gives rise to the Balmer (and other) emission lines through the re-processing of energetic UV photons. The excess infrared flux arises from free-free and bound-free emission in this envelope.

As mentioned in Section 1.1.3, an apparent paradox arises when we consider UV observations. The adopted solution is to assume a two component envelope with the optical emission lines and infrared excess arising from an equatorially concentrated low-velocity dense wind, the UV absorption lines arising in a high-velocity low-density wind originating at high latitudes.

### 1.2.1 Evidence for disc shaped envelopes

#### 1.2.1.1 Optical emission lines

Evidence for the flattened disc geometry comes from the double peaked profiles of emission lines. Many authors have investigated the strength and shape of the opti-

cal emission lines of Be stars as indicators of disc geometry, Dachs (1986) reports a correlation between FWHM(Hα), it's strength, and $v \sin i$. This suggests rotation as cause of line broadening in Be stars, and is suggestive of a flattened envelope.

One problem however is that the widths of both Hα (optically thick) and FeII (optically thin) are wider than the rotational velocity of the underlying star would suggest. Additional broadening mechanisms (electron scattering and non-coherent scattering) can add to the observed width of Hα lines, but the FeII lines should only be kinematically broadened (Hummel & Vranken 1995). The observed line widths therefore suggest that the inner regions of the envelope are rotating more rapidly than the surface of the star. This implies that some mechanism must exist to transfer angular momentum into the wind.

#### 1.2.1.2 IR and radio continuum emission

A small number of bright Be stars have been detected at radio wavelengths (Taylor et al. 1987, 1990). Spectral indices from radio data appear steeper than those found from IRAS observations. This suggests that a turnover in the spectral continuum occurs somewhere between the IR and radio bands.

Three possible explanations for the turnover have been proposed: reacceleration of the wind at large radii, a change in the geometry of the wind at large radii, or a change in the ionisation of the wind at large radii. Waters et al. (1991) predict through theoretical models that the degree of ionisation should be fairly constant throughout the disc.

Chen et al. (1992) suggest that stellar UV radiation cannot penetrate the dense inner regions of the wind, but that a thin disc geometry would allow the UV photons to add a driving force to the outer regions of the disc, reaccelerating the wind.

Waters & Marlboro (1994) show that the radio spectral continuum can be reproduced by a slab model, with density decreasing with the square of radius (ie. a con-

stant outflow velocity). The observed turnover in the spectrum can therefore be explained if we assume a thin, but diverging, inner disc, with a slab-like constant outflow velocity, outer disc. Waters & Marlborough speculate that wind streamlines bent toward the equator by Coriolis forces (as in the wind compressed disc model – see Section 1.3.1.2) act to collimate the inner regions of the disc. At larger radii, the wind has much less velocity perpendicular to the disc plane, but greater velocity in a radial direction. Hence at large radii, the collimating mechanism is much less efficient allowing the disc to flare into a thicker slab.

## 1.3 Formation of Be star envelopes

Many models have been proposed to reproduce the observable properties of Be stars; some with more success than others. Whilst the *ad hoc* models cannot explain the existence of Be stars, it is hoped that by fitting the models to observations, the model parameters may lead to a greater understanding of the physical structure and dynamics of the circumstellar environment of these stars. Other models attempt to explain the occurrence of Be stars, with limited success. It seems that we can create models which recreate the Be phenomenon but cannot fit these to observations, whilst we can create other models which reproduce the observations but provide no clues as to the formation of the Be phenomenon.

One category of *ad hoc* models contains those that attempt to describe the global properties of the circumstellar environment. Usually they specify the geometry of the circumstellar envelope, and certain characteristics such as density distribution and outflow velocity. The second category contains those models which attempt to describe only a particular behavioural characteristic, such as V/R variability or Discrete Absorption Components.

#### 1.3.1.1 Rotationally flattened discs

The earliest attempt to describe the Be phenomenon was proposed by Struve (1931). The model that he proposed involved B type stars rotating at close to their break-up velocity (where the gravitational forces at the equator are cancelled by the centrifugal forces) so that the stars shed material into a circumstellar envelope, which is flattened in to a disc geometry by rotation.

Studies of the rotational velocities of Be stars indicate that while Be stars on the whole rotate more rapidly than analogous B type stars, their rotational velocities are significantly below the break-up velocity. Whilst it seems to be clear that the higher rotational velocities of Be stars play a role in the formation and consequent support of a circumstellar disc, it alone cannot explain the phenomenon. It is more likely that the high rotational velocities serve to alter the potential field such that whatever other mechanisms eject material from the stellar equator, less force is required to perform the task, so that the higher rotators are more susceptible to the effect.

#### 1.3.1.2 The Wind Compressed Disc model

It is clear that rotation plays a large role in the formation of Be star discs. Be stars in general have higher values of $v\sin i$ than normal B type stars, though considerable overlap between the distributions of projected rotational velocities exists. It was initially believed that the higher rotational velocities led to the formation of the Be star discs. However, no Be star has been found with $v\sin i \geq v_{crit}$ where $v_{crit}$ is the critical break up velocity, and so some other mechanism must act to help form the extended envelope. The Wind Compressed Disc (WCD) model attempts to explain circumstellar disc formation though rapid rotation and radiatively driven mass loss.

Bjorkmann & Cassinelli (1993) showed that in a rotating axisymmetric model, wind streamlines are not radial, but are affected by centrifugal and coriolis forces in such a way that they are deflected towards the stellar equator.

In the non-rotating case, beyond the sonic point, the thermal force can no longer support the outflow over gravity, and the radiative force must be greater than the gravitational force if outflow is to continue. In the case of a rotating star, centrifugal forces support the outflow in addition to the radiative force. The centrifugal force decreases with the inverse cube of distance, much slower than the thermal pressure, and so between the sonic point and some distance where the centrifugal force has dwindled enough, outflow can continue though the radiative force is actually less than the graviational force.

Figure 1-4 shows Bjorkmann & Cassinelli's 1-D model predictions for the rotational velocity required to lead to disc creation.

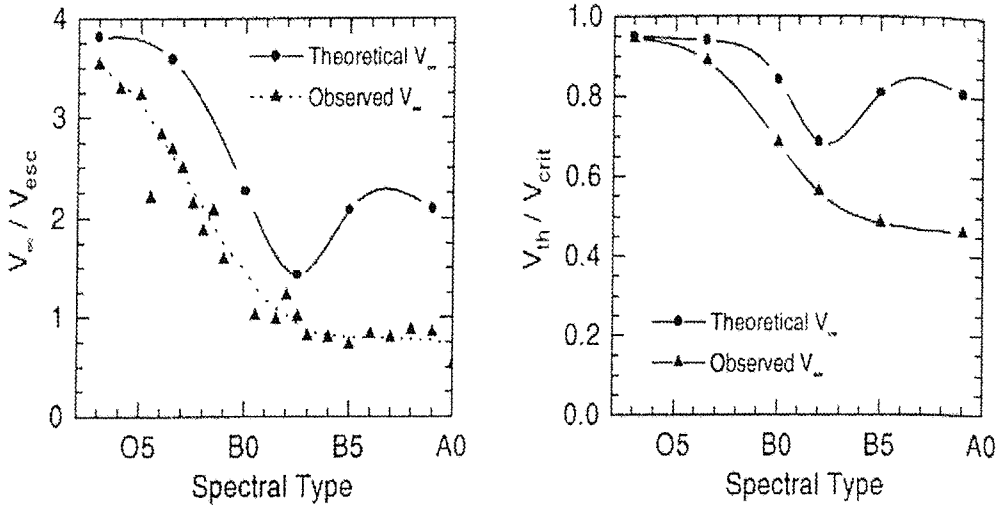


**Figure 1-4.** Wind compressed disc model predictions. Left: the ratio of terminal wind velocity to stellar escape velocity as a function of spectral type. Right: the threshold rotation velocity for disc creation as a fraction of the stellar escape velocity as a function of spectral type. Taken from Bjorkman (1994).

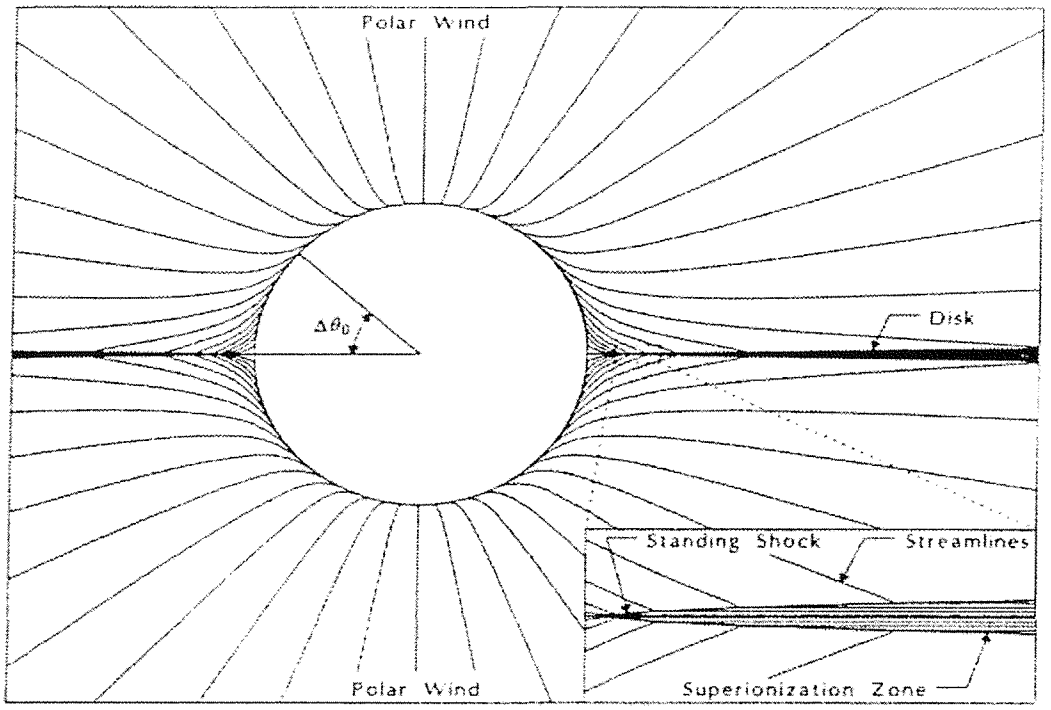


**Figure 1-5.** Two-dimensional schematic of a wind compressed disc. The wind streamlines are shown being deflected toward the equator. The inset diagram shows the standing shocks forming either side of the equator. Taken from Bjorkman & Cassinelli (1993).

Figure 1-5 shows 2-dimensionally the streamlines of the wind, in the rotating star. In a non-rotating star the streamlines would all be radial, but in this rotating case the streamlines fall towards the equator for some distance until the radiative force is larger than the gravitational force and the streamlines bend back towards the radial directions. If the region within which the centrifugal force supports the wind is large enough, the streamlines will impinge on the equator. In this case, the streamlines from opposite hemispheres collide; the velocity of the wind perpendicular to the equatorial plane is supersonic, so the increased density and large pressure gradient causes shocks above and below the equator, hence a well collimated dense low velocity disc forms around the star. At higher latitudes the wind remains high velocity low density, as indicated by UV observations.

It is worth noting that for a disc to form, the relationship between the rotation speed of the star and the radial velocity of the wind must be such that the streamlines meet

at the equator before the radiative force becomes greater than the gravitational force. A fast wind must be accelerated by a greater radiative force, decreasing the size of the region within which the wind is bent towards the equator. On the other hand, a more rapidly rotating star will support a wind centrifugally up to greater distances, and the region in which the wind bends towards the equator is larger. Hence the critical velocity at which the star must rotate in order to form a disc in this way is related to the ratio of the wind terminal velocity to the escape velocity of the star.

Using theoretical values for terminal wind velocities for a range of spectral types, Bjorkmann & Cassinelli (1993) find a minimum in the critical disc forming velocity at a spectral type of B2. Considering the maximum occurence of the Be star phenomena at the same spectral type, the Wind Compressed Disc becomes an attractive explanation for the existence of the circumstellar disc.

However, the predicted densities for a WCD are two orders of magnitude too small. The density can be estimated by equating the gas pressure with the ram pressure of the wind, resulting in a predicted density distribution that follows (for a B2V star):

$$\rho \sim \rho_0 \left( \frac{r}{R_*} \right)^{-n} \qquad (1\text{-}2)$$

with $n = 3$ and $\rho_0 = 10^{-13}$ g cm$^{-3}$.

Waters, Cote & Lamers (1987) fit similar density distributions to infrared fluxes (see 1.1.2), and determined values of $n$ in the range 2.0 – 3.5, and $\rho_0 = 10^{-11}$ g cm$^{-3}$. The radial distribution predicted by the WCD can hence be fitted to the observed infrared fluxes, but the actual densities predicted are too small to explain the magnitude of the infrared excess. A similar result is found if the WCD predictions of

polarization are compared to observation – the same factor of ~100 in density is required to reconcile observation to theory.

It is worth noting that Zaal, Waters & Marlboro (1994) have discovered a star showing emission in the Bracket series (infrared) whilst the Balmer lines are seen to be in absorption. They conclude that a new type of Be star may exist with low density discs only detectable from IR emission lines. The inferred densities are ~100 times less than those found for "classical" Be stars. The Wind Compressed Disc model could explain the existence of these objects, but any unified model for all Be stars would require some further mechanism to apply to the classical Be stars to explain the density of material in the circumstellar disc.

A further problem for the Wind Compressed Disc model is the existence of low velocity shell profiles in many Be stars, which may be transient features. The WCD model leads to thin well-collimated discs. If not quite edge-on, a thin disc can only obscure half of the star, however optically thick. If the disc is seen exactly edge-on, the outer (thicker) parts of the disc obscure the star. The radial velocity in these outer regions should be larger than the inner regions, yet shell absorption features generally show very small or no velocities.

A possible solution to the density problem is that mass loss rates may have been underestimated by an order of magnitude. Bjorkmann (1994) claims that this increase in mass loss would reduce the line-driving force so that streamlines are bent towards the disc more readily. The result of this would be a higher wind velocity normal to the disc plane upon impact at the shock, and hence a higher compression of the disc. Another speculative possibility is that magnetic fields transfer angular momentum into the disc, hence stopping material in the inner disc from falling back onto the stellar surface. Indeed, it is known that some input of additional angular momentum is required to explain the widths of Hα and FeII emission lines in many Be stars (Hummel & Vranken 1995).

Optical and IR emission lines definitely do not show profiles consistent with in-fall near the star so some mechanism must prevent this. A magnetic field is one proposed method of transferring additional angular momentum into the disc to rotationally support it against this in-fall. The presence of magnetic fields might overcome the 'shell profile' problem as, speculatively, magnetic field lines might be frozen into the disc material, causing magnetic stresses through twisting of the field, which could cause large scale disruptions leading to transient obscurations and hence shell profiles.

Another source of variability could be instabilities in the shock. This could lead to a complex structure, altering the geometry and density, affecting radiative driving forces, and indirectly disc thickness. The result is that the disc could be 'clumpy' and geometrically thicker - again allowing a possible solution to the problem of low velocity shell profiles.

#### 1.3.1.3 Rotation-pulsation model

A popular proposition as a mechanism to eject mass into an equatorial disc is Non-Radial Pulsations (NRP), and specifically the interaction of the pulsating modes with the rotation of the star.

Several Be stars have been shown to display non-radial pulsations as seen in the β Cep and 53 Per variables (Baade 1982, 1984a, 1984b; Vogt & Penrod 1983). Vogt & Penrod (1983) linked these NRP to mass loss activity in Be stars, and estimated that the pulsation energy in the case of ζ Oph is large enough to cause significant mass ejection. In the proposed model, the lower potential at the equator due to the rotation of the star allows the effects of NRP to cause equatorial mass-loss. Only the combined effects of rotation and NRP are sufficient to overcome the gravitional potential of the star.

NRPs transfer angular momentum from the interior of a star to the stellar surface, where the material – already 'buoyant' with centrifugal forces – is imparted with

enough angular momentum to launch it from the surface into the circumstellar disc created by previous such ejections. The ejected material transfers angular momentum into the existing envelope as the NRP dissipates (Osaki 1986).

Moreover, it is suggested by Ando (1986) that interaction between the rotation of the star and the NRP can lead to a quasi-periodic cycle of energy exchange between rotational and pulsation. He proposes that this mechanism accelerates the equatorial material to break-up velocity at the acceleration phase of the cycle. Negueruela (1997) questions the strength of the rotation-pulsation model, citing the large number of free parameters and evidence from Smith (1989) indicating a lack of correlated NRPs and Be behaviour in the star λ Eri.

#### 1.3.1.4 The decelerated wind model

The decelerated wind model is rare in that it provides an alternative to the accepted paradigm of Be star envelopes (high-density low-velocity disc with low-density high-velocity polar wind). According to the model, (Doazan 1987, Doazan et al. 1986) the optical/infrared–UV paradox is explained by defining two spherically symmetric zones, centred on the star. The inner zone comprises a hot fast wind globally carrying mass away from the stellar surface, the outer zone contains more dense, slow moving material. The transition from the inner to outer zone occurs when the high-velocity mass outflow meets the interstellar medium, or material from previous ejections – the sudden deceleration giving rise to a dense, slow moving outer region. Polarimetric observations, and direct imaging of Be star discs provide strong evidence however for a flattened disc model.

#### 1.3.1.5 Viscous Excretion Model

The viscous decretion disk model was first proposed for Be stars by Lee, Saio & Osaki (1991). They propose that material ejected from the stellar surface rotates in Keplerian orbits but drifts outwards because of viscous interaction, forming a thin collimated disc.

Okasaki (2000) has calculated certain characteristics of the outflow of viscous discs. Okasaki finds that the outflow in such discs is expected to be highly sub-sonic out to of the order of 100 stellar radii. He also finds that such discs would be stable to global one-armed oscillations with periods matching those observed for V/R variations in Be stars. See the following section for further discussion of V/R variability.

## 1.4 V/R Cycles and associated variability

As already mentioned in 1.1.5.2, many Be stars display variability in the relative strengths of the two peaks in double peaked line profiles. The variations are known as V/R variations (where V and R represent respectively the emission strength of the *violet* and *red* components of the line).

V/R variability is usually quasi-cyclical, developing from V/R > 1, through V/R = 1, to V/R < 1, and so on. The periods of variability are of the order of years, the statistical mean being ~7 years (see Figure 1-6), and are not sensitive to the spectral type – hence mass, size, luminosity – of the underlying B star. When the V/R ratio is < 1 (ie. when the *red* peak is stronger) the whole line profile shifts blueward, similarly when the V/R ratio is > 1 (when the *blue* peak is stronger) the profile shifts redward. Figure 1-7 shows Hα spectra of the Be star HD 245770, clearly indicating a periodic variability in the V/R ratio.

Explanations for the V/R cycles of Be stars rely on non-axisymmetrical discs, where the asymmetrical line profiles are due to some perturbation in the circumstellar disc. Support for this scenario is found in some Be stars with high inclinations, where the underlying star appears to eclipse the perturbed region of the disc. The most successful models involve the precession of one-armed density waves in the circumstellar disc, though other models have been proposed to explain the non-axisymmetry.

### 1.4.1 One-armed global oscillations

Currently the most successful model developed to explain the existence of cyclic V/R variability in Be stars is the one-armed ($m$ = 1) oscillation model due to Kato (1989) and Okazaki (1991).

Theoretically, in a Keplerian (or near Keplerian) thin disc, the only possible oscillations are $m$ = 1 modes of low frequency (Okazaki 1997). The slow precession of a density perturbation results from a small perturbation from Keplerian rotation in the velocity field of the disc. According to the first one-armed oscillation model to be constructed, this perturbation of the velocity field results from the pressure force distribution in the disc (Okazaki 1991). Okazaki needed to assume an outer radius to the disc in order to produce finite oscillation periods. He found that the observed distribution of V/R cycle periods could be reproduced by assuming disc radii in the range $5 < R_{disc}/R_* < 20$. The predicted perturbations precessed around the disc in a retrograde direction.

Later Papaloizou et al. (1992) constructed a model that included the quadrupole potential of a rotationally flattened star. This deviation from a point mass potential forces the particles into precessing elliptical orbits. In this model, the oscillations are confined to the inner regions of the disc, their nature is hence insensitive to the overall dimensions of the disc, and no assumed disc size is necessary. The predicted perturbations precessed around the disc in a prograde direction.

Recently, Okazaki (1997) has investigated a combination of the two effects and found that in late type Be stars, the confinement of the oscillation is due to the quadrupole moment of the central star. However, for early type Be stars, he finds that the confinement of the oscillation is mainly due to the radiative force due to an ensemble of optically thin lines (and optically thin continuum). The results of his model predict prograde precession with frequencies closely matching the distribution of observed V/R cycles.

Observations of correlated V/R and continuum variations are sparse. Such a correlation has been observed in V1294 Aql (Hubert 1994). Hao et al (1996) find that the optical lightcurve of HDE 245770 (the Be star component of the X-ray binary A0535+26) can be fit by a combination of two sine functions of periods 506d and 755d. They propose that the variability is due to geometrical effects of a one-armed oscillation, the longer period being the first overtone, the shorter period being the second overtone.

### 1.4.2 Prograde or retrograde precession?

In the previous section I discussed the different predictions of the various one-armed oscillation models. In determining the applicability of certain models it is often of interest to determine whether the precession of the perturbation proposed to explain the V/R cycle is prograde or retrograde to the rotation of the star/disc.

This determination can only be made with high inclination stars where the central star eclipses the perturbation. A cyclical V/R variation in the Hα line profile of the Be star $\beta^1$ Mon was shown to be consistent with prograde precession of a perturbation (Telting *et al.* 1994).

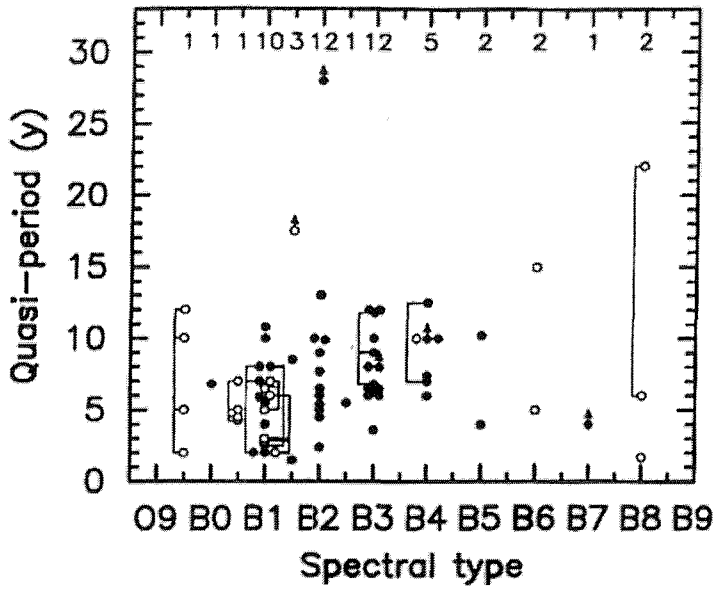


**Figure 1-6.** Distribution of V/R cycle periods by spectral type. Open circles represent stars known or suspected to be binaries. Taken from Okazaki (1996).

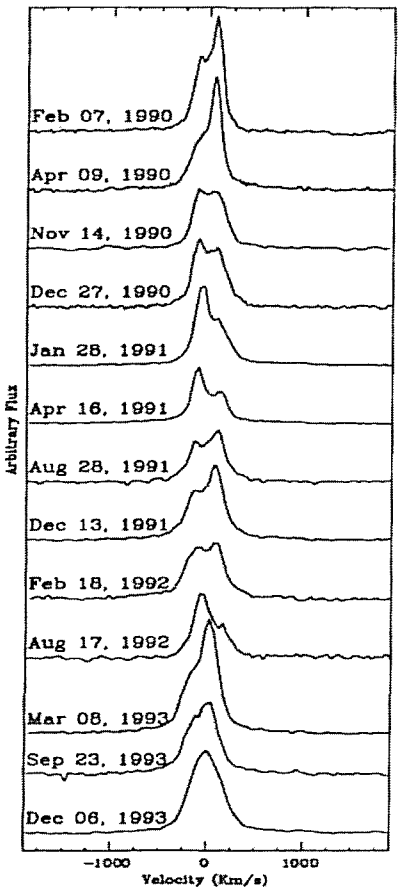


**Figure 1-7.** V/R variations in the Hα line of HD245770, with a periodicity of ~ 18 months (taken from Negueruela et al. (1998).

## 1.5 Summary

A Be star is a non-supergiant star of spectral class O, B, or A, whose spectra show, or have at one time showed, emission in the Hydrogen Balmer lines. Be stars have been identified in the range O5 to A0 with a peak in the distribution around B2. Approximately 10% of all B type stars show Be behaviour. In addition to the line emission, Be stars show an excess continuum flux at optical, infra-red and radio wavelengths.

In explaining the Be star phenomenon, two steps are required. Firstly, a physical model must be developed which reproduces the observations. Secondly, a theoretical model must be developed which explains the development of an object with the physical characteristics of the first model.

Many physical models have been developed with varying success. These models involve a circumstellar envelope around the B star which gives rise to the emission lines and Infrared excess. Observations suggest that this circumstellar envelope is non-spherical, with a dense, slow moving equatorial disc, and a low-density, high velocity wind at higher latitudes. As more observations are made, the physical models have become more and more sophisticated.

The attempts to explain the formation of such physical entities have been less successful. The first simplistic models explained the formation of a circumstellar disc as due to the rapid rotation of the star, though most Be stars are rotating below the critical break-up velocity. One of the most successful models is the wind compressed disc model, which explains the formation of a disc through collimation of an initially spherical wind by coriolis forces. This model however does not produce the required mass in the disc. It is likely that other mechanisms act to initially eject material from the star, then the mechanism proposed in the wind compressed disc model acts to form this material into a thin collimated disc.

The physical models developed to reproduce the observational characteristics of Be stars are limited by the observations available. Study at optical and infrared wavelengths constrains the models of the inner disc region, but the outer regions of discs prove difficult to study, as they are only expected to produce an observable contribution to the spectrum at radio wavelengths. Attempts to detect Be stars at radio wavelengths have had limited success, hinting that a change to the structure and/or dynamics of the disc occurs at some radius to cause a downturn in the spectral slope.

Some Be stars are found to be in binary systems, with an orbiting neutron star companion. In these systems, the neutron star may accrete from any circumstellar material, producing variable X-ray emission. These systems (reviewed in more detail in the following chapter) may provide a method for studying the outer regions of the disc, using the X-ray emission from the neutron star as a probe of the Be star's disc.

# Chapter 2 – Be/X-ray Binaries

In this chapter I review X-ray binaries in general before concentrating on the subclass of this group that have Be star mass donors – Be/X-ray Binaries (Be/XRBs). In particular, I shall review certain aspects of Be/XRBs that are of relevance to the work presented in the following chapters of this thesis.

I review existing literature on the observational characteristics of Be/XRBs, and how these can be related to the properties of the mass donating Be star. In other words, I describe how the orbiting neutron star can act as a probe of the conditions in the circumstellar environment of the Be star in these systems. Finally, I review the ongoing debate as to whether the orbit of the neutron star in Be/XRB systems changes or perturbs the circumstellar environment of the Be star. The results which I present in later chapters may be undermined if it is found that, some kind of macroscopic uncertainty principle prevents us from learning the properties of the circumstellar envelope without it being perturbed from its 'natural' state by the presence of our neutron star probe.

I shall also consider the similarities and differences between Be stars in X-ray binary systems and those which have no binary companion. If we intend to draw global conclusions about Be stars – binary or isolated – from observations of those that exist in X-ray binary systems, it is important to first establish that no fundamental differences exist between the two populations that will undermine the results.

## 2.1 Historical background to X-ray binaries

X-ray astronomy is a relatively young science, born in the 1960's as the X-ray portion of the electromagnetic spectrum became accessible from rocket and balloon borne detectors. Many discrete sources of X-ray radiation were quickly identified, their distribution concentrated in line-of-sight with the Galactic plane implying that the majority of sources were Galactic in origin (Figure 2-1).

The first explanations for the Galactic X-ray sources involved these objects being neutron stars formed in recent supernovae, young enough to be radiating significant thermal energy (Chiu & Saltpeter 1964). However, once instruments had been developed to enable determination of X-ray spectral energy distribution, and allow primitive spatial resolution, the model proved incapable of explaining observations. The Crab X–ray source was found to be spatially extended, and the X-ray source Sco X-1 was shown to have a non-Plankian X-ray spectrum (Jan van Paradijs, 1998).

At the same time, a model had been proposed for quasars that involved accretion of material onto a compact object leading to the emission of X-rays. This led to a proposal that the Galactic X-ray sources were mass exchanging binaries where the accreting component was a compact object (Burbidge 1972; Shklovsky 1967).

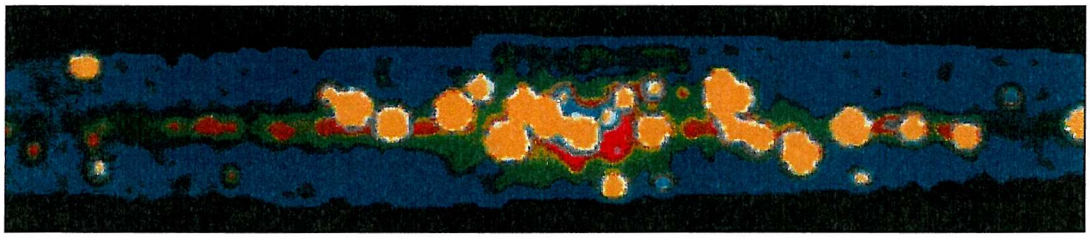

**Figure 2-1.** X-ray image of the Galactic plane from the EXOSAT galactic survey, showing the concentration of bright X-ray point sources at low Galactic latitudes, and towards the centre of the Galaxy.

Following the determination of a 1-arc-minute error box for the X-ray source Cyg X-1 by Rappaport et al. (1971), it was associated with a radio source and a known $8^{th}$ magnitude supergiant star HD 226868 (Hjellming & Wade 1971; Braes & Miley 1971). Assuming a normal mass for the supergiant star, the mass function determined from optical spectroscopic radial velocity measurements implied that the mass of the compact accreting object in the system was greater than 3 $M_{\odot}$ exceeding the theoretical mass limit for a neutron star. The first confirmed X-ray binary system was therefore likely to contain an accreting black hole.

Shortly after the binary mass-transfer nature of Cyg X-1 was determined, the pulsating X-ray source Cen X-3 was identified as a neutron star with a spin period of 4.8-seconds orbiting a $M > 10M_{\odot}$ supergiant with an orbital period of 2.1-days (Giacconi *et al.* 1971; Schrier *et al.* 1972). This was followed by many more identifications of eclipsing X-ray pulsars with early type stars, and a galactic population of high-mass X-ray binary stars (HMXB) was quickly established.

Late in the 1970's a population of X-ray sources concentrated toward the Galactic centre were identified as similar binary systems in which a compact object accretes from a low mass companion ($M < 2\ M_{\odot}$). In these systems the non-degenerate component of the binary fills its Roche-Lobe, transferring mass through the inner Lagrangian point to an accretion disk around the compact object. This accretion disk reprocesses incident X-rays into optical/UV photons which dominate the optical spectrum – in HMXB the optical spectrum is dominated by the mass donor star, which has a bolometric luminosity of similar order of magnitude to the X-ray source.

Figure 2-2 shows the positions on the sky of X-ray binaries taken from the catalogue of van Paradijs (1995). The two maps show HMXBs (top) and LMXBs (bottom, with Globular Cluster sources shown as open circles) plotted in Galactic co-ordinates. It is clear that both distributions are concentrated toward the Galactic plane, and that LMXBs are concentrated toward the Galactic centre.

Ignoring a small number of nearby high-latitude HMXB, van Paradijs (1998) calculates the average latitude for HMXB objects of $< b^{II}_{HMXB} >= 0.4 \pm 1.9°$, consistent with a Population I origin. (See also Figure 3-5 for a comparison of the Be/X-ray binary distribution to the distribution of Population I stars).

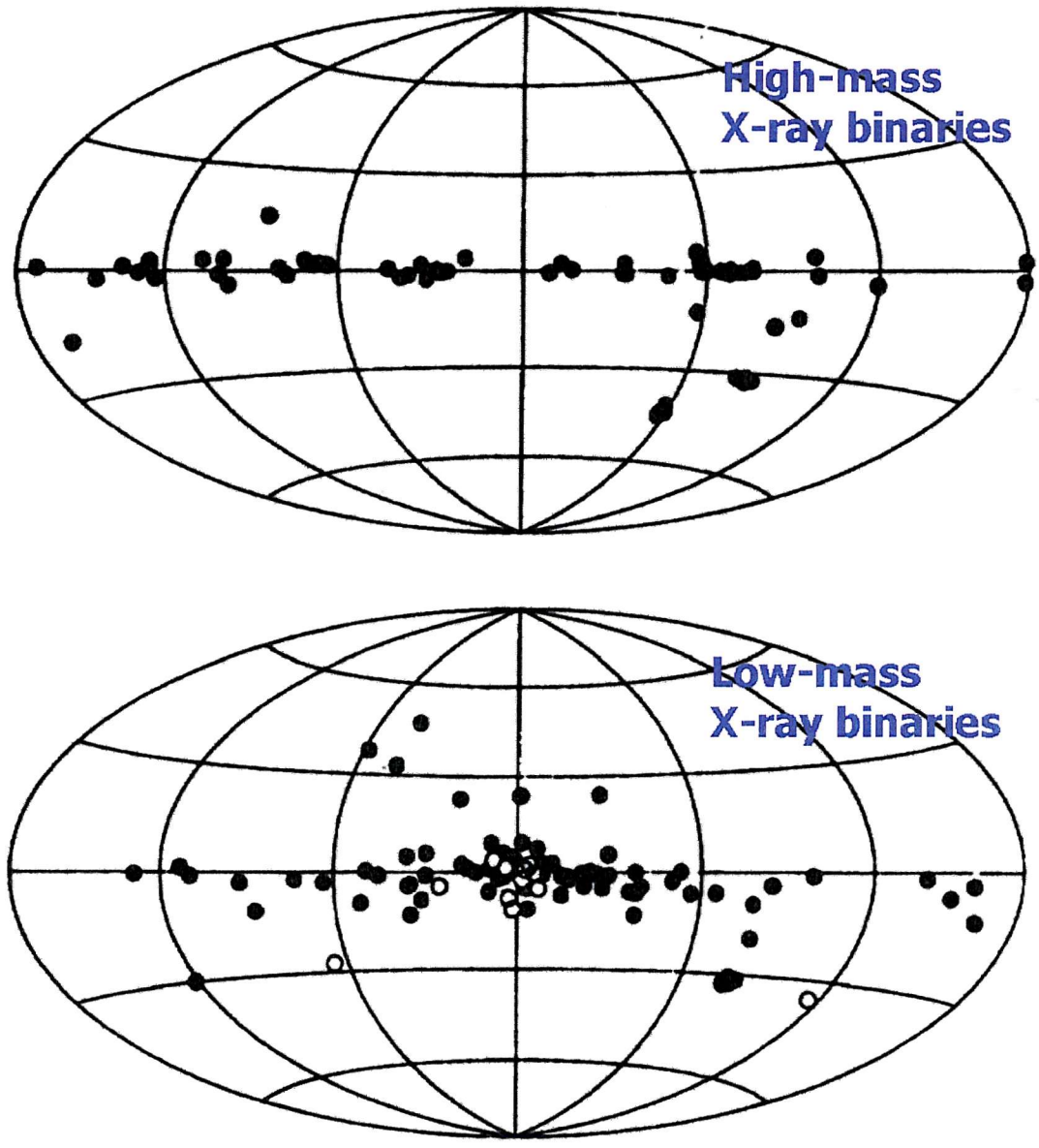


**Figure 2-2.** Sky distributions of (top) high-mass X-ray binaries and (bottom) low-mass X-ray binaries. The open circles in the lower map represent Globular Cluster sources. The maps are based on the catalogue of van Paradijs (1995).

## 2.2 Binary stars

Binary star systems contain two stars orbiting a common centre of mass. The orbits of binary systems follow ellipses described by Kepler's laws of planetary motion. The systems can be characterised by the type of each component (including their masses and radii) and their orbital separation. These parameters also largely determine the behaviour of the binary system.

### 2.2.1 Binary orbits

The orbits of stars in a binary system are described by Newton's general form of Kepler's third law:

$$P^2 = \frac{4\pi(a_1 + a_2)^3}{G(M_1 + M_2)} \tag{2-1}$$

Where $a_1$ and $a_2$ are the semi-major axes of the orbits of stars of mass $M_1$ and $M_2$ respectively, and $P$ is the orbital period. The orbits are generally elliptical, with ellipticity $e$ given by:

$$e^2 = 1 - \frac{b^2}{a^2} \tag{2-2}$$

where $a$ and $b$ are respectively the semi-major and -minor axes of the orbit of one of the stars with respect to the other.

### 2.2.2 Roche potential and Roche lobes

The gravitational potential of a binary system, in a co-rotating frame is described by the Roche potential:

$$\phi(r) = -\frac{GM_1}{|r - r_1|} - \frac{GM_2}{|r - r_2|} - \frac{1}{2}|\omega \times r|^2 \tag{2-3}$$

where $r_1$ and $r_2$ are the distances to the centre of mass of the two components of mass $M_1$ and $M_2$ respectively, $\omega$ is the angular velocity.

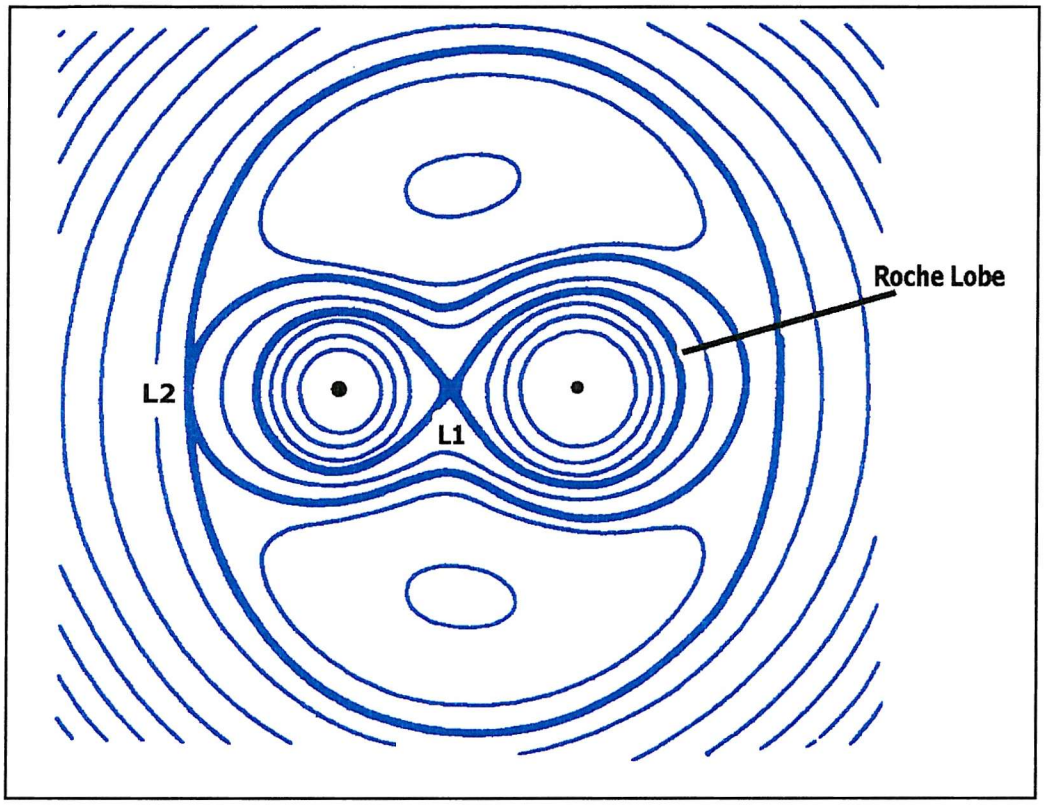


**Figure 2-3.** Equipotential surfaces of a close binary system, showing the L1 and L2 Lagrangian points and the Roche Lobe.

Figure 2-3 shows the equipotential surfaces in a binary system. Close to the surfaces of the individual stars, the potential forms approximately circular contours around each star. A critical contour exists which consists of two lobes, one surrounding each star and connected at a point on the line of centres (a line joining the centres of mass of each star and that of the whole system). These lobes are referred to as Roche lobes, the point at which they meet as the inner Lagrangian point ($L_1$ point). At the $L_1$ point, the net gravity on a particle due to the two stars vanishes – hence matter may pass more easily from the companion to the primary through the $L_1$ point.

The behaviour of the binary system depends to a large extent on the sizes of the two components relative to their respective Roche lobes. Verbunt (1990) gives approximations to the average radius of the Roche lobes (accurate to ~2%):

$$\frac{R_{Roche}(M_1)}{a} \approx 0.38 + 0.2\log\left(\frac{M_1}{M_2}\right) \tag{2-4}$$

and

$$\frac{R_{Roche}(M_2)}{a} \approx 0.46\left(\frac{M_2}{M_1 + M_2}\right)^{\frac{1}{3}}. \tag{2-5}$$

If both binary components lie well within their respective Roche lobes, the system is a detached binary. If one of the stars expands to fill its Roche lobe, the system becomes a semi-detached binary. Material is lost through the $L_1$ point, this material will then fall onto the companion star, either directly or – if the specific angular momentum of the transferred mass is too high for direct accretion – via an accretion disk. If the star that has filled its Roche lobe is the more massive of the binary components, the effect of the transfer of mass will be to reduce the orbital separation of the system, hence reducing the size of the Roche lobes further. In this way, Roche lobe overflow in a close binary system can be self-sustaining if it is the more massive star that is filling its Roche lobe.

If both components fill their Roche lobes, the system becomes a contact binary, sharing a common envelope. Material can eventually be lost from the system through the outer Lagrangian point ($L_2$).

## 2.3 Energy source of X-ray binaries

For a star of mass $M_*$ and radius $R_*$ the gravitational potential energy released by a mass $m$ falling from infinity to the surface of the star is given by the equation

$$\Delta E = \frac{GM_* m}{R_*} \tag{2-6}$$

Where $G$ is the gravitational constant. Not all of this energy will be converted to radiative energy – the efficiency with which gravitational energy is converted to electromagnetic energy is given by

$$e = \frac{GM_*}{R_* c^2} \tag{2-7}$$

Equation (2-7) shows that the efficiency is determined by the compactness of the accreting object ($M_*/R_*$). For a black hole, the efficiency is ~0.4, for a neutron star ~0.1, for a white dwarf, only ~$10^{-4}$.

## 2.4 High Mass X-ray Binaries

X-ray binaries are usually sub-divided according to the type of mass-donor. High-mass X-ray binary systems have mass-donors more massive than ~$10M_\odot$, while the low-mass X-ray binaries have mass-donors less massive than ~$2M_\odot$. Roughly speaking, the reason for the void between 2 – 10 $M_\odot$ is that stars with $M > 10\ M_\odot$ have stellar winds strong enough to power an accreting X-ray source, if the mass-donor is slightly less massive, the wind is generally not strong enough to overcome centrifugal inhibition. Mass donating stars with $M < 2\ M_\odot$ can transfer mass through stable Roche-lobe overflow, but for more massive donors, the overflow is unstable and the neutron star quickly becomes engulfed in material obscuring the X-ray source.

HMXB can be further sub-divided according to the evolutionary status of the mass-donating component. Be/X-ray binaries are Be star/Neutron star binaries in eccentric orbits, the neutron star accreting from the Be star's equatorial disk. In supergiant X-ray binaries, the neutron star orbits an evolved early-type star, accreting from the strong stellar wind. Figure 2-4 shows the relative positions of the two types of mass-donor in the Hertzsprung-Russel diagram. The supergiant systems are characterised by orbital periods of the order of a few days, and are generally persistant X-ray sources. On the other hand, the Be star systems have wide orbits with periods of the order of 10's – 100's days, and are generally transient X-ray sources.

Observationally, approximately equal numbers of Supergiant and Be star X-ray binaries are known in the Galaxy. However, it is believed that Be/X-ray binaries are much more common that Supergiant X-ray binaries. Be/X-ray binaries spend much of their lifetime inactive (A1118–615) and it is expected that there are of the order of 10 inactive Be/X-ray binaries for each active system. In contrast, SGXB tend to be persistent sources, hence only those sources which lie too distant to be detected will remain unknown to us. Bildsten *et al.* (1997) extrapolate observations to estimate that the Galactic Be/X-ray binary systems number $10^2$ – $10^3$, while Meurs & van den Heuvel (1989) consider evolutionary models to estimate that the Galaxy contains ~ $10^4$ Be star/Neutron star binaries, approximately (2-6) x $10^3$ of which are potential X-ray binaries. The Galactic Supergiant systems number ~ 40.

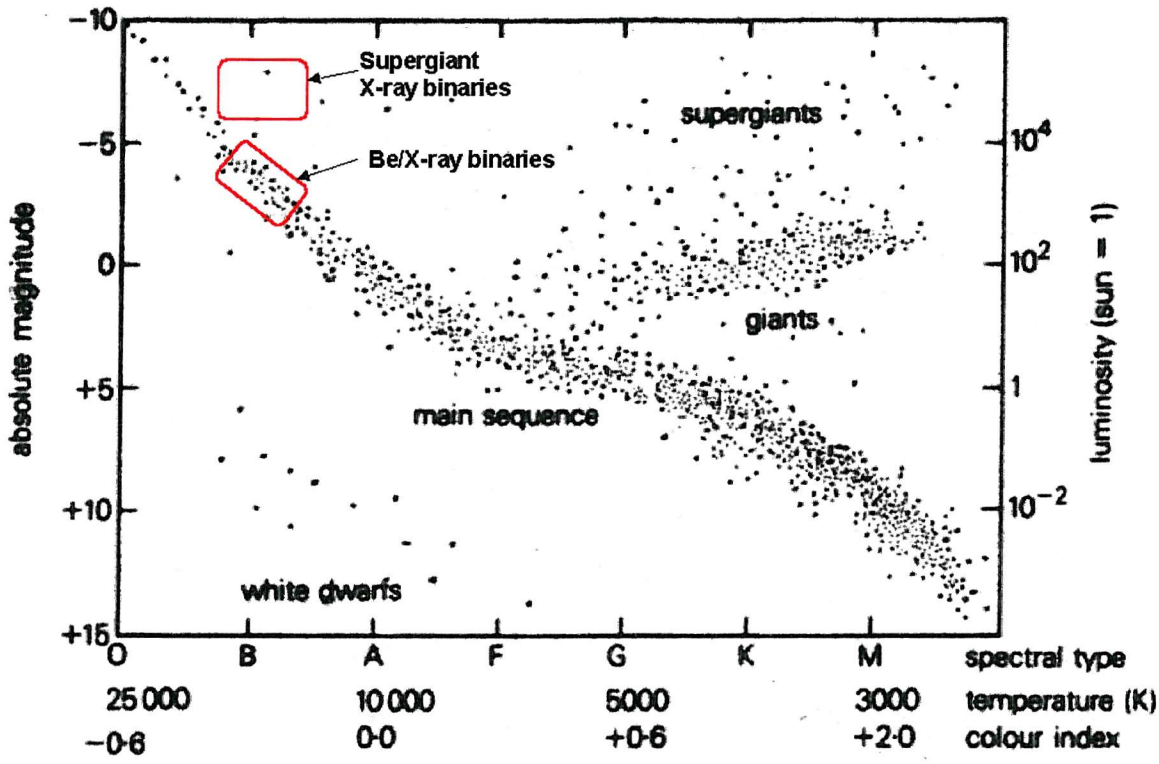


**Figure 2-4.** Hertzsprung-Russel diagram with the positions of the optical counterparts to Supergiant and Be star X-ray binaries marked.

### 2.4.1 Supergiant X-ray binaries

Supergiant X-ray binary systems contain an OB supergiant (luminosity class I-II) earlier than ~B2, transferring mass to a compact companion – neutron star or black hole. The spectral type cut-off at B2 exists because the winds of later type supergiants are not sufficiently strong for the accreting material to overcome the centrifugal barrier imposed by the magnetosphere of the neutron star; see Section 2.5.4). The orbits tend to be short (a few days) with low eccentricity. The close orbit leads to the supergiant filling or nearly filling its Roche-lobe. Mass transfer can then occur either through Roche-lobe overflow (Figure 2-7), or via a strong stellar wind (Figure 2-6), although in reality, there is likely to be less distinction between the two mechanisms as discussed below.

Figure 2-5 shows the Roche-lobe geometry for the SGXB Cen X-3, showing the supergiant only just under-filling its Roche-lobe, and tidally distorted (taken from Audley 1997). This tidal distortion, combined with X-ray heating of the supergiant by the neutron star, sometimes leads to ellipsoidal variations in the optical lightcurves of SGXB.

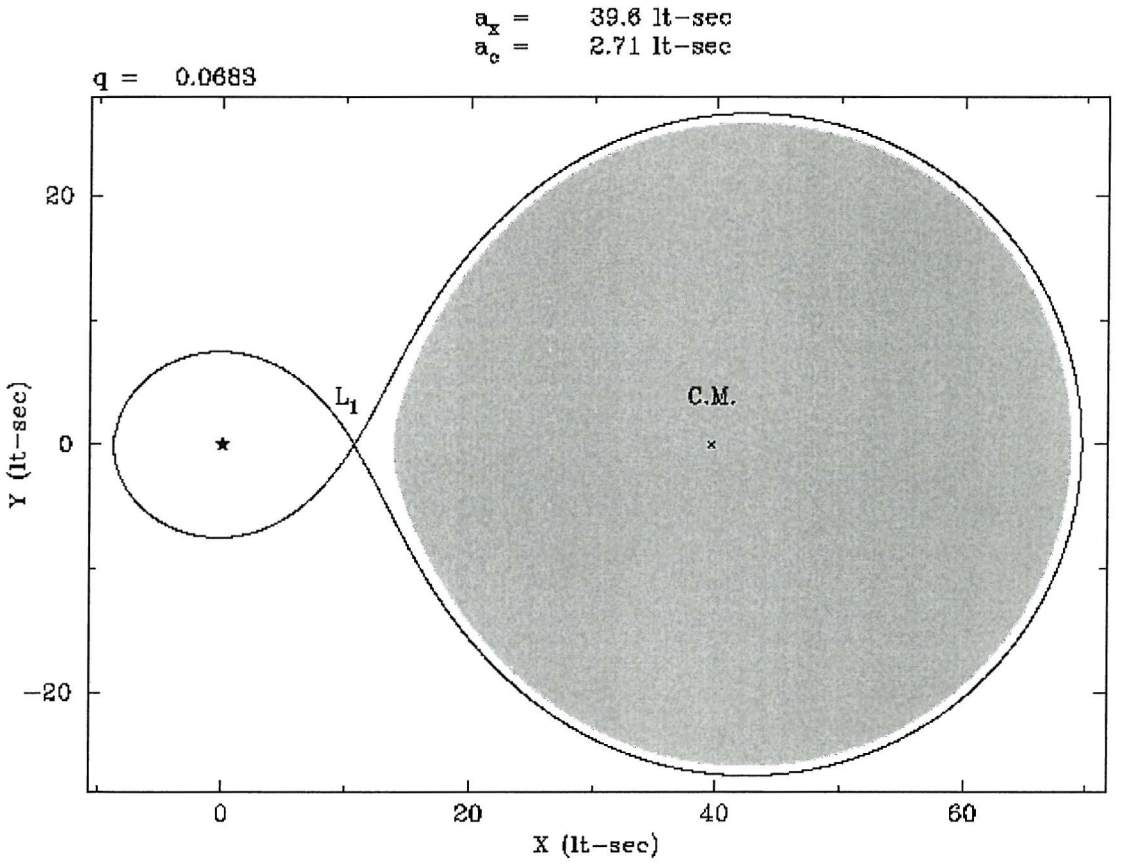


**Figure 2-5.** Roche geometry calculated for a system with masses and orbital separation similar to the Supergiant X-ray binary Cen X-3.

At the two extremes, mass transfer in SGXB depends upon the size of the supergiant relative to its Roche-lobe. However, even for those systems in which the supergiant under-fills its Roche lobe, the stellar wind is strongly enhanced along the line of centres due to the gravitational influence of the compact companion, leading to a tidal stream flowing through the inner Lagrangian point ($L_1$).

In the wind fed model, a neutron star moving with a relative velocity $v_{rel}$ through the stellar wind with sound speed $c_{sound}$ will capture material from a cylinder of radius $r_{capture}$ for which the gravitational potential due to the compact object cancels the kinetic energy of the wind material.

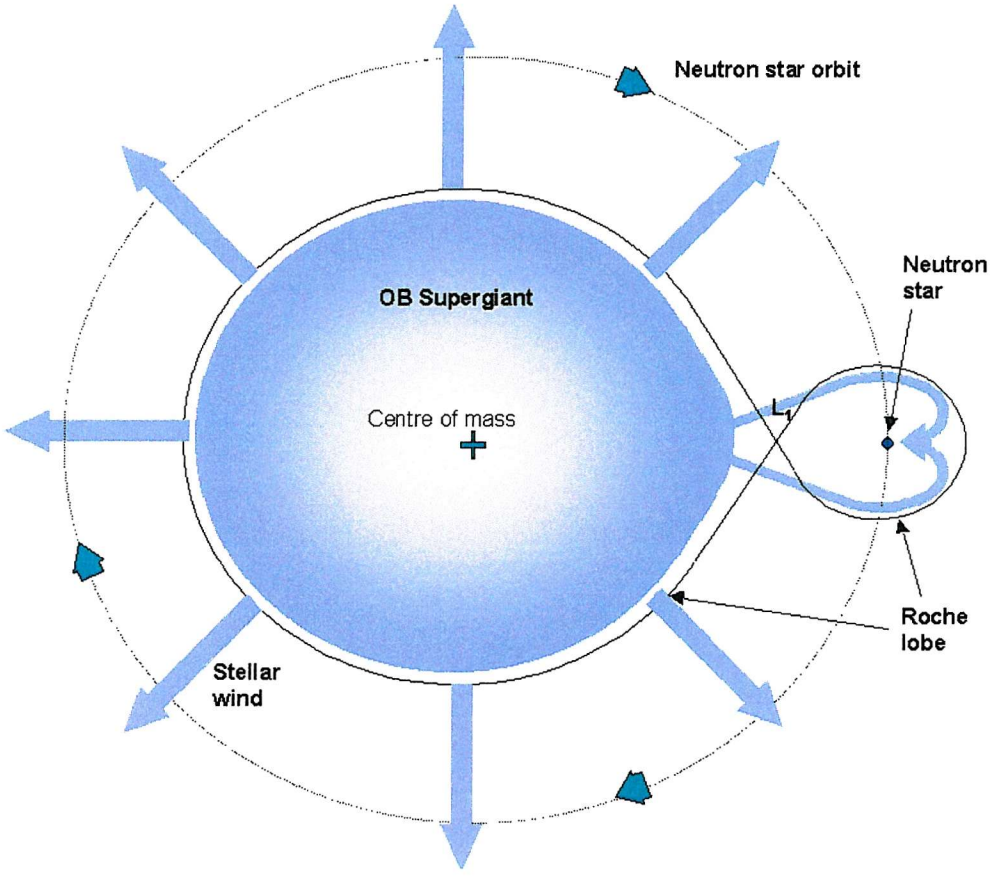


**Figure 2-6.** Mass-transfer via a strong stellar wind in a supergiant X-ray binary. The supergiant is tidally and rotationally distorted, its wind is enhanced through the line of centres by the gravitational influence of the compact companion, leading to a tidal stream through the inner Lagrangian point ($L_1$).

In a Roche lobe overflow model, the radial velocity of the transferred material is much lower than the azimuthal velocity relative to the orbiting compact object and the specific angular momentum of the transferred mass is high. Accretion onto the compact object cannot occur until angular momentum has been lost, so the matter will settle in the lowest energy orbit that conserves angular momentum. Viscous interactions result from the differential Keplerian rotation, transporting angular momentum outwards through the disk, allowing the innermost material to fall onto the compact object.

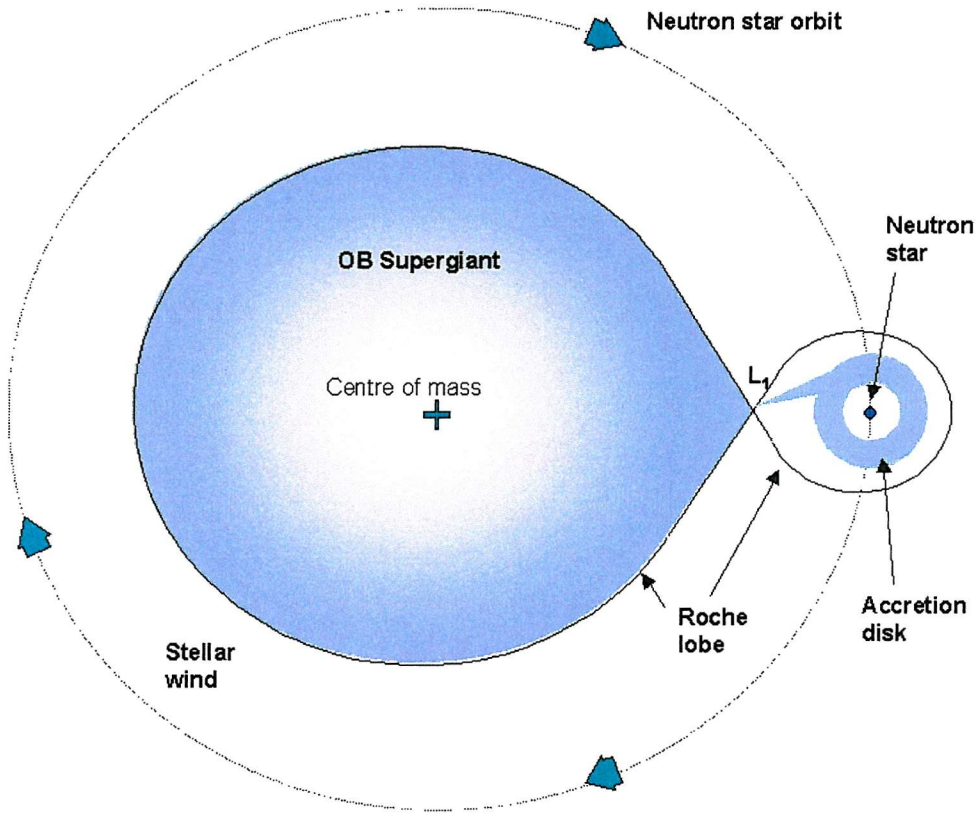


**Figure 2-7 .** Mass transfer via Roche lobe overflow in a supergiant X-ray binary. The supergiant fills its Roche lobe, at the inner Lagrangian point ($L_1$) the net gravity is zero, and material falls into the gravitational well of the compact object, forming an accretion disk.

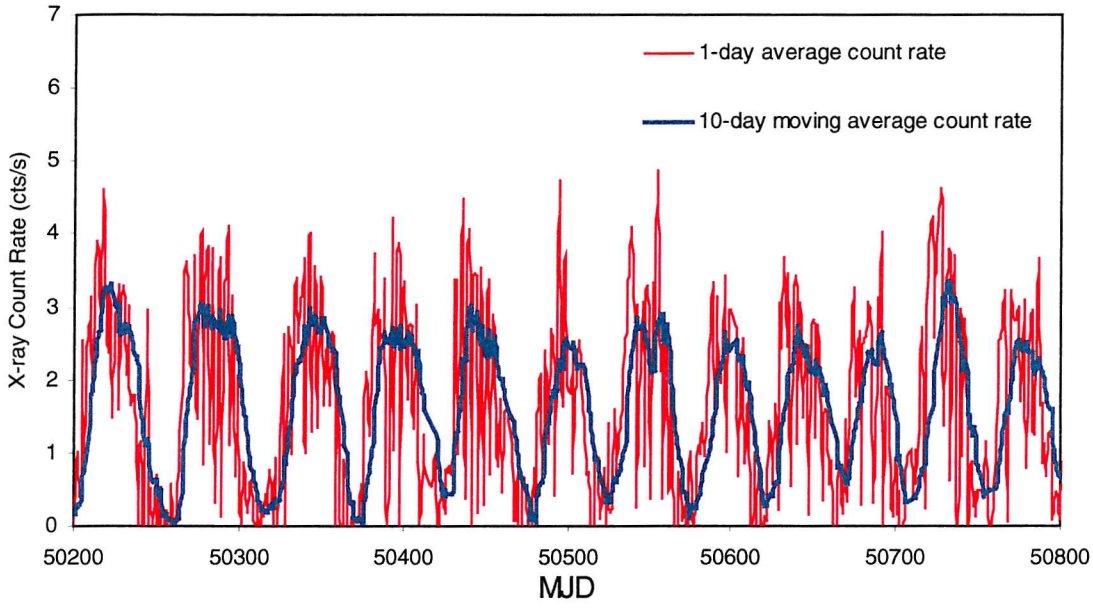


**Figure 2-8.** X-ray lightcurve of the supergiant X-ray binary SMC X-1. The red curve represents one-day average fluxes publicly available from the RXTE ASM, the blue curve is a 10-day moving average of the count-rate.

In some SXRB, the X-ray lightcurves show clear modulation on timescales much longer than the orbital period of the system. Figure 2-8 shows the X-ray lightcurve of the SXRB SMC X-1 created from public data available from the RXTE ASM, showing a clear periodicity with a period of ~ 50 days, compared to an orbital period of 3.89-days. In these systems, the X-ray lightcurve modulation is interpreted as due to a precessing warped accretion disk.

### 2.4.2 Be/X-ray binaries

Be/X-ray binaries were first recognised as a sub-group of X-ray binaries by Maraschi, Treves & van den Heuvel (1976). The mass donor in these systems is a Be star, observationally of spectral type within the range O9 – B2. Orbital periods are of the order of tens of days and can be as long as hundreds of days, and the orbits typically have high eccentricity.

The Be star significantly under-fills its Roche lobe, and does not have a stellar wind as strong as those from Supergiants. The accretion material in these systems comes from the Be star's circumstellar disk, so that the X-ray luminosity of the source shows orbital modulation as well as long term, aperiodic variability due to variations in the structure and dynamics of the Be star's disk. The behavioural characteristics specific to Be/X-ray binaries are discussed in more depth in the following sections.

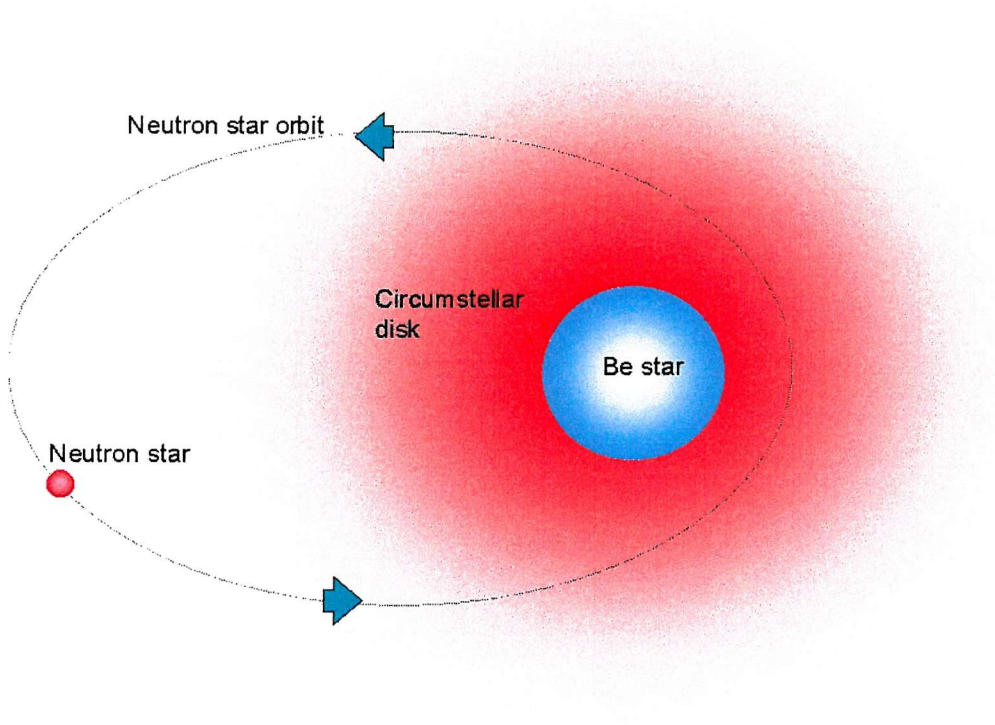


**Figure 2-9.** Schematic of a Be/X-ray binary system. The eccentricity of the neutron star's orbit causes it to encounter varying velocity/density wind material throughout the orbital cycle.

## 2.5 Accreting neutron stars

The nature of the compact object in X-ray binaries is an important factor in determining the emission properties of the system. For instance, the X-ray flux could be emitted by the polar caps of a magnetised neutron star, an accretion disc around black hole, or a shock heated region in an inflow that is essentially spherical. As the bulk of work in this thesis concerns the systems which contain a magnetised neutron star orbiting a Be star, I shall concentrate on neutron stars only.

If the neutron star is highly magnetised, (B ~ $10^{12}$ G) then the accretion flow will be channelled onto the magnetic poles (Davidson & Ostriker 1973), and the source may display pulsations if the rotation and magnetic axes are misaligned (see Section 2.5.1). If the magnetic field is small (B < $10^{10}$ G) then an accretion disc around the neutron star may extend to the surface of the neutron star, where the energy released from the disc/star boundary layer will dominate the emission.

The radius at which the material is threaded onto the magnetic field lines is known as the magnetospheric radius $r_m$, and can be calculated by equating the magnetic pressure to the ram pressure of the inflow. For accretion via an accretion disc, this is given by

$$r_m = 1.5\times10^8 \mu_{30}^{4/7} M_x^{1/7} R_6^{-2/7} L_{37}^{-2/7} \text{ cm.} \qquad (2\text{-}8)$$

Where $\mu_{30}$ is the magnetic moment of the neutron star in units of $10^{30}$ G cm$^3$, $M_x$ is the neutron star mass in solar units, $R_6$ is the radius of the neutron star in units of $10^6$ cm, $L_{37}$ is the X-ray luminosity in units of $10^{37}$ ergs s$^{-1}$ (Ghosh and Lamb 1978, 1979a,b).

### 2.5.1 X-ray pulsars

A large proportion of HMXB display pulsations in their X-ray flux. The existence of X-ray pulsations is an indicator of a highly magnetised accreting object. Pulsations result from a misalignment of the rotational and the magnetic axes of the neutron star. X-ray emission is beamed from the poles of the neutron star, and as the star rotates, these beams sweep across the line of sight leading to the observed pulse profiles in X-ray lightcurves (see Figure 2-10).

Pulsars often show changes in pulse period. Spin-down occurs as angular momentum is transferred from the neutron star to the surrounding medium. Spin-up occurs when the material accreting onto the neutron star adds angular momentum. Elsner and Lamb (1977) showed that close to corotation, when the angular velocity of the neutron star is approximately equal to the Keplerian angular velocity at the radius of the magnetosphere, the net angular momentum transfer can be such that the neutron star spins down even though accretion is taking place.

In Be star systems, where the accretion rate is modulated around the orbit, the spin period of the neutron star tends to spin down throughout much of the orbit, but spin up during periastron passage, when the accretion rate is much higher.

### 2.5.2 X-ray pulse arrival timing

The timing of pulse arrival times allows determination of orbital parameters, and when combined with radial velocity measures of the massive optical component, can provide a complete orbital solution including the masses of the individual stars.

Pulse arrival times can be measured with increasing accuracy, allowing measurement of the delays from the arrival times expected if the neutron star were not in a binary system. These delays are caused by the light-crossing time of the orbit (hence many X-ray astronomers refer to orbital dimensions in units of light-seconds).

### 2.5.3 X-ray pulse profiles

The shapes of X-ray pulse lightcurves various greatly from source to source. A comprehensive atlas of pulse profiles was presented by Rappaport & Joss (1983) and by White et al. (1983). The degree of modulation of the X-ray luminosity varies between ~ 0.1 and 0.9, while the shapes vary between single and double peaked profiles, symmetric or asymmetric, energy dependant or otherwise.

Many of these variations can be attributed to the geometrical alignment of the rotation axis, the magnetic axis, and the line of sight of the observer. However, the structure of the accretion column onto the polar caps is also a factor in the resulting profiles. For a review see references in Joss & Rappaport (1984).

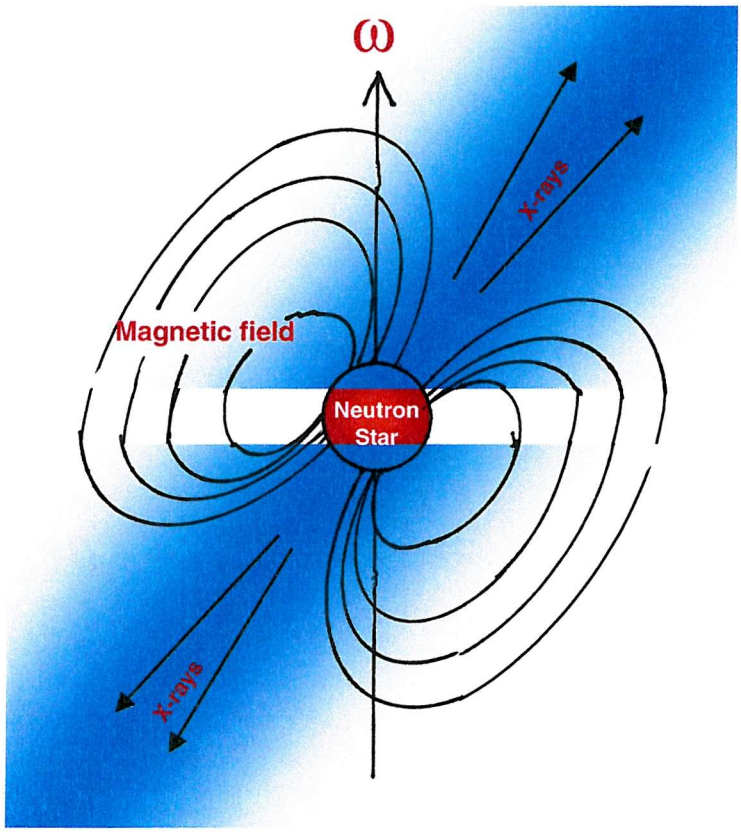


**Figure 2-10.** Schematic of an X-ray puslar showing how the pulsations result from a misalignment of the magnetic and rotation axes of the neutron star. X-rays are emitted in beams from the magnetic poles which sweep across the line of sight leading to periodic pulses of X-ray flux.

Pulse periods range from 10s of milliseconds (e.g. A0538-66 with $P_{pulse}$ = 69-msec) to 100s of seconds (e.g. X Per with $P_{pulse}$ = 835-seconds). When pulse periods are plotted against orbital periods for Be star and supergiant HMXBs, the two populations show different distributions (Corbet 1986). The Be star systems show a strong correlation between orbital period and spin period (Corbet 1984, 1986) whereas for the supergiant systems, the relationship between pulse period and orbital period depends upon the accretion mechanism – by Roche lobe overflow or from the stellar wind.

Corbet explains the correlation in the case of Be/X-ray binaries by considering the neutron stars to be in an equilibrium state, where the spin-down torques applied to the neutron star via interaction with the surrounding medium are cancelled by the opposite torque applied by accreted material. If the neutron star's spin period were greater, accretion would be centrifugally inhibited and the neutron star would spin down. If the spin period were less, the accretion rate would be greater, and the neutron star would spin up. The longer the orbital period, the wider the orbit, and the less dense would be the material around the neutron star – this means that the neutron stars in longer period systems would need to spin down to longer pulse periods before accretion takes place.

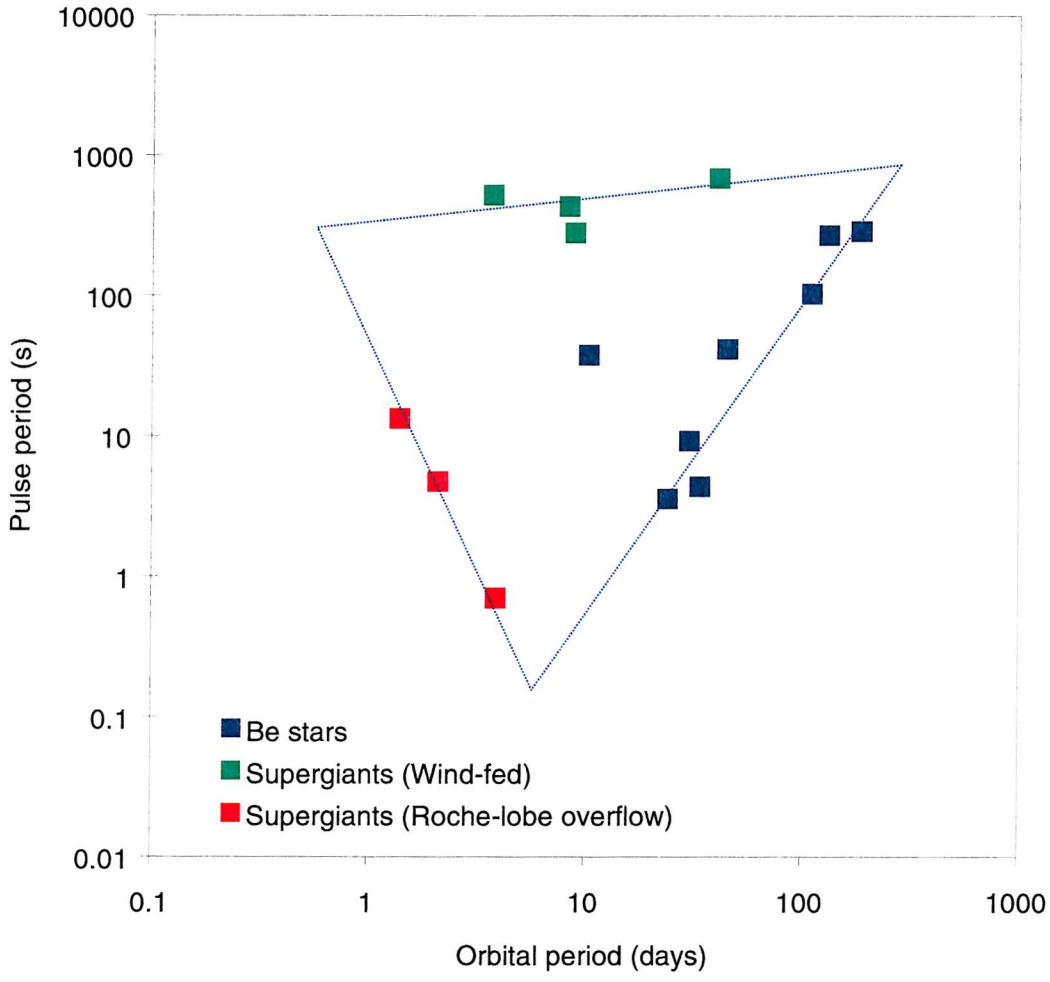


**Figure 2-11.** Corbet diagram (after Corbet 1986) showing the different relationships between orbital period and pulse period for X-ray pulsars in supergiant systems (wind-fed and Roche-lobe overflow-fed) and in Be star systems.

### 2.5.4 Centrifugal inhibition of accretion

Equation (2-8) shows that the radius of the magnetosphere is dependent on the X-ray luminosity – hence also on the accretion rate. If the accretion rate falls, the magnetosphere increases in size, and eventually may extend beyond the corotation radius $r_c$ where the Keplerian angular velocity equals that of the neutron star (and hence the magnetosphere). If this is the case, angular momentum is transferred from the magnetosphere to the infalling material, which is propelled away from the neutron star.

A minimum X-ray luminosity can be calculated as

$$L_{\min} = 2.5\times10^{37}\,\mu_{30}^{2}M_{x}^{-2/3}R_{6}^{-1}P_{s7}^{-7/3}\ \mathrm{erg\ s^{-1}} \qquad (2\text{-}9)$$

below which accretion will cease.

This centrifugal barrier to accretion can lead to much greater modulation of X-ray flux than would be expected purely from eccentric orbits (as investigated in Chapter 4) as the source switches off when the X-ray luminosity drops to $L_{min}$.

## 2.6 Periodic Outbursts in Be/X-ray binaries

In general, Be/X-ray binaries are only detected as transient X-ray sources. The outbursts of X-ray activity displayed by these systems have been subdivided into two categories. Type I outbursts are periodic, recurring at time intervals equal to the orbital period of the system. Type II outbursts are very luminous events, often close to the Eddington limit, with longer duration, and without necessarily any correlation to orbital phase.

The Type I periodic outbursts are explained by the eccentricity of the orbits of Be/X-ray binary systems. On the simplest level, the explanations involve the neutron star being immersed in the circumstellar disk of the Be star during periastron passage, but beyond the disk limits throughout most of the rest of the orbit. The actual contributing factors to the X-ray lightcurve shape are more complicated, and are discussed in more depth in Chapter 4.

The Type II outbursts are generally believed to occur as a result of a large scale mass ejection from the Be star. During Type II outbursts the X-ray luminosity can approach the Eddington limit, and the duration of the outbursts can extend to a number of orbital cycles. The precise mechanism for the mass ejection events is

unclear, but once the ejection has taken place, a shell of ejected material is expected to expand away from the stellar surface, eventually reaching a distance at which it envelopes the orbit of the neutron star and accretion begins. An accretion disk is likely to form around the neutron star, acting as reservoir of material which will dampen orbital modulations, and the outburst will persist until the shell of material has expanded beyond the neutron star's orbit.

Other Be/X-ray binary systems display no outbursts at all, but rather are detected as persistent low luminosity X-ray sources. These systems are usually long period binaries with orbital periods of the order of 100's of days. Due to the wide separation of these systems the neutron star never becomes immersed in the dense circumstellar disc, but rather accretes from a lower density wind. It is likely that the distinction between Be star equatorial and polar winds described in Section 1.1.3 becomes blurred at large distances from the Be star (of order of 10's of stellar radii). In wide orbit Be/X-ray binaries therefore, the neutron star will accrete from a lower density homogeneous wind, leading to little or no orbital modulation of the X-ray luminosity.

Figure 2-12 shows the detections of transient X-ray pulsars by the *BATSE* instrument on the Compton Gamma Ray Observatory (*CGRO*). Of particular note are the periodic (Type I) outbursts shown by the sources GRO J2058+42, A0535+262, 4U 1145-619, 2S1845-024 and EXO 2030+375. Also note the series of detections of the source 2S 1417-624, which begins with a long outburst of Type II, followed by periodic short outbursts (Type I). Figure 2-13 shows the X-ray lightcurve of the Be/X-ray binary 4U1145-619 plotted from the RXTE ASM data.

Even Be/X-ray binaries which at one time show periodic Type I outbursts might at times become inactive for long periods of time. The EXOSAT source EXO 2030+375 for instance was detected by BATSE for an unbroken series of 13 Type I outbursts between MJD ~ 48600 and MJD ~ 49200, then was not detected at all between MJD ~ 49200 and MJD ~ 50100, after which a series of 8 Type I outbursts

was detected. Other sources in Figure 2-12 appear inactive until a series of 5-10 Type I outbursts is seen, followed by further inactivity.

No conclusive theory has been proposed to explain the transition between total inactivity and periodic outbursts, though it is almost certainly related to changes in the structure and dynamics of the Be star's circumstellar disc. In Stevens *et al.* (1997) and in Chapter 3 I present concurrent optical/IR and X-ray flux histories and Hα spectroscopy of the Be/X-ray binary 4U1145-619 and attempt to correlate the X-ray activity to changes in the Be star's envelope.

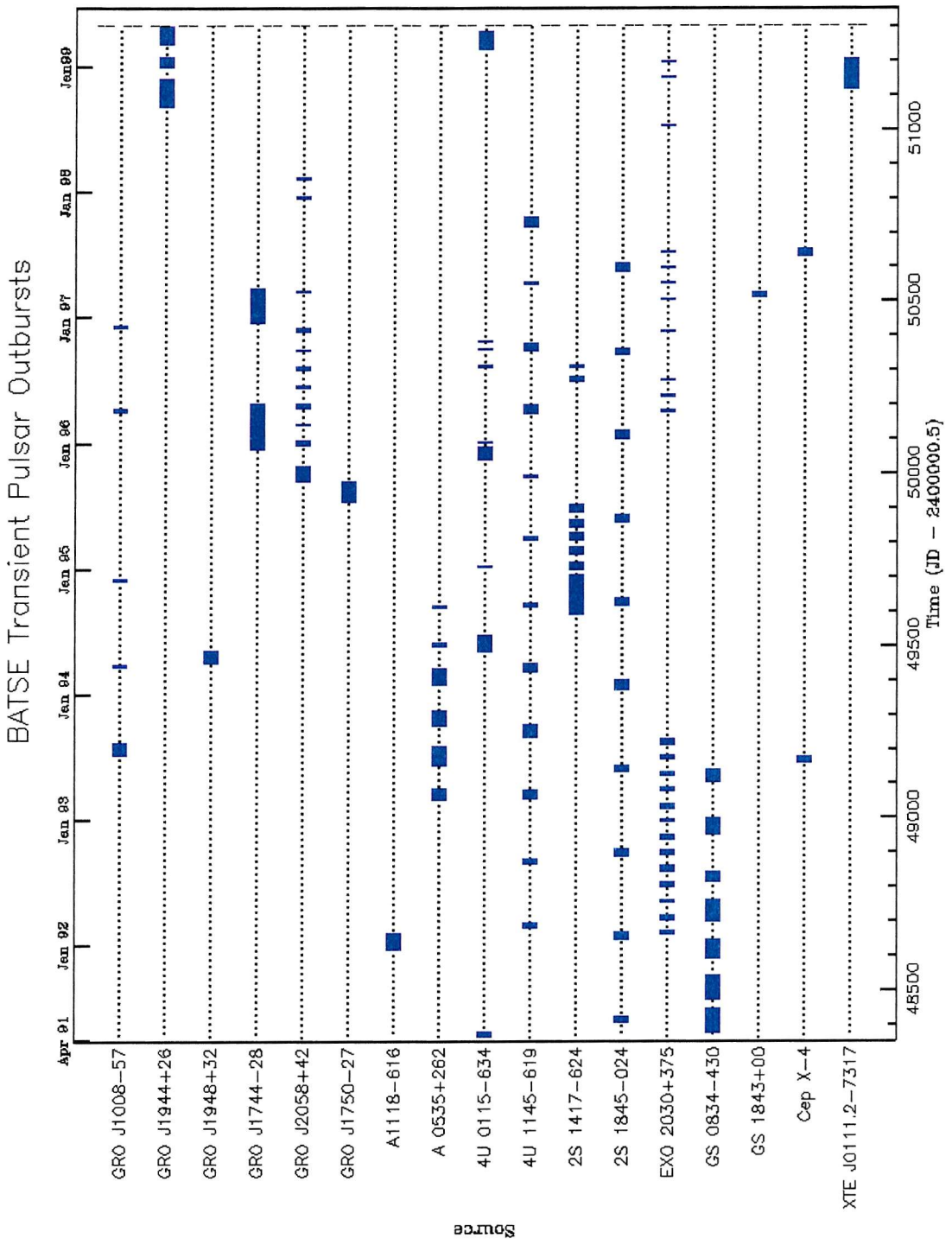


**Figure 2-12.** Summary of all detected outbursts of transient pulsars seen by BATSE since the launch of the Compton Gamma Ray Observatory. Note the periodicity evident in the recurrent outbursts of sources GRO J2058+42, A0535+262, 4U 1145-619, 2S1845-024 and EXO 2030+375.

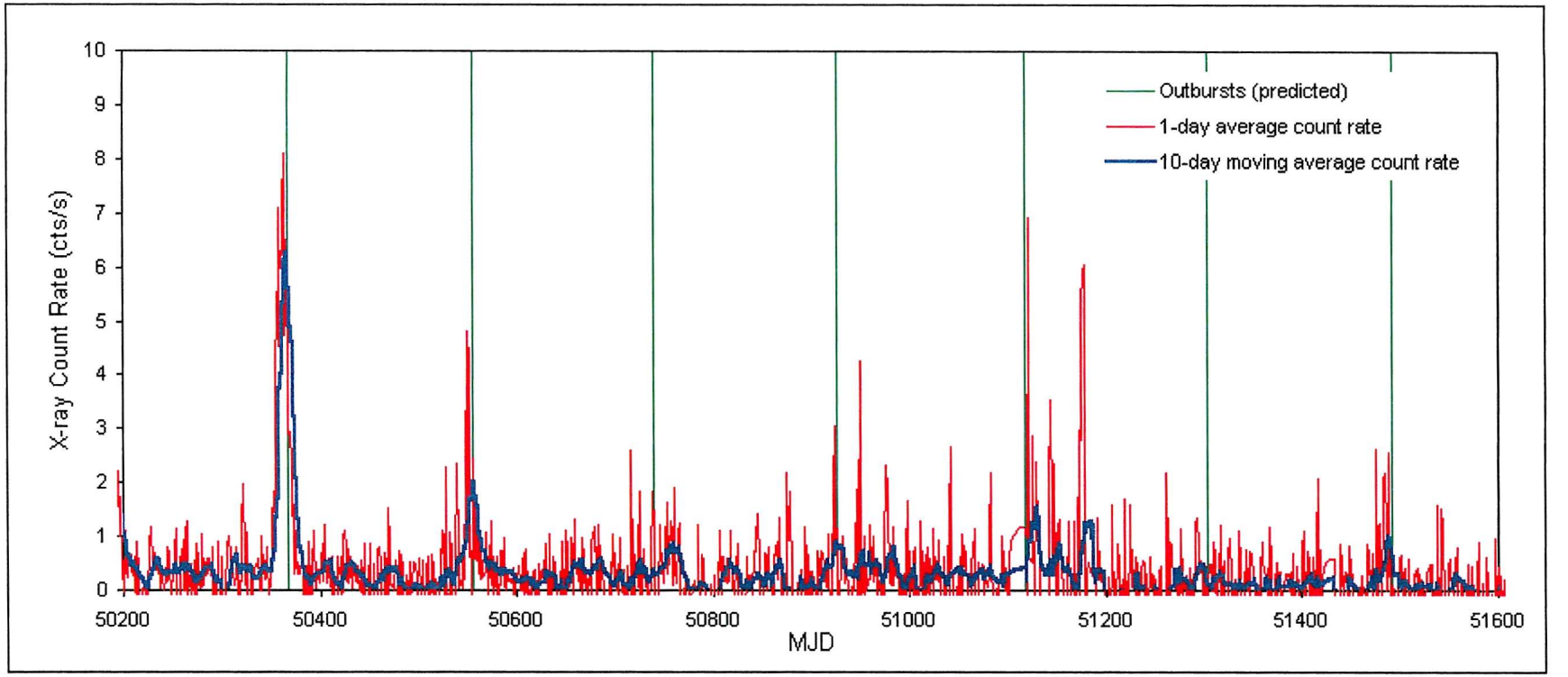


**Figure 2-13.** X-ray lightcurve for 4U1145–619, plotted using public data taken from the *RXTE* ASM. The predicted dates of X-ray outbursts are indicated with green lines.

## 2.7 Be/X-ray binary evolution

### 2.7.1 Origin of High Mass X-ray binaries

High mass X-ray binaries contain an accreting compact object orbiting a 'normal' star of early spectral type, where 'normal' is taken to mean a star which is still supported against gravity by the energy released in nuclear fusion reactions of some kind. The compact object (neutron star or black hole) in these systems must have formed when one star in the binary exploded in a supernova. The very existence of the HMXB systems is thus proof that if certain conditions are met, a binary system can survive a supernova explosion. Our theories for the evolution of HMXB suffer a number of uncertainties, both from uncertainties inherent in single star evolution, and the uncertainties introduced when attempting to extrapolate single star evolution to a binary system.

In trying to apply theories for single star evolution to stars in binary systems, we must take account of the effects of mass transfer between the two stars at various evolutionary stages, the possibility for mass to be lost from the system completely (see for instance Section 2.2.2), and uncertainties in the evolution of a star that has gained or lost a significant mass relative to a non-binary counterpart. Despite these uncertainties, a framework for the origin of HMXB as an expected phase of evolution for certain massive binary systems was developed soon after the discovery of the systems (eg. van den Heuvel & Heise 1972).

#### 2.7.1.1 Surviving a supernova explosion

One obvious problem in explaining the existence of a binary system in which a compact object orbits a non-degenerate star is how the system survived the supernova in which the compact object was born. Single stars evolve on timescales inversely related to their mass, so that in a binary system, the more massive component evolves fastest, and so explodes in a supernova before its less massive companion. The mass lost in the explosion causes a change in the orbit; a simplistic es-

timate for the eccentricity of the new orbit is calculated by assuming that the only change to the system parameters is the mass of the supernova progenitor, so that:

$$e = \frac{\Delta M}{M_1 + M_2 - \Delta M} \equiv \frac{M_{ejected}}{M_{remaining}} \tag{2-10}$$

Where $M_{ejected}$ is the mass lost from the system in the supernova, and $M_{remaining}$ is the mass left in the system after the explosion. This simplistic treatment indicates that a binary system can survive a supernova ($e < 1$) if less than half of the binary mass is lost.

It is the mass transfer between the two stars which leads to a situation in which at the time of the supernova, more than half of the binary mass is held in the less evolved star, and the system can survive. Theories for the formation of HMXB thus rely upon the transfer of mass from the more massive to the less massive star.

#### 2.7.1.2 Mass transfer in massive binaries

Mass transfer sets in when one star in the binary fills its Roche lobe. This may happen while the mass donor is still on the main sequence, if the system is a close binary. Otherwise, mass transfer may occur during the first or second ascent of the giant branch. Verbunt & van den Heuvel (1995) calculate that for a binary with stars of mass $9M_O$ and $5M_O$, mass transfer sets in on the main sequence for $P_{orbital} <$ 3 days, on the first ascent of the giant branch for 3 days $< P_{orbital} <$ 900 days, and on the second ascent of the giant branch for 900 days $< P_{orb} <$ 2000 days (cases A, B, and C mass transfer respectively).

### 2.7.2 Neutron star kick velocities from supernova explosions

Be/X-ray binaries have highly eccentric orbits that can be explained via the imparting of kick velocities on neutron stars at the time of their birth in a supernova explosion. While the eccentricities could be explained by significant mass loss from the system during the supernova, observations suggest that the supernova progenitors are helium-burning stars with $M_{helium} < 4\ M_{\odot}$, requiring kick velocities of ~

50 km $s^{-1}$ to be imparted on the neutron star at birth to reproduce the observed eccentricities.

### 2.7.3 Do Be/X-ray binaries die in Gamma Ray Bursts?

On their discovery, Gamma Ray Bursts (GRBs) were a complete mystery – their short duration and random occurrence prevented detailed study, and it was not possible to ascertain whether the GRBs were Galactic or extra-Galactic in origin. However, the very short observed minimum timescale for variability ($t_{var}$ ~ 1-ms – Barat *et al.* 1984) indicated a source with dimensions similar to those of a neutron star, and a number of GRB models involving neutron stars have therefore been proposed.

Melia, Rappaport & Joss (1986) suggested that GRBs originate near the surface of Galactic neutron stars surrounded by cold degenerate disks. Melia (1988) proposed that such objects might form from Be/X-ray binaries that evolve through a common envelope phase to produce a short period Neutron star/White dwarf binary that decays through gravitational radiation, leading in certain conditions to the disruption of the white dwarf to form the disk.

However, recent efforts (see for instance Kulkarni et al. 1998 and Kulkarni et al. 1999) have provided compelling evidence for a cosmological distance to GRBs (red shifts of $z = 3.42$ and $z \sim 1.6$ reported by Kulkarni et al.), implying enormous releases of energy of the order of $10^{53}$ – $10^{54}$ ergs, which cannot be produced by the Neutron star/cold degenerate disk model.

Currently the most favoured models for GRBs are the merger of two compact objects (Neutron Star – Neutron Star, or Neutron Star – Black Hole) in a binary system, or the accretion induced collapse of a Neutron Star to form a Black Hole. A third model first proposed by Alcock et al. (1986) is the transition of a Neutron Star into a Strange Star (a star made up of degenerate u, d and s quarks). Bombaci & Datta (2000) recently showed that the energy released by such a transition would be in the range $1 - 4 \times 10^{53}$ ergs.

The models that involve the transition of a Neutron Star to either a Black Hole or a Strange Star are worthy of interest in studies of High Mass X-ray binaries, as each could be a final stage of evolution for such a system. In the NS–BH case, the accretion of material from the massive donor causes the Neutron Star mass to rise above some threshold such that collapse into a Black Hole is inevitable. In the NS–SS case, the accretion of material from the massive donor leads to the central density of the Neutron Star core rising above a threshold for the transition of Neutron Star Matter to Strange Quark Matter (SQM). According to Bombaci & Datta (2000) this 'seed' of SQM absorbs neutrons, protons and hyperons, liberating the constituent quarks – the whole of the star's matter is converted in a very short 'detonation time' in the range 1ms – 1s.

It is possible therefore that the final death throes of Be/X-ray binaries are behind one of the most energetic phenomena in the Universe.

## 2.8 Isolated and X-ray binary Be star populations

If studies of Be/X-ray binaries are to be used to infer details about Be stars in general, it is crucial that the X-ray binary Be star population be compared to the general Be star population, and that any differences are understood and taken into account in all studies.

### 2.8.1 Spectral types

As discussed in 1.1.6, the Be star population peaks in occurrence by spectral type at around B2, but Be stars are still found with later spectral types; the population extends into early A type stars.

In the case of Be stars in X-ray binaries, no systems have been found containing Be stars with spectral types later than B2. Negueruela (2000) made a statistical comparison of the two populations, finding a significant probability that the two populations are distinct – i.e. that the difference in spectral type distributions is not down to chance.

The reason for the different spectral type distributions is unclear. One possibility is that the B2 limit for Be/X-ray binaries is a result of the condition that more than half of the pre-supernova mass of the system remains, if the system is to survive the supernova which formed the neutron star. It may be that for this condition to be met for systems with Be stars later than B2, the companion star would not be massive enough to form a neutron star, but would form a Be star-white dwarf binary. Another possibility is that systems containing a neutron star and a Be star later than B2 do form, but have insufficient circumstellar material to overcome the centrifugal barriers to accretion.

### 2.8.2 Interaction between neutron star and circumstellar disc

It is by no means yet certain whether or not the observed behaviour of a Be star in an X-ray binary would be the same if the star were an isolated object. A number of observations have indicated that some degree of perturbation takes place.

Apparao & Tarafdar (1986) attributed the V/R cycles seen in Be/X-ray binaries to the ionisation of regions of the circumstellar disc. In their model, a stronger *violet* peak is seen (V/R > 1) when the neutron star passes through the part of the disc which is moving toward the observer, as a blue shifted X-ray ionised region adds to the line emission. However, this model predicts V/R cycles with periods which are fixed, and always equal to the orbital period of the system. Currently to the author's knowledge, no Be/X-ray binary has been found to display a V/R cycle with a period matching the orbital period.

Reig et al. (1997) identified a correlation between the maximum EW(Hα) displayed by a particular Be/X-ray binary, and the orbital period. They also noted that the strength of Hα emission exhibited by Be stars in X-ray binaries was statistically lower than that exhibited by the general Be star population. They propose two reasons for the correlation.

1) X-rays are only produced if the circumstellar disc extends to the orbit of the neutron star. Hence, wider orbit systems only appear as Be/X-ray binary systems if the circumstellar disc is large enough.
2) The orbit of the neutron star acts to limit the size of the circumstellar disc.

Negueruela (1998) presents spectra of the Be/X-ray binary 4U0115+634 showing variability, and argues that this variability may have been caused by the neutron star. Figure 2-14 shows spectra of the Be star counterpart to the Be/X-ray binary 4U0115+634 taken from Negueruela *et al.* (1998). Both Hα and He I lines are seen to evolve over a period of ~ 1.5 years from a shell profile to single peak, and then to what may be the commencement of a V/R cycle. Negueruela links this behaviour to the occurrence of a large Type II outburst in December 1995 which was followed by a series of periodic (Type I) outbursts modulated on the system orbital period.

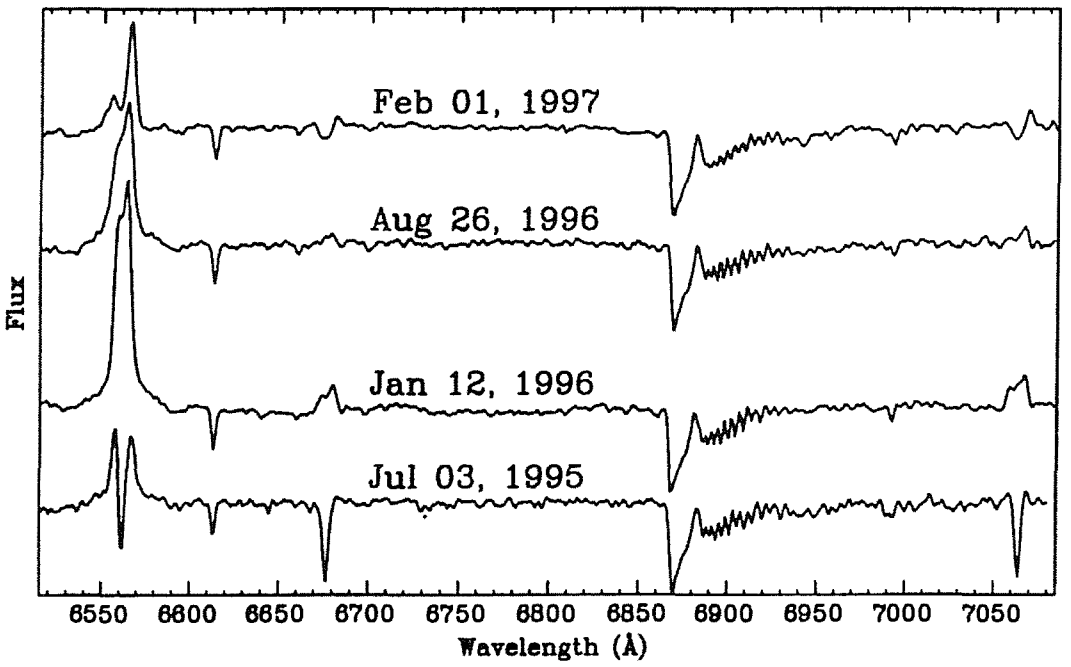


**Figure 2-14.** Spectra of the Be/X-ray binary 4U0115+634 showing the evolution of the Hα and He I lines over ~1.5 years from shell profiles to V/R cycles. Taken from Negueruela et al. (1998).

In Section 4.5 I present a spectroscopic study of the Be/X-ray binary 4U1145–615 over a 5-day period coincident with a predicted X-ray outburst to search for evidence of perturbations in the circumstellar disc.

Recently Negueruela & Okazaki have proposed a model in which binary interaction between the neutron star and Be star acts to truncate the disc of the Be star. Such a scenario is not entirely original, but for the first time a physical model has been developed which describes the effect, and reproduces observations well.

Negueruela & Okazaki develop their model for a Viscous Decretion disc, but claim that the effect would take place in any disc with subsonic outflow. In such a disc, the neutron star applies a negative torque to the disc material, preventing the disc from reaching a steady state, instead the material forms a dense torus close to some radius determined by $n$:1 resonance radii. In such an unstable state, the disc is susceptible to major perturbations (leading to global one-armed oscillations). The $n$:1

radii are determined by the viscosity of the disc material, so that small changes in viscosity lead to alterations in the truncation radii. In this manner, Negueruela & Okazaki seek to explain the sudden transition between states of Be/X-ray binaries. In short period systems, the 'normal' state is one of quiescence, the disc is truncated at radii less than the inner Lagrangian point. Perturbations in the disc may reduce the efficiency of the truncating mechanism, and allow accretion through the inner Lagrangian point when the orbit is close at periastron. In longer period systems, depending on the viscosity, the truncation radius is either

- outside the inner Lagrangian point for the whole orbit, allowing constant accretion
- outside the inner Lagrangian point close to periastron, leading to transient, periodic accretion
- inside the inner Lagrangian point for the whole orbit, preventing accretion.

## 2.9 Neutron stars as probes of Be star discs

In Section 2.3 I described how X-ray binaries are fuelled by the accretion of material from the non-degenerate binary component onto a compact object. In this thesis I am concerned only with those systems in which the compact object is a neutron star. The rate of accretion is determined by the density of material encountered by the neutron star around its orbit, and by the velocity of this material relative to the neutron star.

We have already discussed how observations indicate a change in the structure of Be star discs at radii ~10 $R_*$. At larger radii, the disc should be detectable primarily at radio wavelengths, yet observation fail to detect the radio emission expected from a simple extrapolation of the optical/infrared spectral distribution.

The orbits of Be/X-ray binaries tend to be wide, with periods of 10's of days, implying separations of the order of 10's of stellar radii. The X-ray lightcurves then provide a method of testing models of circumstellar discs at such radii. In Chapter

4 I develop a model for Be/X-ray binary lightcurves and investigate the effects of various parameters on expected lightcurves. I apply the model to observations of the Be/X-ray binary EXO 2030+375, and discuss whether the use of neutron stars as probes of Be star discs might be invalidated by perturbation of the disc from its natural (non-binary) state by the presence of the neutron star.

# Chapter 3 – A long term study of the Be/X-ray binary 4U 1145-619

In this chapter I present a long-term multi-wavelength history of the Be/X-ray binary 4U1145-619. Our own optical spectroscopy and optical and infrared photometry is presented, and complimented by additional photometry and X-ray data collated from the available literature. I use a variety of methods to derive the physical parameters of the system, and dismiss claims that the source lies at a distance of only 500-pc, which would raise questions over the neutron star nature of the accreting compact object in this and other Be/X-ray binary systems.

The optical and X-ray data are examined for correlation between the activity of the Be star and the X-ray luminosity of the accreting neutron star. Our observations show that the circumstellar disc of the Be star V801 Cen was in decline during the period of the observations, and reveal a possible correlation in X-ray behaviour.

Line profile analysis has been performed on the Hα spectra obtained in order to study V/R variations and to put constraints on the dimensions of emitting regions within the Be star's disc.

Analysis of spectra obtained during an X-ray outburst show evidence for binary interaction, supporting recent claims that the circumstellar discs of Be stars in X-ray binaries might be truncated by the presence of the accreting neutron star. Most of the work described in this chapter was presented in Stevens et al. (1997) and Stevens et al. (2000, *in preparation*).

## 3.1 Source History

The Be/X-ray binary 4U1145-619 is a highly variable X-ray source, discovered in observations with the *Uhuru* satellite, and initially catalogued as 4U1145-61. The source has been optically identified with the 9th magnitude B1ve star V801Cen (Bradt et al. 1977; Dower et al. 1978).

In *Ariel 5* observations White et al. (1978) found two X-ray pulsation periods of 292s and 297s from the field of the *Uhuru* source. The large field of view of the instrument and lack of imaging capability prevented them from being able to confirm whether both periods originated in the one source, or whether there were in fact two X-ray pulsars within the field.

The apparent ambiguity was resolved when observations with the imaging proportional counter on the *Einstein Observatory* (Lamb et al. 1980; White et al. 1980) revealed the presence of two pulsars separated by only 15'. The source identified with V801Cen (now designated 4U1145-619) was found to pulsate with the 292s period. The longer 297s period was found to originate in a previously unknown source, designated IE 1145.1-6141, which was later found to be a member of the class of HMXB's with supergiant mass-donor companions (Hutchings, Crampton & Cowley, 1981).

Analysis of the long-term X-ray behaviour of 4U1145-619 revealed recurrent outbursts, with a period of 186.5 days. The observed outbursts are typically of 10 days duration with X-ray flux levels increasing by a factor of ~5 (Watson et al. 1981; Priedhosky & Terrell 1983; Warwick, Watson & Willingdale 1985). During the majority of these observed X-ray outbursts, the pulsed fraction of the total flux is relatively low. This and the low luminosity of the source led White et al. (1983) to list 4U1145-619 as one of the best approximations to a spherically accreting binary system.

The accepted model for this system is that of a long period eccentric binary – the 186.5 day period in X-ray behaviour is then the consequence of phase dependence in the accretion rate from the Be star's circumstellar disc onto the orbiting neutron star.

## 3.2 Observations

### 3.2.1 UBV Photometry

UBV photometry of 4U1145–619 was obtained on 1997 November 11 using the SAAO 1.0-m telescope with the Tek8 CCD detector. The pixel scale was 0.35'' per pixel, and the seeing – as measured from stellar images on the CCD frames – was 2.0''. Synthetic aperture photometry was performed on the CCD images using the PHOT routine in IRAF/DAOPHOT. The measured instrumental magnitudes were subsequently transformed onto the standard UBV system using calibrations derived from observations of a number of E region standards (Menzies et al. 1989) conducted on the same night. The resulting indices are shown in Table 3-1.

**Table 3-1.** Photometry of V801 Cen, the Be star component of the X-ray binary 4U1145-619, obtained from the SAAO on 11$^{th}$ November 1997. The indices are plotted on a *col-our-colour* diagram, along with reddening vector in Figure 3-4.

| V | U-B | B-V |
|---|---|---|
| 9.32 ± 0.03 | -0.81 ± 0.05 | 0.08 ± 0.05 |

### 3.2.2 Infrared Photometry

Infrared photometric observations of V801 Cen were made on thirteen separate occasions between 1993 March and 1998 February, using the MkIII IR photometer on the 1.9-m Cassegrain Telescope at the SAAO. The chopping secondary mirror on the IR photometer defines two effective apertures: on-source (star) and off-source (background). The source was placed alternately in each of the two apertures for a number of cycles until a sufficiently high *signal-noise* ratio was reached, using circular apertures of 9 or 12 arc-seconds, depending on the seeing conditions. All observations were made in the SAAO *JHKL* system (1.25, 1.65, 2.2 and 3.5 $\mu$; Carter 1990). A log of these observations, the measured indices, and corresponding uncertainties is presented in Table 3-2. Corresponding lightcurves are plotted in Figure 3-1. The results show a clear decrease in luminosity in all wavebands, with *J* increasing by ~0.4-mag, and *L* increasing by ~1.3-mag. In the same period of time, the *J-K* index has fallen by ~0.5.

**Table 3-2.** Infrared photometry of V801 Cen, obtained from the SAAO, 1993 to 1998.

| Date | MJD | J | H | K | L | J-K |
|---|---|---|---|---|---|---|
| 1993 Mar 5 | 49052 | 8.24 ± 0.03 | 7.93 ± 0.03 | 7.53 ± 0.02 | 6.98 ± 0.05 | 0.71 ± 0.04 |
| 1993 Mar 8 | 49055 | 8.25 ± 0.02 | 7.95 ± 0.02 | 7.54 ± 0.02 | 6.95 ± 0.03 | 0.71 ± 0.03 |
| 1993 Jun 26 | 49165 | 8.42 ± 0.02 | 8.10 ± 0.02 | 7.67 ± 0.02 | 7.07 ± 0.05 | 0.75 ± 0.03 |
| 1994 Mar 5 | 49417 | 8.66 ± 0.02 | 8.43 ± 0.02 | 8.05 ± 0.03 | — | 0.61 ± 0.04 |
| 1994 Jun 30 | 49534 | 8.48 ± 0.01 | 8.27 ± 0.01 | 7.96 ± 0.01 | 7.46 ± 0.02 | 0.53 ± 0.02 |
| 1995 Feb 21 | 49770 | 8.66 ± 0.01 | 8.44 ± 0.02 | 8.19 ± 0.02 | — | 0.47 ± 0.02 |
| 1995 Feb 23 | 49772 | 8.67 ± 0.01 | 8.45 ± 0.01 | 8.19 ± 0.01 | 7.70 ± 0.06 | 0.48 ± 0.01 |
| 1995 Aug 17 | 49947 | 8.95 ± 0.01 | 8.81 ± 0.01 | 8.63 ± 0.01 | — | 0.32 ± 0.01 |
| 1996 Apr 6 | 50180 | 8.68 ± 0.03 | 8.56 ± 0.01 | 8.40 ± 0.01 | 8.28 ± 0.06 | 0.29 ± 0.03 |
| 1997 Jun 18 | 50618 | 8.98 ± 0.01 | 8.84 ± 0.01 | 8.67 ± 0.01 | 8.40 ± 0.05 | 0.31 ± 0.02 |
| 1997 Jun 19 | 50619 | 9.01 ± 0.01 | 8.87 ± 0.01 | 8.71 ± 0.01 | 8.38 ± 0.06 | 0.30 ± 0.02 |
| 1998 Feb 6 | 50851 | 8.81 ± 0.01 | 8.64 ± 0.01 | 8.45 ± 0.01 | 8.16 ± 0.07 | 0.36 ± 0.02 |
| 1998 Feb 7 | 50852 | 8.83 ± 0.01 | 8.66 ± 0.01 | 8.47 ± 0.02 | 8.40 ± 0.09 | 0.36 ± 0.03 |

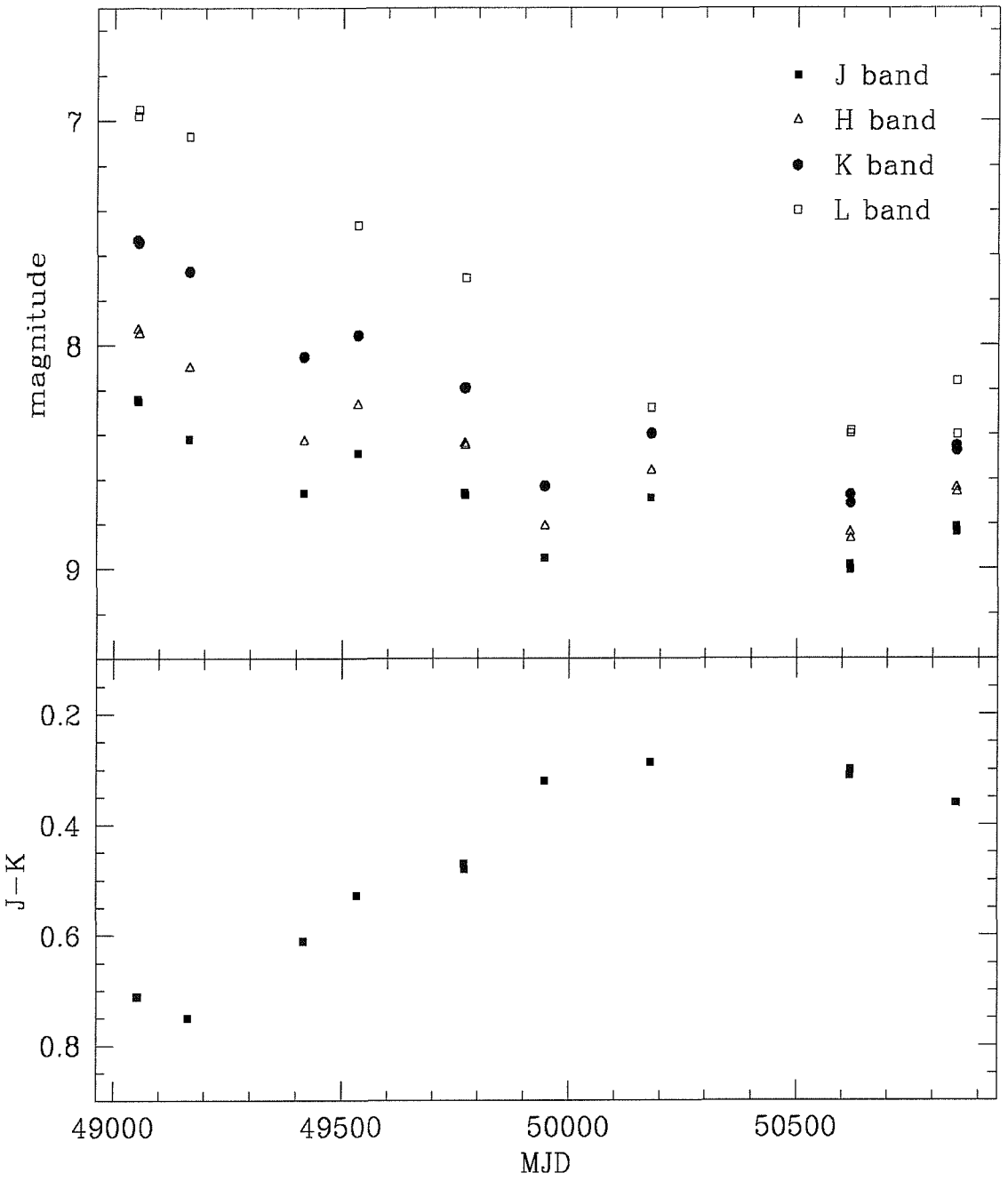


**Figure 3-1. Top:** Infrared *J, H, K* and *L* lightcurves for V801 Cen, the Be star component of the X-ray binary 4U1145-619, obtained from the SAAO between 1993 and 1998. **Bottom:** J – K index for the same period. Refer to Table 3-2 for a complete log of observations and results.

## 3.2.3 Optical Spectroscopy

### 3.2.3.1 Hα and Hβ Spectroscopy

We observed V801 Cen on thirteen occasions with the 1.9-m telescope at the SAAO between 1993 March and 1998 February. On ten of these occasions, spectra were centred on Hα, the remaining three were taken at the blue end of the spectrum, to include Hβ. We also obtained Hα spectra from the AAT on the nights of 1996 March 2 and 1997 March 18.

The SAAO spectra obtained up to and including April 1996 were all taken with the ITS spectrograph and RPCS (Reticon) detector, with grating no.5, giving spectra covering the region $\lambda = 6000 - 6800$ Å and $\lambda = 4400 - 5100$ Å at a dispersion of 0.5 Å/pixel. Data were acquired in two channels (star and sky) simultaneously. SAAO data obtained after this date were taken with the same spectrograph with SITe2 CCD detector.

The AAT spectra were taken with the 82cm RGO camera and TEK 1K CCD, with the 1200R grating, giving a coverage of approximately $\lambda = 6400 - 6600$ Å at a dispersion of 0.234 Å/pixel. AAT and SAAO Reticon data were reduced using the Starlink supported FIGARO package (Shortridge 1991). The SAAO SITe2 data were reduced using IRAF techniques (Massey 1992).

Table 3-3 shows a log of the observations and measured equivalent widths. Nine of the spectra (centred on the Hα line) are shown in Figure 3-2. The Hα profile is generally asymmetric, and in some observations shows a clear double peak. There is a significant variation in the equivalent width of the Hα line: throughout the period of observations, EW(Hα) has decreased by ~ 70 per cent, compared to a typical uncertainty in a single EW(Hα) measurement of ~ 10 per cent. A decrease in the EW(Hβ) is also clear.

**Table 3-3.** Log of spectroscopic observations of V801 Cen between 1993 and 1998. The uncertainty in equivalent width measurements is typically of the order of 10%, and originates primarily from uncertainties in the determination of the local continuum level.

| Date | Site | EW (Å) | |
|---|---|---|---|
| | | Hα | Hβ |
| 1993 March 2nd | SAAO | -38 | — |
| 1993 Mar 4 | SAAO | — | -4.5 |
| 1994 Mar 7 | SAAO | -45 | — |
| 1994 Jul 2 | SAAO | -25 | — |
| 1994 Jul 3 | SAAO | -24 | — |
| 1994 Jul 4 | SAAO | — | -2.5 |
| 1995 Aug 24 | SAAO | -27 | — |
| 1996 Mar 2 | AAT | -16 | — |
| 1996 Apr 3 | SAAO | -13 | — |
| 1996 Apr 4 | SAAO | -14 | — |
| 1996 Apr 5 | SAAO | — | -1.5 |
| 1997 March 18 | AAT | -8 | — |
| 1997 April 11-17 | SAAO | -7 | — |
| 1997 June 20 | SAAO | -9 | — |
| 1998 Feb 3 | SAAO | -8 | — |

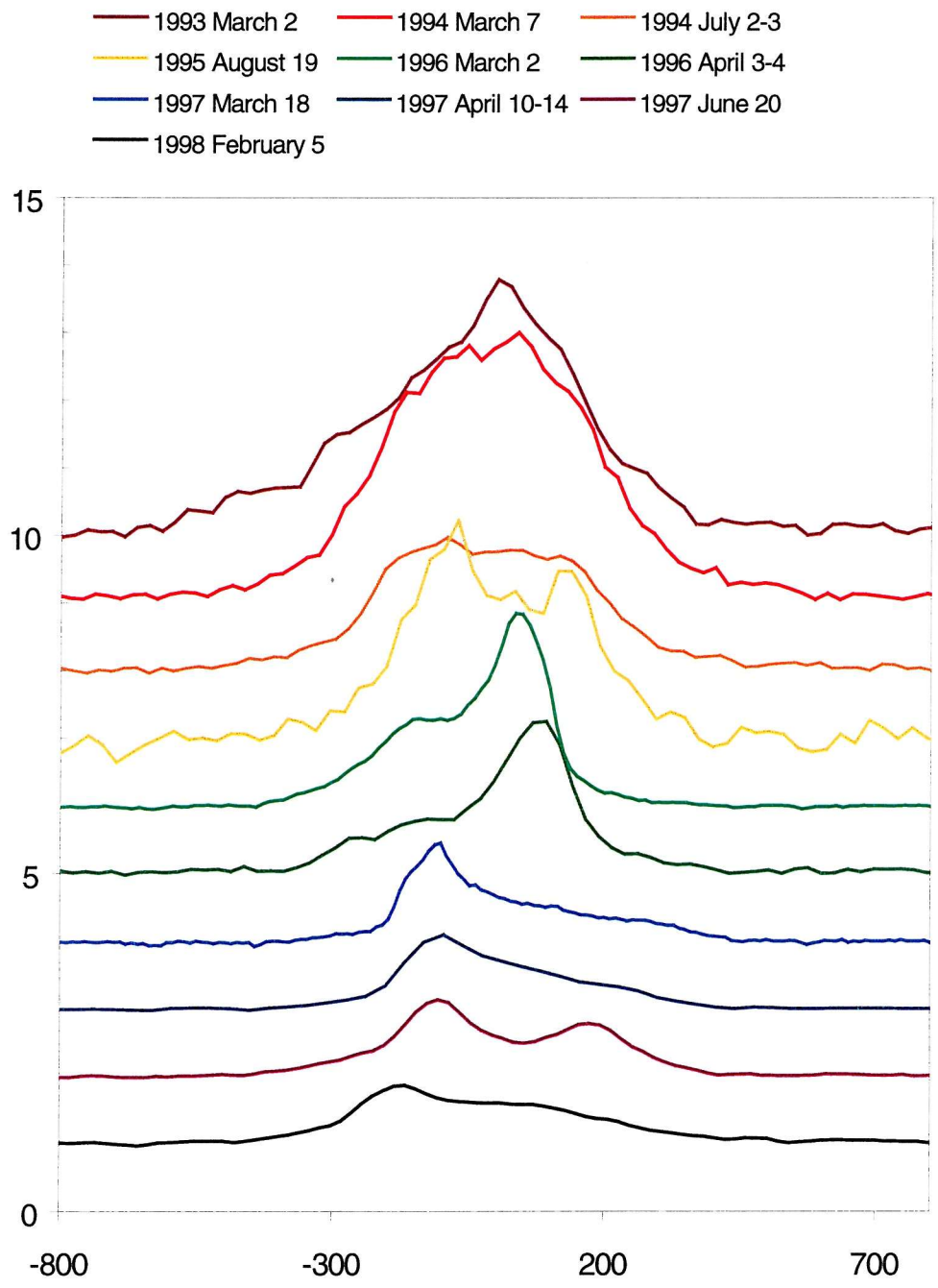


**Figure 3-2.** Hα line profiles of V801 Cen between 1993 and 1998. Spectra were obtained from the SAAO and the AAT. All spectra were normalised to a spline fit to the local continuum, and offset to one another in increments of 1 flux units.

#### 3.2.3.2 Classification Region Spectroscopy

On each night of 1997 June 21 and 23 we obtained a medium resolution, classification region spectrum of V801 Cen. Each spectrum covered the wavelength range ($3600 < \lambda < 4845$)Å at a dispersion of 0.45 Å /pixel. Observations were made on the 1.9-m telescope at the SAAO, with the Cassegrain spectrograph and SITe 2 CCD detector. Data reduction, including flat corrections, extraction of spectra, and wavelength calibration was carried out using the STARLINK supported FIGARO package.

Figure 3-3 shows the weighted mean of the two obtained spectra. A spline function was fit to the continuum and the mean spectrum was normalised to this spline fit. The Hγ line clearly has an emission core, but no emission is apparent in the Hδ line.

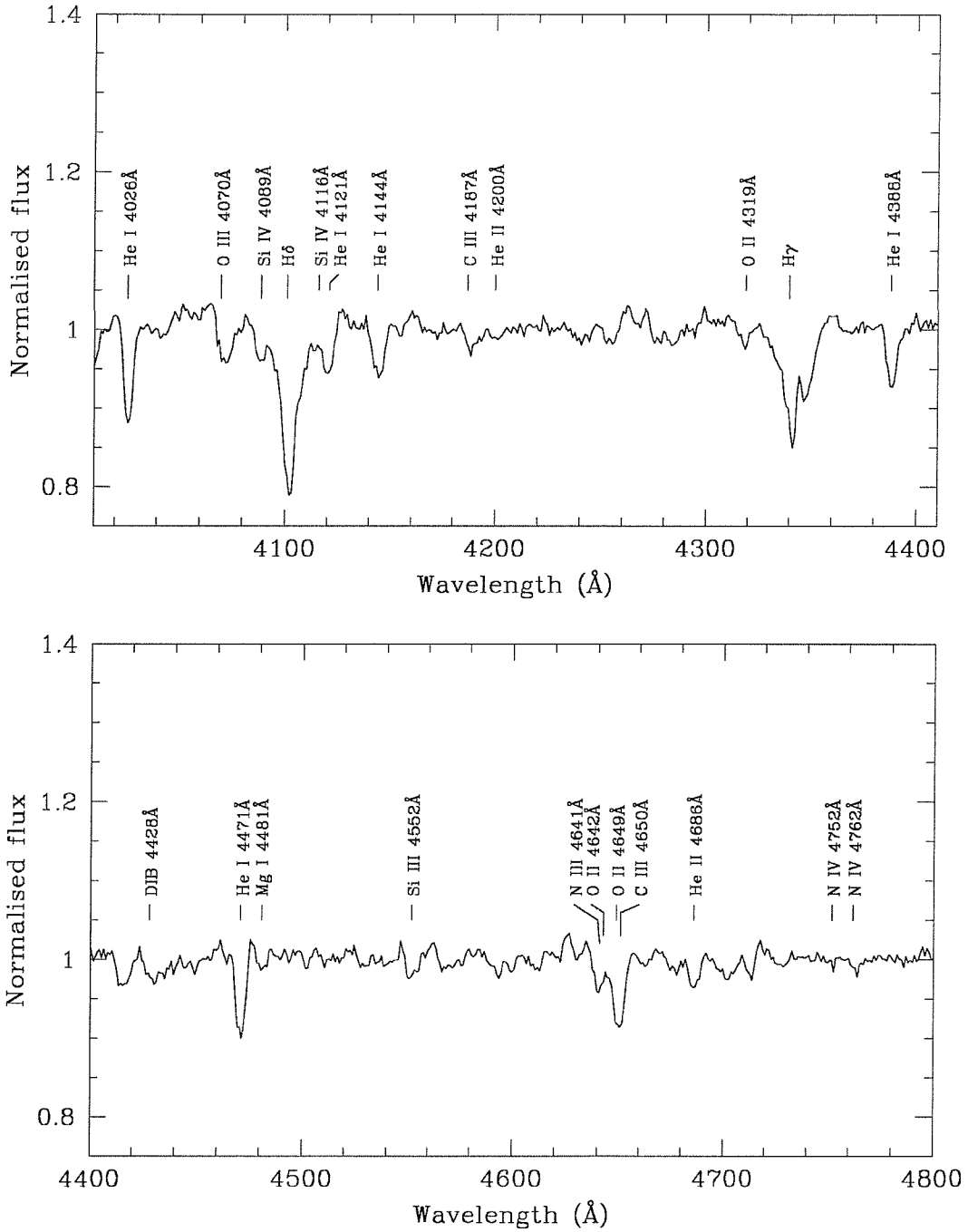


**Figure 3-3.** Classification region spectrum of V801 Cen, the Be star component of the X-ray binary 4U1145–619. The displayed spectrum is a composite of two observations made on 21st and 23rd June 1997.

## 3.3 Astrophysical Parameters

Our long term monitoring of 4U1145-619 at optical and infrared wavelengths is intended to allow a study of the variations in the characteristics of the circumstellar envelope which gives rise to the Be star properties, and to search for correlation between this activity and the X-ray emission from the neutron star which accretes from the circumstellar material. If we are to successfully model the behaviour of the system, it is necessary to first determine the physical parameters of the two binary components and their orbit for input into the developed models.

We have applied a number of techniques to derive the astrophysical parameters of the system:

- UBV photometry
- Strömgren photometry
- Spectral line analysis

The individual techniques and results yielded are described in the following sections.

### 3.3.1 UBV Photometry

The photometric indices shown in Table 3-1 are plotted in the *colour – colour* diagram in Figure 3-4. The reddening vector is plotted, with data labels at intervals of 0.05 in E(B-V). A reddening of E(B-V) = 0.35 is required to bring the observed indices onto the main sequence, leading to de-reddened values of $(B–V)$ = -0.31 and $(U-B)$ = -1.062. This compares with colours for a B0V star of $(B-V)$ = -0.32 and $(U-B)$ = -1.08. Alternatively, adopted reddening values of E(B-V) = 0.3, 0.25 and 0.2 allow spectral types of B0.5II, B1Ib and B2Ia respectively. Allowing an additional uncertainty due to circumstellar reddening, I assume the interstellar reddening, as measured from the UBV photometry to be E(B-V) = 0.35 ± 0.10.

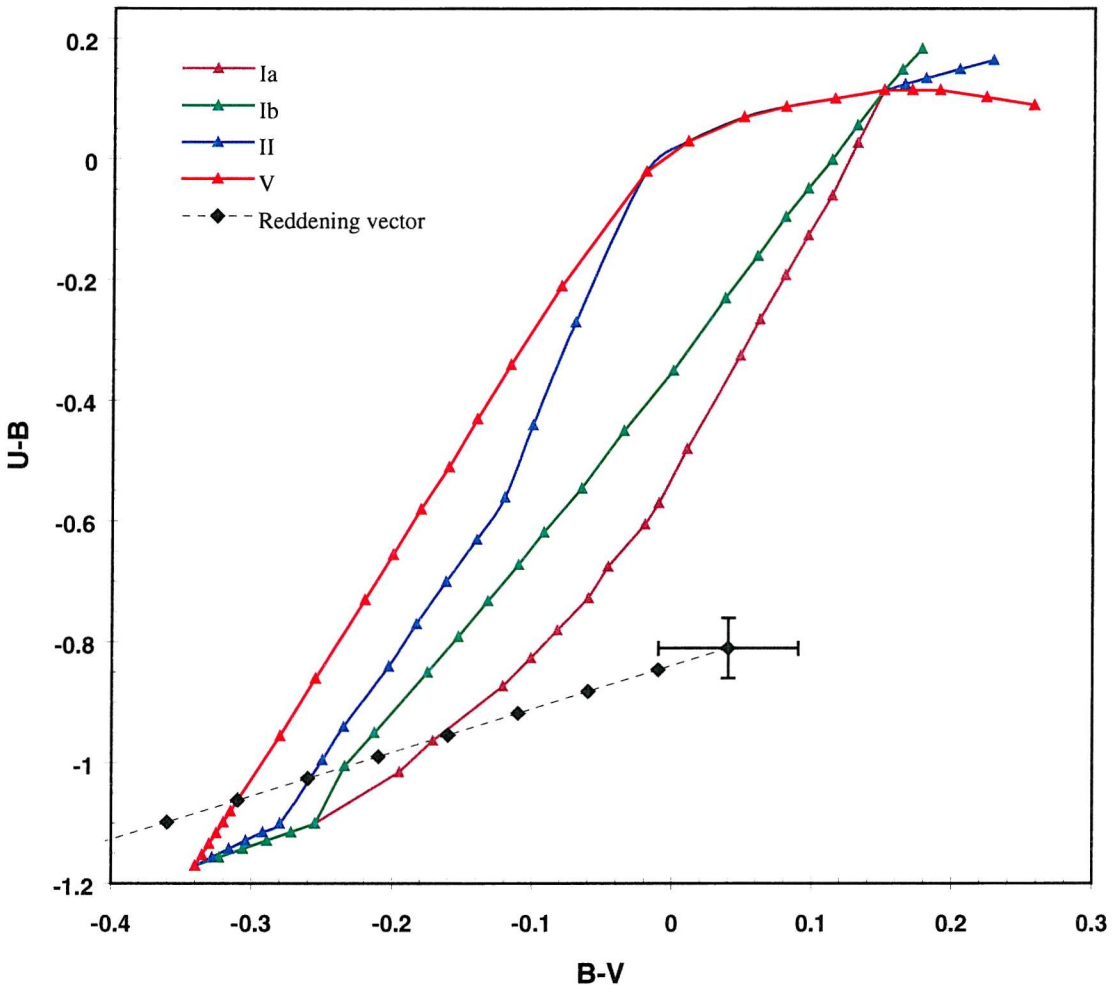


**Figure 3-4.** Location of V801 Cen in Colour-Colour diagram. The actual photometric indices are shown in Table 3-1. Also plotted is the reddening vector, with data points plotted at increments of 0.05 in *E(B-V)*.

### 3.3.2 Strömgren Photometry

By design, the *uvbyβ* photometric system is most suitable for determining the stellar parameters in early-type stars. Unfortunately, the Be star case is somewhat complicated by the presence of emission from the circumstellar disc, so that the observed indices become functions of both the stellar parameters and of the disc parameters.

Fabregat & Reglero (1990) determined transforms for the *uvbyβ* indices to correct for circumstellar effects. The transforms are based upon the *EW*(Hα) parameter, which has been shown to correlate closely with circumstellar continuum and Balmer discontinuity emission (Dachs et al. 1986, 1988; Kaiser 1989).

The major disadvantage with this technique was the necessity for simultaneous photometric and spectroscopic observations; because of the highly variable nature of these stars, any results based on non-concurrent data were subject to unknown systematic error. In a further paper, Fabregat & Torrejon (1998) derived transforms based purely on *uvbyβ* photometry, in this case the *β* index serves as a measure of the Balmer line emission strengths, thus removing the necessity for simultaneous spectroscopic observations.

In Stevens et al. (1997) we presented physical parameters derived using the first method, with Stromgren data taken from the first catalogue of the Long Term Photometry of Variables (LTPV) project at ESO (Manfroid et al. 1991) and *EW*(Hα) data from Cook & Warwick (1987b). The values we presented had first appeared in Reig (1995).

In this work we derive the physical parameters using the second method. Strömgren *uvbyβ* photometric data were taken from Hammerschlag-Hensberge et al. (1980). The observed magnitudes and indices are shown in Table 3-4.

**Table 3-4.** Strömgren photometric data used in the determination of the astrophysical parameters of V801 Cen, taken from Hammerschlag-Hensberge et al. (1980).

| V | b-y | $m_1$ | $c_1$ | *β* |
|---|---|---|---|---|
| 8.950 ± 0.015 | 0.238 ± 0.008 | -0.064 ± 0.010 | -0.241 ± 0.010 | 2.424 ± 0.010 |

#### 3.3.2.1 Circumstellar and interstellar reddening and derived intrinsic photometric indices

The procedure which we have used for determining the circumstellar and interstellar reddening, and hence the intrinsic photometric indices can be summarised as follows, following Fabregat & Torrejon:

- We adopted an iterative technique, assuming initially an intrinsic (not contaminated by circumstellar emission) value $\beta_*$= 2.63, then calculated

$$\Delta\beta = \beta - \beta_* \tag{3-1}$$

We then calculated circumstellar reddening through the equations relating circumstellar effects on the Stromgren indices to the circumstellar effects on the $\beta$ index:

$$E^{CS}(b-y) = -0.339\Delta\beta \tag{3-2}$$

and

$$E^{CS}(c_1) = 0.661\Delta\beta \tag{3-3}$$

From these we calculated *(b-y)* and $c_1$ corrected for circumstellar excesses.

We then made use of the fact that the $c_1$ index is less affected by reddening than the *(b-y)* index. We interpolated the relationship found by Crawford (1978) between $(b-y)_0$ and $c_0$ (and adopting $c_0 \approx c_1$) to find the intrinsic $(b-y)_0$.

From this value of $(b-y)_0$, we calculated *E(b-y)* and then used the relationship

$$E(c_1) = -0.19E(b-y) \tag{3-4}$$

(Balona & Shobbrook 1984) and calculated:

$$c_0 = c_1 - E(c_1) \tag{3-5}$$

A new value for the intrinsic $\beta$ index was then found from the equation:

$$\beta_* = 2.62 - 0.2517c_0 - 0.14c_0^2 + 0.1704c_0^3 \tag{3-6}$$

and the above steps were repeated with the new value for $\beta_*$ in Equation (3-1).

The above steps were repeated until convergence. We found a circumstellar reddening of $E^{CS}(b\text{-}y) = 0.06$ and an interstellar reddening of $E^{IS}(b\text{-}y) = 0.30$.

### 3.3.2.2 Luminosity

The $\beta$ index is the main luminosity indicator for OB stars in the *uvbyβ* photometric system. In the case of Be stars, the index is contaminated by the effects of Balmer emission from the circumstellar envelope, and as we have used the $\beta$ index as a measure of the strength of these effects, we cannot use it to determine luminosity in any direct manner. Following the proposed methods of Fabregat & Torrejon (1998) again, we calculated the absolute magnitude by substituting our derived values of $\beta_*$ and $c_0$ into the equation of Balona & Shobbrook (1984):

$$M_V = 3.4994 + 7.2026\log(\beta_* - 2.515) - 2.3191[g] + 2.9375[g]^3 \tag{3-7}$$

where

$$[g] = \log(\beta_* - 2.515) - 1.6\log(c_0 + 0.322) \tag{3-8}$$

giving $M_V$ = -3.8.

### 3.3.2.3 Effective Temperature

Reig et al. (1996, 1997) calculated an empirical effective temperature calibration for the *uvbyβ* system, based on the $c_0$ index. We used their relationship

$$\log T_{eff} = 0.186c_0^2 - 0.58c_0 + 4.402 \tag{3-9}$$

to find $T_{eff}$ = 2.75 x $10^4$ K.

### 3.3.2.4 Radius

Reig et al. (1997) found a relationship between Bolometric Correction, effective temperature, and stellar radius. The bolometric correction (BC) was found by means of Balona's (1994) relationship:

$$BC = -5.5647 + 18.9446\theta - 19.8827\theta^2 + 6.1302\theta^3 \tag{3-10}$$

(where $\theta$ = 5040 $T_{eff}$) to be BC = -2.72, thus the absolute bolometric magnitude $M_b$ = -6.51. The radius was then found from Reig et al.'s (1997) relationship

$$M_{bol} = 42.36 - 5\log\left(\frac{R}{R_O}\right) - 10\log T_{eff} \tag{3-11}$$

to be $R$ = 6.7 $R_O$.

#### 3.3.2.5 Mass and Gravity

Balona (1994) interpolated the evolutionary calculations of Claret & Gimenez (1992) to find the following relationship:

$$\log M = 31.6409 + 2.6152 \log L - 17.3446 \log T_{eff} + 0.08195 (\log L)^2 - 0.6982 (\log L)(\log T_{eff}) + 2.3879 (\log T_{eff})^2 \quad (3\text{-}12)$$

which, using our values $T_{eff}$= 2.75 x $10^4$ K and $L$ = 3.34 x $10^4$ $L_O$ gives us a mass of $M$ = 15 $M_\odot$. The gravity then follows from

$$\log g = 4.44 + \log M - 2\log R \quad (3\text{-}13)$$

leading to a value of log $g$ = 4.0.

### 3.3.3 Optical Spectroscopy

#### 3.3.3.1 Spectral Classification

The most important features for spectral classification for early type B stars can be summarised from Walborn (1971) and Walborn & Fitzpatrick (1990):

- OIII and CIII blends at ~4070 and ~4650Å indicate a spectral type of B1.5 or earlier.
- As HeII (λ = 4686Å) is weaker than CIII (λ = 4650Å) the spectral type is later than B0.
- The presence of SiIV (λ = 4089Å) indicates a spectral type of B1 or earlier.
- The presence of HeII (λ = 4686Å) indicates a spectral type of B0.5 or earlier.
- The lack of HeII (λ = 4200,4541Å) indicates a spectral type later than B0.2.
- A spectral type of B0.5 is indicated as HeI (λ = 4121Å) ≈ HeI (λ = 4144Å).

The above criteria indicate a spectral type of B0.5Ve for V801 Cen.

### 3.3.3.2 Rotational Velocity

In order to measure the rotational velocity of the underlying B star, we have fitted Gaussian functions to a number of the HeI lines in the composite blue spectrum. HeI lines were chosen so that the measured Doppler broadening effects are dominated by the rotation of the star, as the lines originate in the stellar photosphere. The specific lines used to determine the rotation are listed Table 3-5 along with the best-fit parameters. Using the relationship of Buscombe (1969):

$$\frac{v \sin i}{c} = \frac{FWHM}{2\lambda\sqrt{\ln 2}} \tag{3-14}$$

we then calculated *v*sin*i* for each line we had fit. The mean of these measurements is 275 ± 16-km $s^{-1}$, consistent with the value of 290 km $s^{-1}$ measured by Balona (1973).

**Table 3-5.** Gaussian fits to HeI lines in the spectrum of V801 Cen.

| **Rest wavelength** (Å) | **Fit wavelength** (Å) | **Equivalent Width** (Å) | **FWHM** (Å) | ***v* sin *i*** (km $s^{-1}$) |
|---|---|---|---|---|
| 4026.189 | 4026.22 | 0.7156 | 5.98 | 267.5 |
| 4120.860 | 4120.24 | 0.3174 | 6.31 | 275.7 |
| 4143.759 | 4144.44 | 0.3950 | 6.97 | 303.1 |
| 4387.928 | 4388.26 | 0.4586 | 6.42 | 263.6 |
| 4471.681 | 4471.04 | 0.7160 | 6.61 | 266.3 |

### 3.3.3.3 Diffuse Interstellar Bands

Thirty medium resolution, red spectra of V801 Cen were obtained on 12th April 1997. The observations and subsequent data reduction were described in Section 3.2.3. All spectra were centred on the Hα line and so include the λ = 6613Å Diffuse Interstellar Band (DIB).

Herbig (1975) examined correlations between the equivalent widths of a sample of interstellar lines and *E(B-V)* colour excesses. In the case of the λ6613 Å line, data from 58 stars were used in the initial analysis, but data from stars in Cygnus and Sco-Oph regions were later rejected as it was apparent that the interstellar lines in these regions were systematically weaker for a given value *of E(B-V)*. Herbig derived best-fit linear relationships for the remaining stars, firstly for the case where the zero point is allowed to vary, and secondly for the more realistic case where the zero point is fixed at *EW*(λ6613 Å) = 0 when *E(B-V)* = 0. We will use Herbig's relationship derived after the Cygnus and Sco-Oph data were rejected and for the fixed zero point case:

$$EW(\lambda = 6613) = 318E(B-V)\ \text{Å} \tag{3-15}$$

We measured the equivalent width of the λ=6613 Å interstellar line in each of the 30 spectra. The mean value, weighted according to the *signal/noise* ratio of each individual spectrum, was found to be 80.0 ± 8.0-mÅ, corresponding to *E(B-V)* = 0.25 ± 0.03.

### 3.3.4 4U 1145-619 – A model for the system

The presence of the HeII (λ = 4686-Å) line but lack of the HeII (λ4200 Å) line – in any significant strength – leads us to suggest a spectral type of B0.5 for the star (see Section 3.3.3.1). This is consistent, within the uncertainties, with the parameters derived from Stromgren photometric data in 3.3.2.

We can derive the distance to V801Cen by calculating the distance modulus

$$M_V - V_0 = -5\log d + 5 \tag{3-16}$$

where $M_v$ is the absolute magnitude and $V_0$ is the de-reddened apparent magnitude.

For this calculation we need to determine the apparent *de-reddened V* magnitude from our measurements of interstellar reddening, and to assume a value for the absolute *V* magnitude. In calculating the de-reddened *V* magnitude, we should use data as least contaminated by disc emission as possible. The weighted mean of our interstellar reddening measurements is $E(B-V) = 0.27$, whilst the least luminous *V* magnitude (which we assume to represent the least contamination from disc emission) reported for the star is 9.4 (see Figure 3-7). Using

$$A_V = 3.1E(B-V) \tag{3-17}$$

we find $A_V = 0.837$, hence the de-reddened magnitude $V_0 \approx 8.6$. Using our derived absolute magnitude of $M_V = -3.8$, the distance modulus to the source is $12^m.6$, corresponding to a distance of 3.0-kpc. This compares favourably with the distance of 3.1-kpc derived from Stromgren photometry, and with Tovmassin et al. who place V801 Cen in an OB association at a distance of ~ 2.7-kpc.

**Table 3-6** Derived astrophysical parameters of V801 Cen, the optical counterpart to the Be/X-ray binary 4U 1145-619. Column 2 lists the parameters derived in Stevens et al. (1997), column 3 lists the results of this work.

| | Stevens et al. (1997) | This work |
|---|---|---|
| Spectral Type | B1Ve | B0.5Ve |
| E(B-V) | 0.29 | 0.27 ± 0.03 |
| $T_{eff}$ | 2.55 ($10^4$ K) | 2.75 ($10^4$ K) |
| Mass | 13 $M_O$ | 15 $M_\odot$ |
| Radius | 8 | 6.75 |
| $M_v$ | -3.1 | -3.8 |
| $M_{bol}$ | -5.6 | -6.5 |
| log g | 3.8 | 4.0 |
| Distance | 3.1 ± 0.5 kpc | 3.0 kpc |
| $v \sin i$ | – | 275 ± 16 km $s^{-1}$ |

### 3.3.5 The nature of Be/X-ray binary systems

If Chevalier & Ilovaisky's distance of 500pc were to be adopted, then the absolute visual magnitude of V801 Cen is -0.7, more consistent with a main sequence B6 star than a B1 star. The temperature of such a star would be ~14,000K. The luminosity of the X-ray source would be $\sim 10^{33}$, and the Hipparcos parallaxes transform into a tangential velocity of only 9.1 ± 3.8 km $s^{-1}$. This X-ray luminosity is low for an accreting neutron star, and the optical spectrum of V801 Cen (Figure 3-3) is certainly not consistent with a temperature of only 14,000K.

However, Chevalier & Ilovaisky fail to highlight the large uncertainties in the parallaxes measured for this source, and for the other Be/X-ray binaries in their study. The reciprocal relationship between parallax and distance thus leads to enormous uncertainties in the derived distances, but the authors do not discuss the highly dubious nature of conclusions drawn from such uncertain data. Steele et al. (1998) published a thorough criticism of their methods and conclusions. For the sake of this work, it is worth pointing out that a 2σ error in their data allows 4U1145-619 to lie within the Galaxy, and the 3σ errors place the source somewhere in the known universe!

If the Be/X-ray binary sources were, as Chevalier & Ilovaisky claim, within ~1-kpc of the sun, would the observed sky distributions of the sources be consistent? A rough estimate of the latitude range θ, of a population within a volume with scale height $z_0$ and a radius of $r$ can be found from:

$$\sin\theta = \frac{z_0}{r}. \qquad (3\text{-}18)$$

If the Be/X-ray binaries have a similar scale height ($z_0$ = 100-pc) to the general massive star population (Miller & Scalo 1979), then if they are all nearby ($r$ < 1-kpc), the observed latitude range ought to be ~± 6°. The observed latitude range is much less. Figure 3-5 shows the observed galactic latitude distribution for those objects listed in Table 1 of Bildsten et al. Also plotted are the $1z_0$ contours for a

distribution with scale height $z_0$ = 100-pc (the distribution of massive Population I stars), corrected for the sun's position 15-pc above the Galactic plane. The distribution of Be/X-ray binary sources appears to be completely consistent with the Population I stars; further, if the Be/X-ray binaries were all located much closer, as claimed by Chevalier & Ilovaisky, some explanation would be needed for their excessive concentration within low Galactic latitudes.

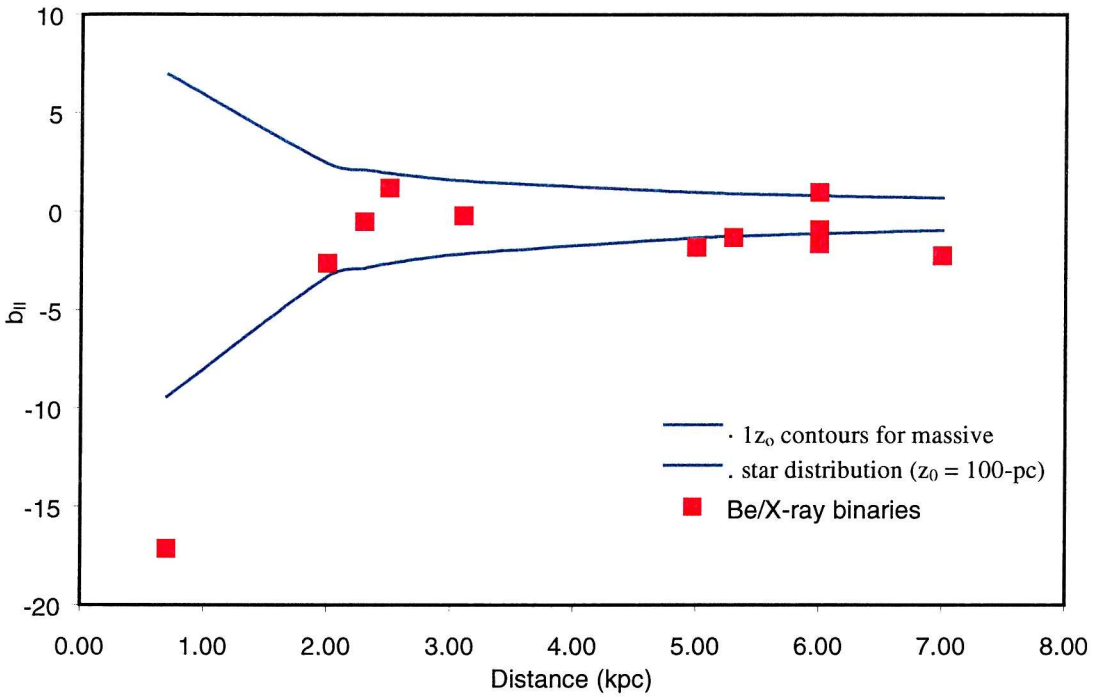


**Figure 3-5.** Observed latitude distribution of Be/X-ray binary systems in Galactic coordinates. Also plotted is the distribution of massive stars (+/- $1z_0$), corrected for the sun's distance above the Galactic plane.

While acknowledging the large uncertainties in the measured parallaxes, it is instructive to calculate the tangential velocity of the source from the Hipparcos data. Chevalier & Ilovaisky calculated tangential velocities for their sample of Be/X-ray binaries using their `Hipparcos' distances. As these `Hipparcos' distances were too small (Steele et al. 1998; this work) the derived tangential velocities will have been underestimated, leading to an artificial difference between the tangential velocities of Be/X-ray binary systems and Supergiant/X-ray binary systems. Chevalier & Ilovaisky did not detect significant parallaxes for the supergiant systems and so used

distances taken from the literature for these sources. Using the Hipparcos proper motions given in Table 3 of Chevalier & Ilovaisky, and an assumed distance of 3-kpc, we derive a tangential velocity of 55 ± 23 km $s^{-1}$. This velocity compares favourably with those found for the Supergiant systems, and supports the evolutionary scenario in which Be/X-ray binary systems form from a B-B binary which survives a supernova explosion in which one of the components explodes to leave a neutron star in a wide eccentric orbit. Chevalier & Ilovaisky's claim *'unambiguously that the Be/X-ray stars are "normal" low velocity stars of the solar neighbourhood'* appears to be based upon unreliable assumptions regarding the accuracy of data in the case of V801Cen, and we believe that the same would be found to be the case for the rest of the Be/X-ray binary population.

In summary, we conclude that 4U1145-619 is a Be star + Neutron star binary, the Be star having a spectral type of B0.5Ve. The system lies at a distance of ~3-kpc, and is probably related to an OB association found by Tovmassin et al. to lie at 2.7 kpc.

## 3.4 Discloss and related X-ray activity

### 3.4.1 Recent Be star activity

The infrared lightcurves in Figure 3-1 show the luminosity of the source to be decreasing in all bands throughout the period of the observations. Short term variations aside, the long-term trend is a decrease of ~1 magnitude. The change in magnitude increases with wavelength, with the change in *J, H, K* and *L* approximately 0.7, 0.9, 0.9 and 1.3 respectively. The Hα and Hβ emission has been in decay during the same period, the one data point in exception being that of 1994 March 7, which is just 10 days (0.05 phase) before the maximum of the large X-ray outburst detected by *BATSE*.

Observations have shown that the Balmer emission and the infrared excess characteristic of Be stars originate in the same circumstellar disc (Dachs and Wamsteker, 1982). Hence a decrease in disc size would result in the observed variations in the infrared magnitudes and the Hα and Hβ emission. Also, as the disc's continuum is cooler than that of the photosphere, it is at longer wavelengths that we expect to see the largest variation in magnitude, again in agreement with the data.

## 3.4.2 Collated source history

In this section I have collated previously published data from observations of 4U1145–619/V801Cen at Infrared, optical and X-ray wavelengths. My aim is to use these data to complement my own, and enable a search for correlated behaviour between the activity of the Be star (as evidenced through variations in optical Balmer emission lines and optical and infrared continuum) and the activity of the X-ray source.

Section 3.4.2.1 describes the historic activity of the Be star as derived both from my own observations, and from data taken from available literature. 3.4.2.2 describes the X-ray flux history of the source, collated from the available literature, and from public databases.

### 3.4.2.1 Be star activity from optical and infrared data

In order to investigate the implications of the optical and infrared data presented here in the context of the past behaviour of the star, data were taken from the catalogue of ESO's Long Term Photometry of Variables project (Sterken et al. 1995).

The data (Strömgren *uvby* photometry, covering the period 1982 to 1994) along with derived indices are shown in Figure 3-7. Of note is the scale of the long-term variability. The range of $V$ magnitude is $\Delta V \sim 0.6$, whilst $\Delta(b-y) \sim 0.2$. As $(b-y)$ increases with optical luminosity, again the data indicate that the variations are greater at longer wavelengths.

Figure 3-6 shows explicitly the relationship between luminosity and colour, represented by $V$ and $(b - y)$ respectively. In the high state, the $(b - y)$ index shows the star to be redder than in the low state. As with the infrared photometry then, the size of the variations and their dependence upon wavelength implies that they are the result of changes in the size of the circumstellar disc. With the new infrared and optical data we now have an indication of the way in which the disc has decayed, recovered and decayed again over 13 years from 1982 December to 1996 April.

The complete data set shows three disc loss episodes (refer to Figure 3-7), corresponding to the two previously observed optical minima, and the current optical decay. Although the infrared and spectroscopic data in the period before our own observations is sparse, they are consistent with the timescale of disc loss and recovery suggested by the optical lightcurve. Similar episodes of disc loss have been observed in other Be/X-ray binary systems. Most notably, X Persei has shown Hα changing from emission to absorption over a period of months (Norton et al. 1991). In the case of 4U1145-619, complete disc loss is clearly not the case at present, despite the decay in strength, as both the Hα and Hβ lines remain in emission.

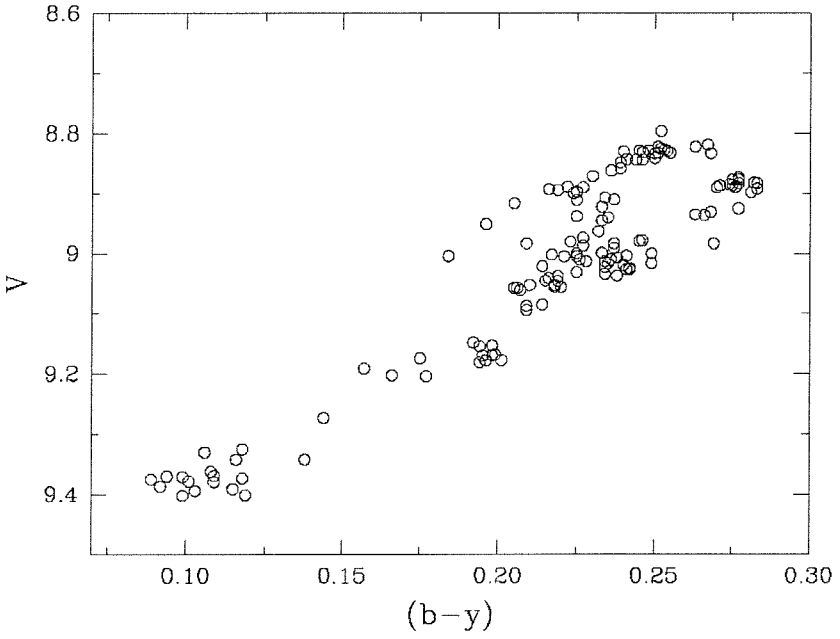


**Figure 3-6.** Colour-magnitude diagram for V801 Cen, using y and (b – y) data taken from ESO's Long-term Photometry of Variables Project catalogues (Sterken et al. 1995).

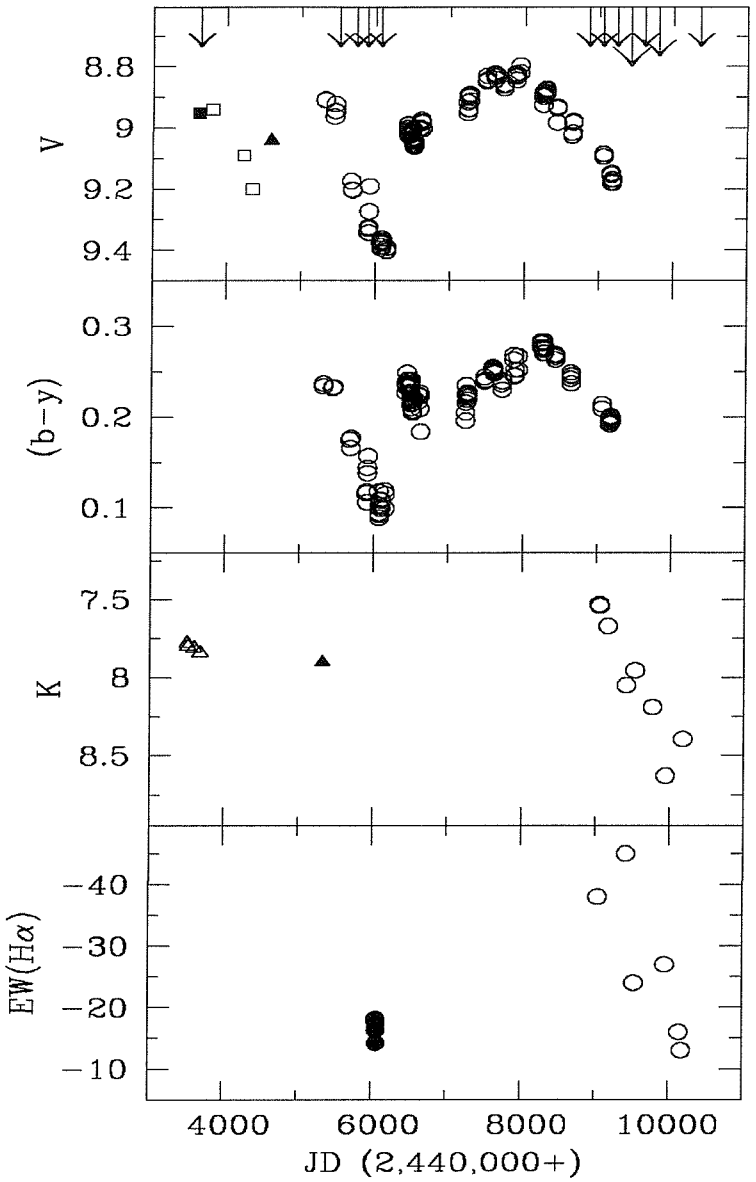


**Figure 3-7. Top and second panel:** Lightcurves of 4U1145-619 for the period 1978--1994, in Strömgren filter bands, data taken from Pakull et al. (1980), ESO's Long Term Photometric Variable Project catalogues (Sterken et al. 1995), Densham & Charles (1982), and from Hammerschlag-Hensberge et al. (1980). Arrows show the dates of detected X-ray outbursts, and are sized to give a crude indication of the intensity of the outburst. **Third panel:** IR *K* band lightcurve from 1978-1996; the open circles represent our data, other data taken from Glass (1979), and Waters et al. (1988). **Bottom panel:** EW(Hα) plot, 1978-1996. Open circles again represent our own data, other data taken from Cook and Warwick (1987b). Note the two previous episodes of disc-loss indicated by a decline in the optical luminosity of the source. Most recent data show a third such disc-loss event.

### 3.4.2.2 X-ray flux history

An X-ray flux history has been compiled from the available literature. All data were transformed to 2 – 10-keV fluxes with the exception of the *EXOSAT* ME data that were given in this energy range originally. The 2 – 10 keV fluxes were calculated assuming a power law spectrum with parameters derived wherever possible from the observations in question. This conversion is for comparison purposes only, and flux values may be in error by as much as a factor of two between one satellite and another. The 2 – 10-kev lightcurve is plotted in Figure 3-8. There is a quiescent flux of $\sim 10^{-10}$ ergs $s^{-1}$ $cm^{-2}$, and for the sake of discussion we shall regard an increase by a factor of five in flux to be an outburst.

The lightcurve then shows a number of outbursts, recurring at the 186.5-day period. Two of the outbursts stand out as the most luminous. The first, a 0.6-Crab (3 – 12 keV) outburst detected by the *Vela 5b* satellite in 1973 is clearly an order of magnitude more intense than the remaining outbursts, with the exception of a 0.5-Crab (20-40 keV) detection by the BATSE instrument on the *CGRO* satellite, in March 1994.

BATSE has detected six outbursts from the source between MJD 48361 and 50231 (Scott M., private communication), though the one *BATSE* outburst plotted in Figure 3-8 was much more intense than the remaining five (Wilson et al. 1994; Scott M., private communication). The most recent X-ray detection is a 0.1-Crab (2 – 12 keV) outburst detected by the *RXTE* satellite's All Sky Monitor (ASM) between 1996 September 29 and October 8, consistent with the 186.5 day period (Corbet & Remillard 1996). The ASM data show a possible flare at the previous predicted outburst epoch, but with far less significance.

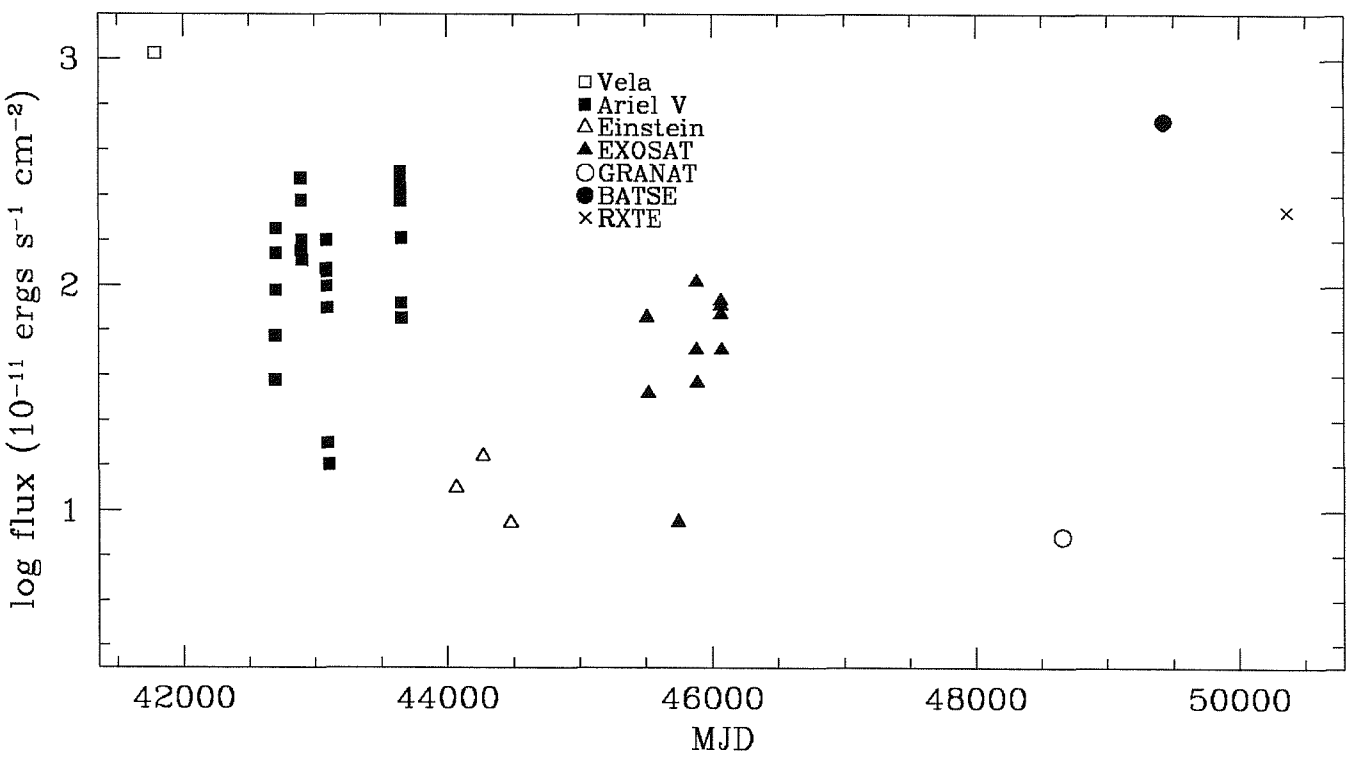


**Figure 3-8.** The X-ray lightcurve of 4U1145-619 for the period 1973 – 1996, in the 2 – 10 keV range. All values except the *EXOSAT* ME points are calculated assuming a power law spectrum. This is to facilitate comparison of measurements made in different energy bands, and values may be in error by as much as a factor of 2 from one satellite to another. Note that the *GRANAT* point is an upper limit. References for X-ray data are: *Vela*, Priedhorsky & Terrel 1983; *Ariel V*, Watson, Warwick & Ricketts 1981; *Einstein*, Mereghetti et al. 1987; *EXOSAT*, Mereghetti et al. 1987; Cook & Warwick 1987a, 1987b; *GRANAT*, Grebenev et al. 1992; *BATSE*, Wilson et al. 1994; *RXTE*, Corbet & Remillard 1996.

### 3.4.3 Correlations between Be star activity and X-ray emission

In Figure 3-7 the epochs of X-ray outbursts are plotted as arrows above the *V* band lightcurve. As in Section 3.4.2.2 we define an outburst as an increase in the X-ray flux by a factor of five or more above the quiescent flux of $\sim 10^{-10}$ ergs $s^{-1}$ $cm^{-2}$. Six BATSE detections are plotted, these corresponding to the six penultimate arrows (Scott M. private communication). There appears to be a correlation between the X-ray and optical behaviour, with X-ray activity increased during periods of optical decline.

Although we cannot however rule out the possibility that the apparent correlation is an artefact of the epochs of the X-ray observations, such a correlation is not unexpected, as the X-ray emission is fuelled by the material in the varying disc. If the material lost from the circumstellar disc is dissipated away from the star, rather than falling back onto the stellar surface, then some fraction of this material should accrete onto the neutron star providing additional fuel for X-ray emission.

This scenario was suggested by Roche et al. (1993) to explain similar correlations in the X-ray and optical/infrared behaviour of the Be/X-ray binary X Persei. However, many Be/X-ray binary systems show correlations of the opposite nature, with increased X-ray activity coinciding with optically bright phases (4U0115+63, Negueruela et al. 1997; A0538-66, Corbet et al. 1985). A distinguishing factor between these two groups is the significant difference in orbital period. Both 4U1145-619 and X Persei are long period binaries, with wide orbits, 4U0115+63 and A0538-66 each have periods less than 30 days, with much smaller orbits.

In the case of the long period binaries, the neutron star may not become immersed in the disc during periastron passage, but rather accrete from the material that is lost radially from this disc during phases of decline in the Be star's activity. Such a scenario would be consistent with spherical accretion.

In such a binary, where the neutron star does not accrete directly from the Be star's disc, but from material lost radially from it, we might expect any orbital modulation of X-ray flux to be of smaller amplitude and smoother in profile than in systems where the neutron star becomes immersed in the disc at periastron. However in the case of 4U1145-619 the orbital modulation in the X-ray lightcurve is significant, with outbursts lasting less than 0.1 phase and increases in flux of an order of magnitude above quiescence.

If this sharp modulation were caused by centrifugal inhibition of accretion (Stella, White & Rosner 1986), then we should not detect quiescent flux from the source. Corbet (1996) showed that X-ray emission may originate from the magnetosphere of the neutron star, even when accretion onto the neutron star surface was prohibited. We note that Corbet finds in the case of 4U1145-619, that this emission should be a factor of 7375 less than the minimum emission from the neutron star's surface. The quiescent flux observed in 4U1145-619 is only a factor of ~5 less than the normal outburst luminosity, suggesting that accretion onto the neutron star's surface is still occurring throughout the entire orbit. The sharp modulation might then indicate an inclination between the planes of the orbit and the Be star's disc, the sharp modulation occurring as the neutron star's orbit crosses the plane of the disc at periastron.

In Chapter 4 we investigate the shapes of X-ray lightcurves produced by adopting some simple models for accretion onto a compact object in orbit around a Be star, and find that the orbital velocity of the neutron star plays a major role in the modulation of the X-ray lightcurve so that even a wide orbit system such as 4U1145–619 should display sharp luminosity peaks at certain phases of their orbits.

### 3.4.4 Accretion mechanisms

The source's relatively low luminosity, wide orbit, and low pulsed fraction during 'minor' outbursts points towards spherical accretion as the source of energy for X-ray emission from 4U1145-619 (White et al. 1983). Arons & Lea (1980) suggested that the area of the accretion hot spot in accreting neutron stars increases as the X-ray luminosity decreases.

For low-luminosity sources ($L_x \leq 5 \times 10^{36}$ erg $s^{-1}$), as is the case with 4U1145-619 during minor X-ray outbursts (see Figure 3-8) assuming the derived distance of 3.1 kpc, the accretion area can be as large as the entire surface of the neutron star. Therefore, the angular momentum of the flow in 4U1145-619 would be low and material would build up outside the magnetosphere before penetrating and falling unevenly over most of the surface of the neutron star.

The large outburst of 1994 March however allows an alternative scenario. At the maximum of the major outburst, the total flux detected by BATSE was 0.5-Crab (20 – 40 keV), with a significant phase averaged pulsed flux of 0.3-Crab (Wilson et al. 1994). This suggests that in this instance at least, accretion was concentrated to a greater degree onto the magnetic poles. Such a difference in the pulsed fraction of the total flux could be interpreted as evidence for the formation of a short-lived accretion disc, which would allow more efficient binding of material to the magnetic field lines.

In support of this hypothesis, the spin period of the neutron star was seen to decrease during the 1994 March outburst, whilst no significant spin-up was detected during the five less intense outbursts seen by *BATSE* between MJD ~ 48361 and MJD ~ 50231 (Scott M., private communication). This scenario would require a change in the circumstellar environment to account for the lack of accretion disc formation at other periastron passages. This requirement would be fulfilled by

having a greater density of circumstellar material resulting from the proposed mass ejection event from the Be star.

Further evidence for the formation of a temporary accretion disc comes from the fact that the March 1994 outburst continued at detectable levels longer than usual after maximum flux. Mereghetti et al. (1987) however give an alternative suggestion that such X-ray lightcurve profiles could be due to the compression of accreting material in the bow shock of the neutron star, followed by the accretion of more dilute "downstream" material.

We also note that shortly before the *BATSE* detection in March 1994, the *EW*(Hα) strengthened to –45Å, with no correlated rise in the infrared luminosity. Either a delay exists between the mechanisms behind the disc's Balmer emission and infrared excess, or an additional Hα component was present, with a source discrete from that of the infrared excess. An accretion disc could produce this Hα emission with no correlated change in the infrared magnitudes.

## 3.5 Spectral Variability

In order to study the variations in the emission lines described in Section 3.2.3.1 and attempt to relate them to changing properties of the circumstellar disc, we have measured a number of parameters that describe each profile.

In optically thin lines, the shape of the line profile is determined primarily by the kinematics of the disc, resulting in the double peaked profiles commonly seen in Be star spectra. The radial (with respect to the observer) velocities of the peaks correspond to the rotational velocities of the disc material at the outer border of the line emitting region (see for example Figure 1. of Horne and Marsh 1986), thus a double peaked profile is an indication that some clear boundary to the emitting region exists. Optically thick lines are further affected by scattering within the disc. Elec-

tron scattering broadening produces wings in the profile that can extend to velocities of order ~1000 km $s^{-1}$, and smears out features which might have been sharp were the line optically thin. Non-coherent scattering broadening was proposed by Hummel & Dachs (1992) as the mechanism behind 'winebottle' profiles (profiles with 'shoulders' in the flanks – for examples see Figure 1 and Figure 4 of Hummel & Dachs (1992)).

NSB arises because the disc has a finite optical thickness in the direction normal to the disc plane. Hence, when we look into the disc (especially for pole-on stars) we see deeper into the disc (where the source function is stronger) in the line wings, as photons which have been scattered out of the line center have a greater escape probability. The result of NSB is expected to be a doubling of the peaks that are due to the disc kinematics. This splitting should be locally symmetrical, so that if an optically thin line shows *violet* (*V*) and *red* (*R*) peaks at velocities $v_{k_V}$ and $v_{k_R}$ respectively, then an optically thick line originating from the same region of the disc will show a peak and a shoulder on each side with velocities $v_{p_V}$, $v_{s_V}$, $v_{p_R}$ and $v_{s_R}$, where, following Hummel & Vrancken (1995 - hereafter HV1995) we assume,

$$\frac{v_p + v_s}{2} = v_k \tag{3-19}$$

Measuring the positions of these peaks and shoulders is difficult, especially as the resolution of many of our spectra is less than $R_{H\alpha} \approx 10000$. Fitting Gaussian functions to the profiles often yields non-unique solutions, so we use the derivative method of HV1995 to recover the positions. The first derivatives of the line profiles were computed, and the minima, maxima and zero crossing points of the resulting function were determined.

The zero crossing points of the first derivative function are used to determine the velocities of the peaks in the line profiles, the minima and maxima of the first derivative function represent the points of inflection in the line profiles. Where two

separate peaks are not clearly defined, but a clear 'shoulder' can be seen in the profile, the velocity of this component was measured as the mid point between two successive points of inflection.

In addition to measuring the velocities of the $V$ and $R$ peaks, we also measured for each profile the kinematical seperation of the $V$ and $R$ peaks $\Delta v_k$, equivalent width of the line (EW, the ratio of line flux to continuum flux), and the ratio of intensities of the $V$ and $R$ peaks $V/R$. In the case of profiles that appear to show NSB splitting, we take the intensity of the $V$ and $R$ peaks to be the mean of the peak and shoulder intensities.

A number of the Hα profiles show only one clear peak, with one or two shoulders in the flank where the weaker peak is expected to be. In these cases we interpret the shoulders as being the weak peaks (either split by NSB or not depending on whether one or two shoulders are visible) which we are unable to resolve from the flank of the stronger peak.

The measured line profile parameters are shown for Hα in Table 3-7 and for He I (6678 Å) in Table 3-8. The rotational separation of peaks is without exception greater for the He I line than the Hα line. This is indicative of the lines originating in regions of different radii. We find the mean ratio of the separation in the two lines to be:

$$\frac{\Delta v_{k_{HeI}}}{\Delta v_{k_{H\alpha}}} = 1.5 \pm 0.2 \qquad (3\text{-}20)$$

In Figure 3-10 we plot the relationship between the separation of peaks due to rotation and the EW's of the Hα and He I (6678 Å) lines. There is a clear correlation between the Hα peak seperation and EW, with regression analysis yielding

$$\log \Delta v_{k_{H\alpha}} = 2.68(\pm 0.20) - 0.23(\pm 0.17)\log(EW) \qquad (3\text{-}21)$$

and a correlation coefficient of $R = 0.952$. The probability that no correlation exists is only $3.8 \times 10^{-4}$. The existence of a similar correlation between the parameters measured for the He I profiles is suggested but is less clear, with

$$\log \Delta v_{k_{H\alpha}} = 2.68(\pm 0.20) - 0.23(\pm 0.17) \log(EW) \tag{3-22}$$

and a correlation coefficient of $R = 0.818$. In this case we find a significant probability of 0.18 that no correlation exists.

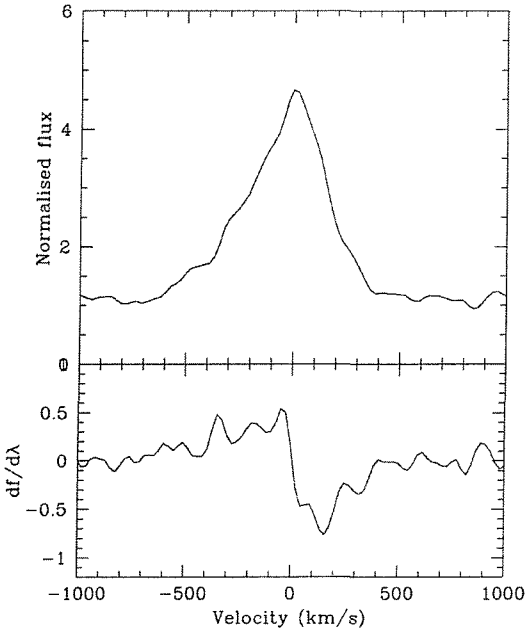


a) 2nd March 1993

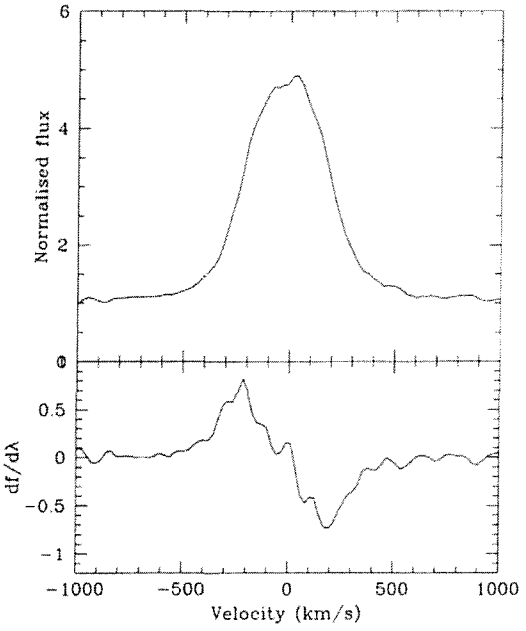


b) 7th March 1994

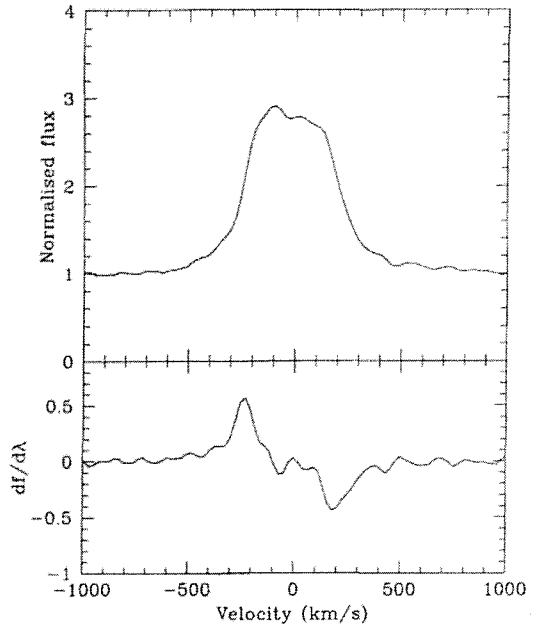


c) 2nd/3rd July 1994

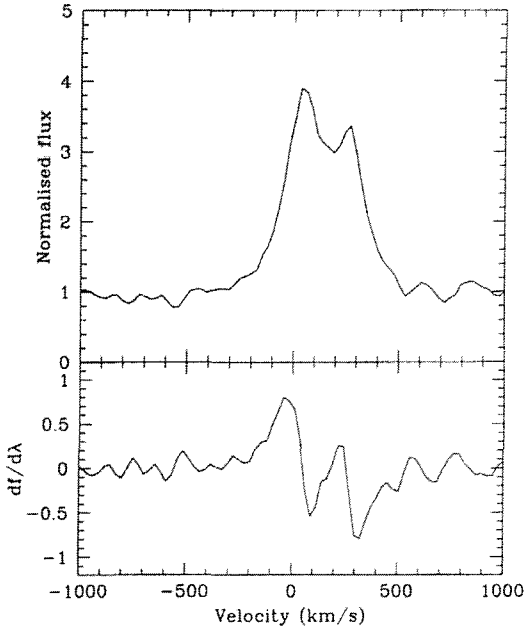


d) 19th August 1995

**Figure 3-9:** ***continued overleaf.***

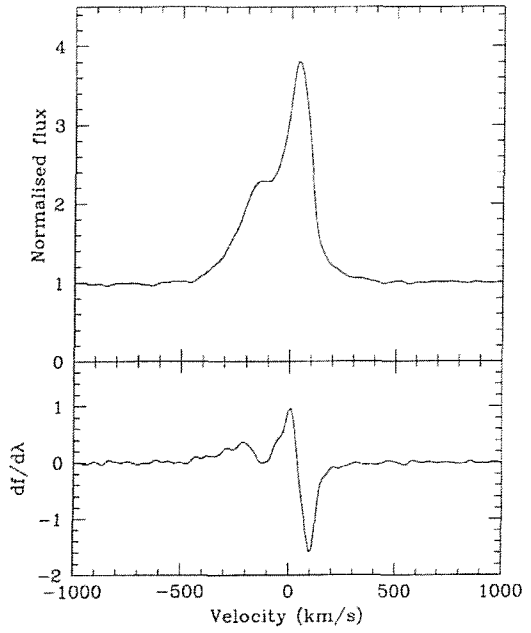


e) 2nd March 1996

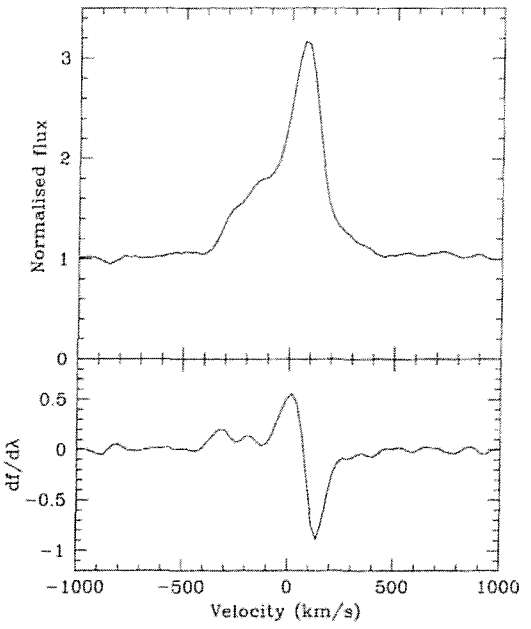


f) 3rd/4th April 1996

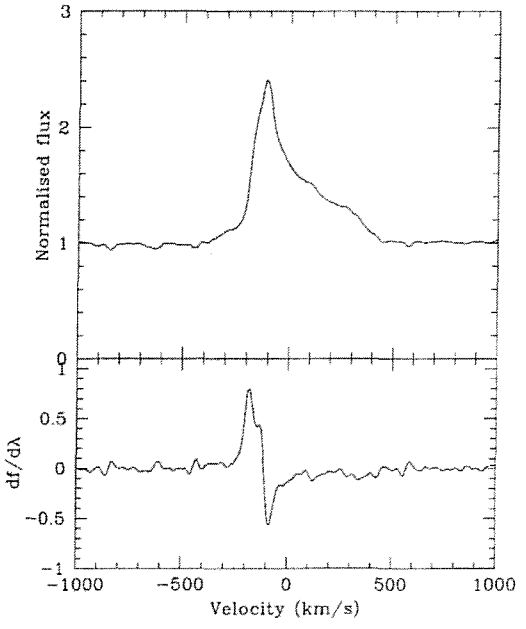


g) 18th March 1997

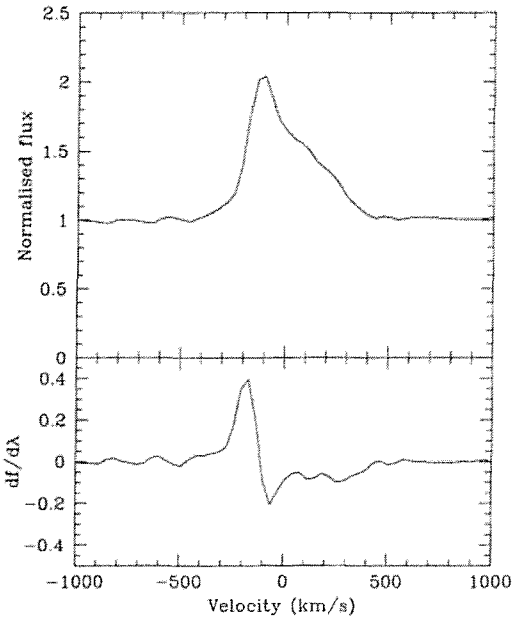


h) 10th – 14th April 1997

**Figure** 3-9: *continued overleaf.*

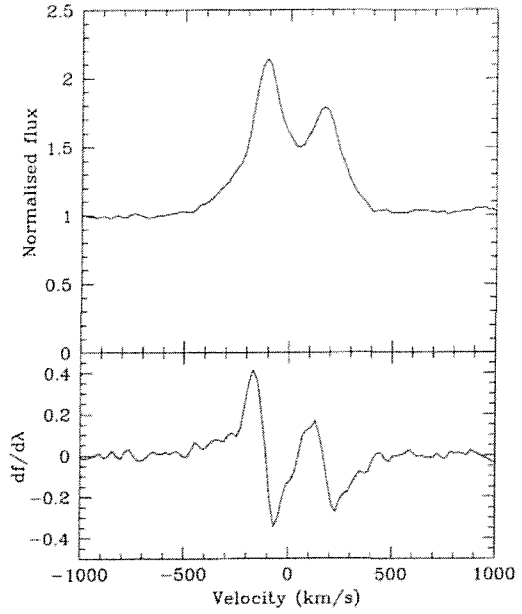


i) 20th June 1997

**Figure 3-9.** Line profiles and first derivatives for the Hα line of V801 Cen.

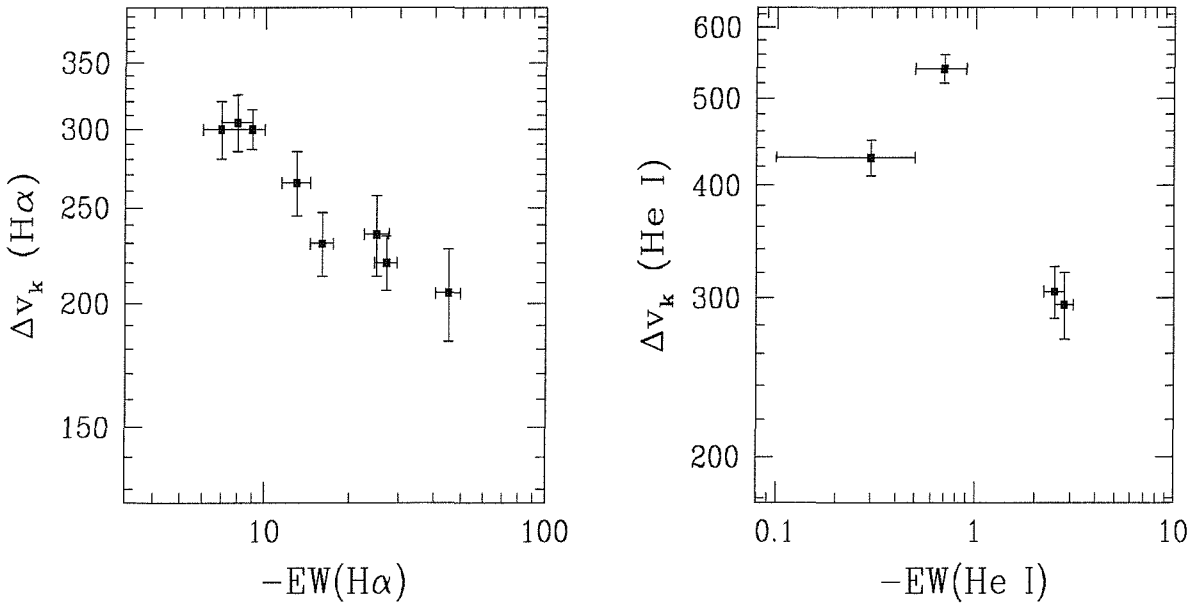


**Figure 3-10.** Relationship between projected rotational velocities ($\Delta v_k$) and strength of line emission (EW), for Hα (left) and He I (6678 Å) (right).

**Table 3-7.** Measured properties of the Hα emission line of V801 Cen from 1993 to 1997

| Date | $V_{PV}$ (km s$^{-1}$) | $V_{SV}$ (km s$^{-1}$) | $V_{PR}$ (km s$^{-1}$) | $V_{SR}$ (km s$^{-1}$) | $EW$ (Å) | log ($V/R$) |
|---|---|---|---|---|---|---|
| 1993 Mar 2 | — | — | — | — | -38 | -0.41 |
| 1994 Mar 7 | -50 | -120 | 70 | 170 | -45 | ~0 |
| 1994 Jul 2-3 | -50 | -150 | 60 | 160 | -25 | 0.03 |
| 1995 Aug 19 | -60 | — | 160 | — | -27 | 0.12 |
| 1996 Mar 2 | -140 | — | 100 | — | -16 | -0.17 |
| 1996 Apr 3-4 | -110 | -230 | 110 | — | -13 | -0.46 |
| 1997 Mar 18 | -70 | -120 | 120 | 300 | -8 | 0.28 |
| 1997 Apr 10-14 | -90 | — | 140 | 280 | -7 | 0.32 |
| 1997 Jun 20 | -80 | — | 220 | — | -9 | 0.16 |

**Table 3-8.** Measured properties of the He I (6678 Å) emission line of V801 Cen from 1993 to 1997

| Date | $V_{Rp}$ km s$^{-1}$ | $V_{Vp}$ km s$^{-1}$ | EW (Å) | log (V/R) |
|---|---|---|---|---|
| 1994 Mar 7 | -160 | 135 | -2.8 | 0.12 |
| 1995 Aug 24 | -135 | 180 | -2.5 | -0.42 |
| 1997 Mar 18 | -126 | — | 0.0$^{\dagger}$ | — |
| 1997 Apr 10-14 | -150 | 280 | -0.3 | 0.12 |
| 1997 Jun 20 | -330 | 210 | -0.7 | -0.31 |

$^{\dagger}$ Assuming a symmetrical profile

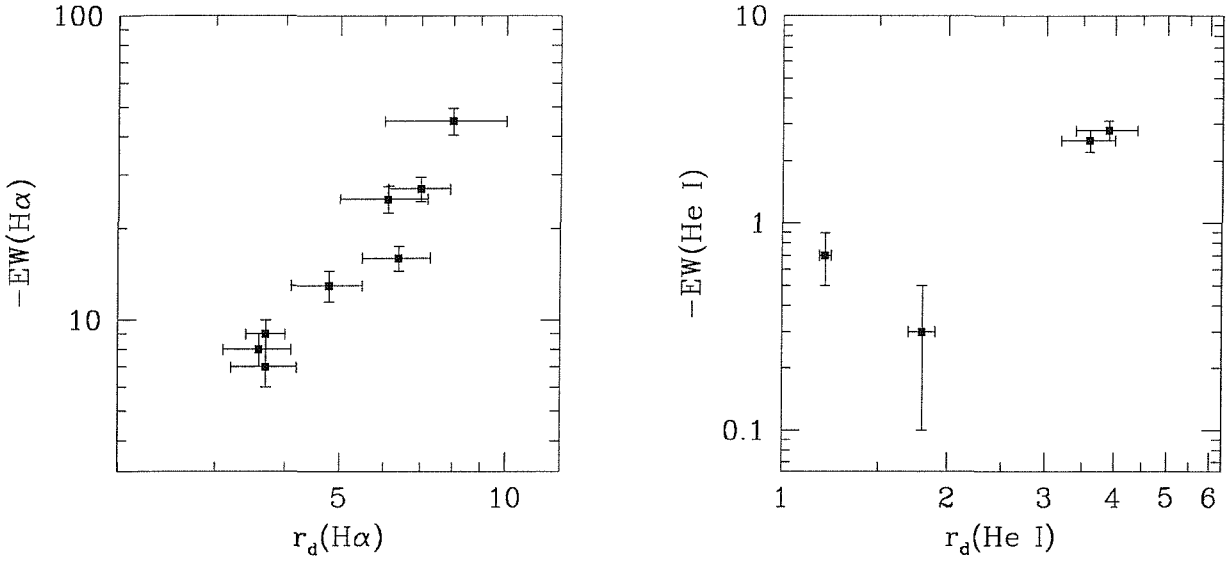


**Figure 3-11.** Relationship between the strength of line emission and radius of emitting region for Hα (left) and He I (6678 Å) (right).

We can estimate the dimensions of disc regions which emit various spectral lines from the separation of peaks in the line profiles. Assuming a near-Keplerian disc, the lines of constant radial velocity form a dipole type pattern, and the each peak in the line profile originates from a crescent shaped region tangential to the outer border of the line emitting region (see for example Figure 1. of Horne and Marsh 1986). Hence the existence of the two peaks clearly indicates the existence of some boundary to the emitting region, and the separation of the peaks is directly related to the radius of this boundary. We use the notation $r_d$ to denote the characteristic emitting radius.

In deriving the dimensions of the Hα and He I (6678-Å) emitting regions, $r_{d,H\alpha}$ and $r_{d,He}$ we assume a power law for the rotational velocity such that

$$v_{rot}(r) = v_{crit}\left(\frac{r}{R_*}\right)^{-j} \tag{3-23}$$

where $R_*$ is the stellar radius, and $v_{crit}$ is the critical break up velocity, which equals the Keplerian velocity at the stellar surface, $v_{rot}(R_*)$. In this model $v_{rot}(R_*)$ is the maximum rotational velocity in the disc, and we assume that the disc begins close to the stellar surface. We can then calculate the radius $r_{d,H\alpha}$ of the Hα emitting region of the disc from the separation of peaks $\Delta v_k = 2\, v_{ro}\, r_{d,H\alpha} \sin i$ by the equation:

$$\frac{r_{d,H\alpha}}{R_*} = \left( \frac{2v_0 \sin i}{\Delta v_k} \right)^{-j} \tag{3-24}$$

Here we can use $v_0 \sin i = v_* \sin i$, the measured rotational velocity of the star, assuming that the star is rotating very close to it's critical break-up velocity. We shall use Balona's (1973) value of $v \sin i = 290$ km s$^{-1}$.

It is unlikely that the velocity law in the disc actually has a constant value of $j$. The total width of even the He I (λ = 6678-Å), (which is unlikely to be affected by electron scattering), exceeds 2 $v \sin i$, implying that some mechanism must transfer angular momentum into the inner disc. In order to estimate the dimensions of the line emitting regions of the disc for Hα and He I, we have assumed that the disc is Keplerian throughout ($j$ = ½). The resulting emitting radii are plotted against the equivalent width of the line emission in Figure 3-11.

## 3.6 Summary

### 3.6.1 Astrophysical parameters

Physical parameters calculated for the optical counterpart V801 Cen show discrepancies with previously published values, but the discrepancies can usually be explained in terms of the circumstellar effects which need to be corrected for in the case of Be stars.

Our results are not consistent with a distance of only ~500pc as has been suggested by some authors on the basis of Hipparcos data, though these claims were based on data with very large uncertainties.

### 3.6.2 Discloss and related X-ray behaviour

The Be/X-ray binary 4U1145-619 is exhibiting signs of disc loss in optical and infrared wavelengths, after two previous such events since 1982. Whilst the infrared excess has decreased by $\Delta K \sim 1$, the disc does not appear to have been lost completely, as the Hα line still shows emission, the last observations showing EW(Hα) = -13 ± 1.3-Å. X-ray luminosities and pulse profiles during normal outbursts are typical of those expected for spherically accreting systems, though there is a possibility of the formation of a short-lived accretion disc during larger outbursts.

Contemporaneous infrared and optical observations over the course of the next optical rise, combined with X-ray observations should confirm the existence or otherwise of any optical/X-ray correlations, and lead to a more complete understanding of the mechanisms fuelling this source, and long period Be/X-ray binaries in general.

### 3.6.3 Spectral variability

A strong correlation has been found between the radius of the emitting region and the strength of the emission in the case of the Hα and He I lines. The Hα line emission is found to originate from a region of the disc between ~ 5 – 10 stellar radii, the He I (λ = 6678-Å) line emission originates from a region between ~ 1 – 5 stellar radii.

# Chapter 4 – Modelling the X-ray lightcurves of Be/X-ray binaries

In this chapter I attempt to reproduce observed Be/X-ray binary lightcurves with a computational model. The model involves solving the orbital motion of the neutron star, and combining this with a model for the Be star's disc before applying equations for accretion onto a compact object in motion relative to the accreted media.

After describing the model, I investigate the effects of various model parameters on the resulting lightcurves. Finally I apply the model to observed X-ray lightcurves of the Be/X-ray binary EXO 2030+375 and find that changes in the phase at which X-ray maximum occurs can be explained through a change in the disc outflow velocity.

The model fit to EXO 2030+375 has already been published in Reig, Stevens, Coe et al (1998).

## 4.1 Introduction

One of the problems faced by theoreticians in trying to explain the Be phenomenon is that the structure of the circumstellar disc is not precisely known. Observations at optical/infrared wavelengths have been modelled well, but only yield information on the structure and dynamics of the disc out to small radii – of the order of 10 $R_*$. At larger radii, the disc should be apparent at radio wavelengths only, yet of many Be stars observed, almost non display the radio emission expected from a simple extrapolation of the optical/infrared spectral distribution. This fact in itself implies a change in the structure of the disc at radii ~ 5 $R_*$, yet frustratingly the lack of radio detections precludes detailed knowledge of the structure beyond this point.

The X-ray emission in Be/X-ray binaries results from the accretion of material from a Be star's equatorial disc onto a neutron star orbiting at separations ~ 10 – 100 $R_*$. It follows then that observations of the properties of the X-ray emission from these systems will tell us about the structure and dynamics of the circumstellar disc itself. In this way, we can use the neutron star as a probe of the circumstellar disc, to constrain models of the disc at radii not observable through optical/infrared/radio observations of the Be star itself.

In this chapter I develop a model for the X-ray luminosity of Be/X-ray binaries, based upon the diverging disc model of Be star discs, and which explicitly allows for both supersonic and subsonic motion of the neutron star relative to the wind material. Through this model I investigate the affects of each model parameter, including a number of different models for the dynamics and distribution of the circumstellar material. I apply the developed model to the X-ray lightcurves of the Be/X-ray binary EXO2030+375 in an attempt to explain changes in the observed lightcurve in terms of changes to the dynamics of the Be star disc. Finally, I present a spectroscopic study of the Be/X-ray binary 4U1145-619 conducted during an

X-ray maximum in order to check for perturbation of the Be star's disc by the orbiting neutron star.

## 4.2 Be/X-ray binary X-ray lightcurve model

### 4.2.1 Accretion onto a compact object

The accretion of material onto an object moving through a cloud of gas was investigated by Hoyle & Lyttleton (1939). They found that the rate of accretion onto the object was given by the equation

$$\dot{M} = \alpha \pi R_a^2 \rho_\infty v_{rel} \tag{4-1}$$

where $v_{rel}$ is the velocity of the object relative to the gas, $\rho_\infty$ is the unperturbed density of the gas, $\alpha$ is a dimensionless parameter of order unity, and $R_a$ the radius of the accretion cross-section or capture radius. The capture radius $R_a$ can be calculated by considering that in order for material to be captured by the accreting object, the kinetic energy per unit mass of the accreted gas must be less than its gravitational potential per unit mass, ie.

$$\frac{1}{2} v_{rel}^2 < \frac{GM_x}{R} \tag{4-2}$$

where $M_x$ is the mass of the accreting object. Hence the radius of the accretion cross-section, referred to as the 'Bondi-Hoyle radius', is

$$R_a = \frac{2GM_x}{v_{rel}^2}. \tag{4-3}$$

These equations are correct only when the motion of the accreting object through the gas is supersonic, so that the accretion is velocity limited. Bondi (1952) considered the case of accretion onto a stationary object. In this case the accretion is pressure limited, and given by

$$\dot{M} = 4\lambda\pi R_B^2 \rho_\infty c_s \tag{4-4}$$

where $c_s$ is the velocity of sound in the (unperturbed) gas, λ is a dimensionless parameter of order unity and $R_B$ is the 'Bondi radius' – analogous to the Bondi-Hoyle radius, but limited not by the velocity of the accreting object relative to the gas, but by the pressure forces acting against gravity. The value of $R_B$ is given by

$$R_B = \frac{GM_x}{c_s^2} \tag{4-5}$$

For cases where the accreting object is not at rest relative to the gas, but where this relative motion is not supersonic, Bondi proposes the following interpolative formula – with a factor of 2 added according to the suggestion of Shima et al. (1985),

$$\dot{M} = \kappa\left(\frac{4\pi(GM)^2\rho}{\left(c_s^2 + v_{rel}^2\right)^{3/2}}\right) \tag{4-6}$$

with κ being a dimensionless parameter analogous to α and λ in equations 4-1 and 4-4. The speed of sound is found by

$$c_s^2 = \gamma\frac{P_\infty}{\rho_\infty} \tag{4-7}$$

with γ being a constant with the value $1 < \gamma < 5/3$, where

$$\left(\frac{P}{P_\infty}\right)=\left(\frac{\rho}{\rho_\infty}\right)^\gamma \tag{4-8}$$

Treating the material in the circumstellar disc as an ideal gas, so that

$$P=\frac{\rho k T_{wind}}{\overline{m}} \tag{4-9}$$

with $\overline{m}$ the mean particular mass, the sound speed is then

$$c_s=\sqrt{T_{wind}\frac{\gamma k}{\overline{m}}} \tag{4-10}$$

Assuming the gas to be mainly hydrogen, if it is completely neutral, then $\overline{m}$ is equal to the mass of the hydrogen atom, if completely ionised, then $\overline{m}$ is approximately half this value (to within the desired precision).

### 4.2.2 The orbits of Be/X-ray binaries

The orbits of Be star X-ray binaries are generally eccentric ($e$ ~ 0.3 – 0.4) with periods of order 10's of days. The parameters specific to this model that require derivation are the separation of the stars, and the two components of the neutron star's velocity, the azimuthal component and the radial (with respect to the Be star) component. In this Chapter, unless explicitly stated otherwise, when I refer to radial velocities, I will be referring to those velocities in a radial direction from the centre of the Be star, and not relative to the observer. All of these quantities need to be determined as a function of orbital phase.

The velocity components of the neutron star's motion will be combined with the later derived velocities of the circumstellar disc material in order to find the velocity of the material relative to the neutron star. The orbital separation will be needed in order to derive the density of the disc material at each orbital phase, given some assumed circumstellar disc model.

In calculating the components of the neutron star's velocity relative to the Be star, and the separation of the two stars as a function of orbital phase (φ), I treat the Be star as being stationary. If the motion of the neutron star about the centre of mass of the binary system describes an ellipse with eccentricity *e*, then the motion relative to the Be star also describes an ellipse of equal eccentricity.

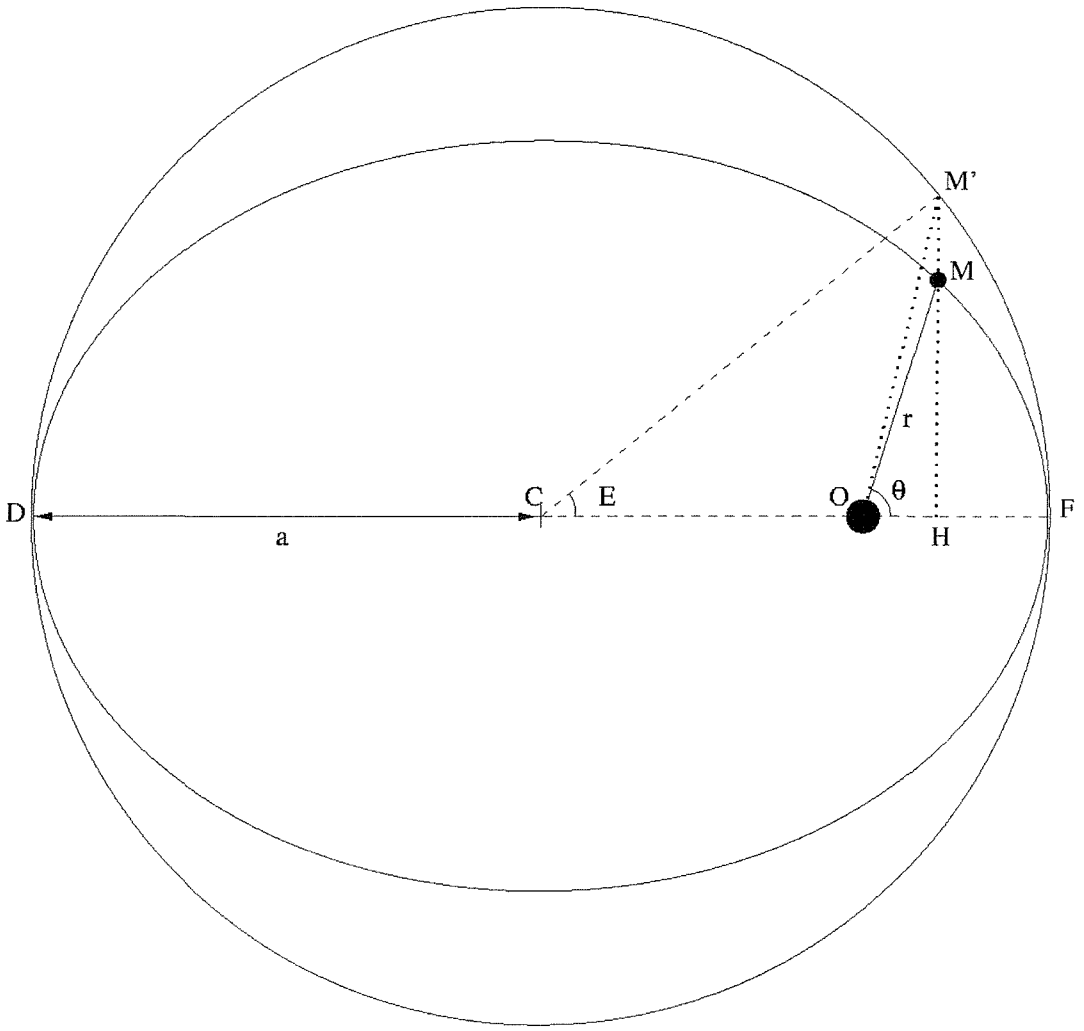


**Figure 4-1.** Geometry of a Be/X-ray binary orbit, illustrating definitions of terms used in the derivation of orbital properties.

Figure 4-1illustrates the definitions of terms that I shall use in describing the geometry of the neutron star's orbit. The neutron star lies at point $M$, its orbit is described by the inner ellipse. The Be star lies at the point O, which is one focus of the ellipse which describes the orbit. This ellipse is an affine transform (in the ratio $\sqrt{1-e^2}$ ) of the outer circle. The distance $\overline{HM}$ is then equal to $\sqrt{1-e^2}\cdot\overline{HM'}$ at all points throughout the orbit. The distance $\overline{CO}$ is equal to $ae$, where $e$ is the eccentricity of the orbit, and $a=\overline{CF}$ is the semi-major axis of the orbit. If $x=\overline{OH}$ and $y=\overline{HM}$ are respectively the horizontal and vertical projections of $r$ (referring to the orientation of Figure 4-1), then we can calculate these co-ordinates both through trigonometric methods

$$\begin{aligned} x &= r\cos\theta \\ y &= r\sin\theta \end{aligned} \tag{4-11}$$

and through geometric methods

$$\begin{aligned} x &= a(\cos E - e) \\ y &= a\sqrt{1-e^2}\sin E \end{aligned} \tag{4-12}$$

Combining equations 4-11 and 4-12, and calculating $r^2$ we then find

$$r = a(1-e\cos E). \tag{4-13}$$

$E$ is referred to as the eccentric anomaly, θ as the true anomaly. The mean angular frequency $\overline{\nu}$ is found in terms of the orbital period $P_{orb}$ by

$$\overline{\nu} = \frac{2\pi}{P_{orb}} \tag{4-14}$$

and I introduce the parameter μ, defined as

$$\mu = \frac{4\pi^2 a^3}{P_{orb}^2} = \bar{\nu}^2 a^3 \tag{4-15}$$

The rotational component of the neutron star's velocity relative to the Be star can then be found in terms of the orbital separation by conserving angular momentum:

$$V_{\theta,ns} = r\frac{d\theta}{dt} = \frac{\bar{\nu}a^2}{r}\sqrt{1-e^2} = \frac{2\pi a^2}{P_{orb}r}\sqrt{1-e^2} \tag{4-16}$$

whilst the total velocity of the neutron star can be found by conserving energy:

$$V_{ns}^2 = \mu\left(\frac{2}{r} - \frac{1}{a}\right) = \frac{4\pi^2 a^3}{P_{orb}^2}\left(\frac{2}{r} - \frac{1}{a}\right) \tag{4-17}$$

The radial component of the neutron star's velocity follows simply then from

$$V_{r,ns}^2 = V_{ns}^2 - V_{\theta,ns}^2 = \frac{4\pi^2 a^3}{P_{orb}^2}\left(\frac{2}{r} - \frac{1}{a}\right) - \left(1-e^2\right)\left(\frac{2\pi a^2}{P_{orb}r}\right)^2 \tag{4-18}$$

with the sign of the radial velocity component being positive when $0 < \varphi < 0.5$ and negative when $0.5 < \varphi < 1.0$ (ie. I adopt the convention of positive velocities corresponding to motions *away* from the Be star).

The eccentric anomaly can be found in terms of orbital phase giving

$$E - e\sin E = \bar{\nu}\varphi \tag{4-19}$$

which must be solved iteratively to find the value of $E$ at a given orbital phase. We can then easily calculate the orbital separation from equation 4-13, and hence the rotational and radial components of velocity from equations 4-16 and 4-17.

### 4.2.3 Be star disc model

The model that I consider is the diverging disc model due to Waters et al. (1986), which was described in Chapter 1. In this model, the circumstellar disc is assumed to diverge with a constant opening angle (of the order of 10°), and has a power-law density distribution such that

$$\rho = \rho_0 \left( \frac{r}{R_*} \right)^{-n} \tag{4-20}$$

with $n$ lying in the range $2 - 3.75$ (from IR continuum modelling, Waters 1986, Waters et al. 1987). It follows from mass conservancy then that

$$V_{r,wind} = V_0 \left( \frac{r}{R_*} \right)^{n-2} \tag{4-21}$$

The rotational velocity of the wind is assumed to follow the law

$$V_{\theta,wind} = V_{crit} \left( \frac{r}{R_*} \right)^{\alpha} \tag{4-22}$$

where $\alpha$ lies between –0.5 (Keplerian velocity distribution) and –1 (angular momentum of out-flowing material is conserved). It is probable that the rotational velocity might follow a Keplerian distribution ($\alpha$ = –0.5) up to some radius, then follow an angular momentum conserving distribution ($\alpha$ = –1) at larger radii.

### 4.2.4 X-ray lightcurve model

From Equation 4-6 it is clear that the shape of the lightcurve is governed by the changes in relative velocity and density of the wind material encountered by the neutron star throughout its orbit. It is also clear that the dependence on relative velocity is much greater than that on density. If temperature effects are taken into

account then the lightcurves may also be affected by changes in the sound speed as a result of temperature changes in the disc. In constructing the model then, I consider in the following sections the orbital velocity of the neutron star, and the density and velocity distribution of the disc, for now following the diverging disc model of Waters et al. (1986).

Code was developed as necessary to determine the various components required to calculate the X-ray luminosity as a function of orbital phase. First the orbital parameters were used to derive the polar components of the neutron star's velocity relative to the Be star, and the separation of the two stars. The separation was then used to determine the wind density and velocity components at the position of the neutron star. Finally, all velocity components were combined to find the total relative velocity of the neutron star relative to the Be star wind, and this and the wind density were used to derive the X-ray luminosity from Equation 4-6.

In the following section I will describe the resulting predicted lightcurves, varying the input parameters to investigate the effects of each on the final lightcurve.

## 4.3 Results

In this section I investigate the effects of the input parameters on the lightcurves predicted by the model described in Section 4-2. The following model parameters were investigated:

- Be star wind parameters
  - Initial wind outflow velocity (at stellar surface)
  - Density/velocity power law gradient
  - Disc rotation model
- Orbital parameters
  - Orbital eccentricity
  - Orbital period

The following sections describe the chosen parameters for each case and the resulting lightcurve predictions.

**Table 4-1.** Orbital parameters input to the lightcurve model to investigate the effects of varying Be star disc parameters (chosen to be those of the Be/X-ray binary system 4U1145–619).

| | |
|---|---|
| Be star mass | 13 $M_\odot$ |
| Be star radius | 8 $R_\odot$ |
| Neutron star mass | 1.4 $M_\odot$ |
| Neutron star radius | 10 km |
| Orbital period | 186.5 days |
| Orbital eccentricity | 0.4 |

### 4.3.1 Dependence on Be star wind parameters

To investigate the effects of the wind parameters on the lightcurves predicted by the model developed in Section 4-2, the orbital parameters input to the model were kept constant. The chosen parameters were the best fit parameters to the Be/X-ray binary system 4U1145–619, where possible the parameters were as derived in Chapter 3, otherwise were taken from the available literature. The orbital parameters used are listed in Table 4-1.

#### 4.3.1.1 Initial wind outflow velocity and power-law gradient

With the orbital parameters fixed in the model as described in Table 4-1, the wind parameters were then varied in the following ways:

- The power law gradient was kept constant at $n$ = 2.0, and the initial outflow velocity varied from 0 to 1000 km $s^{-1}$.
- The power law gradient was kept constant at $n$ = 2.25, and the initial outflow velocity varied from 0 to 500 km $s^{-1}$.
- The power law gradient was kept constant at $n$ = 2.5, and the initial outflow velocity varied from 0 to 100 km $s^{-1}$.
- The power law gradient was kept constant at $n$ = 2.75, and the initial outflow velocity varied from 0 to 50 km $s^{-1}$.
- The power law gradient was kept constant at $n$ = 3.0, and the initial outflow velocity varied from 0 to 20 km $s^{-1}$.
- The power law gradient was kept constant at $n$ = 3.25, and the initial outflow velocity varied from 0 to 10 km $s^{-1}$.
- The power law gradient was kept constant at $n$ = 3.5, and the initial outflow velocity varied from 0 to 6 km $s^{-1}$.
- The power law gradient was kept constant at $n$ = 3.75, and the initial outflow velocity varied from 0 to 3 km $s^{-1}$.
- The power law gradient was kept constant at $n$ = 4.0, and the initial outflow velocity varied from 0 to 1.5 km $s^{-1}$.

The resulting predicted lightcurves are shown in Figures 4-2 to 4-10.

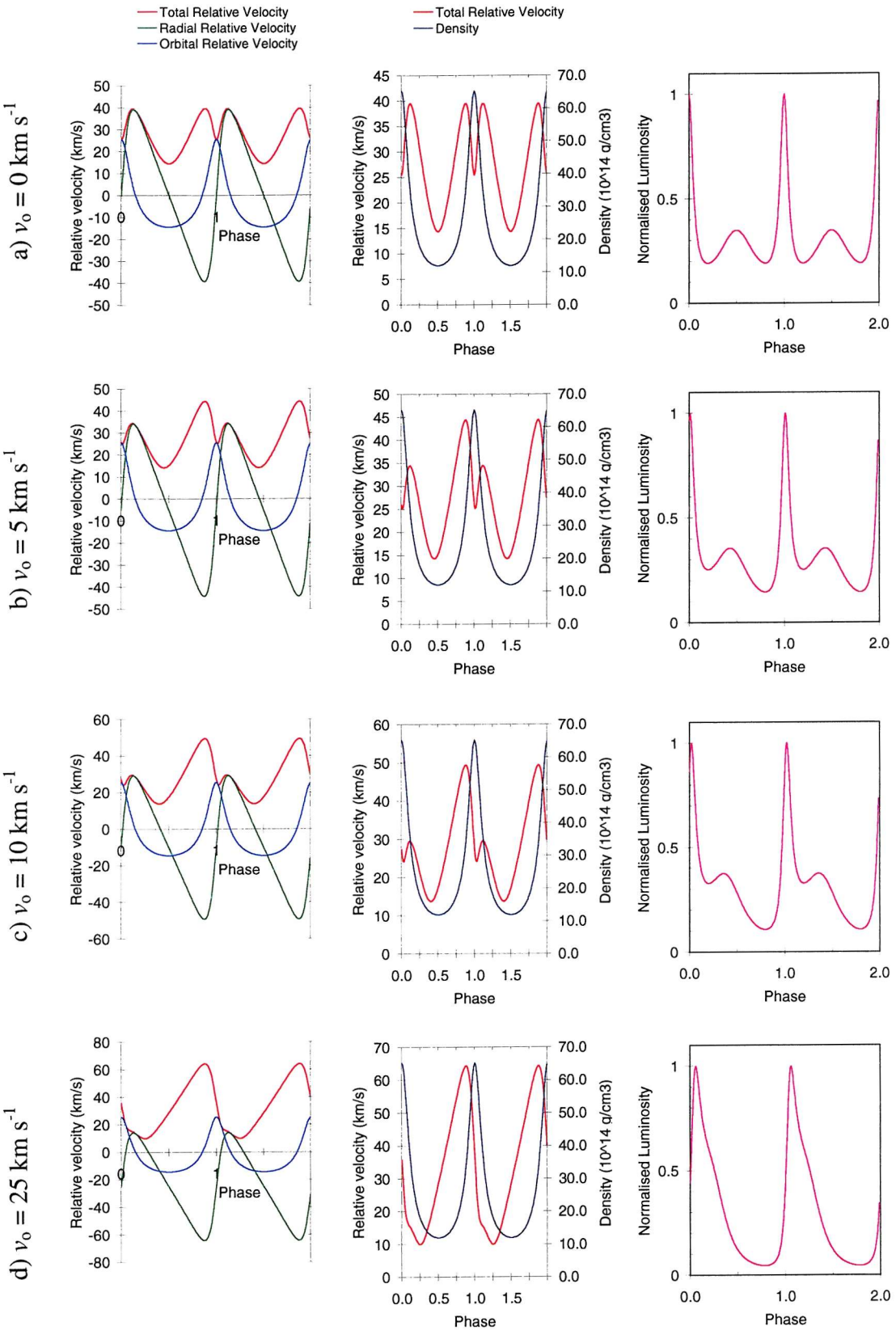


**Figure 4-2.** ***Continued overleaf…***

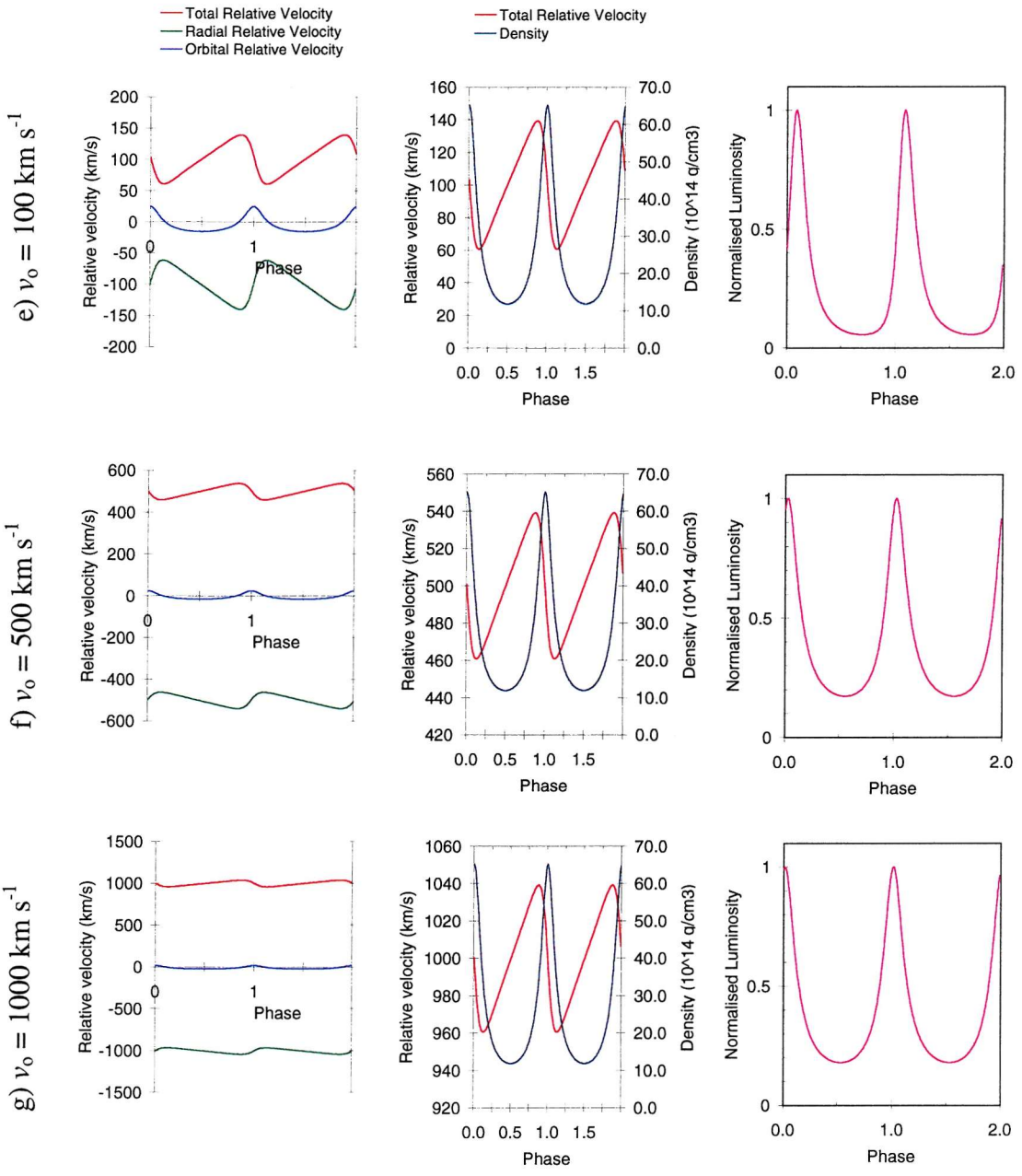


**Figure 4-2.** X-ray lightcurve model predictions for a system with orbital parameters equal to those of the Be/X-ray binary 4U1145-619. The model is as described in Section 4-2, the power-law gradient $n$ = 2.0, the outflow velocity at the stellar surface has been varied from 0 to 1000 km s$^{-1}$.

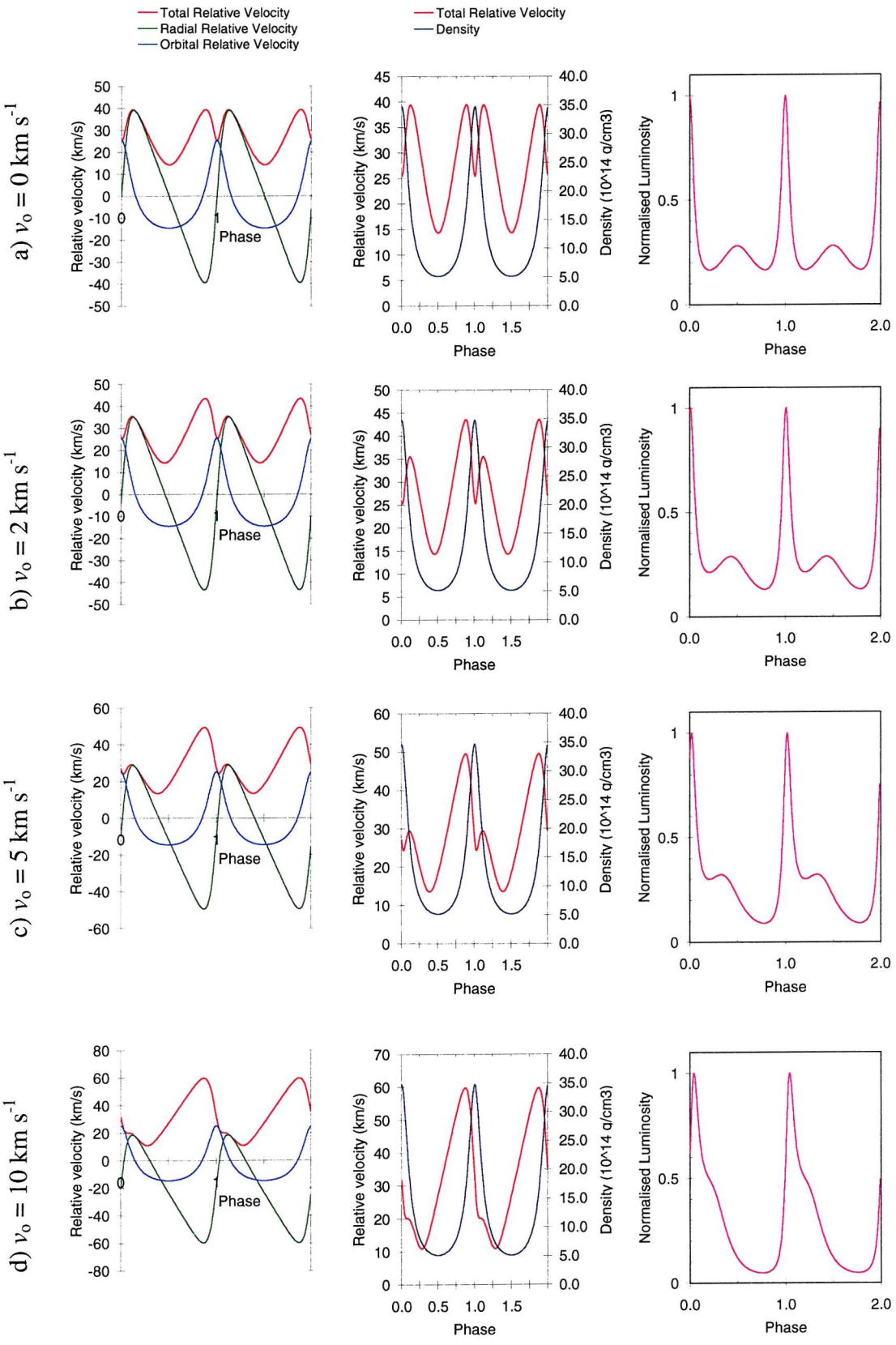


**Figure 4-3.** ***Continued overleaf…***

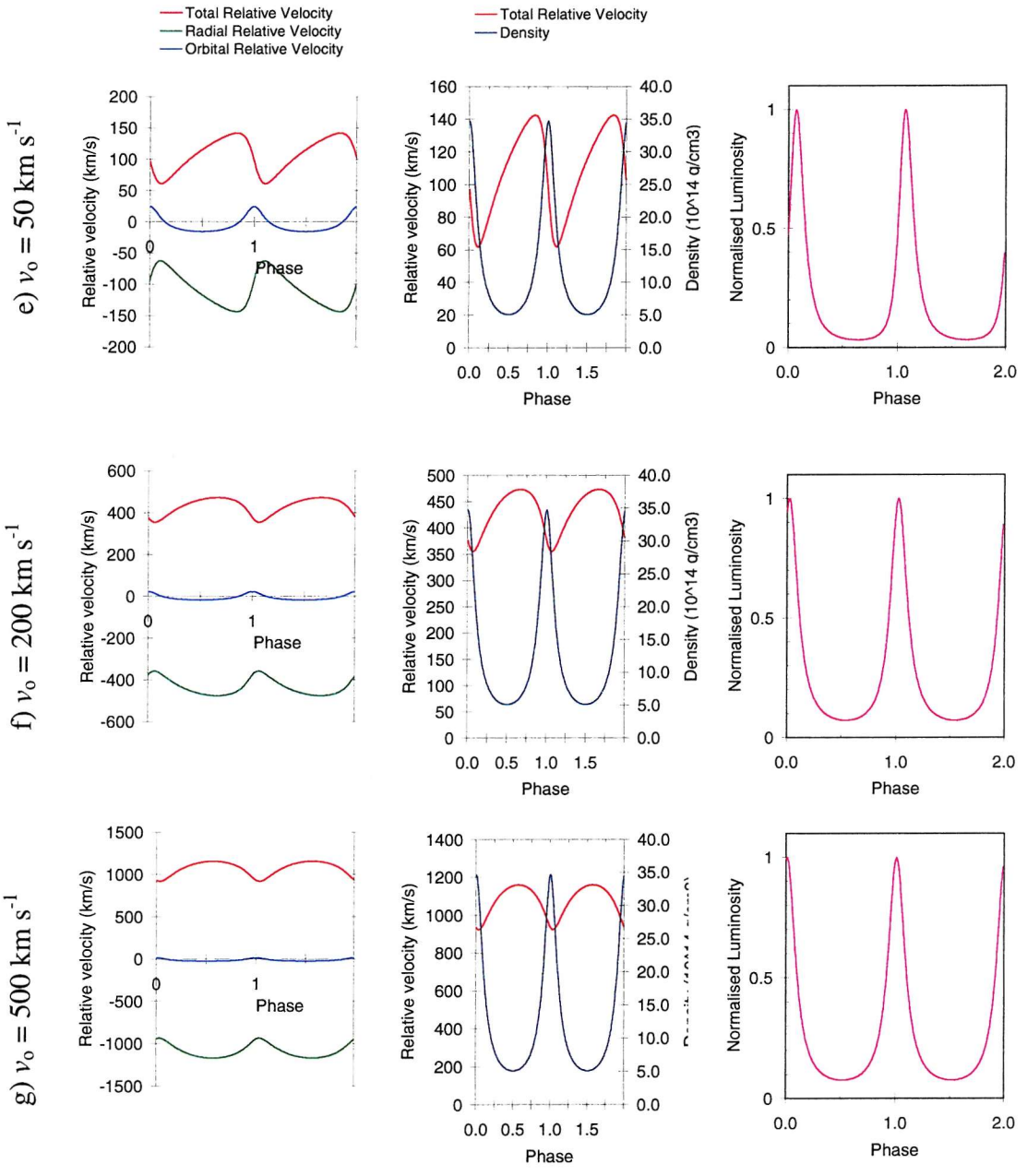


**Figure 4-3.** X-ray lightcurve model predictions for a system with orbital parameters equal to those of the Be/X-ray binary 4U1145-619. The model is as described in Section 4-2, the power-law gradient $n$ = 2.25, the outflow velocity at the stellar surface has been varied from 0 to 500 km s$^{-1}$.

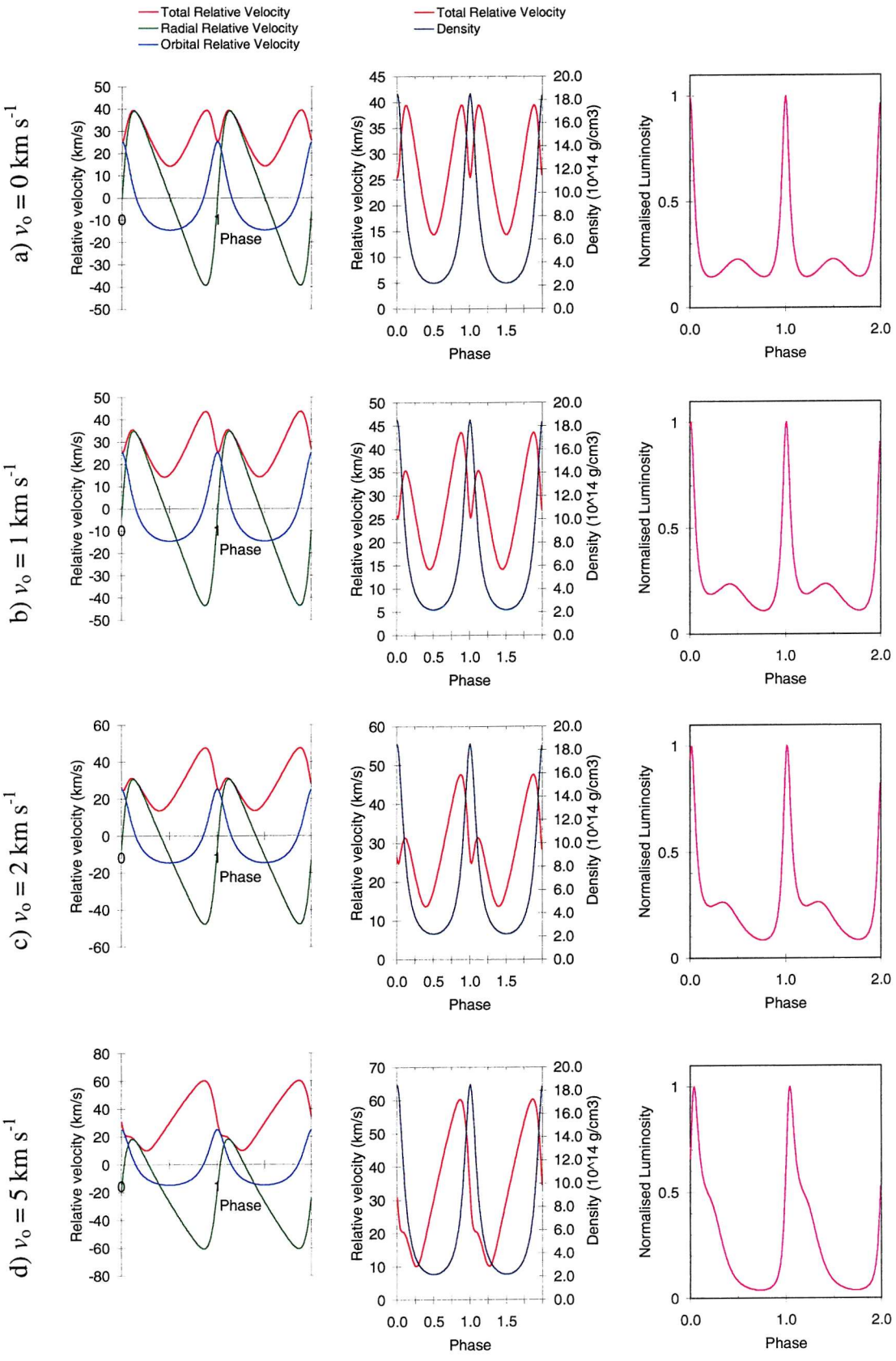


**Figure 4-4.** ***Continued overleaf…***

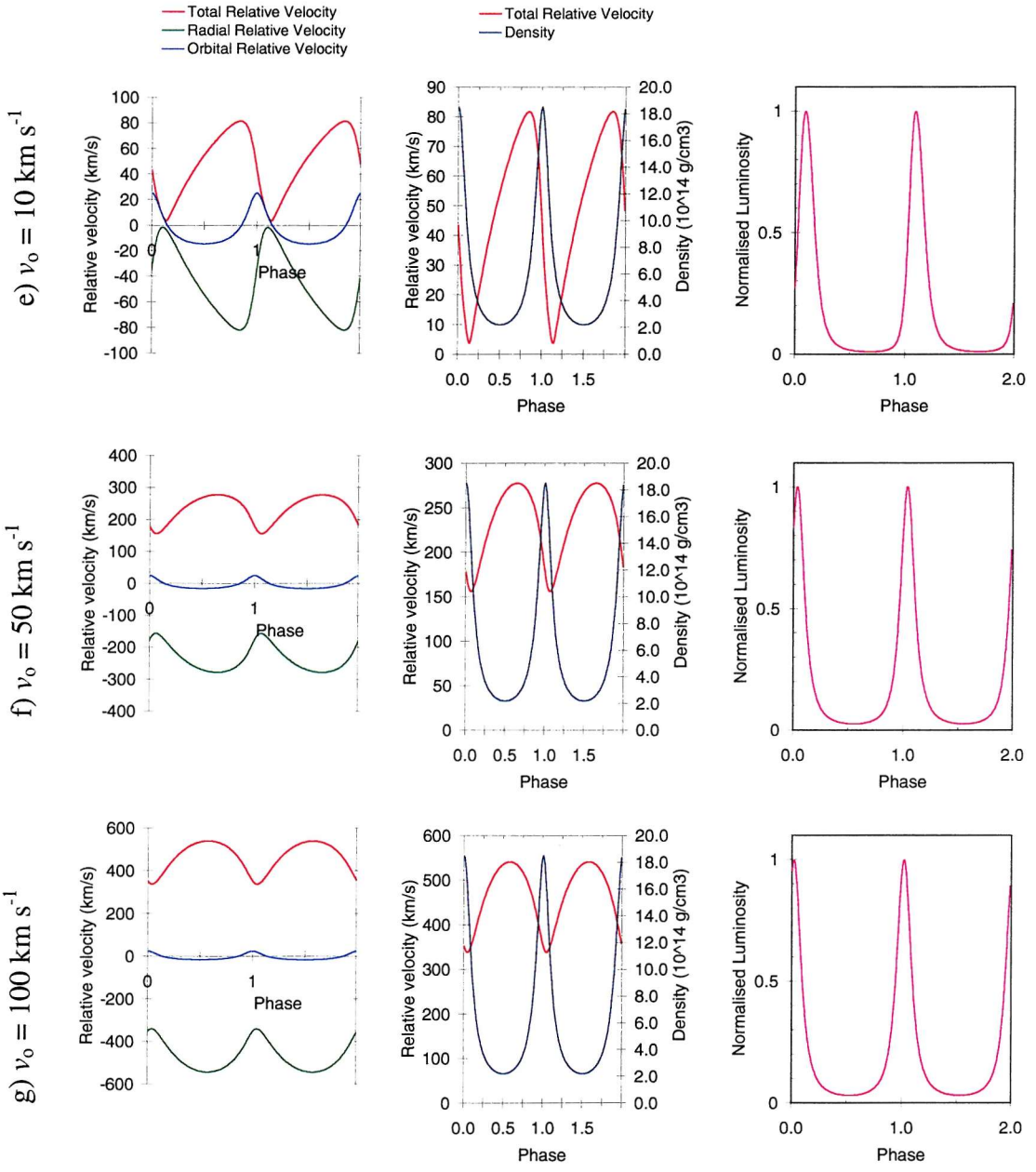


**Figure 4-4.** X-ray lightcurve model predictions for a system with orbital parameters equal to those of the Be/X-ray binary 4U1145-619. The model is as described in Section 4-2, the power-law gradient $n$ = 2.5, the outflow velocity at the stellar surface has been varied from 0 to 100 km s$^{-1}$.

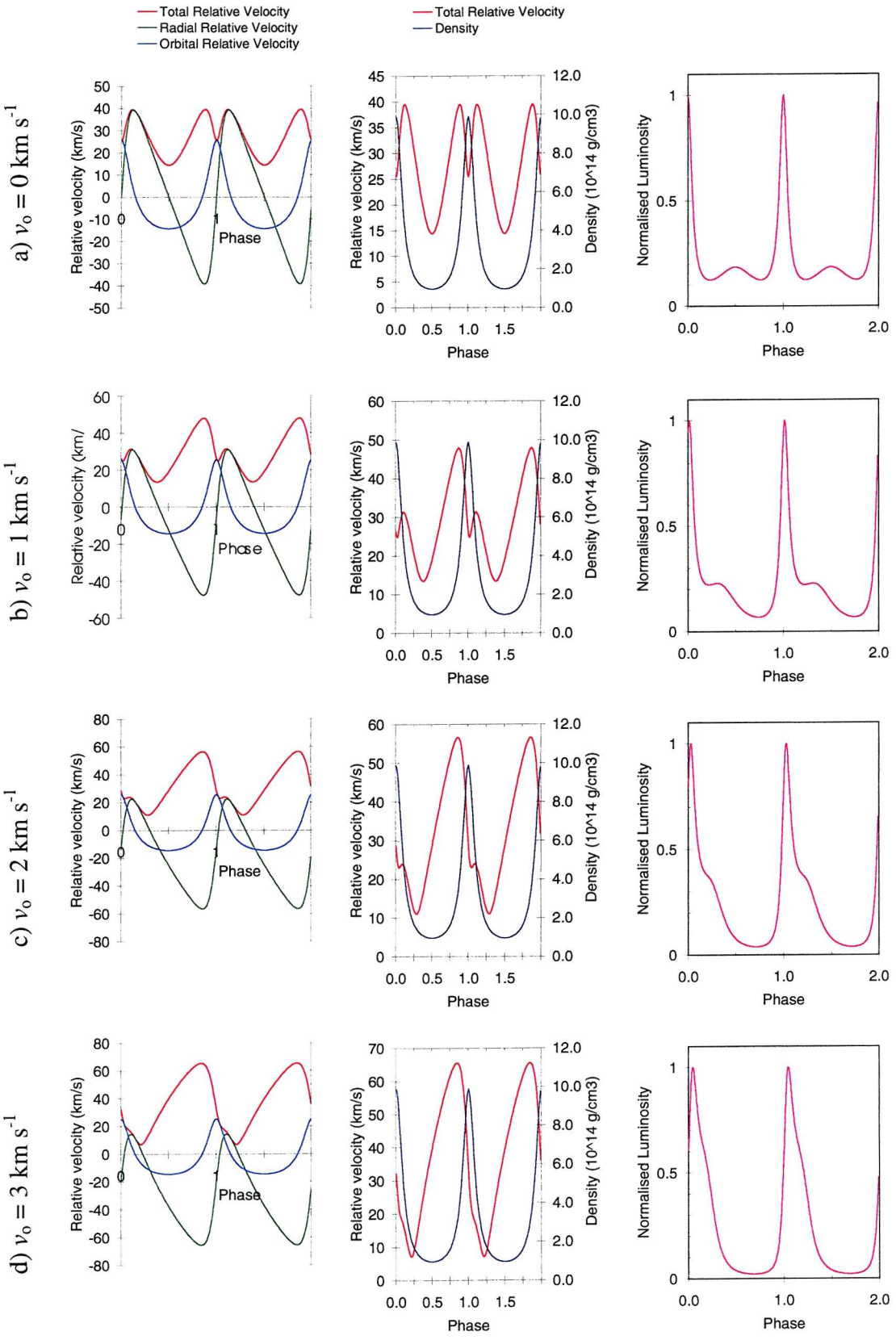


**Figure 4-5.** ***Continued overleaf…***

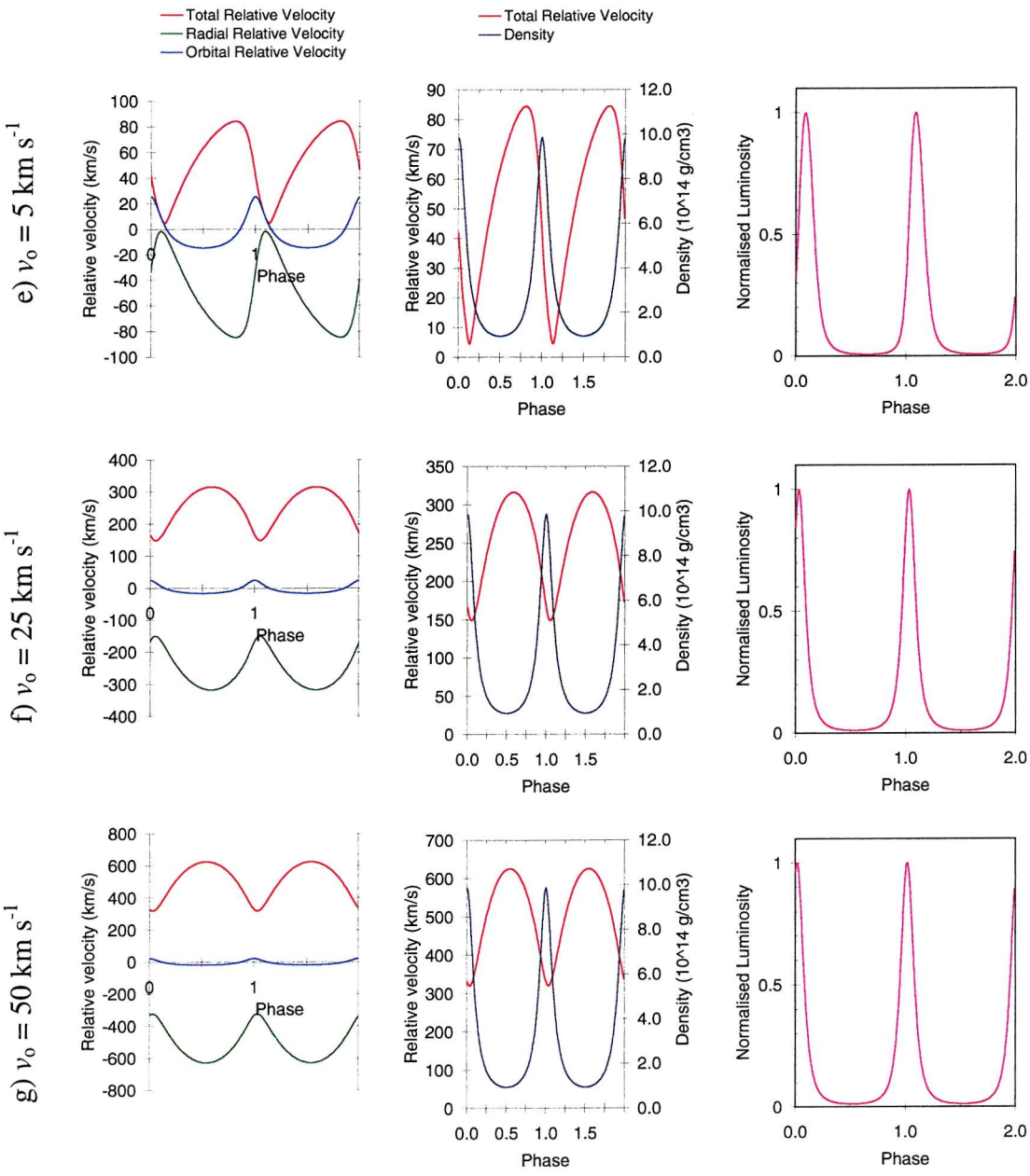


**Figure 4-5.** X-ray lightcurve model predictions for a system with orbital parameters equal to those of the Be/X-ray binary 4U1145-619. The model is as described in Section 4-2, the power-law gradient $n$ = 2.75, the outflow velocity at the stellar surface has been varied from 0 to 50 km s$^{-1}$.

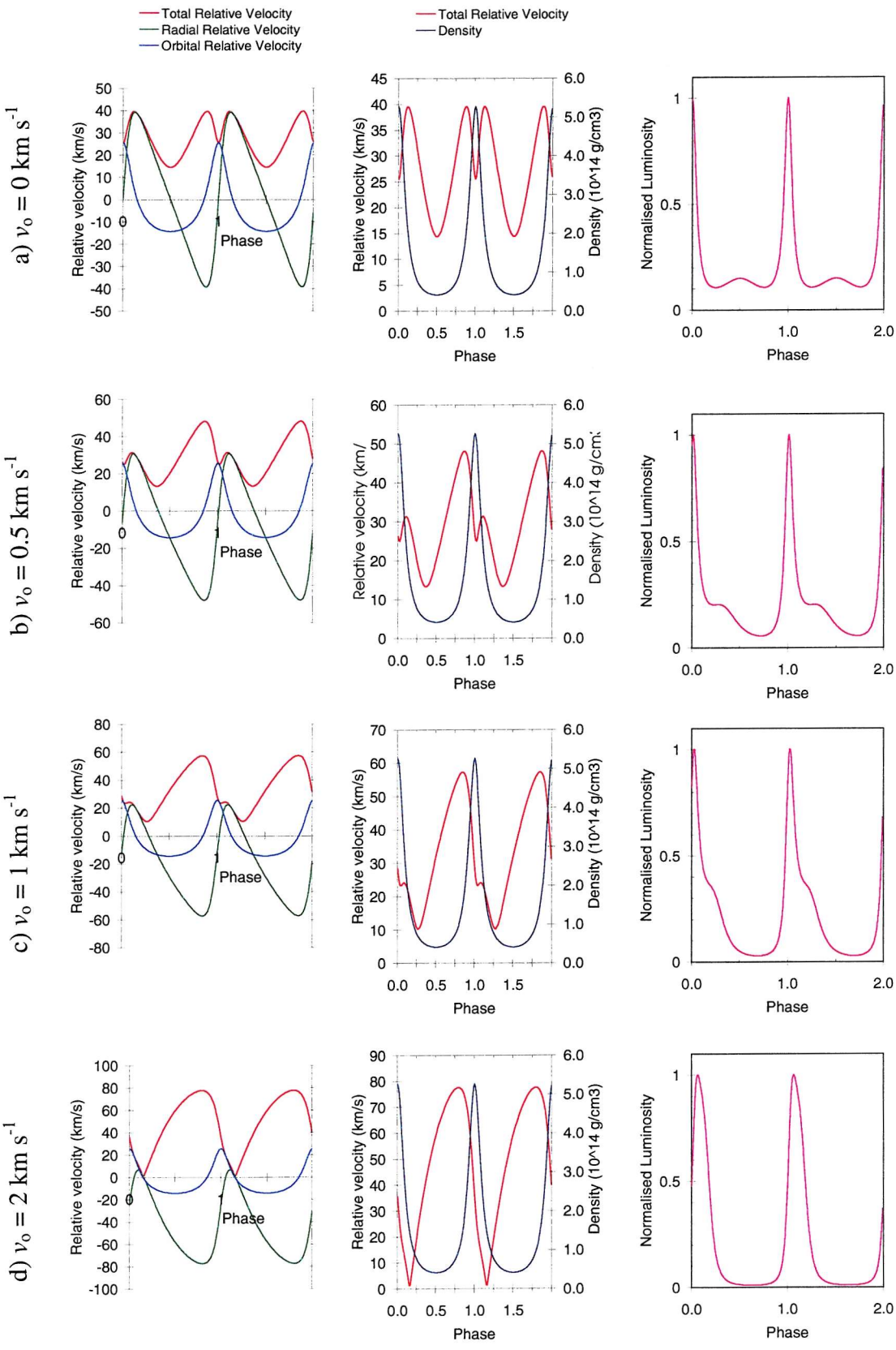


**Figure 4-6.** ***Continued overleaf…***

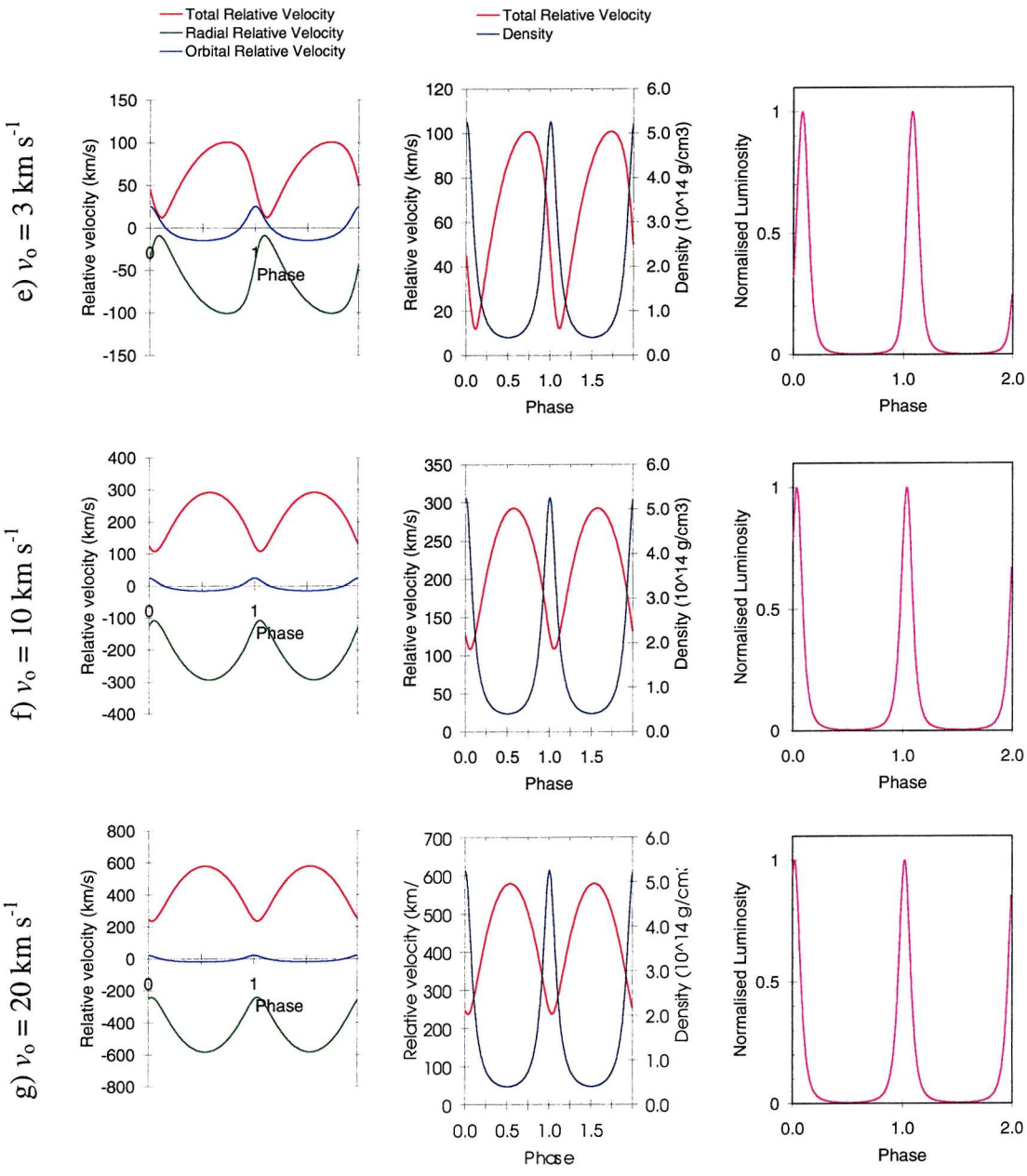


**Figure 4-6.** X-ray lightcurve model predictions for a system with orbital parameters equal to those of the Be/X-ray binary 4U1145-619. The model is as described in Section 4-2, the power-law gradient $n = 3$, the outflow velocity at the stellar surface has been varied from 0 to 20 km s$^{-1}$.

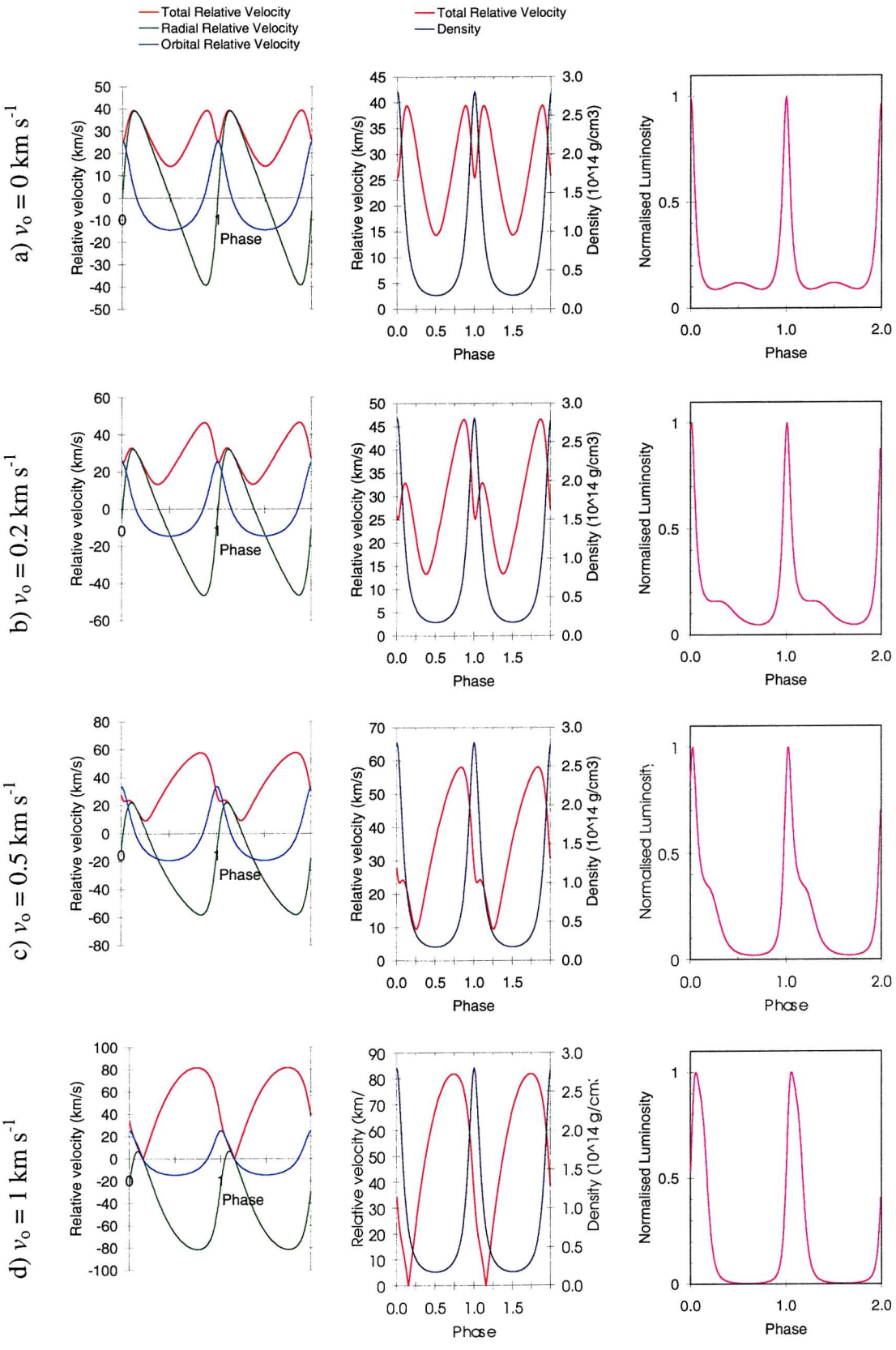


**Figure 4-7.** ***Continued overleaf…***

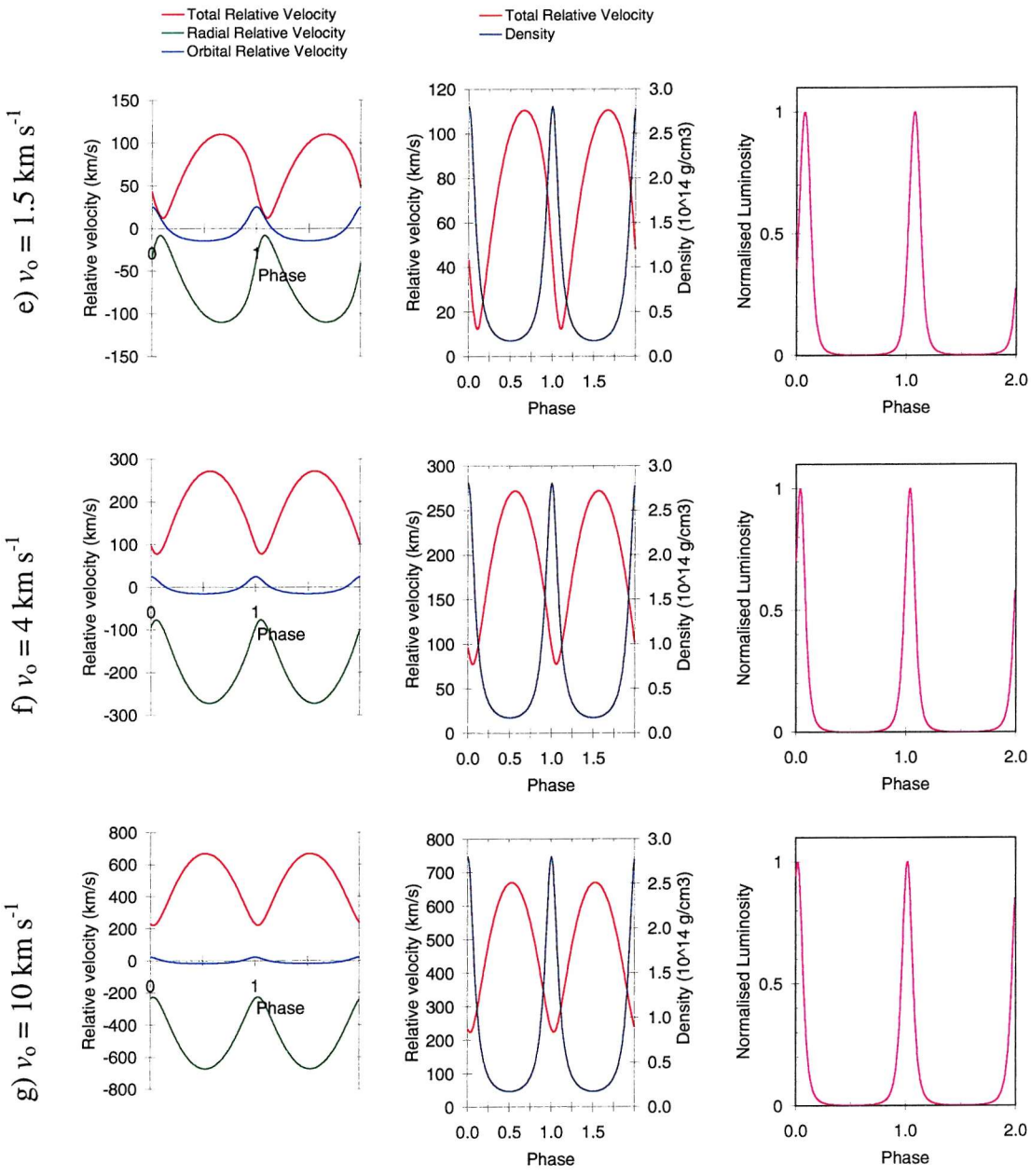


**Figure 4-7.** X-ray lightcurve model predictions for a system with orbital parameters equal to those of the Be/X-ray binary 4U1145-619. The model is as described in Section 4-2, the power-law gradient $n$ = 3.25, the outflow velocity at the stellar surface has been varied from 0 to 10 km s$^{-1}$.

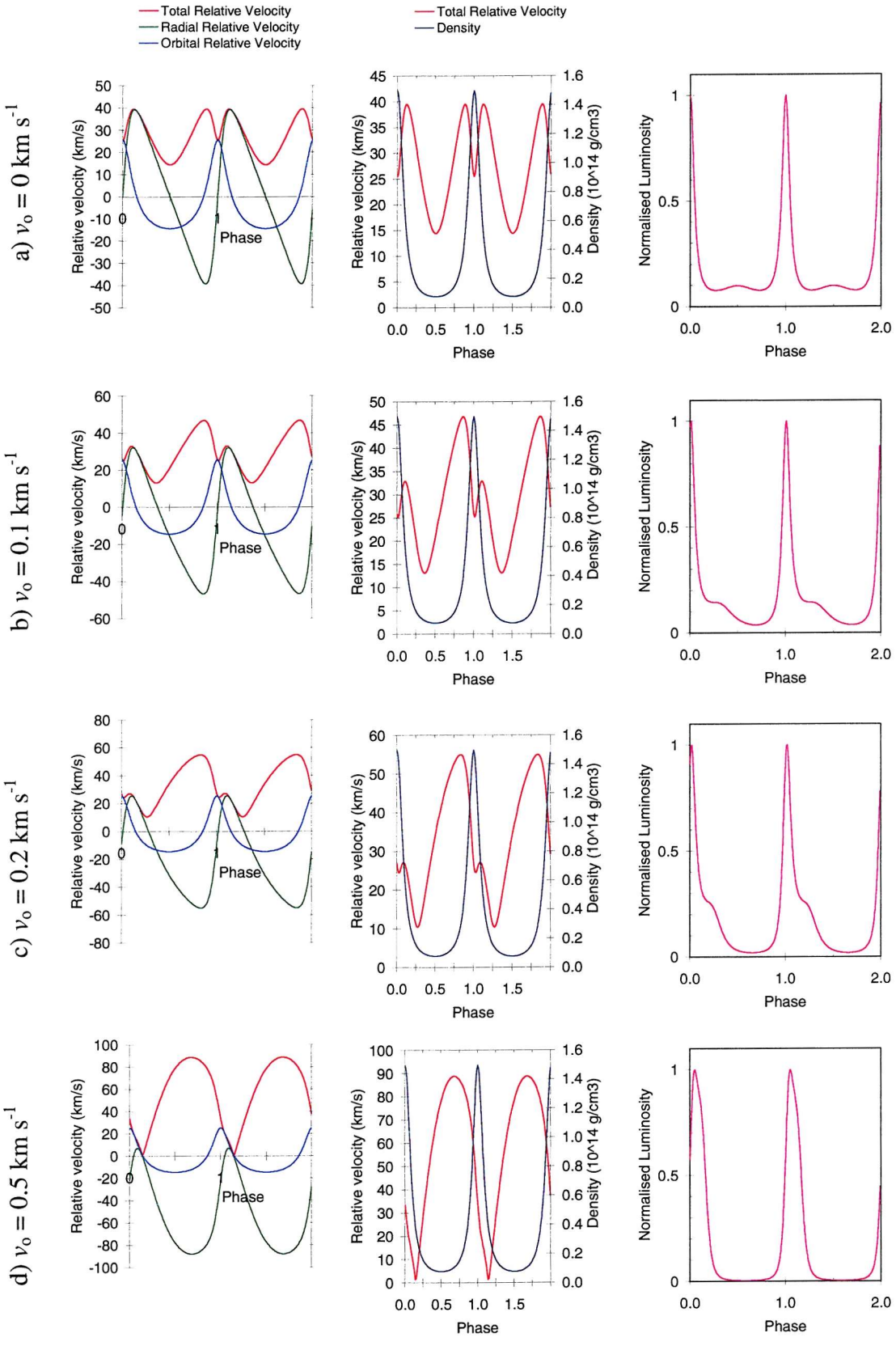


**Figure 4-8.** ***Continued overleaf…***

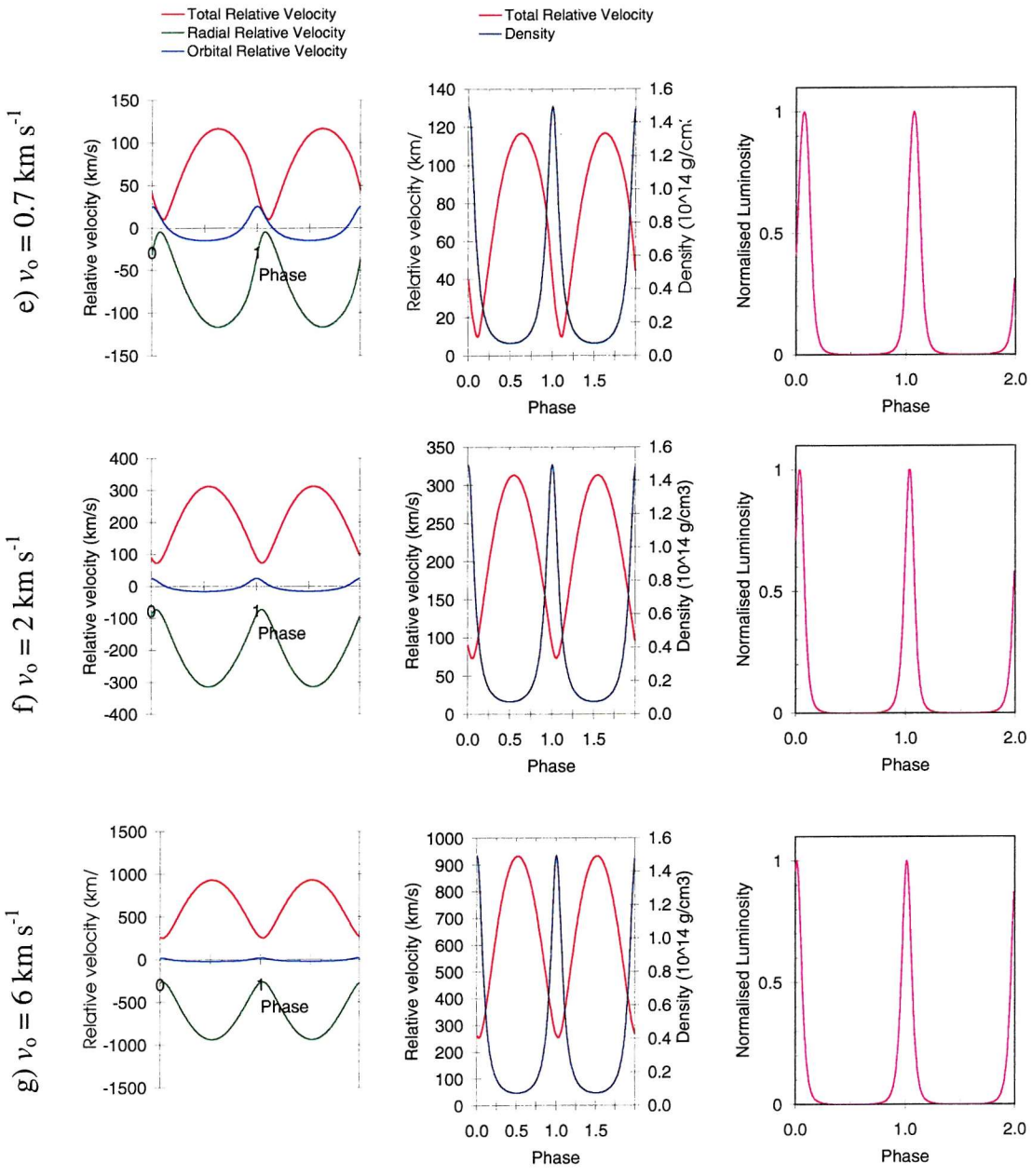


**Figure 4-8.** X-ray lightcurve model predictions for a system with orbital parameters equal to those of the Be/X-ray binary 4U1145-619. The model is as described in Section 4-2, the power-law gradient $n$ = 3.5, the outflow velocity at the stellar surface has been varied from 0 to 6 km s$^{-1}$.

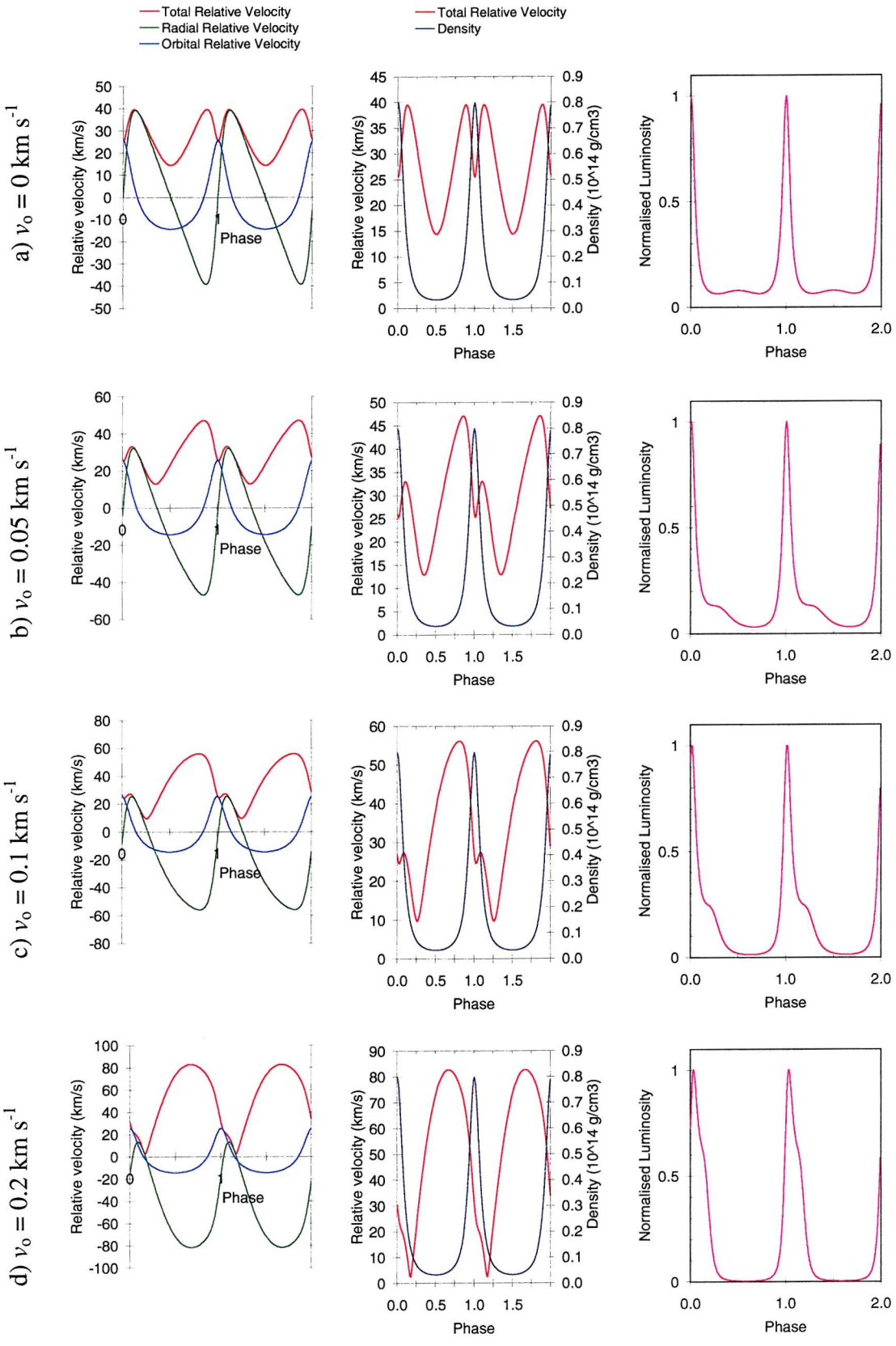


**Figure 4-9.** ***Continued overleaf…***

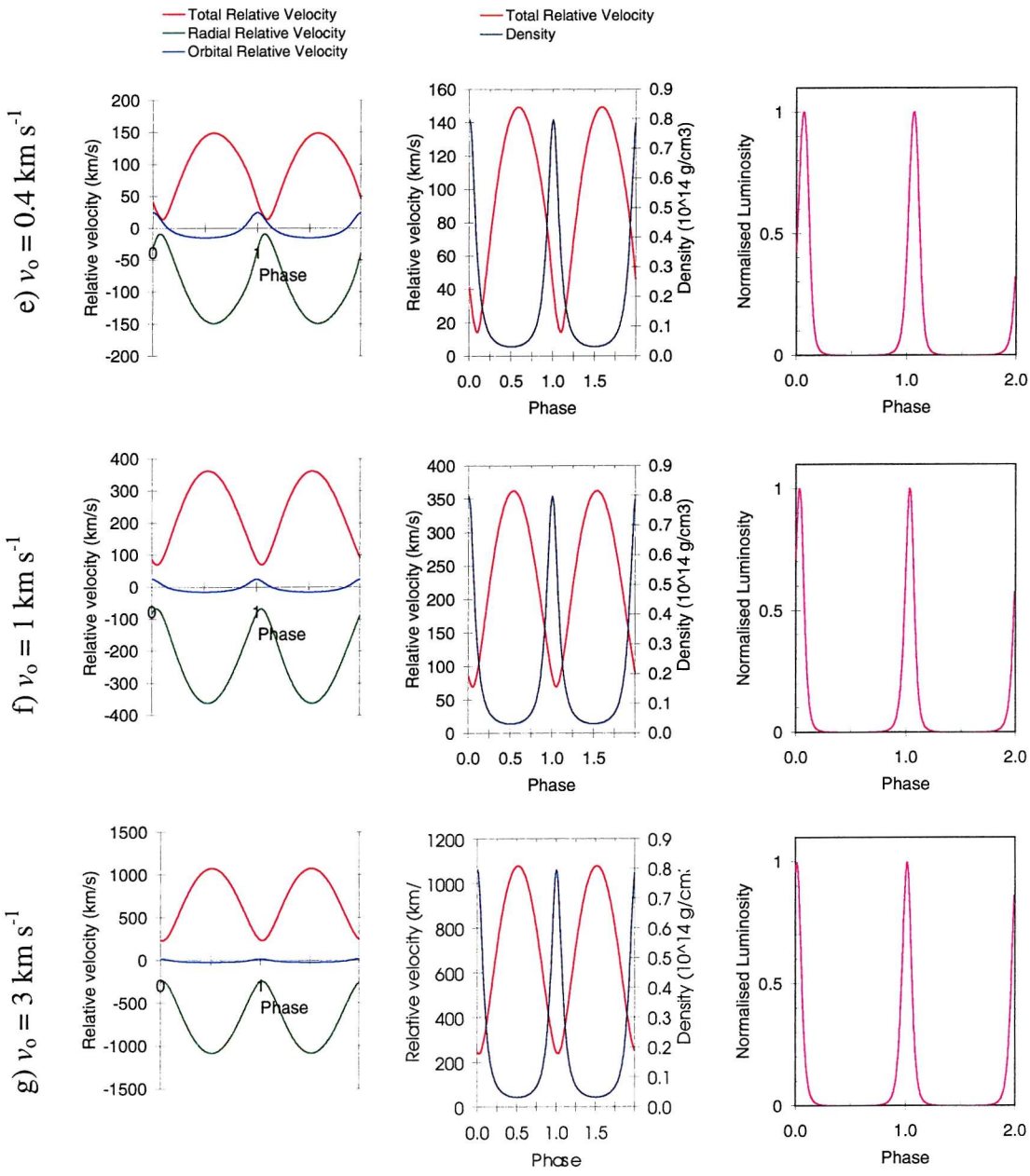


**Figure 4-9.** X-ray lightcurve model predictions for a system with orbital parameters equal to those of the Be/X-ray binary 4U1145-619. The model is as described in Section 4-2, the power-law gradient $n$ = 3.75, the outflow velocity at the stellar surface has been varied from 0 to 3 km s$^{-1}$.

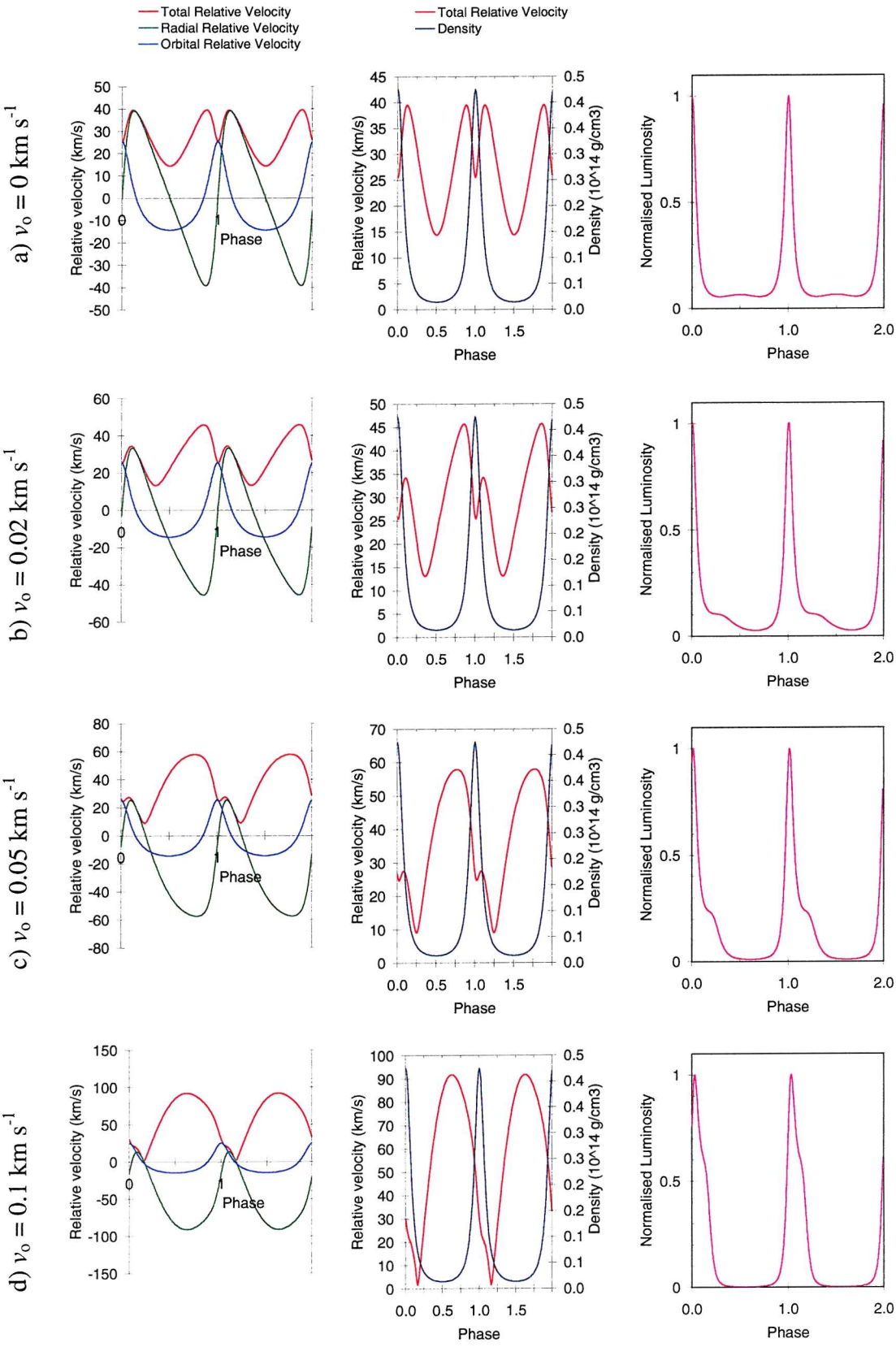


**Figure 4-10.** ***Continued overleaf…***

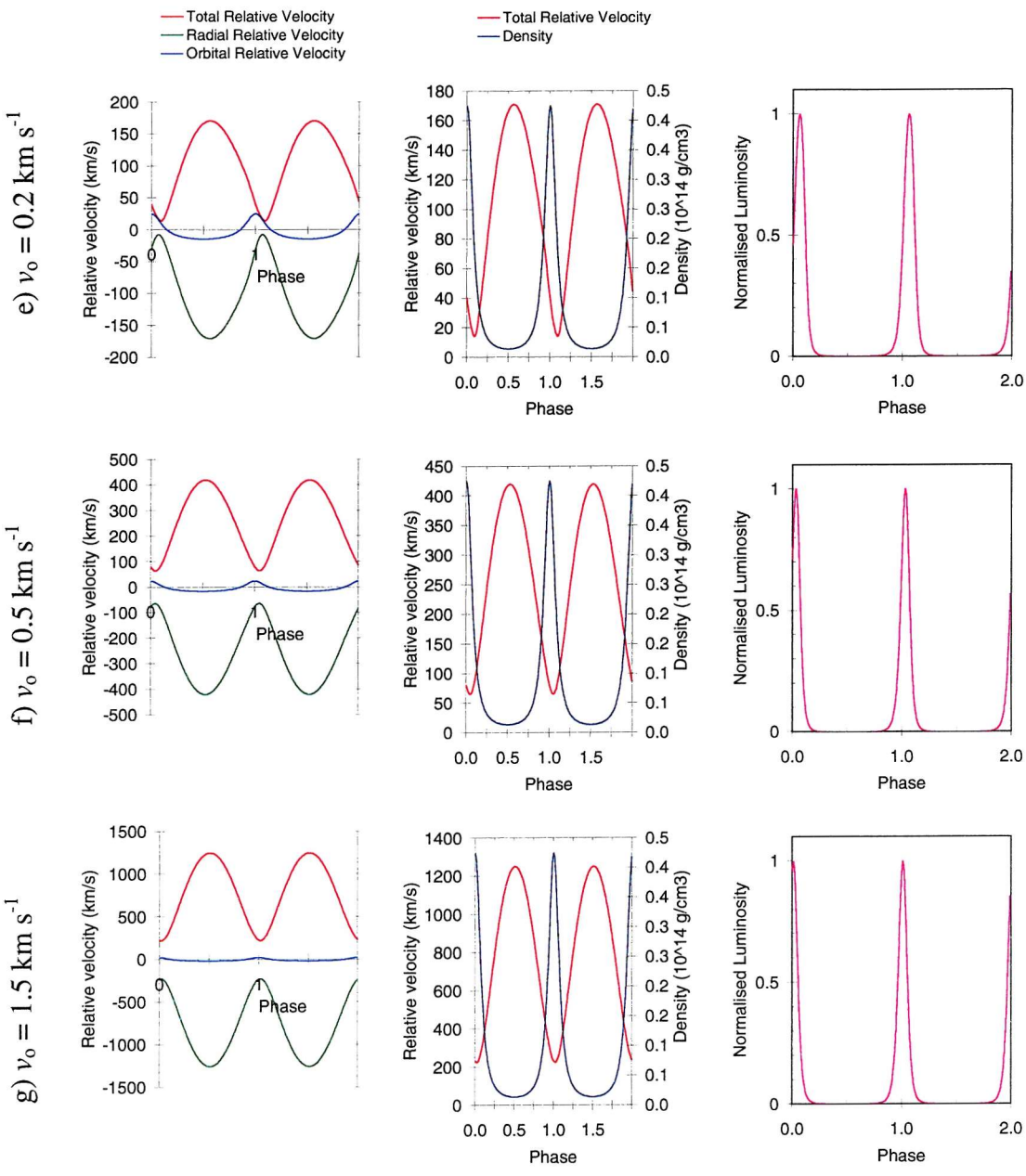


**Figure 4-10.** X-ray lightcurve model predictions for a system with orbital parameters equal to those of the Be/X-ray binary 4U1145-619. The model is as described in Section 4-2, the power-law gradient $n$ = 4, the outflow velocity at the stellar surface has been varied from 0 to 1.5 km s$^{-1}$.

One result which stands out is that at for each value of $n$, extreme values of $v_0$ produce symmetric lightcurves, while intermediate values produce assymmetric lightcurves. The reason for this is that low values of $v_0$ produce lightcurves dominated by orbital motion only, with X-ray maxima when the neutron star's radial velocity with respect to the Be star is zero. With large values of $v_o$, the lightcurves are dominated by the wind outflow velocity, with maxima occurring at periastron when the density is greatest, and where the wind has not yet been accelerated to even greater velocities.

Larger values of $n$ lead to greater wind acceleration, hence as $n$ is increased, the velocity $v_0$ required to produce the symmetric, outflow dominated lightcurves decreases. With $n$ = 2, these lightcurves are produced with initial outflow velocities of ~500 km $s^{-1}$, with $n$ = 4, initial outflow velocities of only 0.2 km $s^{-1}$ lead to similar shaped lightcurves.

#### 4.3.1.2 Disc sound speed/temperature

With the orbital parameters fixed in the model as described in Table 4-1, the wind parameters were then varied in the following ways:

- The power law gradient was kept constant at $n$ = 2.0, and the initial outflow velocity fixed at 0 km s $^{-1}$, the sound speed was then varied from 25 km $s^{-1}$ to 100 km $s^{-1}$.
- The power law gradient was kept constant at $n$ = 2.0, and the initial outflow velocity fixed at 1km s $^{-1}$, the sound speed was then varied from 25 km $s^{-1}$ to 100 km $s^{-1}$.
- The power law gradient was kept constant at $n$ = 3.0, and the initial outflow velocity fixed at 0 km s $^{-1}$, the sound speed was then varied from 25 km $s^{-1}$ to 100 km $s^{-1}$.
- The power law gradient was kept constant at $n$ = 3.0, and the initial outflow velocity fixed at 1 km s $^{-1}$, the sound speed was then varied from 25 km $s^{-1}$ to 100 km $s^{-1}$.

The resulting predicted lightcurves are shown in Figure 4-11. Whatever the chosen parameters of wind dynamics, in each case a disc with a higher sound speed – indicating a higher temperature – produces a simple lightcurve, symmetrical about orbital phase $\varphi = 0$, and with a single luminosity maximum at periastron.

This is because the accretion flow in high sound speed disks is pressure limited; the minimum in relative velocity between Neutron star and disc material seen to occur at apastron (see for example the plots of density and relative velocity in Figures 4-2 to 4-10) does not affect the accretion rate significantly – the modulation of the X-ray luminosity is more closely related to the varying density of material encountered by the neutron star.

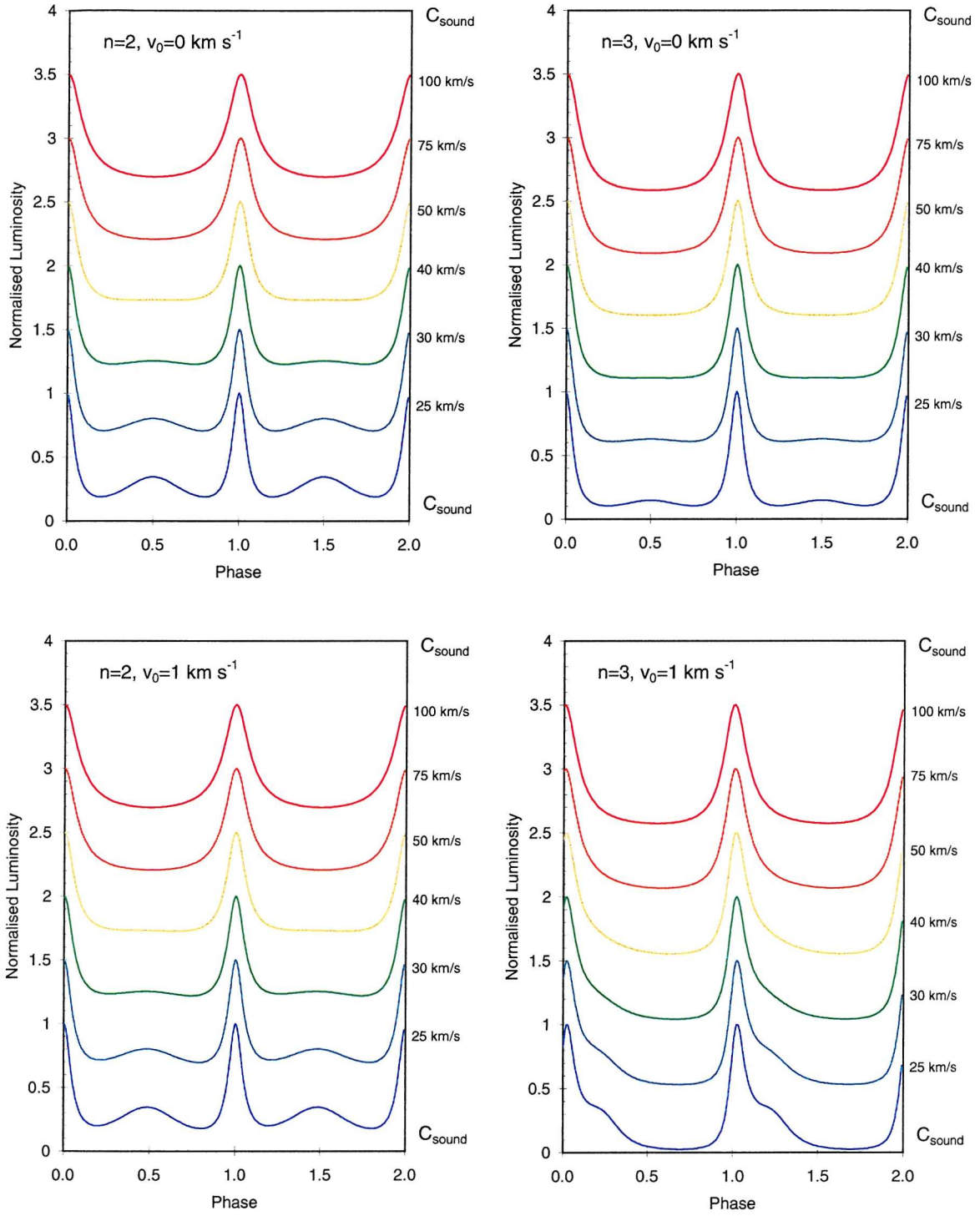


**Figure 4-11.** X-ray lightcurve model predictions for various adopted sound speeds in the Be star disc.

#### 4.3.1.3 Disc rotation model

With the orbital parameters fixed in the model as described in Table 4-1, the wind parameters were then varied in the following ways:

- The power law gradient of the disc density and velocity model was kept constant at $n = 3.0$, and the initial outflow velocity fixed at 1 km s $^{-1}$. The value of $\alpha$ (the density power law gradient) was varied from –0.5 (Keplerian disc) to –1 (conservation of angular momentum in out-flowing material).

The resulting predicted lightcurves are shown in Figure 4-12. At first, as $\alpha$ is decreased from –0.5 a secondary peak grows in strength at orbital phase $\varphi \sim 0.25$. This peak becomes stronger than the peak at periastron and eventually reaches a maximum in strength relative to the periastron peak when $\alpha \sim -0.65$. As $\alpha$ is decreased further, the secondary peak decreases in relative strength, until once again the periastron peak is stronger.

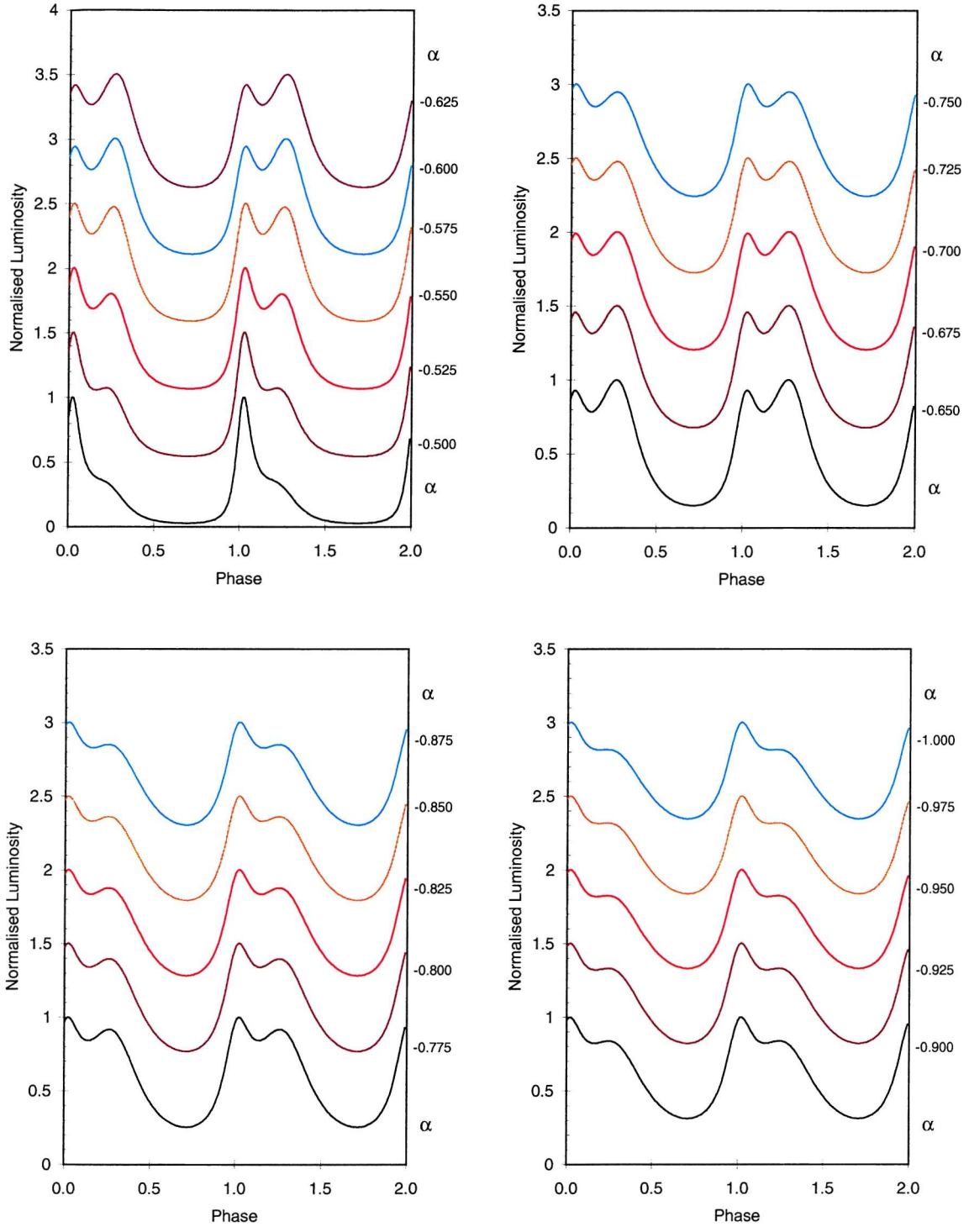


**Figure 4-12.** X-ray lightcurve model predictions for different models of rotational velocity in the Be star disc. In each case the orbital parameters of the systems have been chosen equal to those of the Be/X-ray binary 4U1145-619, the power-law gradient $n$ = 3.0, and the initial outflow velocity of the Be star's wind $v_0$ = 1.0 km s$^{-1}$. The value of α has been varied from -0.5 (Keplerian disc) to –1.0 (conservation of angular momentum in the out-flowing material).

### 4.3.2 Dependence on orbital parameters

To investigate the effects of orbital parameters on the predicted lightcurves, the orbital parameters were varied for a number of chosen disc models. In the following sections, first the effects of orbital eccentricity and then orbital period were investigated.

#### 4.3.2.1 Orbital eccentricity

In order to investigate the effects of orbital eccentricity on the predicted lightcurves, the following models were produced, assuming a Keplerian disc ($\alpha = -0.5$):

- The power law gradient was fixed at a value of $n = 2.0$ and the initial outflow velocity at 0 km s $^{-1}$, the eccentricity was varied from 0 to 0.5
- The power law gradient was fixed at a value of $n = 2.0$ and the initial outflow velocity at 1 km s $^{-1}$, the eccentricity was varied from 0 to 0.5
- The power law gradient was fixed at a value of $n = 3.0$ and the initial outflow velocity at 0 km s $^{-1}$, the eccentricity was varied from 0 to 0.5
- The power law gradient was fixed at a value of $n = 3.0$ and the initial outflow velocity at 1 km s $^{-1}$, the eccentricity was varied from 0 to 0.5

The resulting lightcurves are shown in Figure 4-13. In each case, the effect of increasing eccentricity is to increase the degree of orbital modulation. Also of note is the effect of eccentricity on the symmetry of lightcurves when the wind material has a finite outflow velocity.

*No wind acceleration*

In the case of $n = 2.0$, there is no acceleration of the wind – the material flows outwards at a constant velocity. At large eccentricities, the modulation of the lightcurve is dominated by the variation in density and the radial motion of the neutron star with respect to the Be star – at periastron and apastron where the radial motion

becomes zero, a maximum in luminosity is seen. The relative strength of the periastron peak to the apastron peak increases with increasing eccentricity as the modulation of density increases.

At low eccentricities the radial motion of the neutron star is small, and comparable to the outflow velocity of the wind material. In this regime, the lightcurve becomes asymmetrical as between $\varphi = -0.5$ and $\varphi = 0$ the neutron star's radial motion is of opposite sign to the outflow velocity of the wind, leading to a greater relative velocity than between $\varphi = 0$ and $\varphi = 0.5$ where the two velocity components are of the same sign.

*Constant wind acceleration*

However, in the case of $n = 3.0$, there is a constant acceleration of the wind, so that the larger the eccentricity, the more the lightcurve is dominated by the variations around the orbit of the wind outflow velocity. Secondary luminosity maxima at apastron are not seen, as although the radial motion of the neutron star goes to zero at this point, the outflow velocity of the wind encountered by the neutron star is maximum, so no minimum in total relative velocity is seen.

At low eccentricities, the lightcurve is less dominated by variations in density, and shows a symmetric lightcurve shifted to peak at phase $\varphi \sim 0.1$ as the radial motion of the neutron star at this phase cancels the outflow velocity of the wind.

At larger eccentricities, a strong maximum is seen at periastron, as modulation of the outflow velocity of the wind and the density become more significant. A shoulder appears in this peak at phase $\varphi \sim 0.1$ where the radial motion of the neutron star at this phase cancels the outflow velocity of the wind.

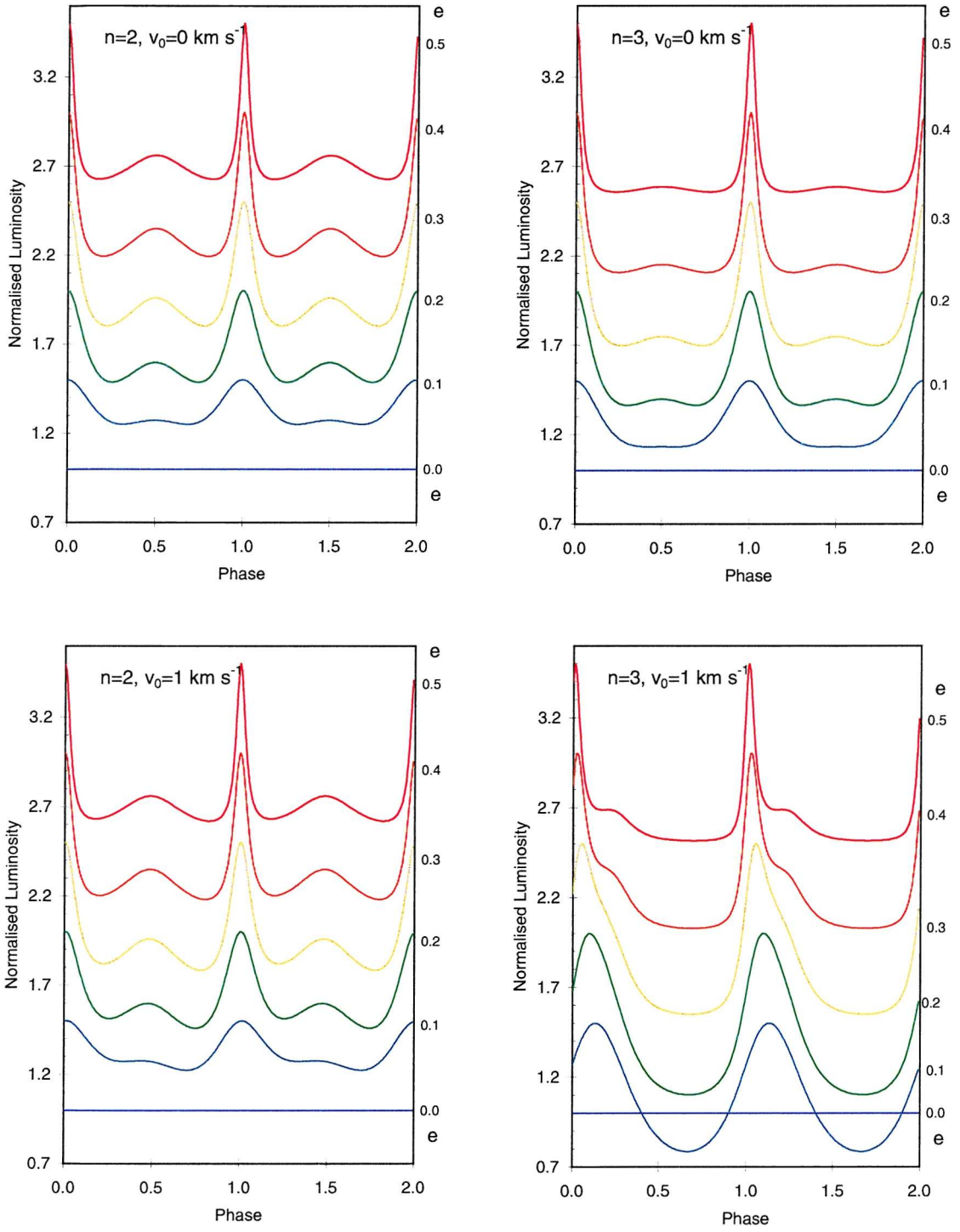


**Figure 4-13.** X-ray lightcurve model predictions for various orbital eccentricities. In each plot, the orbital parameters (except eccentricity) have been chosen equal to those of the Be/X-ray binary 4U1145-619, the wind parameters – annotated on each plot – were kept constant, and the orbital eccentricity varied from 0 to 0.5.

#### 4.3.2.2 Orbital period

In order to investigate the effects of orbital period (and hence orbital separation) on the lightcurves produced by the model, the disc model was fixed and the orbital period input to the model varied between 10 days and 180 days. The resulting lightcurves are shown in Figure 4-14.

At shortest extreme of orbital period the lightcurves are symmetric, with a strong maximum at phase $\varphi = 0$ and a secondary weaker maximum at phase $\varphi = 0.5$. As the orbital period is increased, this secondary maximum shifts to earlier orbital phases, and the periastron maximum shifts to later orbital phases until when we input an orbital period of ~ 90 days, the secondary peak is more of a shoulder in the stronger peak which occurs at phase $\varphi \sim 0.05$. When a period as large as 180 days is input to the model, only a single maximum is seen to occur at phase $\varphi \sim 0.1$.

The shift to earlier phases of the secondary peak can be understood when the relative motion of the neutron star to the wind is considered in the radial direction only. At phase $\varphi = 0.5$ the radial motion of the neutron star is zero, yet the wind has some outflow velocity. At phases slightly earlier than phase $\varphi = 0.5$ the neutron star has some radial motion that will cancel the outflow velocity of the wind. The wider the orbit of the system, the larger the outflow velocity of the wind encountered by the neutron star at any given orbital phase as the wind will have been accelerated over a larger distance. Hence the phase at which the radial velocity of the neutron star cancels the outflow velocity of the wind becomes earlier as the orbit is widened.

At very large orbital periods, the neutron star encounters material that has been accelerated to such an extent that the radial motion of the neutron star is only comparable to the wind outflow velocity close to periastron when the neutron star is at its closest to the Be star. The wind outflow dominates the lightcurve shape and no secondary maximum is seen near apastron. A single maximum is seen at phase $\varphi \sim 0.1$. The slight shift from periastron is due to the outflow velocity of the wind being partially cancelled by the radial velocity of the neutron star.

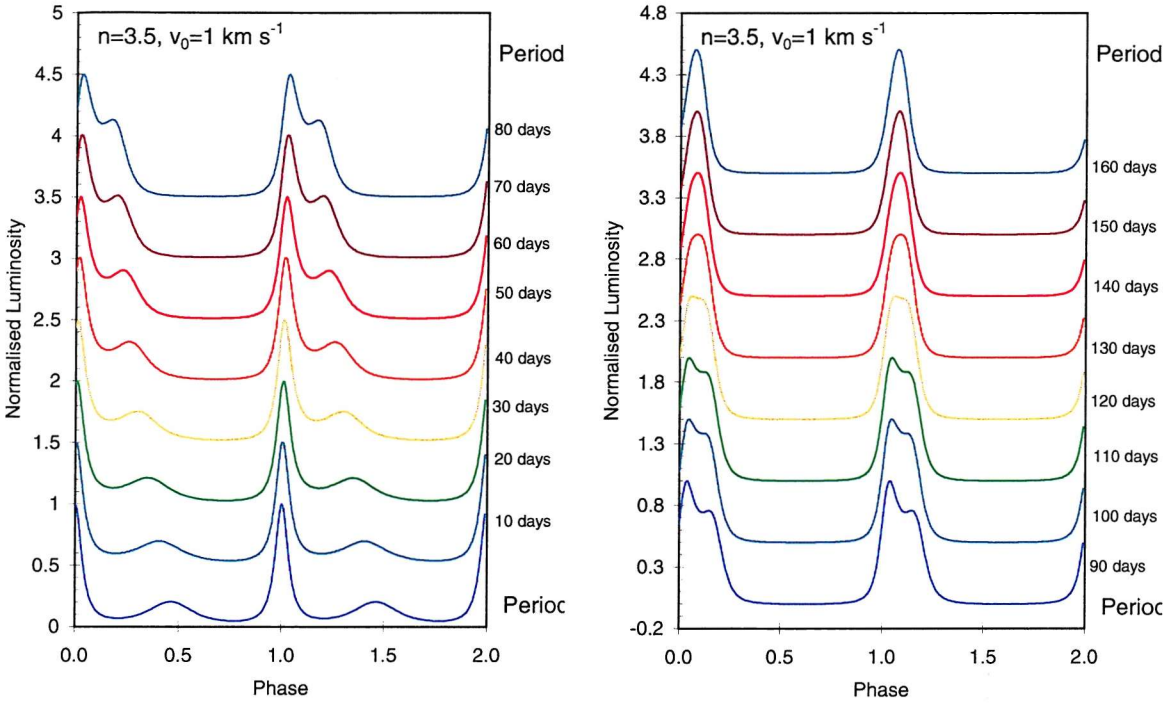


**Figure 4-14.** X-ray lightcurve model predictions for various adopted orbital periods. In each case the initial outflow velocity was kept constant at 1 km $s^{-1}$ and the disc power-law gradient constant at $n = 3.5$.

## 4.4 Modelling the X-ray lightcurve of EXO 2030+375

In the following sections I describe attempts to explain observed lightcurves of the Be/X-ray binary EXO 2030+375 in terms of the model developed earlier in this chapter. The work presented in this section was published in Reig, Stevens & Coe et al. 1998.

### 4.4.1 Source history

The high mass X-ray transient EXO 2030+375 was first detected at X-ray wavelengths in 1985 May 17 during a slew of the EXOSAT satellite. Subsequent pointed

observations revealed the X-ray flux to be strongly modulated with a period of ~ 41.7 s (Parmar et al. 1989). In the X-ray band, EXO 2030+375 shows variability on all timescales. It is a transient X-ray source that alternates between active and inactive periods (Reig & Coe 1998a, hereafter Paper I).

The X-ray activity of EXO 2030+375 consists of periodic outbursts, modulated with the orbital period of 46.02 d (Stollberg 1997) and unpredictable outbursts showing no modulation on orbital period. The former type of outbursts is thought to occur at each periastron passage of the neutron star. These outbursts last for 8 – 10 days and the X-ray luminosity increases by a factor $\leq 10$. The latter outbursts are giant outbursts that do not correlate with the orbital phase but tend to last for several orbital cycles. The X-ray luminosity during these outbursts may reach $10^{38}$ erg $s^{-1}$, close to the Eddington luminosity.

In common with other high-mass X-ray binaries, the continuum spectral shape in the range 1-25 keV can be represented by a power-law spectrum with an exponential cut-off, coupled with a low-energy absorption and, an iron emission line at $\approx$ 6.4-6.6 keV (Reynolds et al. 1993). A two X-ray continuum component model, also including a blackbody component was seen to give acceptable fits by Sun et al. (1994) and Reig & Coe (1998b) (hereafter, Paper II).

Optical CCD photometry (Motch & Janot-Pacheco 1987) and optical spectroscopy and infrared photometry (Coe et al. 1985; 1988) of the counterpart revealed a highly reddened ($E(B\text{-}V) = 3.80 \pm 0.15$) V $\approx$ 20 star showing an infrared excess and H$\alpha$ in emission. These observational characteristics of the counterpart, along with the X-ray behaviour, identified EXO 2030+375 as a Be/X-ray binary system.

### 4.4.2 The X-ray lightcurve of EXO 2030+375

A plot of X-ray transient outbursts detected by *BATSE* was shown in Figure 2-12. The plot shows how a series of transient outbursts by EXO 2030+375 was detected by *BATSE* up to August 1993. Between August 1993 and April 1996 no outbursts

were detected at all. From April 1996 onwards, outbursts were detected once again, at intervals coinciding with the orbital period.

The *BATSE* pulsed limiting flux is ~ 4.2 x $10^{-10}$ erg $s^{-1}$ $cm^{-2}$, in the energy range 20-50 keV. The X-ray flux during a normal outburst is typically one order of magnitude higher. In the present work we have made use of two years worth of data (1996-1998 February) from the *RXTE All Sky Monitor* (*ASM*). See Bradt et al. (1993) for the details on this instrument. Analysis of data obtained with the *RXTE's ASM* reveals that by folding the lightcurve of EXO 2030+375 at the orbital period, a second intensity peak coincident with *apastron* passage of the neutron star is apparent. The X-ray intensity at apastron is about one third of that at periastron, but is detected at ~ 3σ significance level above quiescent flux.

Figure 4-15 shows the ASM XTE lightcurve folded onto the orbital period (46.02 d). One-day average fluxes were folded on the period of 46.02 days and re-binned with a bin size of 0.04 in phase. The lightcurve is normalised to the maximum flux value. The two intensity maxima are clear, one at periastron, one at apastron. There is no significant shift in the phase of the observed maxima from phases $\varphi = 0$ and $\varphi = 0.5$.

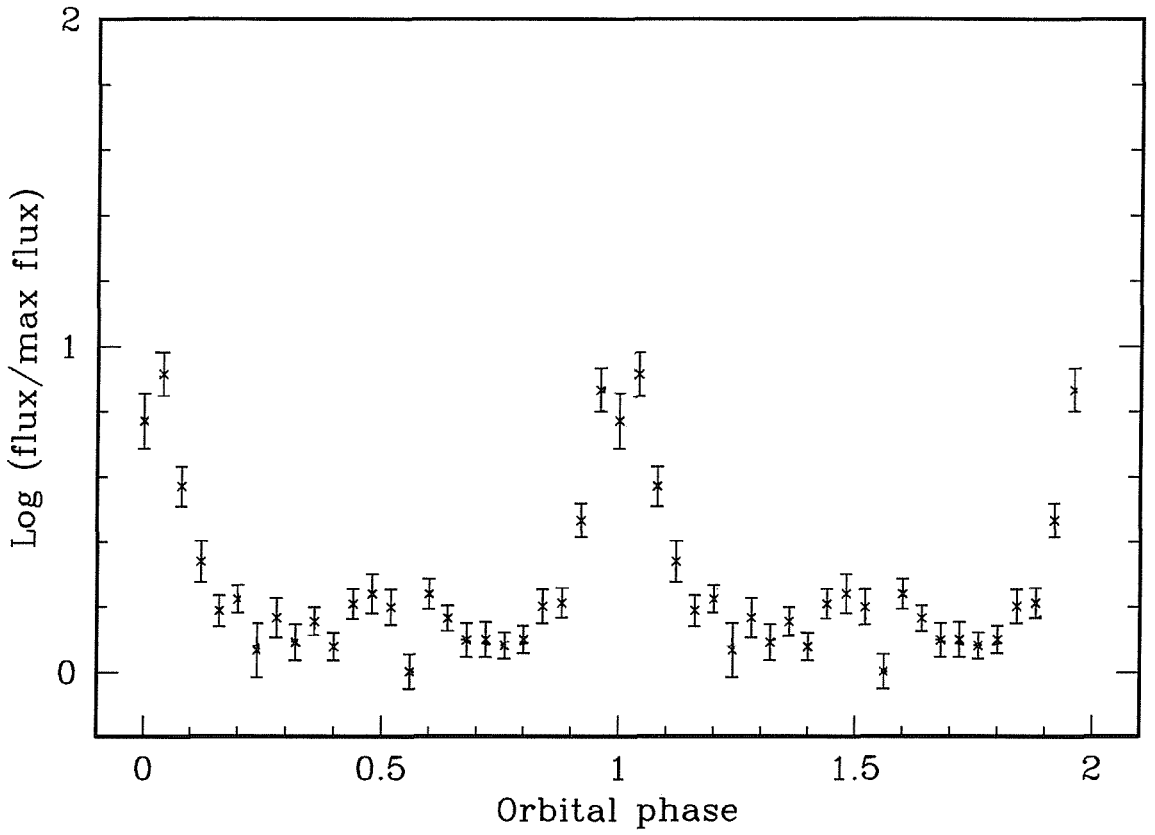


**Figure 4-15.** X-ray lightcurve of the Be/X-ray binary EXO2030+375. Data from the *All Sky Monitor* on the *Rossi X-ray Timing Satellite* were folded on the orbital period of 46.02-days and averaged in bins of 0.04-orbital phase.

The orbital parameters for EXO 2030+375 were input to the X-ray lightcurve developed in Section 4-2. The adopted orbital parameters – taken from Stollberg et al. (1997) – are listed in Table 4-2.

The sound speed included in the model was 25 km $s^{-1}$. This is the sound speed in a circumstellar disc with a temperature of 25,000 K, neglecting the effects of X-ray heating. The power law index $n$ in the density law was fixed at 3.5 (typical for the values derived from IR flux modelling; Waters 1986) and for simplicity the rotational velocities in the wind are assumed to be Keplerian at all orbital separations.

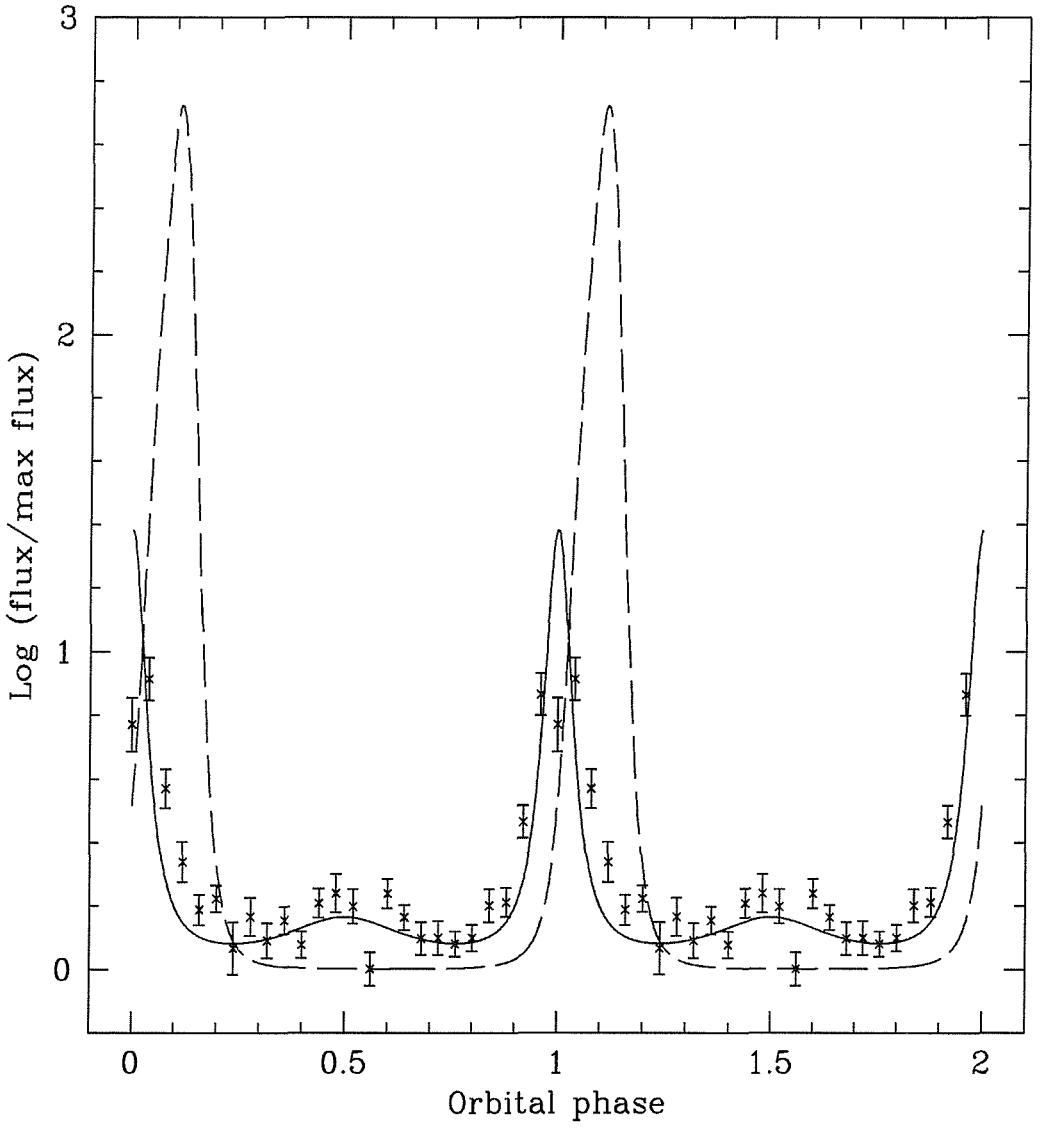


**Figure 4-16.** X-ray lightcurve and model fits for EXO 2030+375

**Table 4-2.** Orbital parameters of the Be/X-ray binary EXO 2030+375 taken from Stollberg et al. (1997)

| | |
|---|---|
| Orbital epoch (MJD) | 48936.5 |
| Orbital period | 46.02 |
| *e* | 0.37 |

The resulting lightcurve predictions are shown in Figure 4-16. The solid line shows the resulting lightcurve with zero outflow velocity $v_0 = 0$, normalised to produce the best fit to the observed lightcurve. The dashed curve shows the model with an outflow velocity at the stellar surface of $v_0 = 1.0$ km s$^{-1}$, normalised by the same factor as the zero outflow velocity model.

The lightcurve predicted for zero outflow velocity shows a strong maximum at phase $\varphi = 0$ , and a weaker second maximum at phase 0.5, due to a minimum in the velocity of the neutron star at this point. When an outflow velocity of 1.0 km s$^{-1}$ is included in the model, the lightcurve maximum is seen to shift to a later orbital phase and no second maximum is seen at apastron.

The zero outflow model fits the data well at low X-ray luminosities, but poorly during the maximum in the lightcurve. We note that X-ray heating effects should act to increase the sound speed in the wind to values ~100 km s$^{-1}$ within the ionisation radius. For typical X-ray luminosities of Be/X-ray binaries during outburst, the ionisation radius may become as large as the radius of gravitational influence of the neutron star, in which case the higher sound speed will result in a decrease in the accretion rate, and hence the X-ray luminosity. A full treatment of the effects of X-ray heating on the lightcurves is beyond the scope of this work, but qualitatively we expect the lightcurve peak to be flattened as the X-ray heating effectively damps the modulation of X-ray flux at high luminosities.

Of note is the difference in shape of the two models. The RXTE ASM data show a lightcurve that peaks at periastron (phase $\varphi = 0.0$), but shows a secondary maximum at apastron (phase $\varphi = 0.5$). Allowing for the damping effects of X-ray heating on the accretion flow, the described model with zero outflow reproduces these features well. The lightcurve model with a finite outflow velocity of 1 km s$^{-1}$ shows only a single peak at phase $\varphi = 0.1$.

During the series of outbursts of the source detected by BATSE prior to the X-ray inactive period in 1993 July, no second maximum was reported, and the peak of the lightcurve was seen to occur approximately 5 days after periastron, at phase $\varphi \sim 0.12$ (Norton et al. 1994). The described model with outflow velocity $v_0$ = 1.0-km $s^{-1}$ reproduces such a shape well. The shift in phase of the peak occurs as the outflow velocity of the wind cancels with the radial component of the orbital motion to move the minimum in the wind-neutron star relative velocity to a slightly later phase. We note that in fact, an outflow velocity of $v_0$ = 1.0-km $s^{-1}$ in this model produces peak luminosity at phase 0.1.

In the case of the Be/XRB EXO2030+375, the separation of the Be star and neutron star at apastron is ~26 $R_*$. At this radius a wind with an initial outflow velocity of 1-km $s^{-1}$ would be accelerated to a velocity of ~130-km $s^{-1}$ if a constant power law index of 3.5 is assumed.

The adoption of a single value of $n$ = 3.5 matches closely the values derived from IR flux modelling by Waters (1986). Changing the adopted value of $n$ will not affect the presence of the secondary maximum at apastron in the case of zero outflow velocity, but will change the relative strengths of the two peaks. A steeper power law will result in a lightcurve that is more highly modulated by the density changes throughout the orbit, so that the maximum at periastron becomes relatively stronger. A less steep power law on the other hand, would result in the maximum at apastron becoming relatively stronger (refer for example to the zero outflow velocity cases in Figures 4-2 to 4-10.

The effect of changing the power law slope on the lightcurve resulting from a wind with 1 km $s^{-1}$ initial outflow velocity is more complicated. For values of $n$ of below 3.25, a second maximum becomes apparent shortly after the larger maximum at periastron, this second maximum then tends towards apastron as $n$ is allowed to drop to 2.0. If $n$ is allowed to take values greater than 3.5, then the lightcurve remains single peaked, but this peak occurs closer to periastron as $n$ increases.

## 4.5 Possible evidence for Be star disc perturbation by an orbiting neutron star

The previous sections have shown how the lightcurves of Be/X-ray binaries can be modelled as X-ray emission due to the release of gravitational potential energy as material from the Be star's disc accretes onto an orbiting neutron star. The model developed assumes a simple disc model with disc density and outflow velocity described as a power law function of radius, and with the disc's rotation being Keplerian. The resulting predicted lightcurves match observations well, and were fit to observations of the X-ray lightcurves of the Be/X-ray binary system EXO 2030+375 in order to explain a shift in the orbital phase at which lightcurve maximum occurs, and the appearance of a double peaked lightcurve.

There have been claims that the orbiting neutron star will perturb the Be star's disc to the extent that the discs of isolated Be stars and those of Be stars in Be/X-ray binaries cannot be compared. Reig et al. (1997) found a correlation between the Hα emission strength and the orbital period in Be/X-ray binaries, which indicated that some interaction mechanism between an orbiting neutron star and the Be star's disc acts to limit the extent of the disc. Negueruela et al. (1998) presented spectroscopic evidence of disc perturbation by orbiting neutron stars. If such perturbation does occur, then the results of fitting X-ray lightcurve models to observations should be treated with care; the disc would be like some quantum particle which is changed by the very act of observation. If we are to use neutron stars as probes of Be star discs, and apply the findings to Be stars in general, we first need to be satisfied that the disc is not significantly changed by the presence of the neutron star.

In the following sections, I describe observations of V801 Cen – the optical counterpart to the Be/X-ray binary 4U1145–619 – made over a 5 day period concurrent

with the periastron passage of the neutron star, and search for evidence of perturbations in the Be star's disc.

## 4.5.1 Observations

During a five day period 1997 April 10 – 14, we observed V801 Cen on consecutive nights. A total of 40 spectra were obtained using the SITe2 spectrograph and 1.9-m telescope at the SAAO. These data were reduced using standard IRAF routines (Massey 1992). Thirty of the spectra were taken on just one night, (12 – 13 April) in order to search for variations in the Hα line strength and line profile on timescales of minutes and hours. The date of the observations was chosen to coincide with the periastron passage of the neutron star, predicted from the periodic recurrence of X-ray maxima.

## 4.5.2 Spectra variability

### 4.5.2.1 Variability on timescales of minutes and hours

The spectra of April 12 and 14 were obtained at intervals of a few minutes, spanning a period of ~3.5-hours and ~30-minutes respectively. We searched each of these data sets for significant variability but found none above the level of noise in the spectra. We then used the data of April 12 to search for variability on the timescale of hours. To increase the S/N ratio the spectra were binned temporally into ~30-minute bins, giving 8 spectra which were each the mean of 3 or 4 individual spectra. The resulting spectra are shown in Figure 4-17, with the right hand plot showing the residuals after subtraction of a mean spectrum. No significant variability can be seen. Similar analysis was performed on the He I (6678 Å) line profiles, and again no variations were seen above the level of the noise in the spectra.

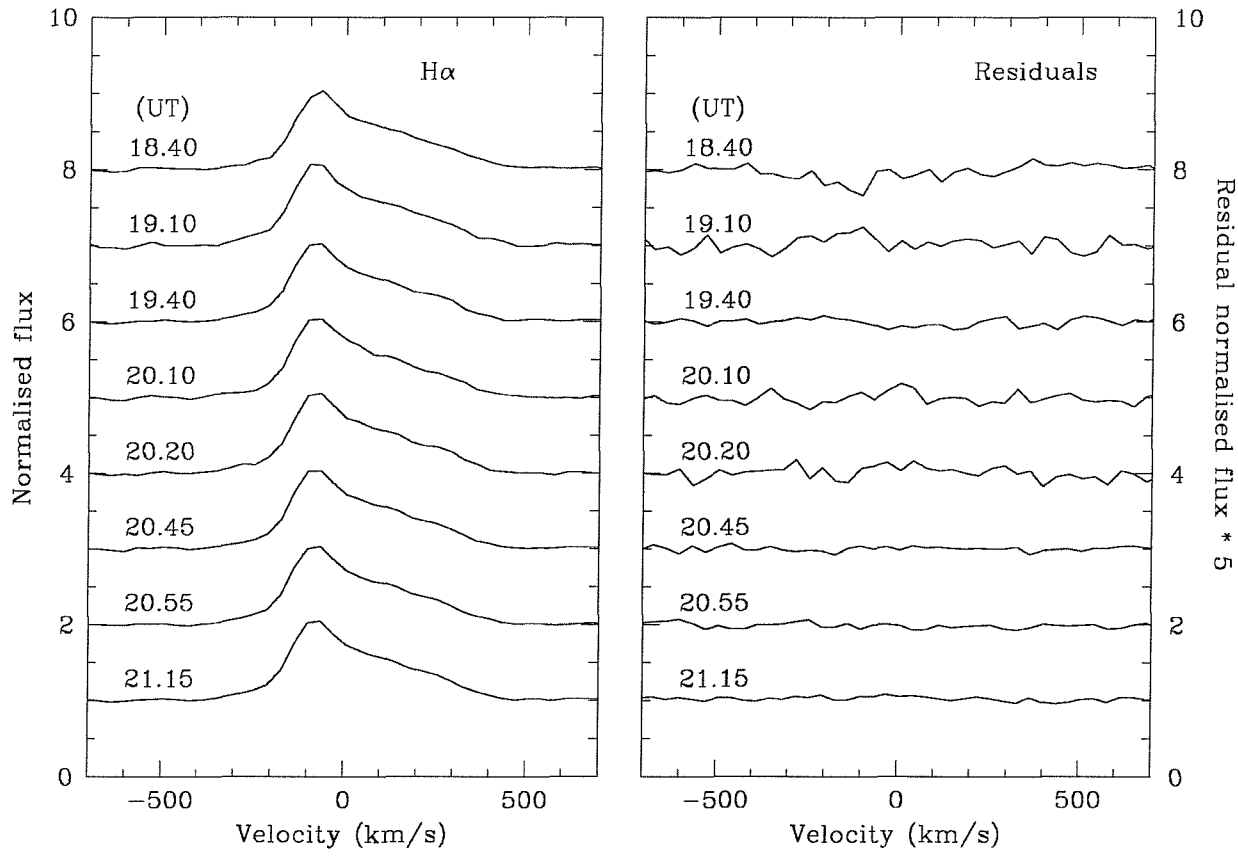


**Figure 4-17. Left:** Hα line profiles of V801 Cen on the night of 1997 April 12. Spectra were obtained at intervals of a few minutes, and have been binned into approximately 30 minute bins. **Right:** Residuals after subtraction of a mean spectrum.

#### 4.5.2.2 Night to night variability

In order to search for night to night variations we created mean spectra for each night before comparison. Figure 4-18 shows the resulting line profiles. In this case, the residual spectra were created by subtracting the mean spectrum from the 14$^{th}$ April (the last night of observation) to show more clearly the variability. The residuals remaining after subtraction indicate an emission component approximately symmetrical about the rest wavelength with a peak separation of $300 \pm 35$ km s$^{-1}$ decreasing in strength throughout the five nights. The results of similar analysis for the He I (6678 Å) line are shown in Figure 4-19. In this case

the profiles show no apparent variations over the five nights above the level of the noise in the spectra.

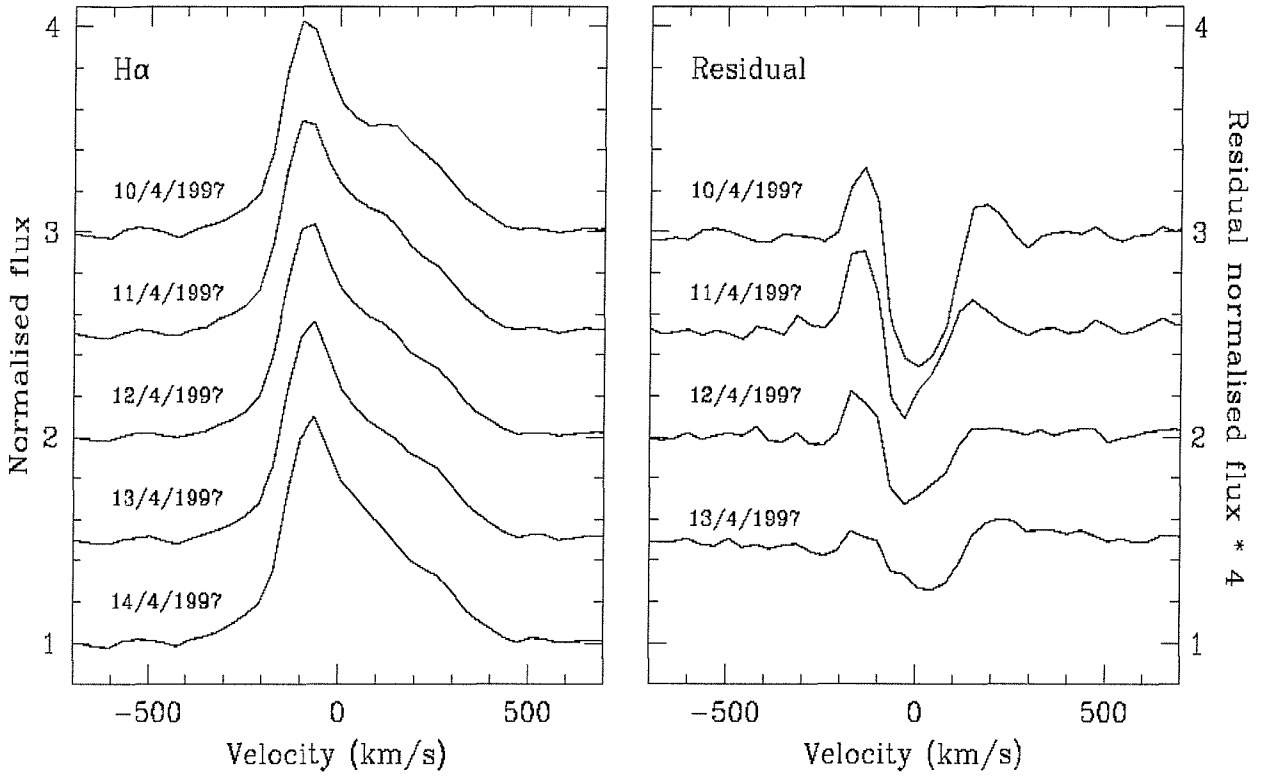


**Figure 4-18. Left:** Hα line profiles of V801 Cen on 5 consecutive nights in 1997 April. Where multiple spectra were obtained on one night, a mean of these spectra is shown. **Right:** Residuals after subtraction of the 14$^{th}$ April spectrum.

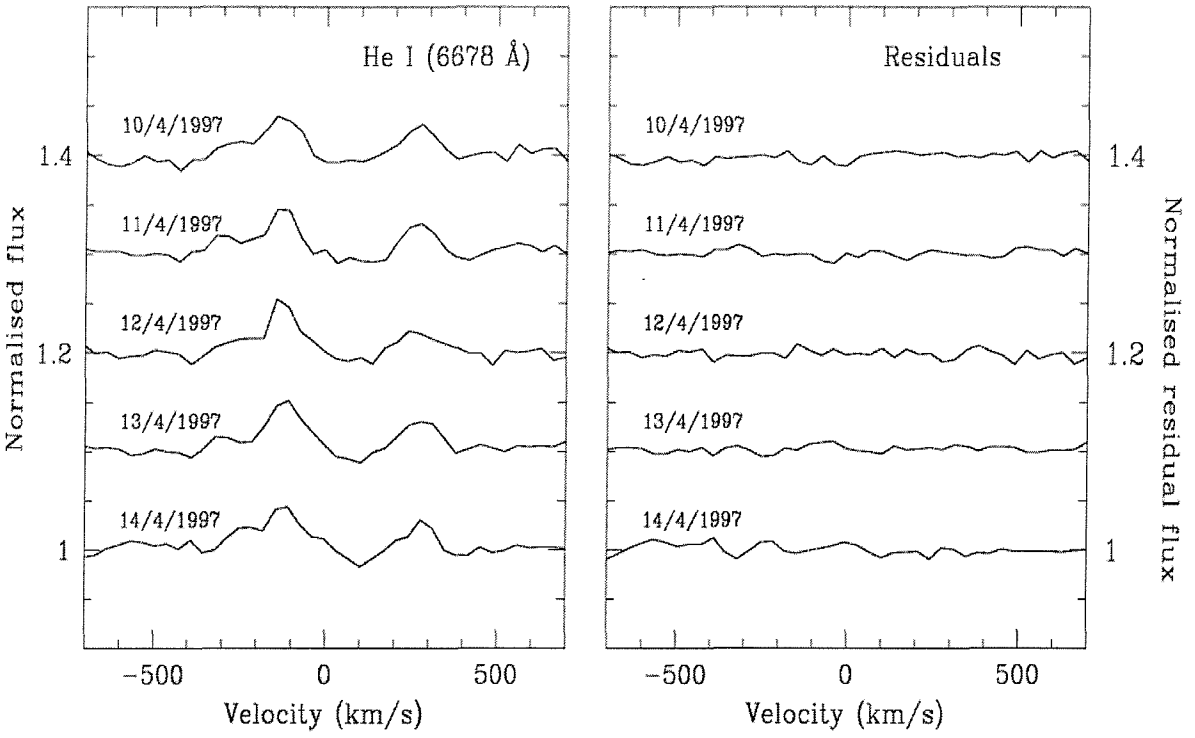


**Figure 4-19. Left:** He I ($\lambda$ = 6678) line profiles of V801 Cen on 5 consecutive nights in 1997 April. Where multiple spectra were obtained on one night, a mean of these spectra is shown. **Right:** Residuals after subtraction of a mean spectrum.

### 4.5.3 Cause of night to night variability

We can rule out an accretion disc as the source of the variable emission component as the velocities of the two peaks in the residuals would then be expected to be much larger (of the order of $10^3$ – $10^4$ km $s^{-1}$ for a Keplerian accretion disc). Therefore, if the variability is caused by the neutron star, it must be in the form of an interaction with the Be star's circumstellar disc.

Assuming that the circumstellar envelope has a disc geometry, and that the material in this disc moves in Keplerian orbits, then the characteristic radii of regions emitting various lines can be determined from the separation of peaks ($v_k$) in the observed line profiles from the equation:

$$\frac{r_{em}}{R_*} = \left( \frac{2v_* \sin i}{\gamma \Delta v_k} \right)^2$$

where $v_* \sin i$ is the observed projected stellar rotational velocity, and $\gamma$ is the ratio of the (un-projected) stellar rotational velocity to the critical break up velocity $v_{crit}$ (see for instance Hummel & Vrancken 1995). From the mass and radius derived in Chapter 3 (13 $M_O$ and 8 $R_O$) we find $v_{crit}$ = 557 km $s^{-1}$. Upper and lower limits can be placed on the radius $r_{var}$ of the region contributing the varying flux by assuming first that the star is rotating at its critical break up velocity ($\gamma$ = 1) and secondly that the inclination of the normal to the disc with the line of sight $i = 90°$.

The projected rotational velocity of the Be star is $v \sin i$ = 290 km $s^{-1}$ (Balona 1973), and the peak separation measured from the residuals in Figure 4-18 is 300 ± 50 km $s^{-1}$. Adopting $\gamma$ = 1 then we find $r_{var}$ = 3.7 ± 0.9 $R_*$. In the second case, where we assume that the inclination is 90°, $\gamma$ = 290/557 = 0.52, giving $r_{var}$ = 13.8 ± 3.5 $R_*$.

Using a mass for the Be star of 13 $M_\odot$ a mass of 1.4 $M_\odot$ for the neutron star, and assuming an orbit with eccentricity $e$ = 0.4 (typical for Be/X-ray binaries, see for instance Table 3. of Bildsten et al. 1997), we find the semi-major axis of the orbit to be $a \sim 41\ R_*$, the periastron separation to be $d_p \sim 25\ R_*$, and the radius of the Roche lobe of the Be star at periastron to be $r_{rl} \sim 13\ R_*$.

Hence, with high inclinations, and correspondingly low values of $\gamma$, the radius of the Roche lobe of the Be star at periastron passage will be of the order of the radius of the varying region of the disc, suggesting that the observed variations could be due to some form of binary interaction.

## 4.6 Summary

### 4.6.1 Model predictions

The lightcurve model developed in Section 4.2 reproduces a wide range of observed lightcurve shapes.

For all adopted values of power–law gradient $n$, the lightcurves for zero outflow discs show X-ray maxima both at periastron and at apastron. At periastron the neutron star has no radial motion with respect to the Be star, and the density of disc material passed through by the neutron star is higher at this phase than at larger orbital separations. At apastron, again the neutron star has no radial motion relative to the Be star, and although the neutron star at this phase encounters the lowest density material around its orbit, the effect of the reduced relative velocity is more significant, and a maximum the X-ray luminosity results (albeit of a lesser scale than that at periastron).

As the outflow velocity increases from zero, the shape of the lightcurve changes. At first the apastron maximum remains, but shifted to earlier orbital phases as the outflow velocity increases, at the same time, the periastron maximum tends to be shifted to later orbital phases. To understand this, we must consider the radial motion of the neutron star relative to the Be star, which will act to cancel the outflow velocity in the wind at phases between 0 and 0.5. For low outflow velocities, the orbital motion of the neutron star still plays a role in the shape of the lightcurve but as outflow velocities increase, the lightcurves become dominated by the wind dynamics.

By including the sound speed of the disc, the model implicitly took into account cases of both sub-sonic and super-sonic accretion flows. A higher disc temperature leads to a higher sound speed in the disc.

The effect on the predicted lightcurves of increasing the sound speed is to make the lightcurve shape far less dependant on the orbital motion of the neutron star and the wind velocity as the accretion rate becomes pressure limited. The modulation of the X-ray luminosity in this regime is dominated by the varying density around the orbit.

In the super-sonic accretion regime, where the sound speed in the disc is lower, the motion of the neutron star and the velocities in the wind become more important, resulting in the more complicated lightcurve shapes, often with double maxima.

Increasing the eccentricity of the orbit has the effect of increasing the amplitude of modulation of the lightcurve. In the case of disc models with a finite accelerated wind velocity, adopting larger orbital periods – and hence wider orbits – leads to lightcurves which are dominated by the outflow velocity of the wind, as the neutron star orbits at the larger distances from the Be star where the the wind is accelerated to greater velocities.

Other models have been proposed to explain the recurring outbursts displayed by Be/X-ray binaries. Bildsten et al. 1997 cite several authors who suggest the formation of accretion discs around the neutron star during the giant outbursts that are not correlated with orbital phase. Bildsten et al. suggest that accretion discs may be present around the neutron stars also during series of recurring outbursts. In fact I have myself suggested that an accretion disc may have been present around the neutron star in 4U1145–619 during an unusually large outburst (though one which was coincident with periastron passage).

Bildsten et al. claim that in such a scenario, the X-ray luminosity is governed more by the amount of material allowed to accrete from the inner edge of the accretion disc onto the neutron star than by the amount of material being captured from the wind. They propose that the recurring outbursts coincident with periastron passage are caused by orbital modulation of tidal torques. However, in their solution, the effect of the increased tidal torques at periastron is to increase the mass accreted

onto the outer regions of the accretion disc, leading to enhanced accretion from the inner regions of the disc onto the neutron star some time later.

The time delay between the enhanced accretion onto the accretion disc and onto the neutron star is the global viscous timescale, of the order of weeks. For those Be/X-ray binaries for which orbital solutions have been determined, the X-ray maxima have been found to occur within a few days of periastron passage. To the authors knowledge, only one case of X-ray outbursts occuring as late as a few weeks after periastron passage is that of 2S1417-624 cited by Bildsten et al. in which the outbursts all occurred close to *apastron*.

### 4.6.2 Model fit to the X-ray lightcurve of EXO 2030+375

We have reproduced well the observed X-ray lightcurve of the Be/X-ray binary system EXO 2030+375. In particular, a number of observational peculiarities can be explained by simple variations in the model parameters. The appearance of second X-ray maxima at apastron is explained by adopting low (approaching zero) outflow velocities.

An observed shift in the orbital phase at which X-ray maximum occurs can again be explained by increasing this outflow velocity. This has the effect that between phase 0 and 0.5, the radial velocity of the neutron star relative to the Be star (due to the eccentricity of the orbit) and the outflow velocity of the wind partly cancel, and the point at which the relative velocity between the neutron star and the wind material that it moves through occurs slightly later than phase zero.

This simple model is based upon a number of assumptions. The structure of Be star circumstellar discs is not completely known, and we have followed others in assuming the disc model. The radial extent to which such a simple power law description of the disc structure would be valid is also uncertain. Radio observations of Be stars indicate a change in the disc structure to a steeper power-law at radii of the order of a few tens of stellar radii (Taylor et al. 1990). Any such steepening of

the power law describing the density and velocity of the disc would alter the ratio between the strengths of the two maxima, so that the apastron peak is less luminous than in the case where the power law remains constant at all radii.

It should also be noted that other explanations for apastron maxima in X-ray luminosity have been proposed. A double peak in the X-ray lightcurve could also result if the planes of the Be star's disc and the orbit are not aligned. Such an inclination could occur if the neutron star received a kick during the supernova explosion in which it formed. However, inclinations greater than a few degrees are only expected to occur in systems with highly eccentric long period orbits. Furthermore, as the maxima in the X-ray lightcurve in such a scenario are due to the orbit of the neutron star crossing the disc plane, the occurrence of the maxima at periastron and apastron would require the coincidence of the periastron and apastron of the orbit with the disc crossing points of the orbit.

Bildsten et al. (1997) discuss an alternative model for Be/X-ray binary lightcurves in which tidal forces on an accretion disc lead to X-ray maxima a few weeks after periastron passage. In fact, if a mechanism were identified by which the periastron tidal forces on the accretion disc act to increase the accretion rate onto the neutron star from the inner disc as well as increasing the accretion from the wind onto the outer disc, then the result would be the occurrence of a maximum at or close to periastron passage, followed a few weeks later by a second maximum. This would represent an alternative scenario to explain the double peaked lightcurve seen in EXO 2030+375.

Under the above assumptions, the difference in the X-ray lightcurve shown by the source during the two series of outbursts (the currently observed one and the one previously detected by BATSE) can be explained by a difference only in the outflow velocity of the wind, with all other parameters equal. The presence of a small outflow velocity during the 1993 outburst and no (or negligible) outflow velocity during the 1996 outburst can explain the observed difference in orbital phase of

lightcurve maxima, and the presence in the recent lightcurves of a second maximum at apastron.

### 4.6.3 Binary interaction

Hα line profiles of V801 Cen obtained concurrently with an X-ray outburst show variations on the time-scale of days. In particular, over five days of observations, a double peaked emission component, symmetric about the rest wavelength, is seen to decrease in strength. The variations are consistent with emission from some radius of the disc decreasing in strength, with the radius of this region constrained by $3.7\ R_* < r_{em} < 13.7\ R_*$. The time-scale of the observed variability and the coincidence with the periastron passage of the neutron star lend weight to the possibility of binary interaction. Whilst this large range allows the possibility that the variations are caused by the passage of the neutron star and the subsequent rapid change in size and orientation of the Roche lobe, these data cannot exclude the possibility that the observed variations are intrinsic to the Be star, and would still be seen if the Be star were not in a binary system. To resolve this ambiguity, observations of the source at a range of orbital phases are encouraged, to search for similar variability when the neutron star is at a much larger distance from the Be star.

# Chapter 5 – Optical Counterparts to Be/X-ray Binaries in the Magellanic Clouds

In this chapter I present a search for the optical counterparts to X-ray sources in the Magellanic Clouds believed to be High Mass X-ray Binaries. The fields of X-ray sources in the Magellanic Clouds believed to be Be/X-ray binaries have been searched for possible Be star counterparts. $BVR_c$ and $H\alpha$ CCD imaging was employed to identify early type emission stars through colour indices and $H\alpha$ fluxes. Subsequent spectroscopy of a number of sources confirms the presence of $H\alpha$ emission in each case, validating the employed photometric selection method.

Based on the positional coincidence of emission line objects with the X-ray sources, I identify Be star counterparts to the *ROSAT* sources RX J0032.9-7348, RX J0049.1-7250, RX J0054.9-7226 and RX J0101.0-7206, and to the recently discovered *ASCA* source AX J0051-722. I confirm the Be star nature of the counterpart to the *HEAO1* source H0544-66, and derive the spectral classification of the Be star counterpart to the *ROSAT* source RX J0117.9–7330. In the field of the *ROSAT source* RX J0051.8-7231 I find that there are three possible counterparts, each showing evidence of $H\alpha$ emission. I find a close double in the error circle of the *EXOSAT* source EXO 0531.1-6609, each component of which could be a Be star associated with the X-ray source. Similarly, in the field of the *ROSAT* source RX J0053.8–7226 I find 2 possible counterparts (whereas in Buckley et al. 1998, we found only one candidate and associated this object with the X-ray source).

Most of the work in this chapter has been published in Stevens, Buckley & Coe (1999), Coe et al. (1998) and Buckley et al. (1998).

## 5.1 Introduction

External galaxies can serve as useful laboratories in which to test theories of stellar evolution and to investigate the effects of different environmental characteristics on the formation and evolution of stellar objects. The Magellanic Clouds are ideal candidates for study due to their proximity to our own Galaxy. Many interesting differences between Magellanic Cloud populations and their Galactic counterparts have been discovered, sometimes with profound consequences.

Recently Paczyński & Pindor (2000) have tested the validity of the 'Cepheid Distance Scale' in determining cosmological distances; they showed that the period-flux relationship upon which the distance scale depends is not universal after finding significant differences between LMC and SMC variable amplitudes. The Cepheid distance scale has importance for determining the distances to galaxies at mid-cosmological distances, in order to calibrate other, further reaching distance scales, and so this result from studies of our Galaxies nearest neighbours has implications as far reaching as cosmological distance determinations.

In the field of Be star research, many authors have claimed more frequent occurrences of emission lines amongst early type stars in the Magellanic Clouds than in the Galaxy. The reasons are uncertain, mostly because the very cause of the Be star phenomenon itself is unclear. Often cited as a possible factor is the difference in metallicity of the three environments (Galaxy, LMC and SMC). However, until we have a unified model of Be stars which successfully reproduces the occurrence and all observed behaviour, any attempt to explain the population differences in our local galaxies can not be tested in a reliably complete manner.

### 5.1.1 X-ray binaries in normal galaxies

X-ray binaries (both low- and high-mass) constitute a significant component of the X-ray emission of a normal galaxy. Therefore, our knowledge of Galactic X-ray binaries can aid in the interpretation of (often spatially unresolved) X-ray observations of external galaxies. On the other hand, observations of external galaxies provide us with ideal laboratories for the study of sample populations of X-ray binaries each with different star formation histories, chemical composition, galaxy structure and age.

Unless the galaxies have large inclinations to the line-of-sight, observations are not affected by large absorption, and uncertainties in distance affect all sources in the same way, easing comparisons between sources and the study of the population as a whole. Perhaps one of the greatest advantages of studying stellar populations in external galaxies is the ease with which distributions of classes of object can be mapped. This then allows associations to be drawn between classes of object and galactic components (e.g. disk, spiral arms, bulge, halo), and highlights irregularities which might indicate localised phenomena (i.e. localised star-bursts).

The Magellanic Clouds (MC's) present a unique opportunity to study stellar populations in galaxies other than our own. All of the advantages described above are applicable to studies of Magellanic Cloud sources, with the added benefits that their relative proximity is close enough to allow study with modest sized ground based telescopes, and the inclination of the clouds to our line-of-sight does not lead to large line-of-sight absorption.

### 5.1.2 High Mass X-ray Binaries in the Magellanic Clouds

Previous studies have often highlighted on differences between the populations of HMXB's in the Magellanic Clouds and those in the Galaxy. Pakull (1989) remarks that the X-ray luminosity distribution of the Magellanic Cloud sources appears to be shifted to higher luminosities relative to the Galactic population – Clark et al.

(1978) reported observations of a number of Magellanic Cloud sources which appeared to be emitting above the Eddington limit. It has also been suggested that there is a higher incidence of High Mass X-ray binary sources which contain black holes in the Magellanic Clouds (see Clark et al. 1978; Pakull 1989; Schmidtke et al. 1994).

Clark et al. (1978) attributes the higher luminosities to the lower metal abundance found in the MC's. Motch & Pakull (1989) interpreted abnormally weak NIII Bowen emission lines in spectra of LMXBs in the LMC as indicative of reduced CNO abundance. In the proposed scenario, lower metal abundance in the MCs reduces the opacity of the accreted material, allowing a higher accretion rate.

Proposing a solution to the over-abundance of black-hole candidate systems, Pakull (1989) refers to evolutionary scenarios of van den Heuvel & Habets (1984) and de Kool et al (1987) for black hole formation in binary systems, which appear to favour low metal abundance environments. Very massive black-hole progenitors must evolve to red supergiant status *before* filling their Roche lobe, otherwise mass is lost through Roche lobe overflow so that the star is no longer massive enough to form a black hole. This only occurs if the mass loss through stellar wind has not been too great earlier in the star's life. Black hole formation is then preferred in a low abundance environment where it is expected that mass loss rates would be reduced (Pakull 1989).

Unfortunately, the comparisons between the Magellanic Cloud populations and Galactic populations are limited by the small numbers of optically identified sources in the Clouds. In order to facilitate a complete study of the differences between the HMXB populations of the Magellanic Clouds and the Galaxy, we have begun a program to identify the optical counterparts to X-ray sources believed to be Magellanic Cloud Be/X-ray binaries.

**Table 5-1.** Optically unidentified X-ray sources in the Magellanic Clouds observed in this study. Column 4 gives the uncertainty radius (90%) for the best X-ray position.

| Source | RA (J2000) | Declination (J2000) | Uncertainty radius (arcsec) |
|---|---|---|---|
| RX J0032.9 – 7348 | 00 32 55.1 | -73 48 11 | 62 |
| RX J0049.1 – 7250 | 00 49 04.6 | -72 50 53 | 22 |
| AX J0051 – 722 | 00 50 55.8 | -72 13 38 | 10 |
| RX J0051.8 – 7231 | 00 51 53.0 | -72 31 45 | 11 |
| RX J0053.8 – 7226 | 00 53 55.6 | - 72 26 44 | 15 |
| 1WGA J0054.9 – 7226 | 00 54 56.1 | -72 26 45 | 11 |
| RX J0101.0 – 7206 | 01 01 03.2 | -72 06 57 | 10 |
| RX J0117.6 – 7330 | 01 17 | - 73 30 | 12 |
| EXO 0531.1 – 6609 | 05 31 12.0 | -66 07 08 | 9 |
| H0544 – 665 | 05 44 15.5 | -66 33 50 | 30 |

Table 5-1 lists the X-ray sources in the Magellanic Clouds observed in this study. Column 4 gives the uncertainty (90% confidence) in the best X-ray position in arc-seconds. Many of the positions are derived from *ROSAT* detections with uncertainties of the order of a few arc-seconds. In galactic fields, sub-ten arc-second resolution would normally be adequate for an unambiguous optical identification, but owing to the crowded nature of Magellanic Cloud fields, even some of the *ROSAT* sources have X-ray positional uncertainties that allow several possible optical counterparts.

For this reason we decided upon a program of CCD imaging to select candidates based on their colour indices and $H\alpha$ fluxes. Once a shortlist of candidate counterparts was found, follow up spectroscopic observations were made, to obtain $H\alpha$ spectra of these candidates, in order to confirm Be star identifications, and to confirm Magellanic Cloud membership through radial velocity measurements.

In Section 5.2 I describe the observations made, in Section 5.3 I present the results and discuss individual sources, finally in Section 5.4 I discuss the general HMXB populations of the Magellanic Clouds and the Galaxy in the light of our results.

## 5.2 Observations

### 5.2.1 CCD Photometry

All of the CCD images used in this work were obtained from the SAAO between 1995 November and 1996 October. In addition, observations of the field of RX J0117.9-7330 in January 1996 used in this Chapter, and in Coe et al. (1998) were kindly provided by Phil Charles. A complete log of the observations is shown in Table 5-2. Our own data were obtained during two separate observing runs, as described below.

On 1995 November 26 we obtained $BV(RI)_C$ and Hα images of the field of the X-ray source RX J0053.8-7226. Data were obtained with the 1.0-m telescope and the Tek8 CCD. Observations were made in photometric conditions with good seeing (FWHM ~1"). These data were reduced using *DoPHOT* to perform PSF fitting photometry (Mateo & Schechter 1989). The resulting instrumental magnitudes were transformed onto the standard system using observations of E region standard stars (Menzies et al. 1989).

The remainder of the CCD imaging data were obtained during 1996 October 1 – 7. These observations were made using the 1.0-m telescope and Tek8 CCD, plus 3x *Shara* focal reducer. The resulting pixel scale was 1.05" per pixel, with a total image size of 519x519". All of the fields were observed through $R_C$ and Hα filters. In addition, a number of the fields were observed through $BV$ and $I_C$ filters. The

Hα filter used was an interference filter centred on a wavelength of 6562 Å, with a width of 50 Å.

The use of the focal reducer, whilst originally considered necessary to provide a field of view adequate to search the larger X-ray error circles, introduced significant vignetting which was not satisfactorily removed by flat-field corrections. Analysis of the sky background in a number of images showed that flat-field errors were below the 1- % level within 4' of the image centre, but grew much larger at the image extremities. In subsequent analysis we therefore rejected any measurements of objects that lay further than 4' from the image centre.

**Table 5-2.** Log of CCD imaging observations made with the 1.0-m telescope at the SAAO. *Continued overleaf.*

| Date of observation | Source | Filter band | Exposure (s) |
|---|---|---|---|
| 1996 January 24 | RX J0117.6-7330 | *B* | 200 |
| | | *R* | 200 |
| 1996 January 25 | RX J0117.6-7330 | *B* | 200 |
| | | *V* | 200 |
| 1996 January 26 | RX J0117.6-7330 | *B* | 200 |
| | | *V* | 200 |
| | | *R* | 200 |
| 1996 January 27 | RX J0117.6-7330 | *B* | 200 |
| | | *V* | 200 |
| | | *R* | 200 |
| 1996 January 28 | RX J0117.6-7330 | *B* | 200 |
| | | *V* | 200 |
| | | *R* | 200 |
| 1995 November 26 | RX J0053.8-7226 | *U* | 600 |
| | | *B* | 300 |
| | | *V* | 200 |
| | | $R_C$ | 200 |
| | | $I_C$ | 200 |
| | | *Hα* | 1000 |
| 1996 October 1 | RX J0032.9–7348 | *B* | 200 |
| | | *V* | 200 |
| | | $R_C$ | 200 |
| | | *Hα* | 1000 |
| | RX J0051.8–7231 | $R_C$ | 150 |
| | | *Hα* | 1000 |
| | RX J0101.0–7206 | $R_C$ | 150 |
| | | *Hα* | 1000 |
| | H0544–665 | *B* | 200 |
| | | *V* | 200 |
| | | $R_C$ | 100 |
| | | *Hα* | 1000 |

**Table 5-2.** *Continued from previous page.* Log of CCD imaging observations made with the 1.0-m telescope at the SAAO.

| Date of observation | Source | Filter band | Exposure (s) |
|---|---|---|---|
| 1996 October 2 | RX J0049.1–7250 | $B$ | 300 |
| | | $V$ | 300 |
| | | $R_C$ | 100 |
| | | $H\alpha$ | 1000 |
| | RX J0054.9–7226 | $B$ | 300 |
| | | $V$ | 200 |
| | | $R_C$ | 200 |
| | | $H\alpha$ | 1000 |
| 1996 October 3 | RX J0117.6-7330 | $B$ | 200 |
| | | $V$ | 200 |
| | | $R_C$ | 100 |
| | | $H\alpha$ | 1000 |
| 1996 October 4 | RX J0117.6-7330 | $B$ | 200 |
| | | $V$ | 200 |
| | | $R$ | 100 |
| 1996 October 5 | RX J0117.6-7330 | $B$ | 200 |
| | | $V$ | 200 |
| 1996 October 6 | RX J0117.6-7330 | $B$ | 200 |
| | | $V$ | 200 |
| | | $B_{NARROW}$ | 1000 |
| | | $\beta_{WIDE}$ | 200 |
| 1996 October 7 | RX J0117.6-7330 | $B$ | 200 (+ 20 x 60sec) |
| | | $V$ | 200 (+ 20 x 60sec) |
| | | $R$ | 100 |

Due to the crowded nature of the fields, profile-fitting photometry was necessary to obtain accurate instrumental magnitudes without contamination from nearby objects. PSF fitting photometry was carried out using IRAF/DAOPHOT. In each field between 30 and 50 stars were used to model the PSF as a 2-dimensional Gaussian function with additional wings described by a Lorentzian function. This produced fits with smaller residuals than a simpler single Gaussian function component. The resulting instrumental magnitudes were transformed to the standard system using observations of a set of E and F region standard stars (Menzies et al. 1989). A $H\alpha$ magnitude scale was calibrated by defining the zero point such that a $R_C - H\alpha$ index has a value of zero for main sequence, non-emission line stars, and becomes larger than zero for emission line stars.

For each field observed, an *emission–colour* diagram was plotted, with the $R_C - H\alpha$ emission index on the vertical axis, and the $B - V$ colour index on the horizontal axis. As demonstrated by Grebel (1997), when such a diagram is plotted for Magellanic Cloud fields, where all objects lie at the same distance and are affected by the same reddening, Be stars can be clearly distinguished by their blue colour, and high emission index.

### 5.2.2 Systematic errors

Comparing photometry of other objects observed during this run with photometry obtained on other occasions without use of the focal reducer indicated that errors of up to 0.1 in magnitude could have resulted from fitting a poorly sampled PSF. In addition, some observations were made in conditions that were slightly below photometric quality, introducing systematic errors. As the method of identification of Be star candidates is through their *relative* positions in the *emission–colour* diagram, we have confidence that these systematic errors do not undermine our results, however, in recognition that the individual values are subject to systematic errors, the axes of the plots are labelled *r–Hα* and *b-y*. It is important to note that these are not narrowband photometric indices (as sometimes indicated by lower case labels).

### 5.2.3 Optical spectroscopy

Optical spectra were obtained during 4 separate observing runs. A complete log of spectroscopic observations is shown in Table 5-3.

**Table 5-3.** Log of spectroscopic observations made with from the AAT and with the 1.9-m telescope at the SAAO.

| Source | Date of observation | Wavelength range | Dispersion |
|---|---|---|---|
| RX J0117.6–7330 | 1996 January 18 | 4240 – 5004 Å | 0.79 Å/pixel |
| | 1996 January 18 | 6092 – 6857 Å | 0.79 Å/pixel |
| | 1996 October 5 | 6035 – 7011 Å | 0.52 Å/pixel |
| | 1996 October 6 | 3135 – 8290 Å | 2.76 Å/pixel |
| | 1996 October 7 | 4147 – 5253 Å | 0.59 Å/pixel |
| RX J0053.8-7226$_{East}$ | 1997 October 2 | 3800 – 7779 Å | 2.2 Å/pixel |
| RX J0053.8-7226$_{West}$ | 1997 October 2 | 3800 – 7779 Å | 2.2 Å/pixel |
| AX J0051–722 | 1998 February 3 | 6295 – 7042 Å | 0.42 Å/pixel |
| RX J0101.0–7201 | 1998 February 3 | 6295 – 7042 Å | 0.42 Å/pixel |
| EXO 0531.1–6609 | 1998 February 3 | 6295 – 7042 Å | 0.42 Å/pixel |
| | 1998 February 5 | 3800 – 7779 Å | 2.2 Å/pixel |
| H0544–665 | 1998 February 3 | 6295 – 7042 Å | 0.42 Å/pixel |
| | 1998 February 5 | 3800 – 7779 Å | 2.2 Å/pixel |
| RX J0032.9–7348 | 1998 February 4 | 6295 – 7042 Å | 0.42 Å/pixel |
| RX J0051.8–7231 | 1998 February 4 | 6295 – 7042 Å | 0.42 Å/pixel |
| RX J0054.9–7226 | 1998 February 4 | 6295 – 7042 Å | 0.42 Å/pixel |
| | 1998 February 5 | 3800 – 7779 Å | 2.2 Å/pixel |

In January and October 1996 spectra were obtained of the candidate counterpart to RX J0117.6–7330. The January observations were made at the AAT, with the 1200V grating on the RGO spectrograph, giving a dispersion of 0.79-Å/pixel. The October observations were made at the SAAO 1.9-m telescope with RPCS (Reticon) detector on the ITS spectrograph. Spectra were obtained at 0.52-Å/pixel (6035 – 7011 Å), 0.59-Å/pixel (4147 – 5253 Å) and 2.76-Å/pixel (3135 – 8290 Å).

On 1997 October 2, low-resolution spectra (FWHM ~7-Å) of candidate counterparts to RX J0053.8–7226 were obtained from the 1.9-m telescope at the SAAO with the *SITe2* CCD detector which was recently commissioned as a replacement to the RPCS. On this occasion a flux standard (EG 21) was observed to allow flux calibration of the spectra.

Data were obtained of a number of sources from the same telescope/instrument combination during 1998 February 3 – 5. On 1998 February 3 and 4, spectra were obtained with a spectral range of 6295 – 704 5Å and dispersion of 0.43 Å/pixel. On 1998 February 5, low-resolution spectra were obtained with a range of 3800 – 7780 Å, and a dispersion of 2.3 Å/pixel.

On 1998 February 5, a flux standard was observed, as well as a smooth spectrum standard for the removal of telluric features. All low-resolution spectra obtained on this night have subsequently been flux calibrated, and telluric features to the red of Hα have been removed.

Spectra were optimally extracted, and wavelength scales were calibrated and applied using arc-lamp spectra obtained before and after each target observation, the solutions temporally interpolated to the time of the target observation.

## 5.3 Results and discussion of individual sources

### 5.3.1 RX J0032.9-7348

This source was discovered by Kahabka & Pietsch (1996, hereafter KP1996) in *ROSAT* pointed observations made in 1992 December and 1993 April. The unabsorbed bolometric luminosity they derive from the 1993 observations is 2.5 x $10^{36}$ ergs $s^{-1}$, whilst the 1992 December flux was a factor of ~6 less. From the X-ray spectrum, length of the X-ray high state (at least 5 days in 1993 April), and long term variability, KP1996 propose a likely HMXB nature for the source. The X-ray position was determined to an accuracy of ± 62 arc-seconds (KP1996).

We obtained *BVR* and Hα images of the field on the night of 1996 October 1. Figure 5-2 shows the *emission–colour* diagram for stars in the field, the left hand plot showing all stars in the field, the right hand plot showing only those stars within a field centred on the X-ray position, with a radius 124 arc-seconds (twice the positional uncertainty). On this plot, we further identify those stars that lie within the X-ray error circle by plotting with filled circles.

The field population is predominantly evolved red stars, with only six early type stars detected within the 124-arc-second area. Of these early type stars, two show clear excess *Hα* flux. The strongest *Hα* excess is seen from a star that lies within the X-ray error circle (~12 arc-seconds from the X-ray position, marked as object 1 in Figure. The other *Hα* source (object 3 in Figure 5-2) lies ~100 arc-seconds to the north of the X-ray position. Besides object 1, only one other object within the error

circle is identified as an early type star from its *B–V* colour (object 2, which we identify with GSC 0914101338).

Table 5-4 lists the photometry for the 9 objects within the X-ray error circle detected in each of the *BVR* and *Hα* frames.

Our medium resolution spectrum of object 1 shows Hα in emission with an equivalent width of EW(*Hα*) = –35 Å. No He I (λ = 6678-Å) feature is seen above the level of the continuum noise. The *Hα* line is single peaked, and centred on λ = 6566.5 ± 0.5-Å.

Assuming that the deviation from the rest wavelength of Hα is purely due to the radial velocity of the star, we derive a velocity of *171 ± 23* km $s^{-1}$, consistent with the systemic radial velocity for the SMC of *166 ± 3* km $s^{-1}$ found by Feast (1961). This object is the most probable optical counterpart for RX J0032.9-7238.

**Table 5-4.** Photometry of objects within the 90% confidence X-ray error circle of RX J0032.9-7348

| Object | V | B-V | V-R | R-Hα |
|---|---|---|---|---|
| 1 | 16.26 ± 0.05 | 0.01 ± 0.07 | 0.04 ± 0.06 | 0.68 ± 0.06 |
| 2 | 15.11 ± 0.04 | -0.13 ± 0.06 | -0.14 ± 0.05 | 0.10 ± 0.06 |
| 3 | 13.62 ± 0.04 | 0.59 ± 0.06 | 0.39 ± 0.05 | 0.12 ± 0.06 |
| 4 | 16.69 ± 0.05 | 1.05 ± 0.07 | 0.70 ± 0.06 | 0.18 ± 0.06 |
| 5 | 16.13 ± 0.05 | 2.07 ± 0.10 | 1.38 ± 0.08 | 0.14 ± 0.10 |
| 6 | 15.14 ± 0.04 | 1.1 ± 0.06 | 0.84 ± 0.05 | 0.22 ± 0.06 |
| 7 | 14.36 ± 0.04 | 0.6 ± 0.06 | 0.39 ± 0.05 | 0.12 ± 0.06 |
| 8 | 17.16 ± 0.06 | 0.96 ± 0.08 | 0.57 ± 0.07 | 0.17 ± 0.08 |
| 9 | 15.79 ± 0.05 | 1.15 ± 0.08 | 0.7 ± 0.06 | 0.16 ± 0.07 |

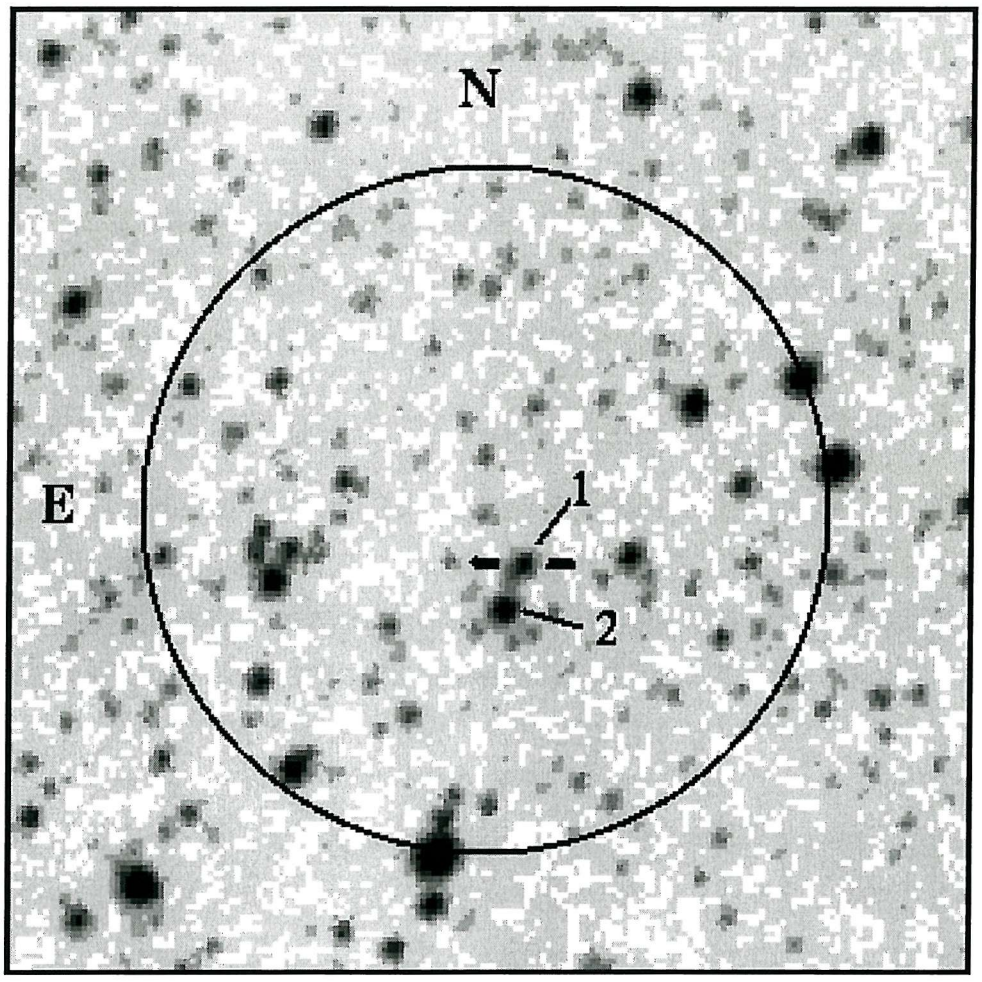


**Figure 5-1.** 3 x 3 arc-minute finding chart for the RX J0032.9-7348 with proposed counterpart marked as object number 1.

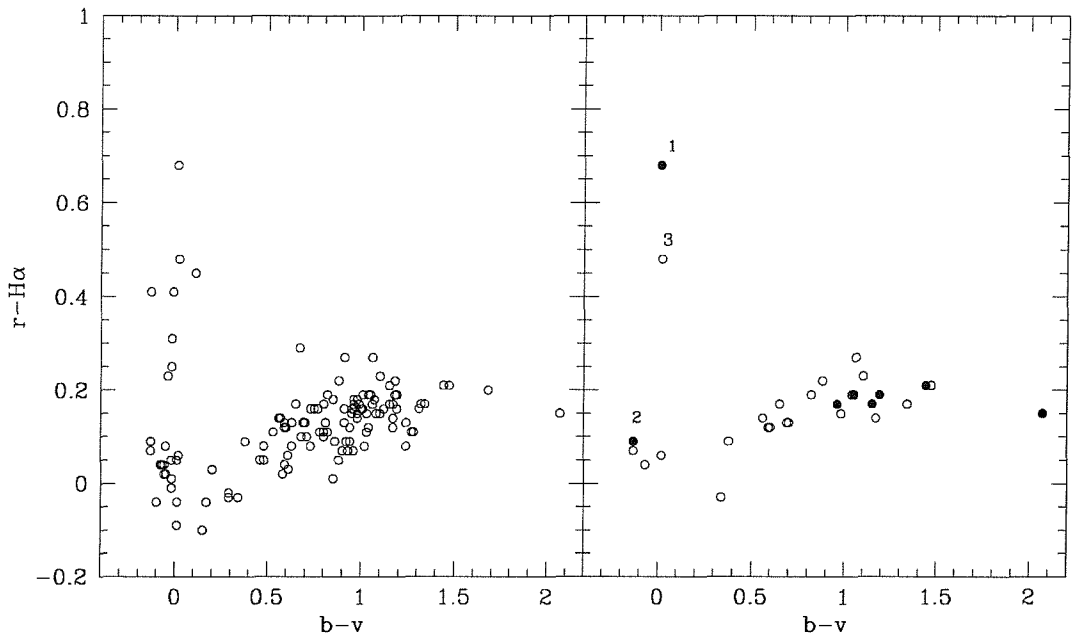


**Figure 5-2.** Emission-colour diagram for objects in the field of RX J0032.9-7348. The proposed counterpart is marked as object number 1. Left-hand plot shows all objects in CCD frame, right hand plot shows those objects within 124 arc-minutes (twice the uncertainty radius) of the best X-ray position. Objects lying within the uncertainty radius are plotted as filled circles. (See also note concerning axis labels in Section 5.2.2).

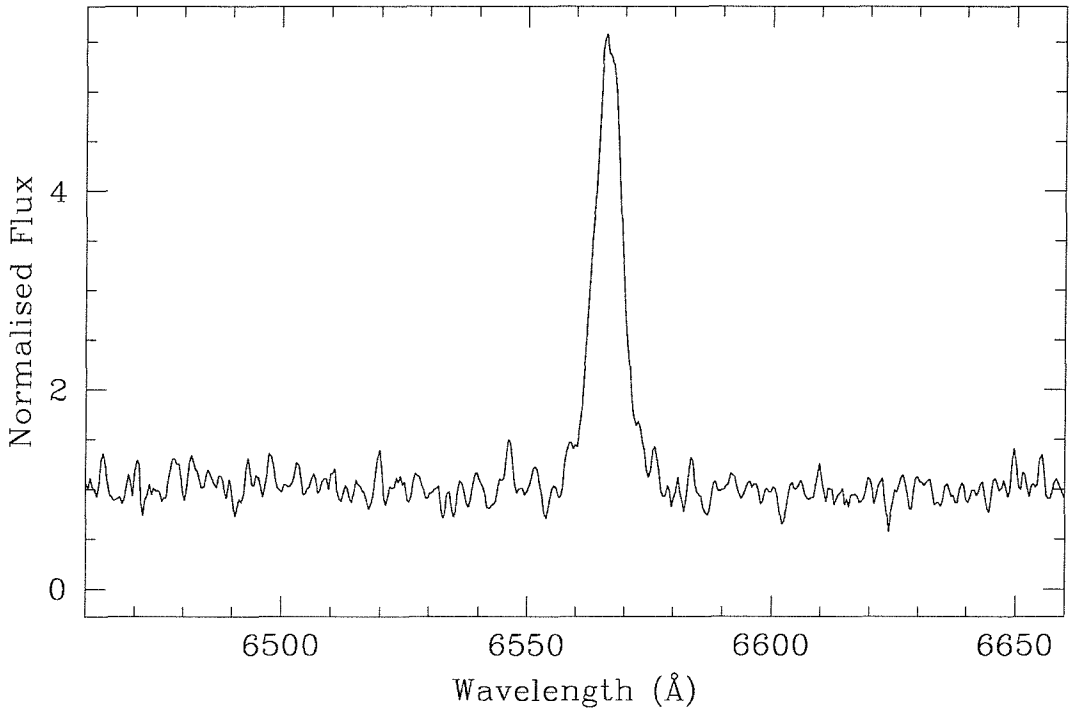


**Figure 5-3.** Hα spectrum of the proposed counterpart to RX J0032.9-7348.

### 5.3.2 RX J0049.1-7250

This source was discovered with *ROSAT* (KP1996) in pointed observations. It appears highly absorbed, and its X-ray luminosity was found to be variable by a factor of more than 10. KP1996 concluded that the source probably lay behind the SMC, with a maximum luminosity of ~$10^{38}$ ergs $s^{-1}$, but they could not rule out a time variable background AGN nature for the source.

A new X-ray pulsar was discovered by the *RXTE* satellite during observations centred on the position of SMC X-3. A pulsation was detected with a period of 74.8 ± 0.4 seconds (Corbet et al. 1998b). Follow up observations with the *ASCA* satellite made on 1997 November 13 detected pulsation with a period of 74.675 ± 0.006 seconds (Yokogawa & Koyama 1998). The 2 arc-minute X-ray error circle from the *ASCA* observations contained the ROSAT error circle for RX J0049.1-7250. Kahabka & Pietsch (1998) report that the source showed a high degree of variability, having gone undetected in a 35 kilosecond *ROSAT* HRI observation on 1997 May 9-25, and concluded that a Be/X-ray binary nature was probable for the source.

A finder chart is shown in Figure 5-4 with the *ROSAT* error circle marked. Figure 5-5 shows the emission-colour diagram for objects detected in *BVR* and *Hα* frames. The left hand plot shows all stars in the field, the right hand plot shows those objects within 44 arc-seconds of the X-ray position (twice the positional uncertainty), with those objects that lie *inside* the X-ray error circle plotted as filled circles. The majority of field stars are evolved red objects, whilst amongst the early type stars ~20% show Hα emission.

Only one Be star is found within the X-ray error circle, lying only 3 arc-seconds from the X-ray position (marked as object 1 in Figure 5-4 and 5-5). The other Be star which appears on the right hand plot in Figure 5-5 (object 2) lies 25 arc-seconds from the X-ray position (also marked as object 2 on the finder chart in Figure 5-5). *V* magnitudes and photometric indices for 4 objects within the X-ray error circle detected in all frames are shown in Table 5-5.

Based on the positional coincidence, object 1 is most probably the counterpart to the X-ray pulsar, though it is possible that future X-ray observations may move the X-ray error circle to include object 2.

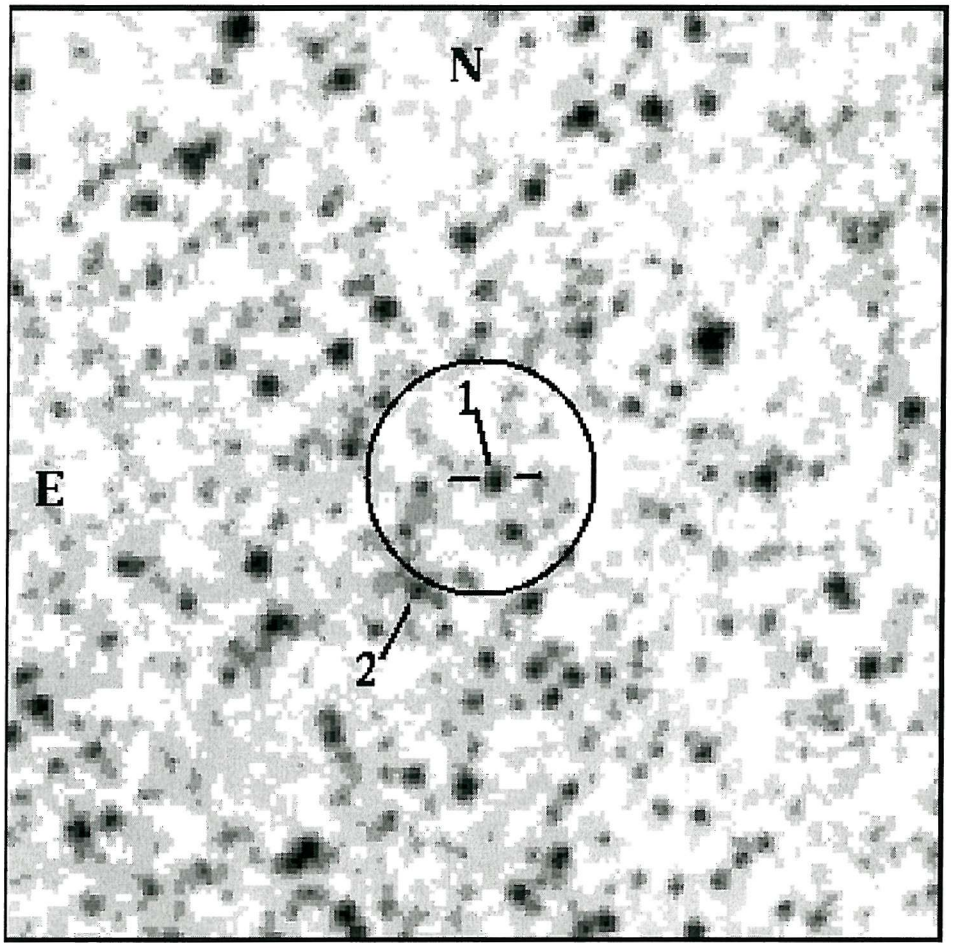


**Figure 5-4.** 3 x 3 arc-minute finding chart for RX J0049.1-7250 with proposed counterpart marked as object number 1.

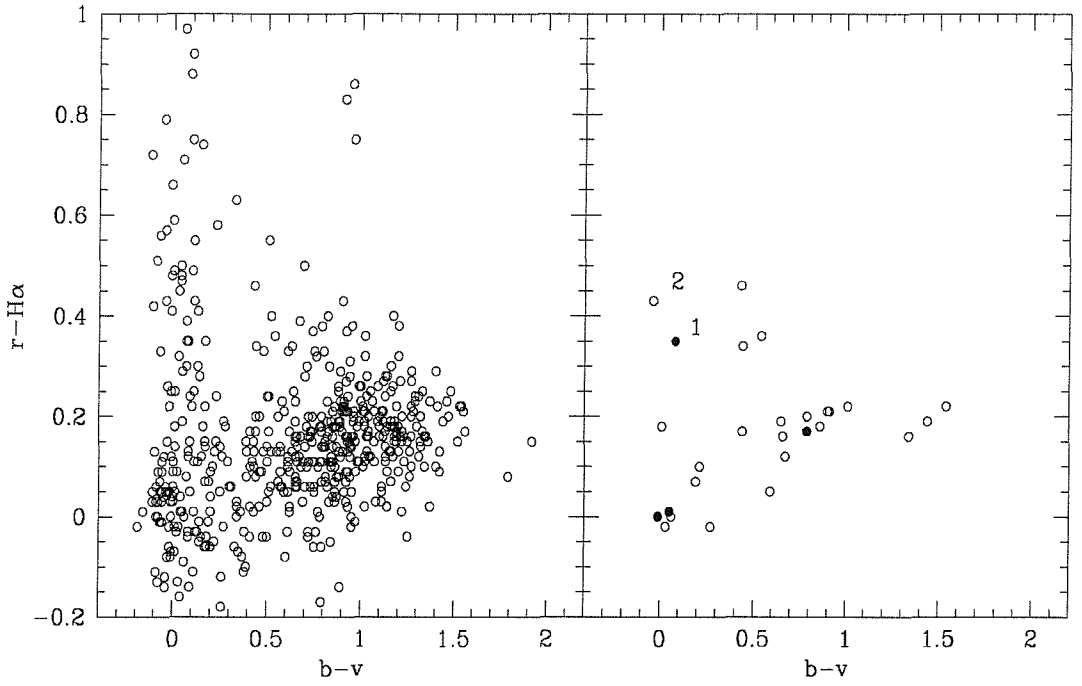


**Figure 5-5.** Emission Colour Diagram for objects in the field of RX J0049.1-7250. The proposed counterpart is marked as object number 1. Left hand plot shows all objects in CCD frame, right hand plot shows those objects within 44 arcminutes (twice the uncertainty radius) of the best X-ray position. Objects lying within the uncertainty radius are plotted as filled circles. (See also note concerning axis labels in Section 5.2.2).

**Table 5-5.** Photometry of the objects within the X-ray error circle of RX J0049.1-7250.

| Object | V | B-V | V-R | R-Hα |
|---|---|---|---|---|
| 1 | 16.28 ± 0.06 | 0.08 ± 0.08 | 0.02 ± 0.08 | 0.32 ± 0.07 |
| 3 | 17.40 ± 0.04 | -0.01 ± 0.05 | -0.03 ± 0.07 | -0.03 ± 0.10 |
| 4 | 17.24 ± 0.03 | 0.05 ± 0.04 | -0.07 ± 0.07 | -0.02 ± 0.08 |
| 5 | 17.12 ± 0.05 | 0.79 ± 0.10 | 0.46 ± 0.06 | 0.14 ± 0.05 |

### 5.3.3 AX J0051-722

This source was first detected as a 91.12 second pulsar in *RXTE* data (Corbet et al. 1998a) though was initially confused with the nearby 46 second pulsar RX J0053.8-7226 (Buckley et al. 1998). Further observations with *ASCA* revealed two pulsars in the field with an approximate 2 to 1 ratio in periods, the 91 second period belonging to the new source, AX J0051-722. Further observations with *ROSAT* reduced the positional uncertainty to 10 arc-seconds.

We performed spectroscopic observations of the brightest object in this error circle on 1998 February 3. The spectrum shown in Figure 5-7 shows the $H\alpha$ line strongly in emission, with an equivalent width of –22 Å. The centre of the line corresponds to a velocity of 165 ± 24 km $s^{-1}$, consistent with SMC membership.

We have no photometry of objects in this field, but estimate $V \sim 15$ from Digitised Sky Survey images. This, together with the $H\alpha$ emission and radial velocity indicates an early Be star in the SMC. With an X-ray positional uncertainty of only 10 arc-seconds, we conclude that this Be star is the optical counterpart to the X-ray pulsar.

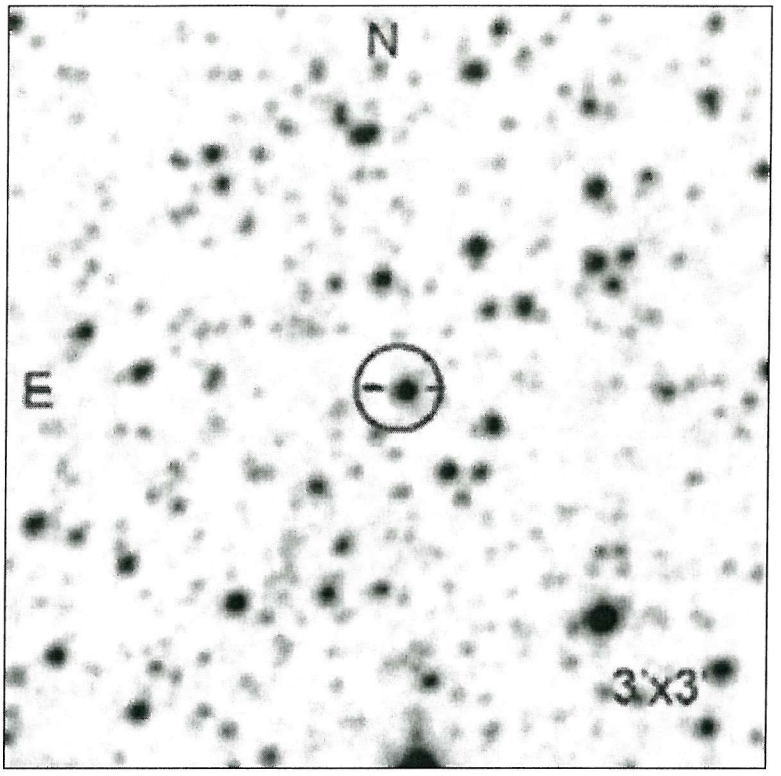


**Figure 5-6.** 3 x 3 arc-minute finding chart for AX J0051-722 with proposed counterpart marked.

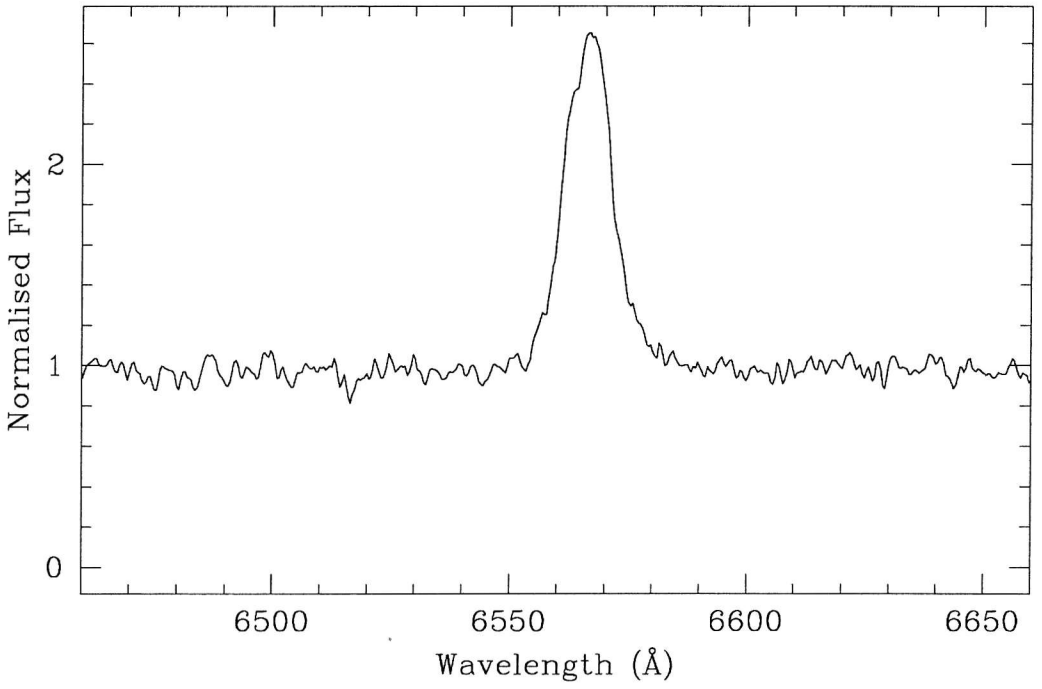


**Figure 5-7.** Hα spectrum of the proposed optical counterpart to AX J0051-722.

### 5.3.4 RX J0051.8-7231

RX J0051.8-7231 was discovered in *Einstein* observations. The X-ray error circle included the bright SMC star AV 111, which was suggested as the optical counterpart. (Bruhweiler et al. 1987, Wang & Wu 1992).

The source displays time variability, as demonstrated by an increase in luminosity by more than a factor of ten in ~1 year, and by a factor of ~5 in 5 days (KP1996). The X-ray luminosity, time-variability and hard spectrum led KP1996 to suggest a Be/X-ray binary nature for the source.

Israel et al. (1997) detected pulsation from the X-ray source, with a period of 8.9-seconds. They obtained optical CCD images of the field, and concluded that both AV111 and a second star (star 1) within their error circle displayed $H\alpha$ activity. In fact, both AV111 and star 1 are excluded from the error circle derived by KP1996, which contains only one object visible in the DSS image (star 2). AV111, star 1 and star 2 are marked in Figure 5-8.

On 1998 February 2 we obtained a medium resolution Hα spectrum of this object, which is shown in Figure 5-9. $H\alpha$ is in emission with EW($H\alpha$) = -3.0 ± 1.0-Å. The line is centred at a wavelength of 6565.0 ± 1.5-Å, indicating a radial velocity of 102 ± 67 km $s^{-1}$, consistent with SMC membership.

The smaller *ROSAT* error circle of Kahabka & Pietsch seems to favour the identification of star 2 as the optical counterpart to RX J0051.8-7231, though in the light of the $H\alpha$ activity detected by Israel et al. we cannot rule out star 1, whilst AV111 appears a less likely candidate.

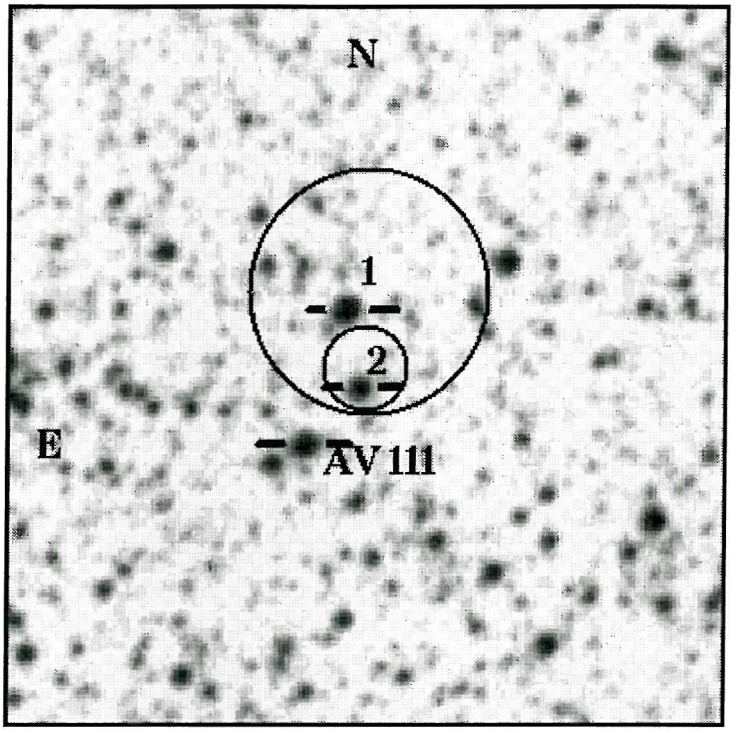


**Figure 5-8.** 3 x 3 arc-minute finding chart for RX J0051.8-7231. The candidate counterpart observed in this work is marked as object number 2, the object marked as number 1 is the object reported to show Hα activity by Israel et al.

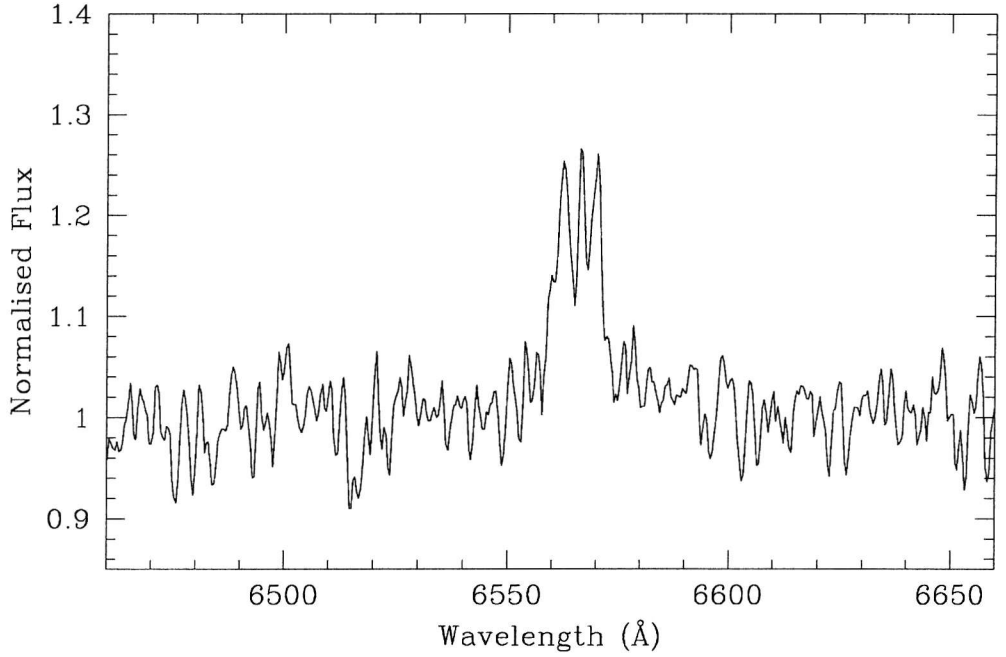


**Figure 5-9.** Hα spectrum of star 2 – a candidate counterpart to RX J0051.8-7231.

### 5.3.5 RX J0053.8-7226

This source was first detected in *Einstein* pointings (Bruhweiler et al 1987) and was subsequently detected in a number of *ROSAT* pointings. We have previously reported analysis of archival *ROSAT* data in Buckley, Coe, Stevens et al. (1998; hereafter BCS1998), finding the source to be a transient, and determining the currently most precise X-ray position of R.A. = $00^h\ 53^m\ 55.6^s$, Dec = $-72^o\ 26'\ 44''$ with a 90% confidence radius of 15″.

In 1997 November, an X-ray source identified as XTE J0053-724 went into outburst and revealed a 92-second pulse period (Corbet et al. 1997, IAUC 6788). The source was originally (incorrectly) identified with the X-ray source SMC X-3, but later observations with *ASCA* in 1997 December revealed that the pulsating source was actually 8' away from SMC X-3, at a position coincident with the *ROSAT* position we had determined for RX J0053.8-7226.

Figure 5-10 shows an optical image of the field obtained from the Digital Sky Survey, with the best *ROSAT* error circle marked. Object 1 marked in Figure 5-10, is a close double (separated by ~2 arc-seconds on a East–West axis). On 1995 September 22 we obtained low-resolution spectra of this double (reported in BCS1998). The observations indicated that one of the objects was a strong source of Hα emission, and subsequent spectra were obtained with the stellar image driven to either extreme of the slit decker, thus excluding most light from one of the two objects each in turn. This enabled us to determine that the $H\alpha$ emission originated from the fainter, *easternmost* star.

CCD photometry obtained in November 1995 is presented in Table 5-6. Object $1_{East}$ is very blue, the colours, magnitude and presence of $H\alpha$ emission are all consistent with the object being a Be star in the SMC.

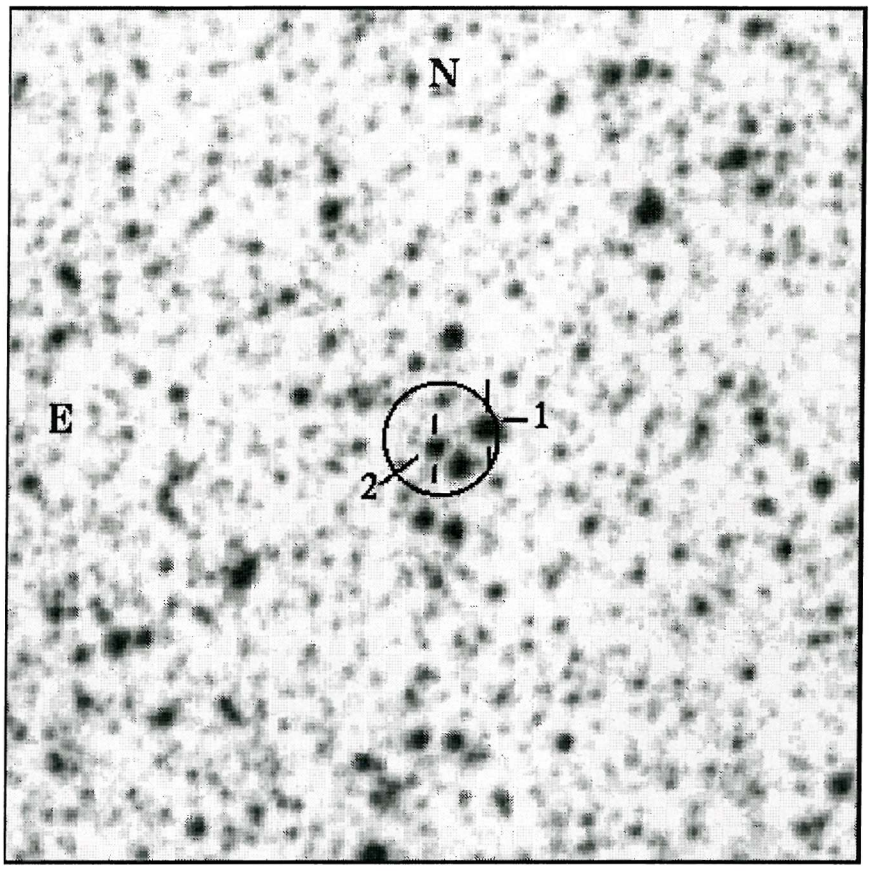


**Figure 5-10.** 3 x 3 arc-minute finding chart for RX J0053.8-7226 with proposed counterpart marked as object number 1. This object is a double – the Easternmost component is proposed as the Be star counterpart.

The identification spectra reported in BCS1998 were obtained from the SAAO using the 1.9-m telescope and the Cassegrain spectrograph with RPCS (Reticon) detector. With this instrumental configuration we were unable to obtain spectra of each component reliably uncontaminated by the other.

Further optical spectra were obtained from the SAAO using the 1.9-m telescope and the recently commissioned SITe2 CCD detector on the Cassegrain spectrograph. With this instrumental configuration we were able to obtain spectra spatially resolved along the direction of the slit. With the slit orientated along an East–West direction we were thus able to resolve the spectra of the two stars. The observations were kindly made by H. Winkler on 1997 October 2$^{nd}$. A flux standard was

observed immediately after the target to allow flux calibration of the resulting spectra.

The two flux calibrated spectra are shown in Figures 5-12 and 5-13. The Western component of the double shows a blue continuum with strong Ca H & K and Balmer absorption lines. The relative strength of the G-band with respect to *Hα* suggests an early F type star. The Eastern component shows *Hα* in emission with EW(*Hα*) = –11.6 ± 0.9-Å. Equivalent widths and radial velocity measurements determined from Gaussian fits to the *Hα* and *Hβ* lines in the RPCS and the SITe 2 spectra are shown in Table 5-7.

The CCD images obtained to search for the optical counterpart to 1WGA J0054.9-7226 (see Section 5.2) included the field of RX J0053.8-7226. We subsequently plotted an *emission–colour* diagram for RX J0053.8-7226. The result in Figure 5-11 shows that while object $1_{East}$ is confirmed as a Be star (with $R - H\alpha = 0.27$), the object marked as number 2 in Figure 5-10 is also a Be star, and one with stronger *Hα* emission, with $R - H\alpha = 0.47$. The identification of either star as the counterpart to RX J0053.8–7226 cannot be confirmed until either higher resolution X-ray images are obtained to provide a more precise X-ray position (for instance with AXAF), or correlated X-ray/optical activity is observed.

**Table 5-6.** Photometry of the two components of the double star marked as object number 1 in the finding chart in Figure 5-10.

| Object | V | U – B | B – V | $V - R_C$ | $R - I_C$ |
|---|---|---|---|---|---|
| $1_{East}$ | 14.93 ± 0.02 | -0.87 ± 0.03 | -0.05 ± 0.04 | 0.07 ± 0.05 | 0.01 ± 0.05 |
| $1_{West}$ | 14.08 ± 0.01 | 0.11 ± 0.02 | 0.37 ± 0.01 | 0.35 ± 0.01 | 0.32 ± 0.01 |

**Table 5-7.** Results of Gaussian fits to Hα and Hβ in spectra of the candidate counterpart to RX J0053.8-7226 (Eastern component of double object number 1 in Figure 5-10).

| Date | Hα | | Hβ | |
|---|---|---|---|---|
| | Velocity | EW | Velocity | EW |
| 22 September 1995 | 177 ± 15 km $s^{-1}$ | –13.1 ± 0.9 | – | – |
| 2 October 1997 | 157 ± 15 km $s^{-1}$ | –11.6 ± 0.9 | 186 ± 50 km $s^{-1}$ | –0.8 ± 0.2 |

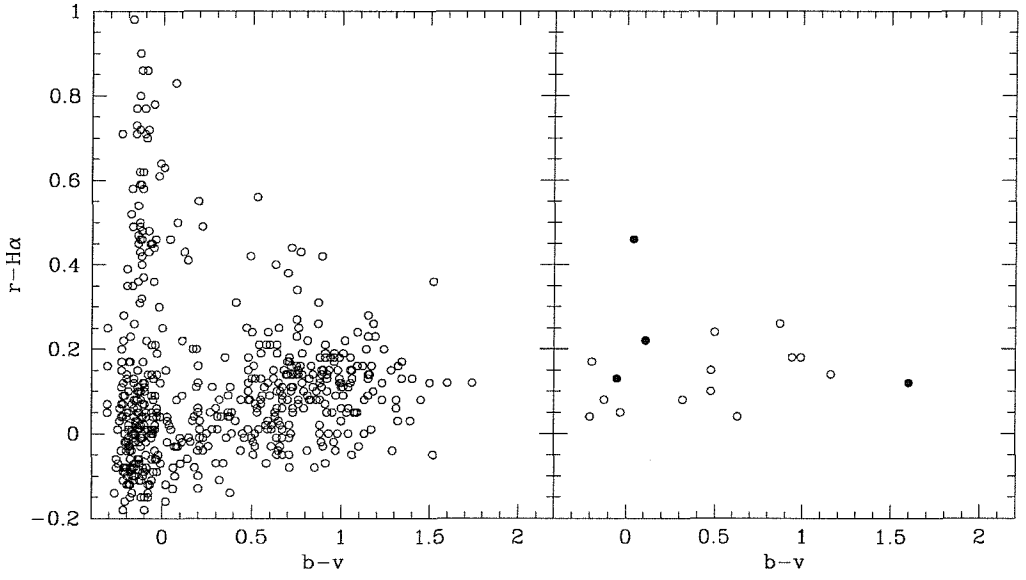


**Figure 5-11.** Emission-colour diagram for objects in the field of RX J0053.8-7226. The left hand plot shows all objects in the CCD frame, the right hand plot shows all objects within 30" (twice the positional uncertainty) of the X-ray position. Objects lying within the uncertainty radius are plotted as filled circles. (See also note concerning axis labels in Section 5.2.2).

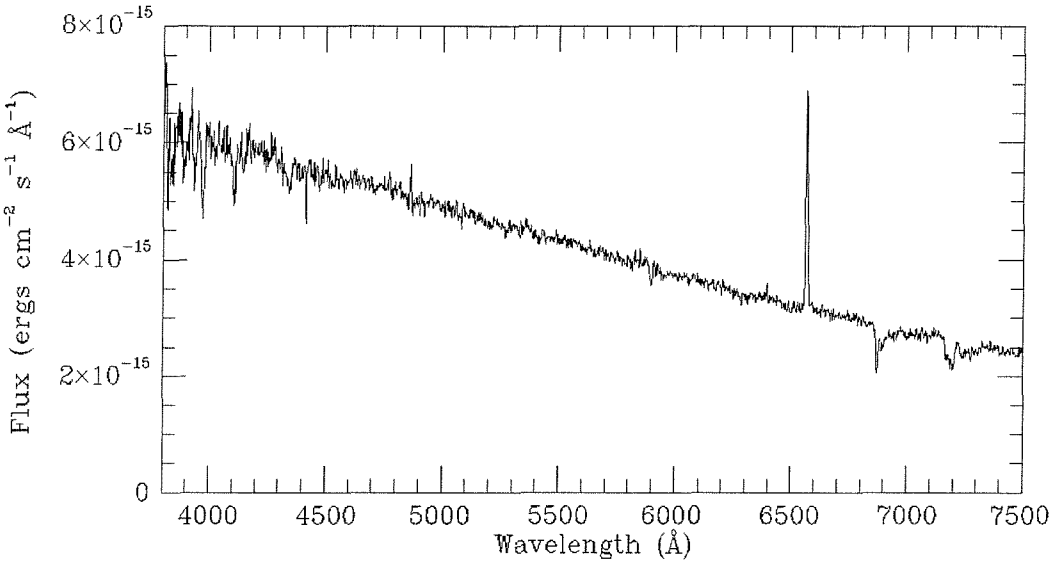


**Figure 5-12.** Hα spectrum of the *Eastern* component of the pair of stars marked as object 1 in Figure 5-10.

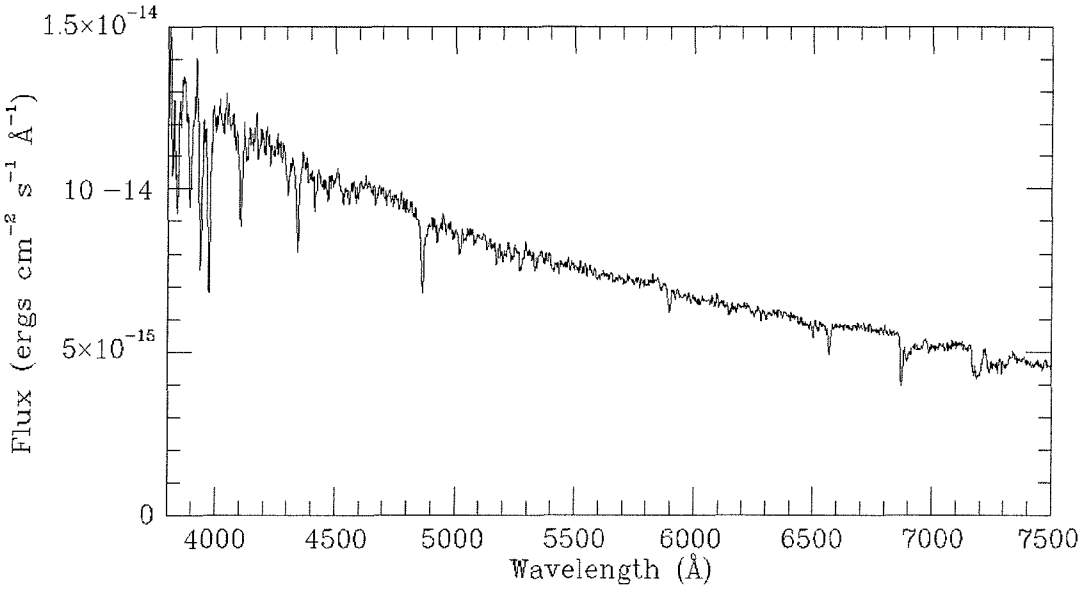


**Figure 5-13.** Hα spectrum of the F2 star ~2 arcsec west of the proposed Be star optical counterpart.

### 5.3.6 RX J0054.9-7226

This source appears in a number of catalogues based on *Einstein* observations of the SMC (Inoue Koyama & Tanaka 1983, source #35; Bruhweiler et al.1987, source #9; Wang & Wu 1992, source #35), and was detected by *ROSAT* (KP1996). KP1996 rejected an X-ray binary nature due to the lack of time variability (on a time-scale of hours).

Observations made with the *RXTE* satellite on 1998 January 20 detected a 59 second pulsar, with a positional uncertainty of ± 10 arc-minutes, consistent with the position of RX J0054.9-7226 (Marshall & Lochner 1998). Subsequent observations with *SAX* reduced the positional uncertainty to a radius of 50 arc-seconds, confirming the identification with RX J0054.9-7226, and refining the pulse period to 58.969 seconds (Santangelo & Cusumano 1998). Israel (1998) further reduced the uncertainty in X-ray position to a 10 arc-second radius from the analysis of archival ROSAT data.

We obtained *BVR* and $H\alpha$ images of the field on the night of 1996 October 5. The *emission – colour* diagram for the field is shown in the left-hand plot of Figure 5-15. The right hand plot contains those objects that lie within 20 arc-seconds of the X-ray position (twice the radius of the X-ray error circle), with those objects that lie within the error circle plotted as filled circles.

Four objects are detected within the X-ray error circle, all identified as early type stars by their $B - V$ colours. Of these, only one shows strong $H\alpha$ emission, with a $R - H\alpha$ value of 0.49 (marked as object 1 in Figures 5-14 and 5-15).

We obtained spectra of this object (object 1) on the nights of 1998 February 4 and 5. The medium resolution $H\alpha$ spectrum obtained is shown in Figure 5-16. The Hα line shows strong emission, with an equivalent width of EW($H\alpha$) = –25 ± 2-Å. Fitting a single Gaussian to the line yields a radial velocity of 137 ± 28-km $s^{-1}$, con-

sistent with SMC membership. The low-resolution spectrum in Figure 5-17 shows Hβ also clearly in emission.

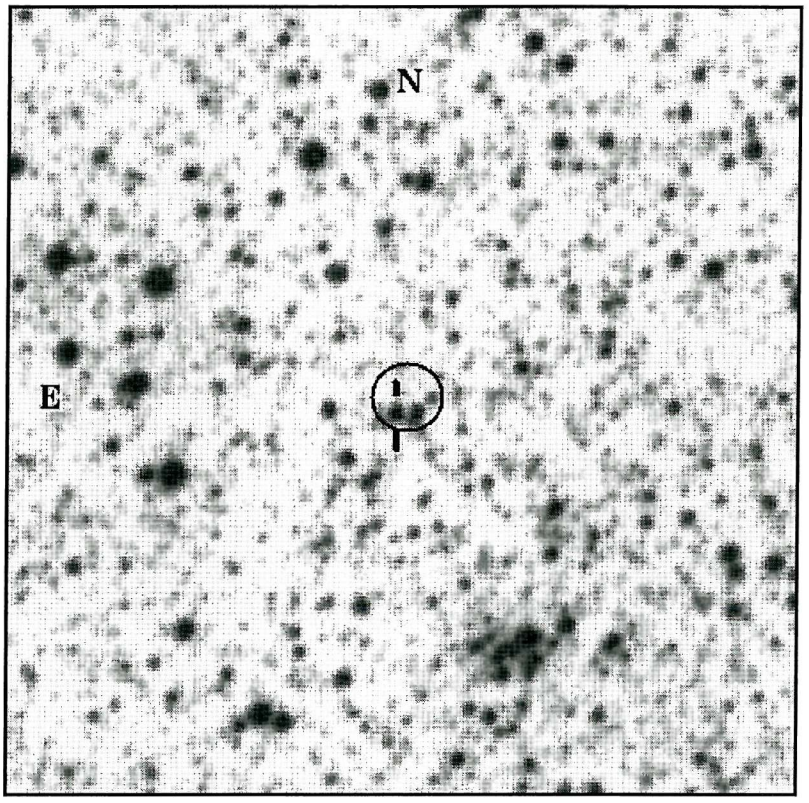


**Figure 5-14.** Finding chart for RX J0054.9-7226

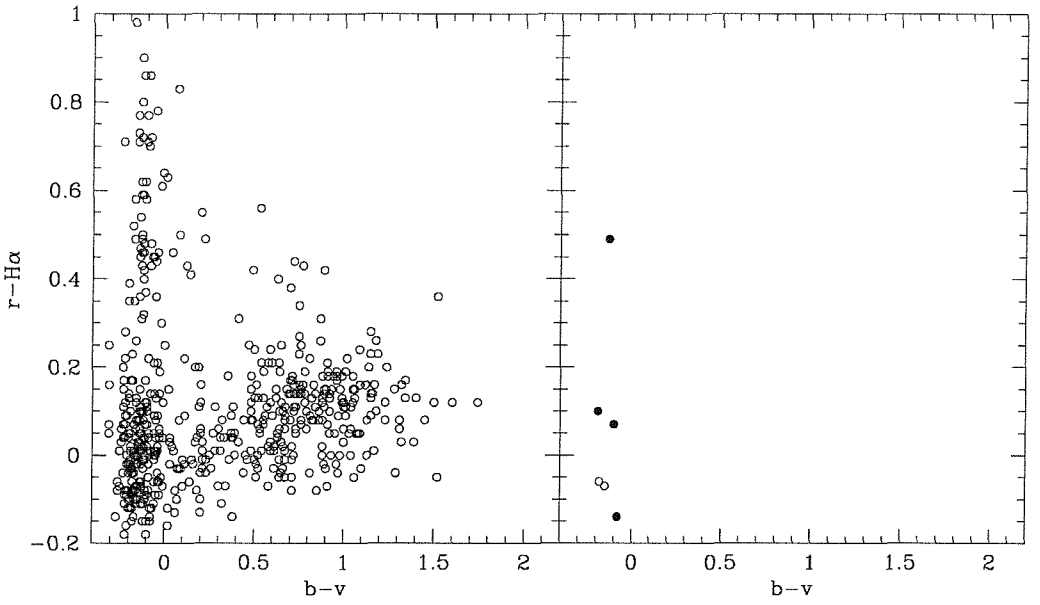


**Figure 5-15.** Emission-Colour diagram for objects in the field of RX J0054.9-7226. The left hand plot shows all objects in the CCD frame, the right hand plot shows all objects within 20" (twice the positional uncertainty) of the X-ray position. Objects lying within the uncertainty radius are plotted as filled circles. (See also note concerning axis labels in Section 5.2.2).

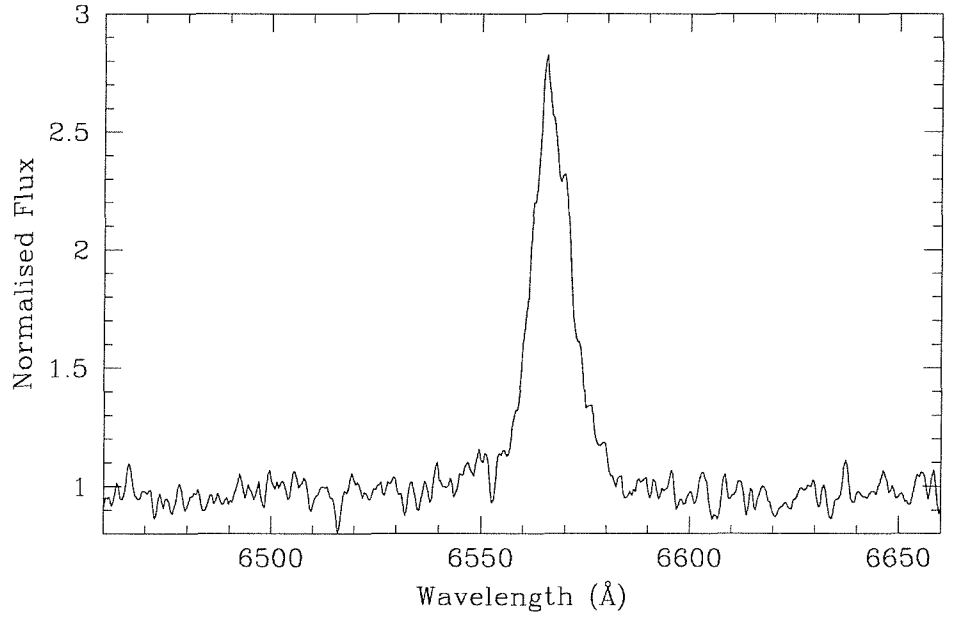


**Figure 5-16.** Hα spectrum of the proposed optical counterpart to RX J0054.9-7226

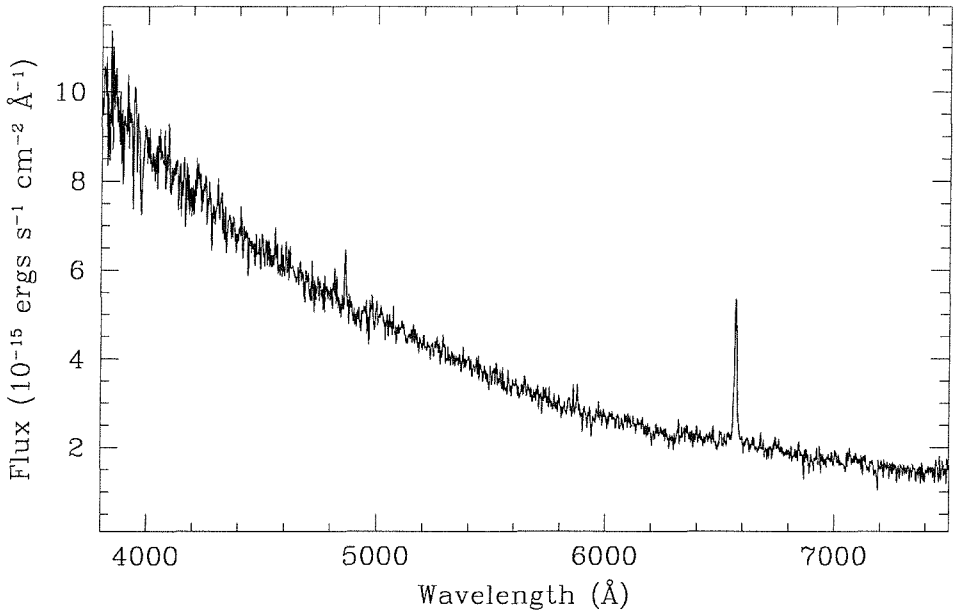


**Figure 5-17.** Low resolution flux calibrated spectrum of the proposed optical counterpart to RX J0054.9-7226

### 5.3.7 RX J0101.0-7321

This X-ray source was discovered in *ROSAT* pointed observations in 1991 October. Observations approximately 6 months later failed to detect the source, suggesting a transient nature (KP1996). KP1996 claim that the source is most likely associated with a 15-16$^{th}$ magnitude Be star. To the authors' knowledge, no observations of this star have previously been published.

We obtained $R_C$ and $H\alpha$ images of the field of RX J0101.0-7321 on 1995 October 1$^{st}$. Figure 5-19 shows the measured $H\alpha$ magnitudes plotted against the measured $R_C$ -band magnitudes. A clear linear relationship exists between $R_C$ and $H\alpha$; the scatter at magnitudes $R_C > 15.5$ can be attributed to uncertainties in the $H\alpha$ magnitudes.

Three points show Hα excesses that appear to be much greater than the local scatter of points, these points are numbered on the plot. Objects 2 and 3 each lie a few arc-minutes from the X-ray position, whilst the error associated with this position is only 11 arc-seconds. Object 1 lies only 10 arc-seconds from the X-ray position (See the finder chart in Figure 5-18).

On 1998 February 3 we obtained an $H\alpha$ spectrum of object 1. The spectrum, shown in 5-20, has a strong $H\alpha$ emission line, with EW($H\alpha$) = –60 Å. The $H\alpha$ line is centred at a wavelength of 6566.0 ± 0.5-Å, corresponding to a velocity of 148 ± 23-km s$^{-1}$. These data confirm that object 1 is a Be star in the SMC. As this is the only such object within several arc-minutes of the X-ray position, we identify object 1 as the optical counterpart, and confirm a Be/X-ray binary nature for this X-ray source.

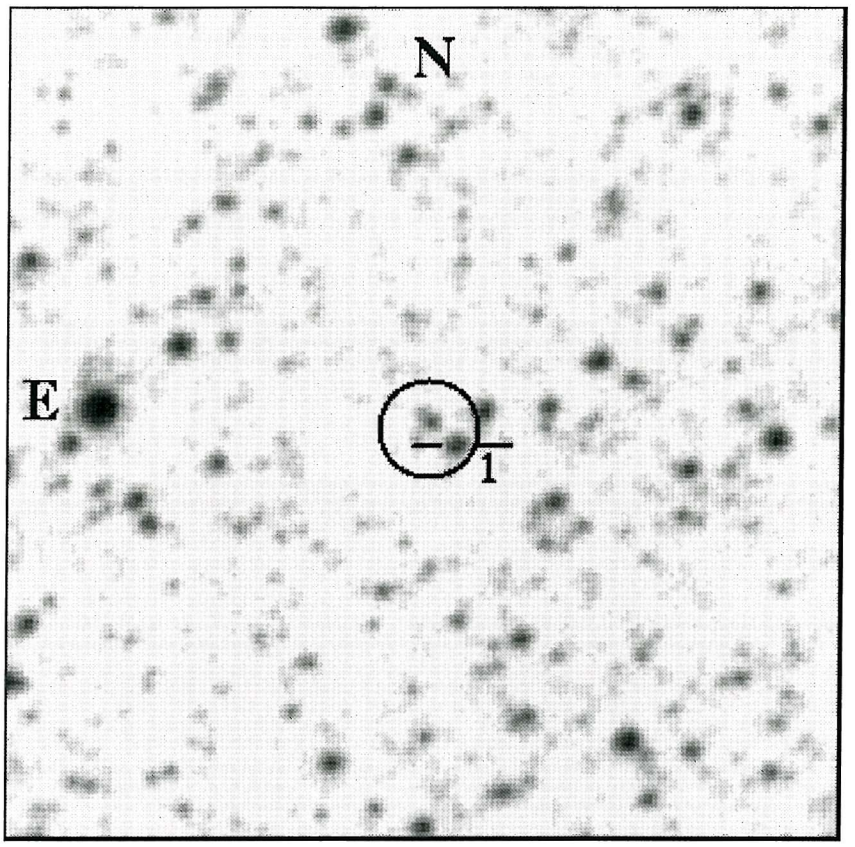


**Figure 5-18.** 3 x 3 arc-minute finder chart for RX J0101.0-7321.

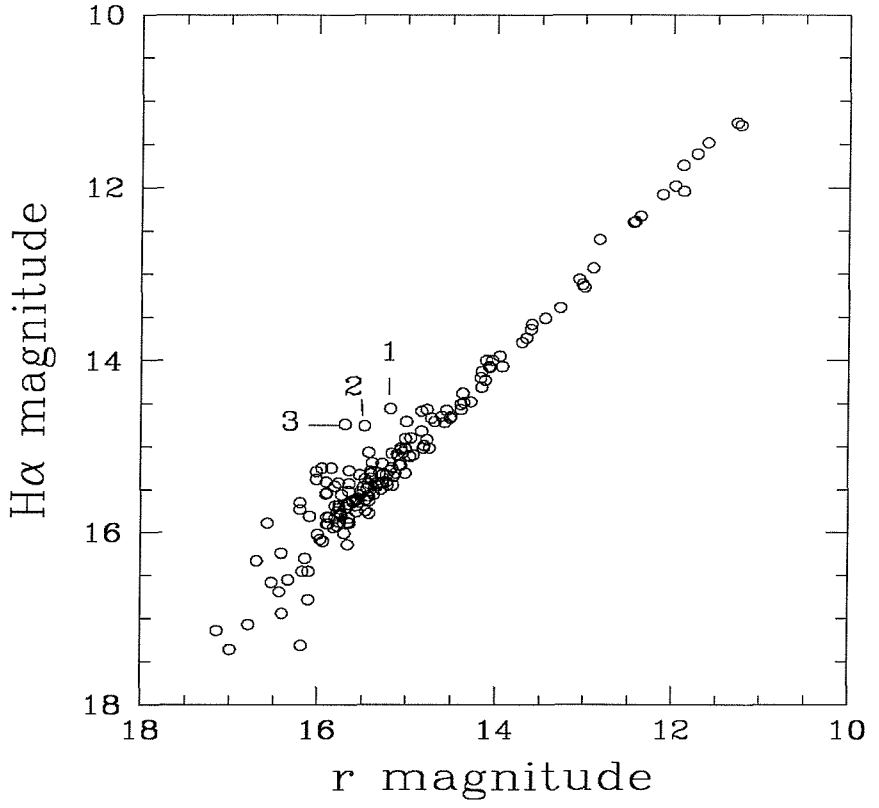


**Figure 5-19.** *Hα* vs. $R_C$ diagram for objects in the field of RX J0101.0-7321. (See also note concerning axis labels in Section 5.2.2).

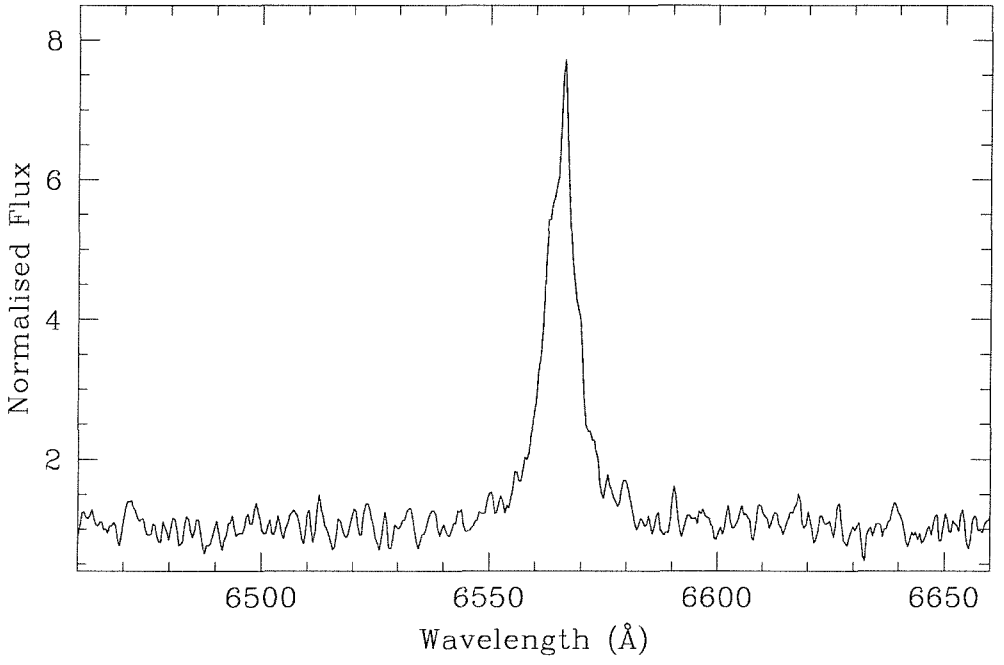


**Figure 5-20.** *Hα* spectrum of the proposed optical counterpart to RX J0101.0-7321.

### 5.3.8 RX J0117.6-7330

This X-ray transient was discovered by *ROSAT* on 1992 October 1 (Clark, Remillard & Woo 1996, 1997), located 5 arc-minutes from the known SMC X-ray binary SMC X-1. The X-ray error circle contained only one object brighter than ~15$^{th}$ magnitude. This optical candidate was reported to be a Be star by Charles, Southwell & O'Donoghue (1996).

Optical photometry of the proposed counterpart was obtained from the SAAO in 1996 January and October. The results are shown in Table 5-8. No significant variability is seen on the timescale of months or days. In addition, on 7$^{th}$ October 1996, we cycled between *B* and *V* filters continuously for 1 hour, finding no variability significant above the errors in the observations (approximately 0.03 magnitudes).

**Table 5-8.** Optical photometry of the counterpart to RX J0117.6–7330.

| Date | B ( ± 0.03) | V ( ± 0.03) | R ( ± 0.03) |
|---|---|---|---|
| 1996 January 24 | 14.24 | – | 14.20 |
| 1996 January 25 | 14.23 | 14.23 | – |
| 1996 January 26 | 14.26 | 14.23 | 14.17 |
| 1996 January 27 | 14.24 | 14.25 | 14.16 |
| 1996 January 28 | 14.33 | 14.22 | 14.16 |
| 1996 October 3 | 14.33 | 14.26 | 14.22 |
| 1996 October 4 | 14.26 | 14.27 | 14.22 |
| 1996 October 5 | 14.27 | 14.29 | – |
| 1996 October 6 | 14.26 | 14.26 | 14.19 |
| 1996 October 7 | 14.27 | 14.28 | 14.20 |

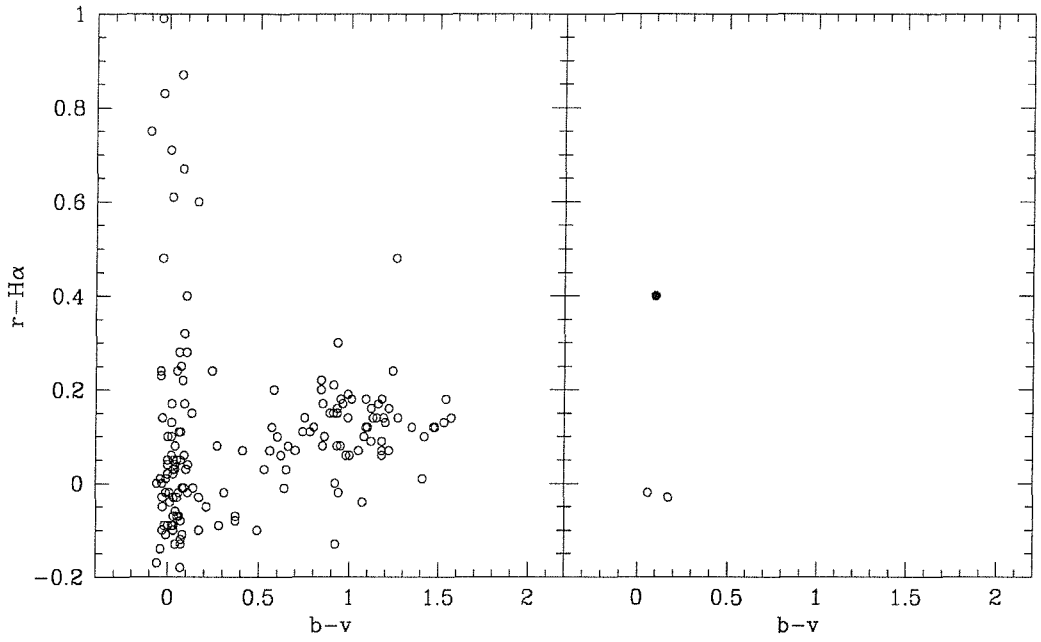


**Figure 5-21.** Emission-colour diagram for objects in the field of RX J0117.6-7330. The left hand plot shows all objects in the CCD frame, the right hand plot shows all objects within 20" (twice the positional uncertainty) of the X-ray position. Objects lying within the uncertainty radius are plotted as filled circles. (See also note concerning axis labels in Section 5.2.2).

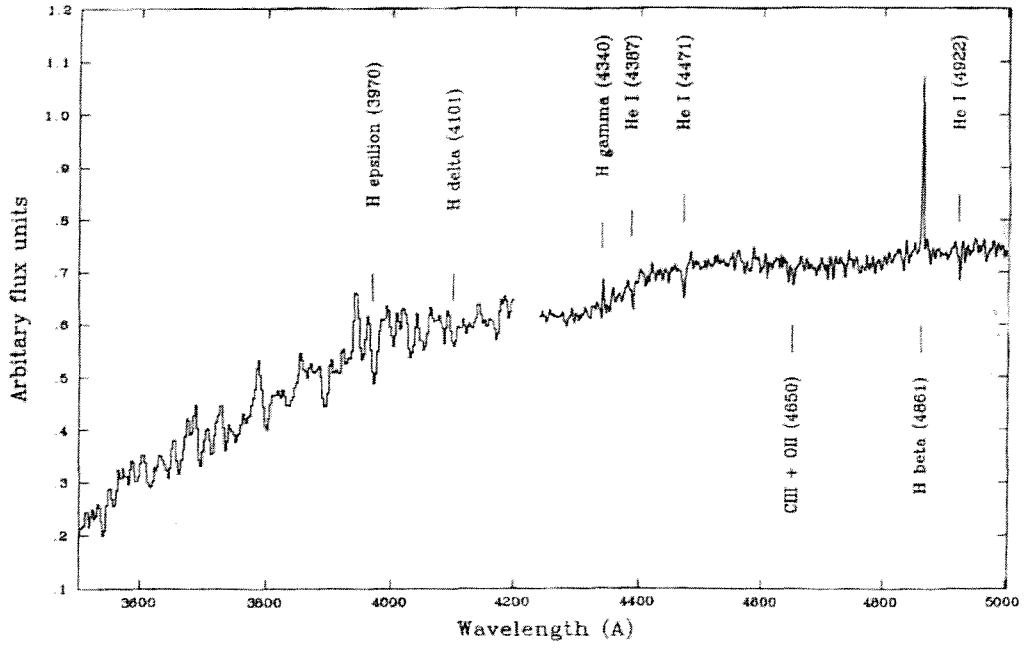


**Figure 5-22.** Classification region spectrum of the proposed counterpart to RX J0117.6–7330. The spectrum is a composite of spectra obtained on 1996 January 18th and October 6th.

Figure 5-21 shows the *emission – colour* diagram for objects in the field. Clearly only one object within 3 times the positional uncertainty shows a $B-V$ index and $H\alpha$ emission index consistent with a Be star nature. This object corresponds to the object in the X-ray error circle identified by Charles, Southwell & O'Donoghue (1996).

Hα spectra were obtained on 1996 January 18th (2 spectra) and 1996 October 5th (2 spectra). The EW($H\alpha$) for each were measured to be 16.0 ± 0.3, 16.9 ± 0.4, 21.6 ± 1.2 and 16.9 ± 1.1 Å.

#### 5.3.8.1 Spectral classification

Classification region spetra were obtained of this object on 18th January 1996 and 6th October 1996. These spectra have been combined in Figure 5-22. Following Walborn & Fitzpatrick (1990) the following conclusions can be drawn from these spectra:

- The presence of He I lines at λ = 4387-Å and at λ = 4471-Å indicates a spectral type in the range B0 – B5.
- The lack of He II lines in the spectrum suggests a spectral class later than B0.5.
- The absence of Si IV indicates a spectral type of B1 or later.
- Weak C III/O III blend indicates B1 – B2 with luminosity class V.
- The lack of Mg II (λ = 4481-Å) indicates B0 – B2.

From these criteria, a spectral type of B1–2Ve is suggested.

We also measured the $\beta$ index for this object on October 6th 1996. This was found to be 2.478 ± 0.005. The $\beta$ index (Crawford & Mander 1966) provides a measure of luminosity class for O- and B-type stars. However, in the case of Be stars the $\beta$ index becomes a function of both the luminosity of the star and the $H\beta$ emission from the circumstellar disc.

Fabregat & Reglero (1990) give corrections for *uvby* and $\beta$ indices for Be stars, using the measured $H\alpha$ equivalent width as a parameter giving a measure of the circumstellar Balmer emission. For the $\beta$ index they find an intrinsic (corrected for circumstellar emission) value $\beta_*$ given by:

$$\beta_* = \beta - 0.0044EW(H\alpha) + 0.026 . \quad (5\text{-}1)$$

Our values of EW($H\alpha$) and $\beta$ then lead to $\beta_* = 2.583 \pm 0.005$. The error is only a formal photometric error, as Fabregat & Reglero do not give an uncertainty for their correction.

The value for the intrinsic $\beta$ index is consistent with a luminosity class III for spectral class B0 – B0.5. However, an uncertainty of $\pm$ 0.02 in the correction of Fabregat & Reglero would allow luminosity class III, spectral type B0 – B2, and luminosity class V, spectral type B0 – B1.

With all of the above taken into consideration, we assign a spectral type for RX J0117.6–7220 of B0–1 III-V.

### 5.3.9 EXO 0531.1-6609

This source was discovered by *EXOSAT* during deep observations of the LMC X-4 region in 1983 (Pakull et al. 1985). It was detected again in 1985 by the *SL2 XRT* experiment. The lack of detection in *EXOSAT* observations made between these dates demonstrates the transient nature of the source. The object was identified with a Be star by Pakull (private communication). The counterpart proposed by Pakull is the northern component of a close double. A finder chart for the field is shown in Figure 5-23 with the ROSAT X-ray error circle marked.

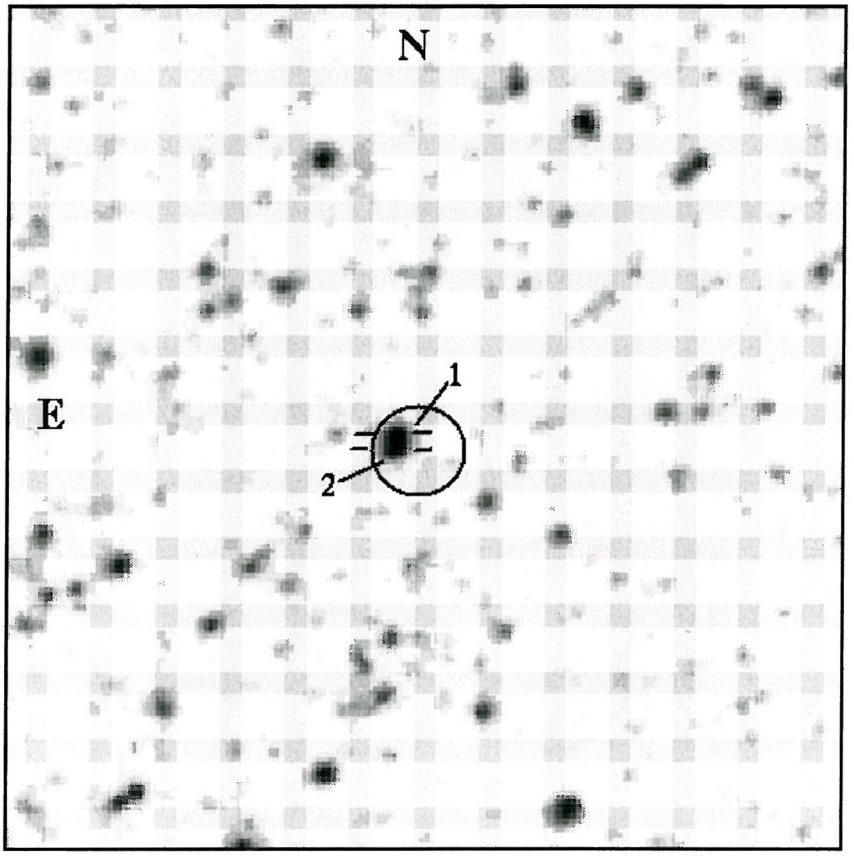


**Figure 5-23.** 3 x 3 arc-minute finder chart for EXO 0531.1-6609.

The components of this double are marked 1 and 2 in Figure 5-23. The positions of the two objects in the *emission – colour* diagram in Figure 5-24 indicate that both have weak Hα emission. With our chosen criterion of a Be star having $R - H\alpha \geq 0.2$ then object 1 is the only Be star within the X-ray error circle, with $R - H\alpha = 0.21$. Object 2 has $R - H\alpha = 0.15$. Within the uncertainties however, our data do not favour one object over another as emission line objects.

On 1998 February 3 we obtained a spectrum of the northern component of the double. The resulting spectrum shown in Figure 5-25 confirms the presence of Hα emission, with EW(Hα) = -10.0 ± 1.0 Å. The line is centred on a wavelength of 6568.7 ± 0.5 Å, corresponding to a velocity of 272 ± 23 km $s^{-1}$. On 1998 February 5 we obtained a low resolution, flux calibrated spectrum of this object (shown in Figure 5-26), showing Hβ also in emission with EW(Hβ) = -0.5 ± 0.2 Å. No spectrum has yet been obtained of the Southern component of the double.

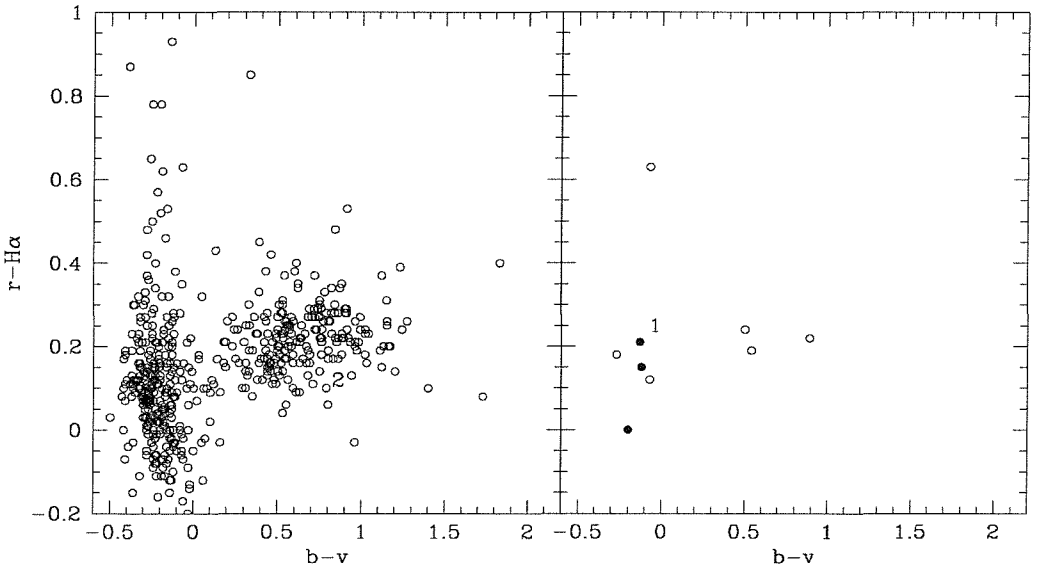


**Figure 5-24.** Emission-colour diagram for objects in the field of EXO 0531.1-6609. The left hand plot shows all objects in the CCD frame, the right hand plot shows all objects within 18" (twice the positional uncertainty) of the X-ray position. Objects lying within the uncertainty radius are plotted as filled circles. (See also note concerning axis labels in Section 5.2.2).

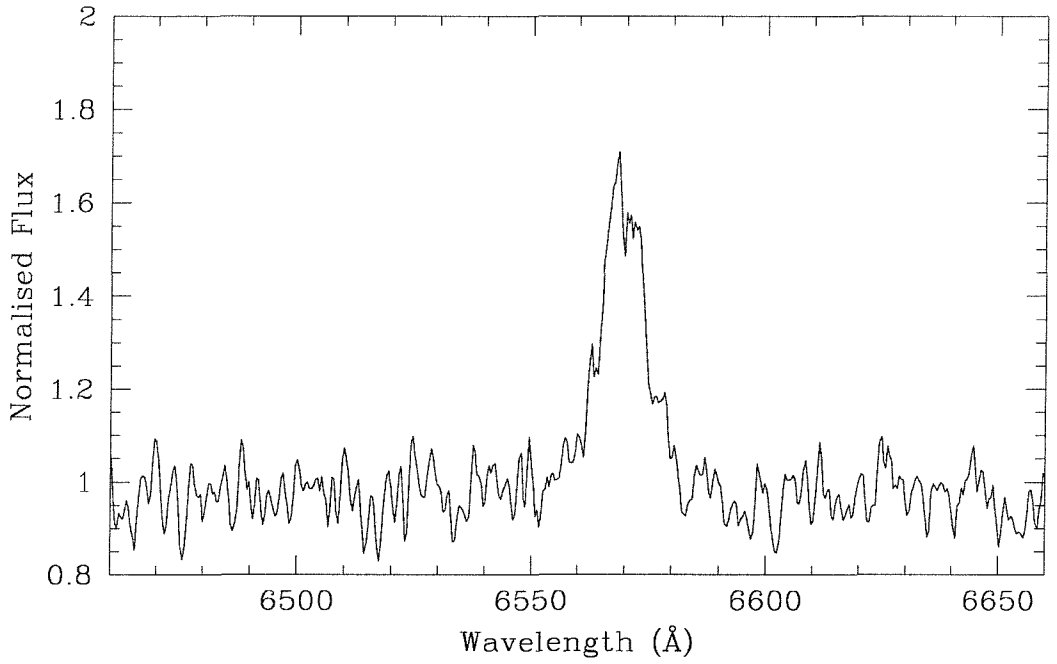


**Figure 5-25.** Hα spectrum of the northern component of the pair of candidate optical counterparts to EXO 0531.1-6609.

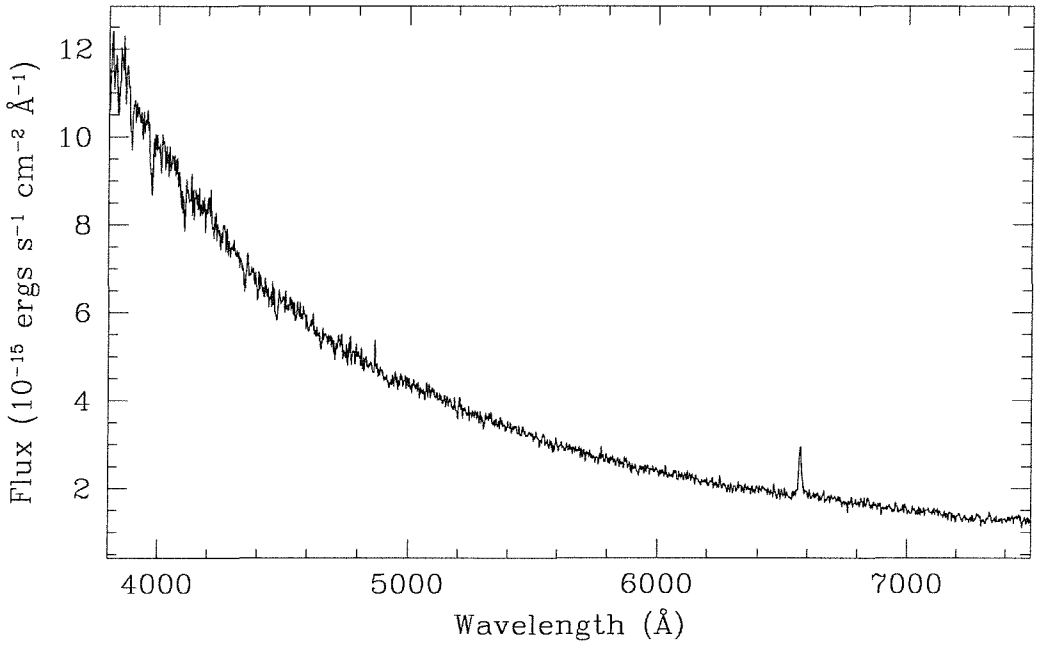


**Figure 5-26.** Low-resolution flux calibrated spectrum of the Northern component of the pair of candidate optical counterparts to EXO 0531.1-6609

In order to determine which object is the counterpart to the X-ray source, it will be necessary to obtain an X-ray position to sub-arc-second accuracy, possible with the forthcoming *AXAF* mission, or to find optical/infrared variations in one of the objects which correlate with X-ray behaviour.

### 5.3.10 H0544-644

This source was discovered with the *HEAO-1* scanning modulation collimator by Johnston, Bradt & Doxsey (1979).

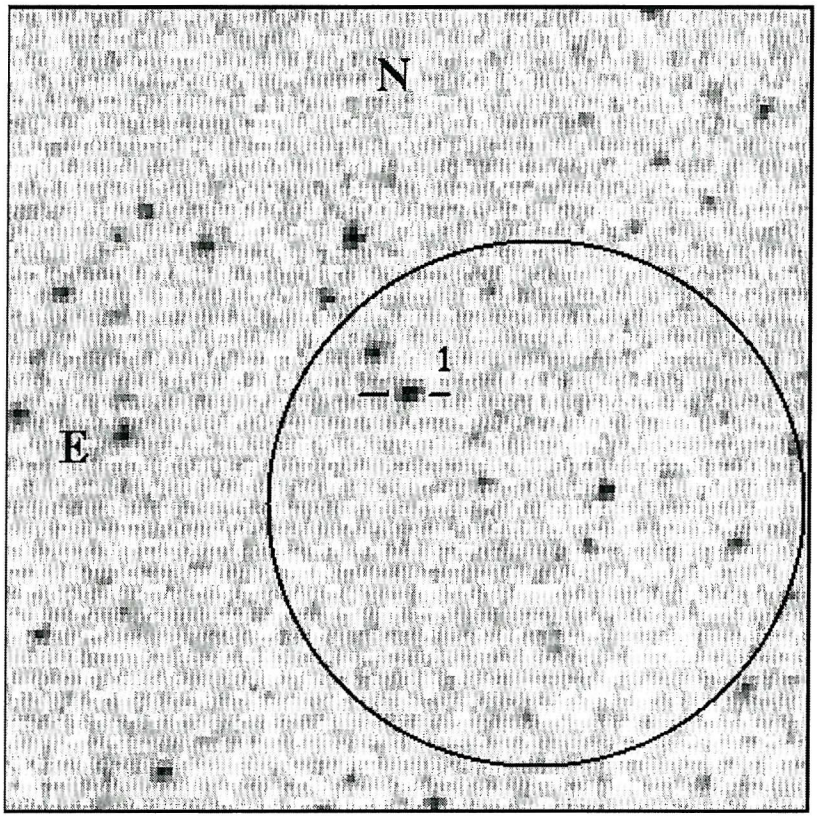


**Figure 5-27.** Finding chart for H0544-665 with proposed counterpart marked as object number 1.

The brightest object within the X-ray error circle (star 1 in Figure 6 of Johnson, Bradt & Doxey 1979) was found to be a variable B0-1 star (van der Klis et al. 1983 and references therein) but no emission lines have been observed in its spectrum to identify it as a Be star. Van der Klis et al. (1983) published photometry that showed a negative correlation between optical magnitudes and colour indices, typical of Be stars whose variability is due to variations in the circumstellar disc. The authors expressed concern at the lack of other obvious Be star spectral characteristics, but suggested that the object may be a Be star in a low state of activity.

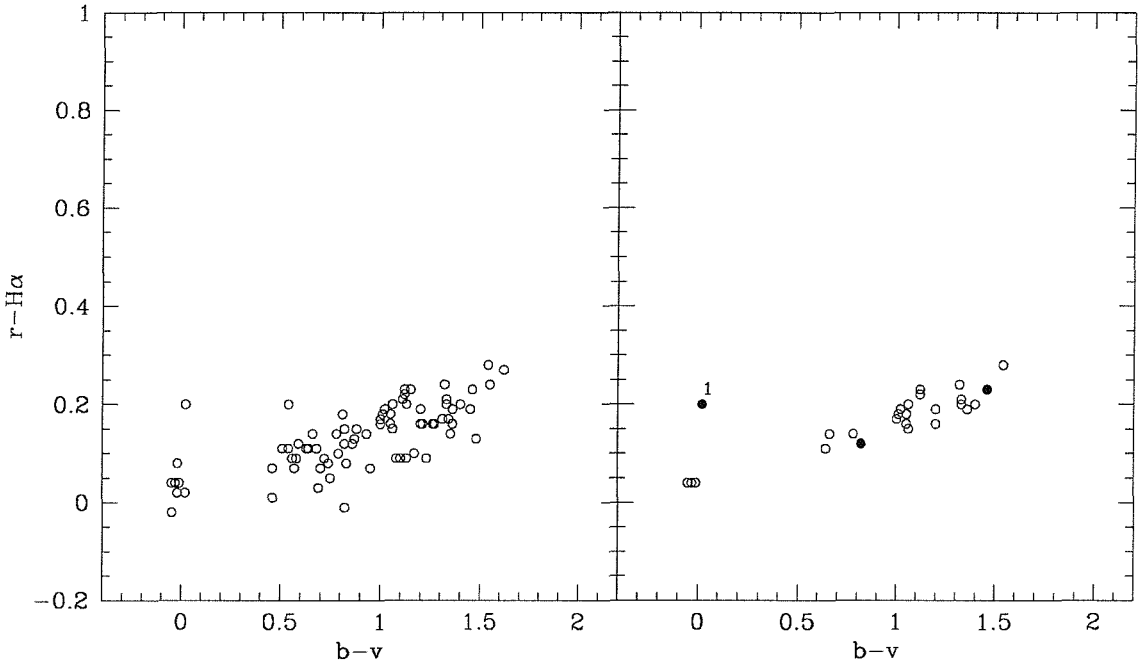


**Figure 5-28.** Emission-colour diagram for objects in the field of H0544-665. The left hand plot shows all objects in the CCD frame, the right hand plot shows all objects within 1' (twice the positional uncertainty) of the X-ray position. Objects lying within the uncertainty radius are plotted as filled circles. (See also note concerning axis labels in Section 5.2.2).

Figure 5-28 shows the *emission – colour* diagram for objects in the field. In the 4 arc-minute radius area searched, only one object displays *B-V* colours and *R-Hα* index indicative of a Be star, this object is identified as object 1 in Figures 5-27 and 5-28, and corresponds to the object 1 of Johnson, Bradt & Doxey (1979).

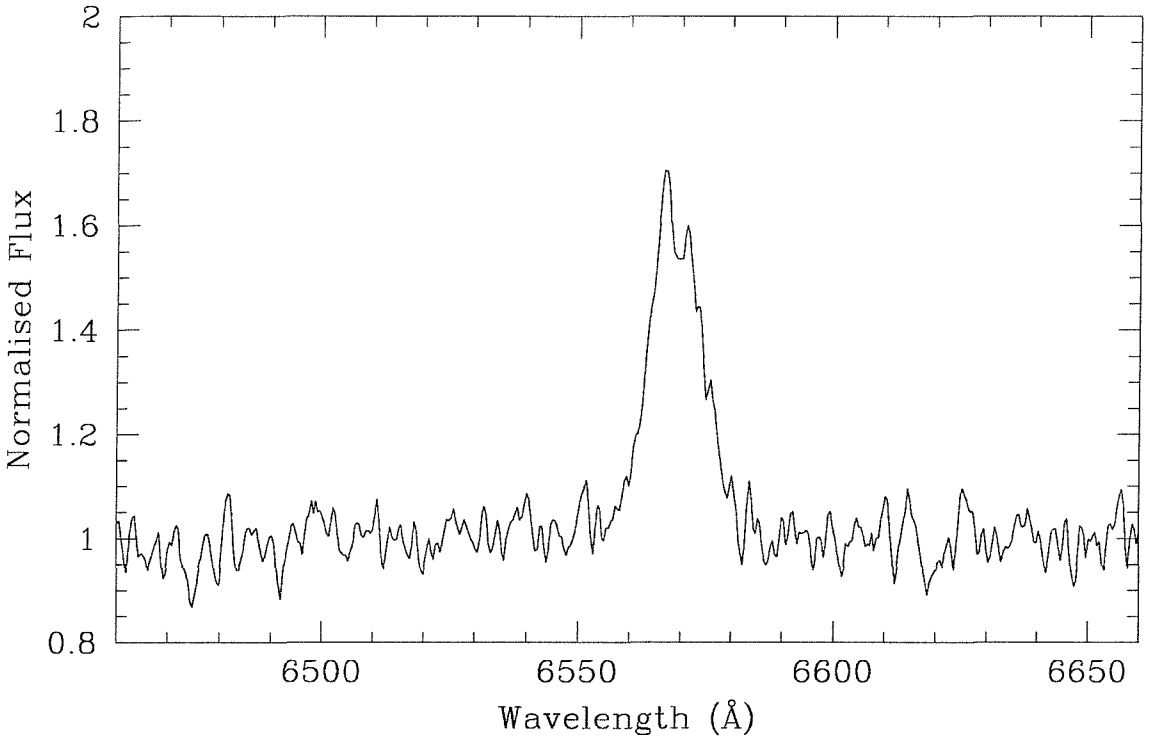


**Figure 5-29.** Hα spectrum of the proposed counterpart to H0544-665.

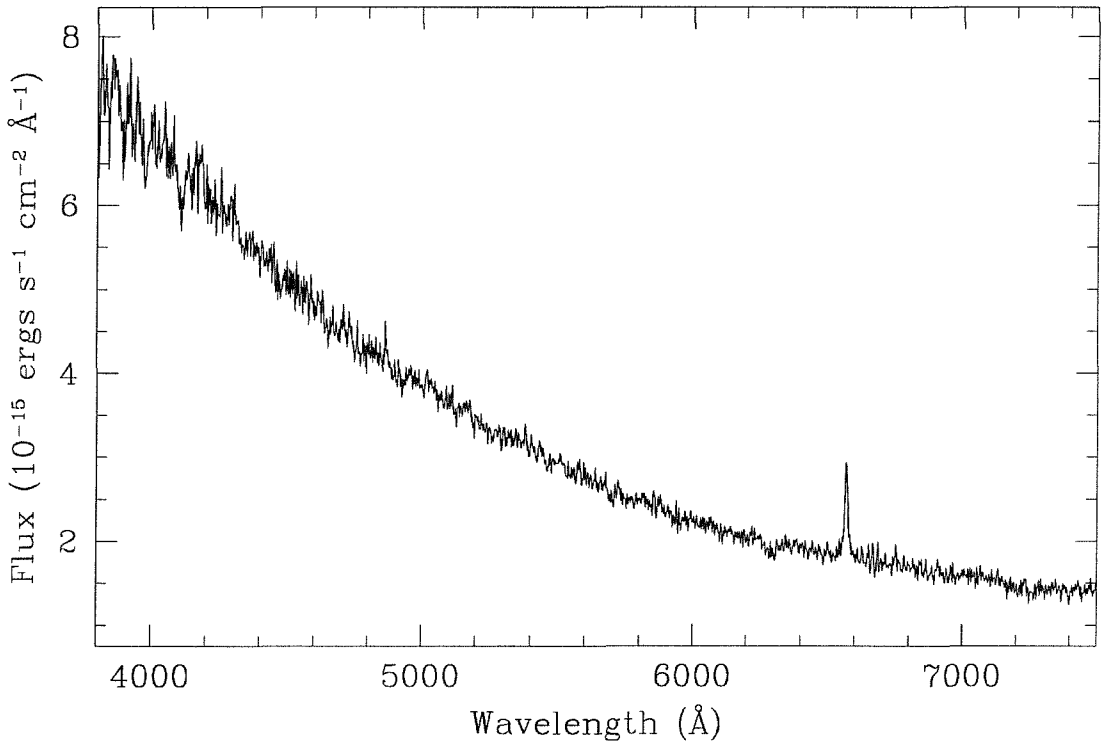


**Figure 5-30.** Low-resolution flux calibrated spectrum of the proposed counterpart to H0544-665.

We obtained optical spectra of this object in 1998 February, these are shown in Figures 5-29 and 5-30. The Hα line is clearly in emission, with an equivalent width measured from the medium resolution spectrum EW(Hα) = 8.7 ± 1.0 Å. The profile is double peaked with a peak separation of 181 ± 30 km $s^{-1}$, the mean velocity of these peaks is 282 ± 20 km $s^{-1}$, consistent with the LMC velocity of 275 km $s^{-1}$ given by Westmerlund (1997), but lower than the 369 ± 42 km $s^{-1}$ measured for Balmer absorption lines in this object by van der Klis et al (1983). The low resolution spectrum in Figure 5-20 shows also weak Hβ emission with EW(Hβ) = -0.7 ± 0.5 Å.

To the authors' knowledge, these observations represent the first detection of emission lines in the spectrum of this star. We confirm a LMC Be star nature and, due to the lack of other emission line objects in or near the X-ray error circle, we conclude that this star is the optical counterpart of the X-ray source.

## 5.4 Discussion

The photometric method used to identify Be star candidates has proved successful. In each case where spectroscopic observations have been made, the Be star nature of the object has been confirmed. The strength of this approach is illustrated in 5-31 which shows the relationship between the measured $R - H\alpha$ index from photometric data and the EW(Hα) of each object for which both such data were available. There appears to be a direct correlation, with the exception of one obvious point – RX J0101.0-7321. This seemingly anomalous point may be explained by variability, as the photometric and spectroscopic observations were made over 1 year apart. The indication is that the Be star counterpart in this system underwent some change between 1996 October and 1998 February, which resulted in a large increase in the amount of circumstellar material. Apart from the difficulty of unpredictable variability highlighted by this case, our approach is clearly an excellent method of identifying Be star counterparts to Magellanic Cloud X-ray sources.

A note of caution must be added to the above discussion. We must be careful to assess the probability of finding by chance a Be star in a given area of sky in order to estimate the confidence of our identifications. From the 7 fields examined photometrically in all of *B*, *V*, *R* and *Hα*, a total of 277 objects matched our criteria for Be status. The total area of sky covered by our sample is 352 square arc-minutes. This gives an average Be star occurrence of 0.8 per sq. arc-minute. It is clear that in the case of some of the objects, which have ~ arc-minute. sized error circles, the size of these positional uncertainties need to be reduced, or simultaneous variability observed between the X-ray and optical/infrared bands, before definite confirmation of the counterparts is established.

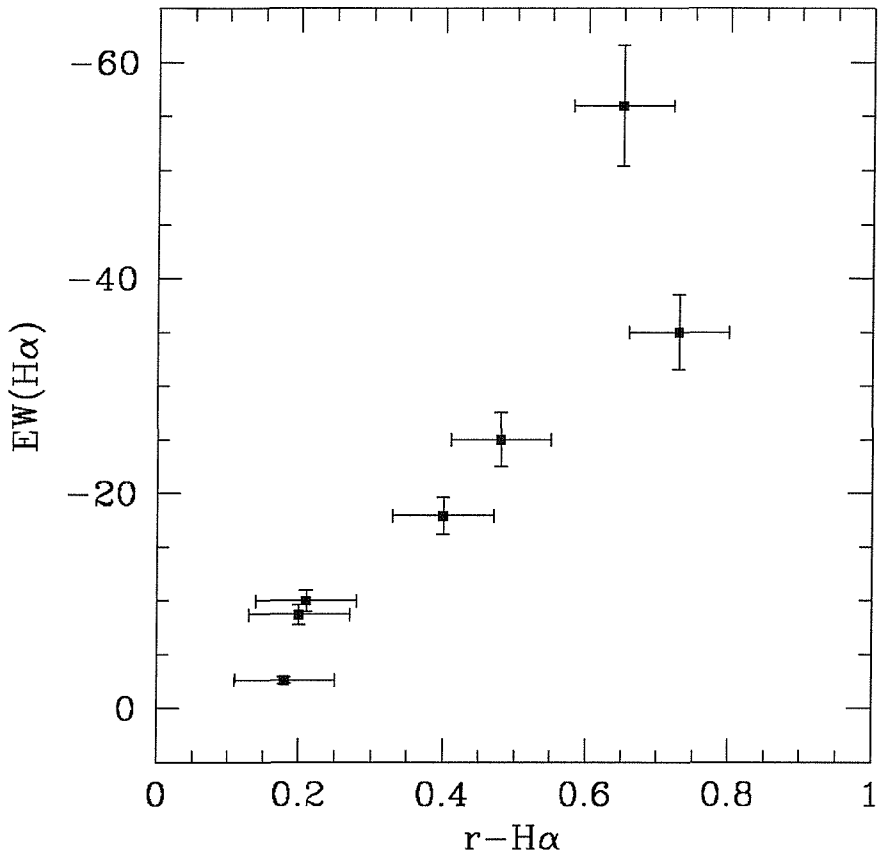


**Figure 5-31.** Relationship between EW(Hα) and R-Hα for optical counterpart candidates in this study

The number of Be/X-ray binary systems known in the Magellanic Clouds is now increased to 12 in the SMC and 7 in the LMC, including those sources in this study for which we have confidence in an unambiguous identification of an optical counterpart of Be (III–V) spectral type. These numbers compare with 29 known in our own Galaxy. Scaling simply by mass, we should expect the number of Be/X-ray binaries in the LMC and SMC to be 0.1 and 0.01 times the number in the Galaxy respectively. In fact we find, especially in the SMC, what appears at first to be an abnormally large Be/X-ray binary population.

The discrepancy might be explained through consideration of a number of points:

a) Studies of cluster populations in the SMC have shown a higher proportion of Be stars amongst early type stars than in the Galaxy; this may be due to the effects of metallicity on a radiatively driven wind. If a higher proportion of B type stars in the SMC have circumstellar envelopes, then for a given population of B star/Neutron star binaries, a higher proportion of SMC systems than Galactic systems would be accreting X-ray systems.

b) The star formation history of the SMC may have resulted in a hump in the stellar age distribution such that a higher proportion of SMC stars are of the appropriate age to have evolved into Be/X-ray binary systems. Such a scenario would require an increase in star formation activity ~$10^7$ years ago. Supporting evidence for such a hypothesis comes from the HI work of Staveley-Smith et al (1997) who deduce from studies of six expanding shells in the SMC a dynamical age of 5.4 Myr. They conclude that there must have been an exceptional degree of star formation throughout the SMC at this time.

# Chapter 6 – Conclusions and further work

## 6.1 Summary of significant results

The conclusions reached from the work described in this thesis are summarised in the following sections.

### 6.1.1 4U1145–619

The Be star V801 Cen – the optical counterpart to the Be/X-ray binary 4U1145-619 was shown from a number of photometric and spectroscopic methods to be a B0.5Ve star at a distance of 3-kpc. It was shown that if the distances to other Be/X-ray binaries derived through similar methods are accepted instead of the distances derived from Hipparcos observations, then the accepted Be/X-ray binary model of accreting neutron stars orbitting Be stars is preferred over any other model.

The circumstellar disc of V801 Cen has been shown to be in decline during the period of this study. The infrared magnitudes have increased, whilst the infrared photometric indices indicate the source becoming 'bluer' in colour. The equivalent width of the Hα line decreased from a maximum of –45Å to a minimum of –7Å.

Analysis of the line profiles of V801 Cen during this period of decline showed that the extent of the emitting radius in the disc was also decreasing in size.

### 6.1.2 Be/X-ray binary lightcurve models

The X-ray lightcurve model developed in Chapter 4 was found to fit observed lightcurves well. In particular, the model was fit to X-ray observations of the Be/X-ray binary EXO 2030+375, indicating that a change in the outflow velocity in the Be star's disc could have caused a phase shift observed in the X-ray maximum.

Spectroscopy of V801 Cen (=4U1145-619) during an X-ray outburst suggests evidence for perturbation of the Be star's disc by the motion of the neutron star during periastron passage. This important result prompts caution in applying simple models to Be/X-ray binary lightcurves, and also in using studies of Be/X-ray binaries to infer properties of Be stars in general.

### 6.1.3 Optical counterparts to Magellanic Cloud Be/X-ray binaries

I have identified Be star counterparts to the *ROSAT* sources RX J0032.9-7348, RX J0049.1-7250, RX J0054.9-7226 and RX J0101.0-7206, and to the recently discovered *ASCA* source AX J0051-722 and confirmed the Be star nature of the counterpart to the *HEAO1* source H0544-66.

For a number of other Be/X-ray binaries, I have identified a number of candidate optical counterparts which require further study to determine an unambiguous counterpart.

The technique of plotting all field objects on a R–Hα/B-V diagram was found to be extremely effective in identifying emission line objects. Using CCD images covering areas of many square arcminutes, this proves an efficient way of identifying candidate counterparts to unidentified X-ray sources.

## 6.2 Possibilities for further investigation

### 6.2.1 Disc perturbation by orbiting neutron star

Many studies of Be/X-ray binaries have been made in an attempt to learn more about Be stars in general. If the spectroscopic variability found in V801 Cen during periastron passage of its orbiting neutron star companion is confirmed to be due to binary interaction, then such studies must be interpreted with caution.

Further investigation is strongly encouraged. High quality observations of the source (and other Be/X-ray binaries) throughout many orbital phases is desirable in order to search for similar variability at other orbital phases – hence reducing the likelihood of being caused by binary interaction, or repeated appearance of the variations only during periastron passage would add weight to the suggestion that the passage of the neutron star through its closest approach to the Be star (and the associated rapid change in the potential field) significantly perturbs the disc material.

### 6.2.2 Enhanced X-ray lightcurve models

While the X-ray lightcurve model employed in Chapter 3 has proven useful in providing an interpretation of the observed behaviour of the source EXO 2030+375, there are many factors not considered by the model.

As discussed in Chapter 3, X-ray heating of the circumstellar disk close to the neutron star will result in an inconstant sound speed, as this have some dependency on the X-ray luminosity. The model also considers only a 2-dimensional system, with no provision for an inclination between the planes of the orbit and the circumstellar disk. Another factor that could be considered is the structure of the circumstellar disk itself, and how the predicted lightcurves vary between different disk models.

### 6.2.3 Identification of optical counterparts to Be/X-ray binaries

The CCD imaging technique employed in Chapter 5 to search for optical counterparts to Be/X-ray binaries in the Magellanic Clouds proved extremely successful. The technique in its current form works because generally speaking, all objects in the CCD frames obtained are subject to the same degree of interstellar reddening.

The technique could be applied in Galactic fields if the Q parameter is used on the X axis of the plot, in place of the B-V index. The Q parameter is a function of U-B and B-V and presents a reddening independent measure of intrinsic colours.

### 6.2.4 Association of LMC/SMC HMXBs with SNRs

The distances of the Magellanic Clouds make them an ideal laboratory to study spatial characteristics of stellar populations. Hughes & Smith (1994) identified two Be/X-ray binaries in the SMC which are spatially coincident with supernova remnants. As Be/X-ray binaries form when one component of a double massive star binary explodes in a supernova to leave a neutron star, it is no great surprise to find these associations.

A radio survey could be undertaken of the fields of LMC and SMC HMXBs to search for extended radio emission that could be identified as emission from a supernova-remnant (SNR). If a sample of HMXB/SNR associations could be established, then these would put constraints on the kick velocities imparted to neutron stars in SN explosions by considering the separation between the spatial position of the HMXB and the centre of the SNR.

# Acknowledgements

Here already? It's time for me to thank everyone who has been of help, and take the Mickey out of everyone else. Even as I start to think of all the people who deserve a mention here, I start to feel nostalgic and wish I could be back.

First and foremost I would like to thank Malcolm Coe for his supervision and encouragement. Sorry it took so long! I expect that you didn't believe that I would ever finish this – I'm glad to prove you wrong, and I hope that it's worth the wait.

Thanks to Chris, for being a great mate all these years, and being an inspiration to me by finishing yours first! Thanks for the trips, for the Bank of Chris, driving me to Safeway's, introducing me to the joys of whisky (why start with a White Horse though?), and most of all, for agreeing to be my best man, and not embarrassing me too much in the speech. Top work fella.

Also many thanks to the rest of the Be/X-ray binary *massive*...

Iain Steele - for showing me how to recover from a taxi ride in La Palma, (I'm afraid it didn't help me the next time).

Nacho – can we have our stereo back please?

Simon 'Clarkie' Clark - thanks for all the encouragement along the way (I'm talking about the encouragement toward lunchtime pints), and for having some decent musical taste (though you really didn't get it about Paradise Lost did you?).

Pablo 'Pau' 'El Ligon' Reig - cheers for help, discussions, beers, strange Spanish humour, and for making great paella. Thanks for the beers in Crete as well. I hope everything works out just fine, and hope neither of us will be buying whisky for the other for a long time.

Thanks to 'Hairy' Nick Haigh - for being hairy (what else) and for livening up the office after Nacho nicked our stereo. Many thanks for the best observing trip ever ("and it is a trip").

And other Astronomy people...
Dave Buckley – massive thanks for all your help. For obtaining data, for hospitality in Cape Town and Sutherland (thanks also to Jean). Sorry you didn't like the Pixes (or any of my music collection come to think of it...).

Thanks to Tom Marsh for helpful discussions and a couple of observations.

Thanks to Andy Newsome for having all the answers when my C code core dumped, and for being living proof to convince me that growing long hair would have been very BAD.

Thanks to Charlotte for being blond and dizzy, and to Rachel for just being dizzy. Many thanks for putting me up when I've needed to visit Southampton to get this finished. Hope I didn't leave you with too much washing-up.

And all the people in my post-Astronomy life...

Thanks to my new employers, PricewaterhouseCoopers, for giving me a job and paying off my student debts for me.

Thanks to 'Sheriff' Shu Pillinger and 'Regular' Matt Ember for being English at a time when no one else was, for memories of cerveza and cava and dry cleaned

socks with lottery tickets stapled inside, Barcelona Vs Brazil in the pouring rain and 2 hour lunch breaks by the beach in the sun.

Thanks to James Hector Stevens, for being the only person I've ever met with the same name as me, and then working with me and confusing our secretary into psychiatric problems.

Thanks to the rest of the November 2nd posse, the ETL's (Niel 'spell yer name right' Copeland, Steve 'I think my hair's on fire but, huh...' Harmer, Charlotte 'Dizzy – must be the name' McAllister and Jo Malhotra) and the rest of the gang – Big, Bernie, Scoot, JBInit(), Farah, Dee, Fergal, Rich, Dom, Orla, Simon, Catriona, Vicky, Umair, Cagney.

Thanks to the L3 gang, Granty for showing me how to kick Kenan where it hurts, Mandy for being a cowboy and introducing everyone to the 'World of Pain', Big Pete for being more laid back than me. No thanks to *'Food-Trolley-Man'* for coming twice a day and making me fat.

Thanks to my Mum & Dad, for all their support and encouragement along the way, for a place to escape to in the holidays, and for occasional pestering to finish writing up. Hope you read it from cover to cover!

Last of all, but in no way least, and in many ways most. Many thanks, for many reasons, to my wife, Lisa, firstly for saying yes, for putting up with my habits, and pestering me to get this far. Thank-you for being so supportive, for putting up with my papers all over the spare room, and not complaining when I spend all weekend working. I honestly think that without you behind me, I'd never have been frightened enough to finish this. Hope you enjoy life as Mrs Dr Jim.

# Bibliograph y


Alcock C., Farhi E., & Olinto A., 1986, ApJ, 310, 261

Ando H., 1986, A&A, 163, 97

Aarons J., Lea S.M., 1980, ApJ, 235, 1016

Apparao K.M.V., Tarafdar S.P., 1986, A&A, 155, 423

Audley M., 1997, PhD thesis, NASA/Goddard, available at
http://lheawww.gsfc.nasa.gov/users/audley/diss/diss.html

Baade D., 1982, A&A, 105, 65

Baade D., 1984a, A&A, 134, 105

Baade D., 1984b, A&A, 135, 101

Balona L., 1994, MNRAS, 268, 119

Barat C., *et al.* 1984, ApJ, 285, 791

Bianchi L., & Bernacca P.L., 1980, A&A, 89, 214

Bildsten L., *et al.* 1997, ApJS, 113, 367

Bjorkmann J.E., & Cassinelli J.P., 1993, ApJ, 409, 429

Bjorkmann J.E., 1994, in *Pulsation, Rotation and Mass Loss in Early Type Stars*, IAU Symposium No. 162, Eds. Balona L.A., Henrichs H.F., le Contel J.M., (Kluwer, Dordrecht), p. 455

Bombaci I., & Datta B., 2000, ApJ, 530, *in press*

Bradt H.V., McClintock J., 1983, ARA&A, 21, 13

Bradt H.V., *et al.*, 1977, Nature, 269, 21

Braes L. L. E., & Miley G. K., 1971, Nature, 232, 246

Briot D., & Zorec J., 1994, in *Pulsation, Rotation and Mass Loss in Early Type Stars*, IAU Symposium No. 162, Eds. Balona L.A., Henrichs H.F., le Contel J..M., (Kluwer, Dordrecht), p 356

Bruhweiler F.C., Klinglesmith III A., Gull T.R., Sofia S., 1987, ApJ, 317, 152

Buckley D.A.H., Coe M.J., Stevens J.B., Angelini L., White N.E., Giommi P., 1998, IAU Circ, 6789

Burbidge G., 1972, Comments ApSS, 4, 105

Carter B.S., 1990, MNRAS, 242, 1

Chen et al. 1992, ApJ, 384, 604

Chiu H.Y., & Saltpeter E.E., 1964, Phys. Rev. Lett., 12, 413

Claret A., Giménez A., 1992, A&AS, 96, 255

Clark G., Doxsey R., Li F., Jernigan J. G., van Paradijs J., 1978, ApJ, 221, L37

Clark J.S., 1997, PhD thesis, University of Southampton

Clark J.S., & Steele I.A.S., 2000, A&AS, 141, 65

Coe M.J., Everall C., Fabregat J., Gorrod M.J., Norton A.J., Reglero V., Roche P., Unger S., 1993, A&AS, 97, 245

Cook M.C., Warwick R.S., 1987a, MNRAS, 225, 369

Cook M.C., Warwick R.S., 1987b, MNRAS, 227, 661

Corbet R.H.D,. 1984, A&A, 141, 91

Corbet R.H.D., 1984...

Corbet R.H.D., Mason K.O., Branduardi-Raymont G., Cordova F.A., Parmar A.N., 1985, MNRAS, 212, 565

Corbet R.H.D., 1996, ApJ, 457, L31

Corbet R.H.D., Remillard R., 1996, IAU Circ., 6486

Corbet R., Marshall F.E., Lochner J.C., Ozaki M., Ueda Y., 1998a, IAU Circ, 6788

Corbet R., Marshall F.E., Lochner J.C., Ozaki M., Ueda Y., 1998b, IAU Circ, 6803

Coté & Waters 1987, A&A, 176, 93

Crawford D.L., 1978, AJ, 83, 48

Crawford D.L., Mander J., 1996, AJ, 71, 114

Dachs J., Wamstecker W., 1982, A&A, 107, 240

Dachs J., Hanuschik R., Kaiser D. Rohe D., 1986, A&A, 159, 276

Dachs J., Kiehling R., Engels D., 1988, A&A, 194, 167

Davidson K., Ostriker J.P., Ap J., 179, 585

Densham R.H., Charles P.A., 1982, MNRAS, 201, 171

Dougherty S.M., & Taylor A.R., 1992, Nature, 359, 808

Dougherty S.M., & Taylor A.R., 1994, in *Pulsation, Rotation and Mass Loss in Early Type Stars*, IAU Symposium No. 162, Eds. Balona L.A., Henrichs H.F., le Contel J.M., (Kluwer, Dordrecht), p. 416

Dower R.G., Apparao K.M.V., Bradt H.V., Doxsey R.E., Jernigan J.G., Kulik J., 1978, Nature, 273, 364

Fabregat J., Reglero V., 1990, MNRAS, 247, 407

Feast M.W., 1961, MNRAS, 122, 1

Giacconi R., *et al.,* 1971, ApJ, 167, L67

Glass I.S., 1979, MNRAS, 187, 807

Ghosh P., Lamb F.K., 1978, Ap J., 223, L33

Ghosh P., Lamb F.K., 1979a, Ap J., 232, 259

Ghosh P., Lamb F.K., 1979b, 234, 296

Grebel E.K., 1997, A&A, 317, 448

Grebenev S.A., Pavlinski M.N., Syunyaev R.A., 1992, SvA Lett., 18, 228

Hammerschlag-Hensberge G., *et al.*, 1980, A&A, 85, 119

van den Heuvel E.P.J., & Heise J., 1972, *Nature Phys. Sci.*, 239, 67

van den Heuvel E.P.J., Habets G.M.J., 1984, Nature, 309, 591

Hjellming R.M., & Wade C.M., 1971, ApJ, 168, L21

Hummel W., & Vrancken, M., 1995, A&A, 302, 751

Hutchings J.B., Crampton D., Cowley A.P., 1981, AJ, 86, 871

Inoue H., Koyama K. & Tanaka Y., 1983 in *Supernova remnants and their X-ray emission* Eds. Danziger I.J., Gorenstein P., (Reidel, Dordrecht), p. 237

Israel G.L., 1998, IAU Circ., 6822

Israel G.L., Angelini L., White N.E. & Giommi P., 1995, IAU Circ., 6277

Israel G.L., Stella L., Angelini L., White N.E., Giommi P. & Covino S., 1997, ApJ., 484, L141

Jascheck M., Sletteback A., & Jascheck C., 1981, Be star Newsletter, 4, 9

Jernigan J.G., Bradt H., van Paradijs J., Rappaport S., 1978, IAU Circ., 3225

Johnston M.D., Bradt H.V., Doxsey R.E., 1979, ApJ, 233, 514

Joss P.C., Rappaport S.A., 1984, AnRevA&A, 22, 537

Kahabka P., Pietsch W., 1996, (KP1996) A&A, 312, 919

Kahabka P., Pietsch W., 1998, IAU Circ., 6840

Kaiser D., 1989, A&A, 222, 187

van der Klis M., van Paradijs J., Charles P.A., Thorstensen J.R., Tuohy I., Elso J., 1983, MNRAS, 203, 279

de Kool M., van den Heuvel E.P.J., Pylyser E., 1987, A&A, 183, 47

Kulkarni S.R., et al. 1998, Nature, 393, 35

Kulkarni S.R., et al. 1999 Nature, 398, 389

Lamb R.C., Market T.H., Hartman R.C., Thompson D.J., Bignami G.F., 1980, ApJ, 239, 651

Lee U., Saio H., & Osaki Y., MNRAS, 250, 432

Lewin W.H.G., van Paradijs J., van den Heuvel E.P.J., 1995 (Eds.) *X-ray binaries* (Cambridge University Press, Cambridge)

Manfroid J., *et al.*, 1991, *First Catalogue of Stars Measured in the Long–Term Photometry of Variables Project (1982 – 1986)*, ESO Scientific Report No. 8

Maraschi L., Treves A., & ven den Heuvel E.P.J., 1976, Nature, 259, 292

Marshall F.E., Lochner J.C., 1998, IAU Circ., 6818

Melia F., 1988, ApJ, 335, 965

Melia F., Rappaport S., & Joss P.C., 1986, ApJ, 305, L51

Menzies J.W., Cousins A.W.J, Banfield R.M., Laing J.D., 1989, SAAO Circulars, 13, 1

Mereghetti S., Bignami G.F., Caraveo P.A., Goldwurm A., 1987, ApJ, 312, 755

Meurs E.A., & van den Heuvel E.P.J., 1989, A&A, 226, 88

Miller G.E., & Scalo J.M.,. 1979, ApJS, 41, 513

Negueruela I., 1997a, PhD thesis, University of Southampton

Negueruela I., *et al.*, 1997b, MNRAS, 284, 859

Norton A.J., *et al.*, 1994, MNRAS, 253, 579

Osaki Y., 1986, PASP, 98, 30

Okasaki, 2000, *private communication*

Paczyński B., & Pindor B., 2000, ApJ (*submitted*)

Pakull M., Motch C., & Lub J., 1980, IAU Circ., 3476

Pakull M., 1989, in *Recent Developments of Magellanic Cloud Research,* Eds. de Boer K.S., Spite F., Stasinska G. (Observatoire de Paris, Paris)

Pakull M., Brunner H., Pietsch W., Taubert R., Beurmann K., van der Klis M., Bonnet-Bidaud J.M., 1985, Space Sci. Rev., 40, 371

van Paradijs J., 1995, in *X-ray Binaries*, Eds: Lewin W.H.G., van Paradijs J, & van den Heuvel E.P.J. (Cambridge University Press) p. 536

van Paradijs J., 1998, (astro-ph 9802177)

Preidhorsky W.C., & Terrel J., 1983, ApJ, 273, 709

Rappaport S.A., Zaumen W., & Doxsey R., 1971, ApJ, 168, L17

Rappaport S.A., Joss P.C., 1983, in *Accretion-Driven Stellar X-ray Sources*, ed. Lewin W.H.G., van den Heuvel P.J., (Cambridge University Press)

Reig P., Fabregat J., Coe M.J., Roche P., Chakrabarty D., Negueruela I., Steele I., 1996a, A&A, 311, 879

Reig P., Coe M.J., Stevens J.B., Negueruela I., Clark J.S., Buckley D.A.H., Fabregat J., Roche P., 1996b, in *2nd Integral Workshop – The Transparent Universe*, ESA SP-382

Reig P., Fabregat J., Coe M.J., 1997, A&A, 322, 193

Reig P., Stevens J.B., Coe M.J., Fabregat J., 1998, MNRAS, 301, 42

Roche P., *et al.*, 1993, A&A, 270, 122

Santangelo A., Cusumano G., IAU Circ., 6818

Schmidte P.C., Cowley A.P., Frattare L.M., McGrath T.K., Hutchings J.B., Crampton D., 1994, PASP, 106, 843

Schrier E., *et al.* 1972, ApJ, 172, L112

Shklovsky I. S., 1967, ApJL, 148, L1

Shortridge K., 1991, *Starlink Miscellaneous User Document no. 13*, Rutherford Appleton Laboratory

Smith M.A., 1989, ApJS 71, 357

Staveley-Smith L., Sault R.J., Hatzidimtrou D., Kesteven M.J., McConnel D., 1997, MNRAS, 289, 225

Stella L., White N.E., Rosner R., 1986, ApJ, 308, 669

Sterken C., *et al.*, 1995, A&AS, 113, 31

Stevens J.B., Reig P., Coe M.J., Buckley D.A.H., Fabregat J., Steele I.A., 1997, MNRAS, 288, 988

Stevens J.B., Buckley D.A.H., Coe M.J., 1999, MNRAS, 309, 421

Stevens J.B., Coe M.J., Buckley D.A.H., 2000, *in preparation*

Struve O., 1931, ApJ, 73, 94

Taylor A.R. et al. 1987, MNRAS, 228, 111

Taylor A.R., Dougherty S.M., Waters L.B.F.M., Bjorkman K.S., 1990, A&A, 231, 453

Telting & Kaper, 1994, A&A, 284, 515

Telting J.H., Heemskerk M.H.M., Henrichs H.F., Savonije G.J., 1994, A&A, 288, 558

Terrel J., Preidhorsky W., 1984, ApJ, 285, L15

Vakili F., Mourard D., Stee P., 1994, IAUS, 162, 435

Verbunt F., & van den Heuvel E.P.J., in *X-ray Binaries*, Eds: Lewin W.H.G., van Paradijs J, & van den Heuvel E.P.J. (Cambridge University Press) p. 457

Vogt S.S., Penrod G.D., 1983, ApJ, 275, 661

Walborn N.R., Fitzpatrick E.L., 1990, PASP, 102, 379

Wang Q., Wu X., 1992, ApJS, 78, 391

Warwick R.S., Watson M.G., Willingdale R., 1985, Space Sci. Rev., 40, 429

Waters L.B.F.M., 1986, A&A, 162, 121

Waters L.B.F.M., Cote J., & Lamers H.J.G.L.M., 1987, A&A, 185, 206

Waters L.B.F.M., Taylor A.R., van den Heuvel E.P.J., Habets G.M.H.J., Persi P., 1988, A&A, 198, 200

Waters L.B.F.M., et al. 1991, A&A, 244, 120

Waters L.B.F.M., Marlborough J.M.,. 1994,

Watson M.G., Warwick R.S., Ricketts M.J., 1981, MNRAS, 195, 197

Westerlund B.E., 1979, *The Magellanic Clouds*, Cambridge University Press, Cambridge.

White N.E., Parkes G.E., Sanford P.W., Mason K.O., Murdin P.G., 1978, Nature, 274, 664

White N.E., Becker R.H., Pravdo S.H., Boldt E.A., Holt S.S., Serlemitos P.J., 1980, ApJ, 239, 655

White N.E., Swank J.H., Holt S.S., 1983, ApJ, 270, 711

Wilson R.B., Finger M.H., Stollberg M., Prince T.A., Grunsfeld J.M., Harmon B.A., Zhang S.N., 1994, IAU Circ., 5955

Yokogawa J., Koyama K., IAU Circ., 6835

Zaal P.A., Waters L.B.F.M., Marlborough J.M., Geballe T.R., 1994, in *Pulsation, Rotation and Mass Loss in Early Type Stars*, IAU Symposium No. 162, Eds. Balona L.A., Henrichs H.F., le Contel J.M., (Kluwer, Dordrecht), p. 420

Zhang S.N., *et al.* 1996, A&AS, 120, 227